LEVERAGING FIRST-PRINCIPLES MODELING FOR DEEPER INSIGHTS INTO BIOMASS PROCESSING

by

Tyler Ray Josephson

A dissertation submitted to the Faculty of the University of Delaware in partial fulfillment of the requirements for the degree of Doctor of Philosophy in Chemical Engineering

Spring 2017

LEVERAGING FIRST-PRINCIPLES MODELING

FOR DEEPER INSIGHTS INTO BIOMASS PROCESSING

by

Tyler Ray Josephson

Approved: _____

Abraham M. Lenhoff, Ph.D.
Chair of the Department of Chemical and Biomolecular Engineering

Approved: _____

Babatunde A. Ogunnaike, Ph.D.
Dean of the College of Engineering

Approved: _____

Ann L. Ardis, Ph.D.
Senior Vice Provost for Graduate and Professional Education

I certify that I have read this dissertation and that in my opinion it meets the academic and professional standard required by the University as a dissertation for the degree of Doctor of Philosophy.

Signed: _____

Dionisios G. Vlachos, Ph.D.
Professor in charge of dissertation

I certify that I have read this dissertation and that in my opinion it meets the academic and professional standard required by the University as a dissertation for the degree of Doctor of Philosophy.

Signed: _____

Stavros Caratzoulas, Ph.D.
Professor in charge of dissertation

I certify that I have read this dissertation and that in my opinion it meets the academic and professional standard required by the University as a dissertation for the degree of Doctor of Philosophy.

Signed: _____

Raul F. Lobo, Ph.D.
Member of dissertation committee

I certify that I have read this dissertation and that in my opinion it meets the academic and professional standard required by the University as a dissertation for the degree of Doctor of Philosophy.

Signed: _____

Bingjun Xu, Ph.D.
Member of dissertation committee

I certify that I have read this dissertation and that in my opinion it meets the academic and professional standard required by the University as a dissertation for the degree of Doctor of Philosophy.

Signed: _____

J. Ilja Siepmann, Ph.D.
Member of dissertation committee

To know wisdom and instruction,
to understand words of insight,
to receive instruction in wise dealing,
in righteousness, justice, and equity;
to give prudence to the simple,
knowledge and discretion to the youth -
Let the wise hear and increase in learning,
and the one who understands obtain guidance,
to understand a proverb and a saying,
the words of the wise and their riddles.

King Solomon, *c. 970–931 BC*

ACKNOWLEDGEMENTS

Scientific research is increasingly interdisciplinary and collaborative, and my work does not stand alone. Over the years I have spent at the University of Delaware, I have come to know many talented people who have helped me, guided me, developed me, and supported me.

First, my advisor Dion Vlachos, who has inspired me as a scientist and a leader. I am grateful to you for guiding the trajectory of my PhD, connecting me with collaborators, and teaching me how to promote and communicate my research in presentations and proposals.

Equally as important, my advisor Stavros Caratzoulas, who has served as my technical mentor, trained me in MD and DFT, and taught me to be fastidious in research and to be skeptical of my own work; I have become a better scientist and researcher because of you.

My dissertation committee. Each of you has had a unique contribution to this dissertation, and has helped mold the research and myself as a scientist.

My fellow researchers who have contributed experiments and calculations to the work culminating in this thesis, George, Christina, Vlad, Jeff C., Glen, Jack, and Lisa, as well as Kramer Brand, Jay Labinger, and Mark Davis at CalTech, and Limin Ren, Qiang Guo, Robert DeJaco, Swagata Pahari, Michael Tsapatsis, and Ilja Siepmann at the University of Minnesota. Special Vlachos group members who have provided feedback, ideas, and friendship include my officemates Jeff, Sai, Evangelos, Jack, and Lisa, my frequent conference travel buddies Glen, Alex, and Stephen, as well as Matt M., Taylor, Hannah, Molly, and Sunitha. Thank you for joining me on these adventures in catalysis.

Lanny Schmidt for introducing me to biomass catalysis and reaction engineering, and for inspiring me with his vision for farm-scale biorefineries.

My community in Newark, who has provided friendship, prayers, and encouragement throughout my PhD. These include my roommate and best man, Jeff Ralston, my friends in InterGrad Christian Fellowship, Abby, Yun, Anne, Becky, Heather, Kofi, Offei, Julie, Baily, Madelyn, Katie, Elisabethe, and Tyler, and my church family at Calvary Baptist Church, especially CG and Liz, Mary Elizabeth, Annette, Lloyd, and my Sunday School students, and my classmates in Chemical Engineering, especially Scott, Stephen, and Eyas.

My parents, Donalee and Kirby, for your love, care, wisdom, and example, and for encouraging and nurturing my early love for science and sustainability.

My wife Lilian for your constant love and support, for your patience, wisdom, advice, and insight, for believing in me, for managing and organizing countless things in my life, and for your utter care and concern for my well-being and my future.

And finally my Lord and Savior, Jesus Christ; your unconditional love offers me peace and contentment when I struggle, and your perfect example and sacrifice offer me humility and perspective when I succeed.

TABLE OF CONTENTS

LIST OF TABLES

LIST OF FIGURES

ABSTRACT

Demands for sustainable products are increasing due to growing awareness of the environmental liabilities of petroleum-derived fuels and chemicals. This has driven investment in alternative, renewable chemicals from biomass. To enable production of these new chemicals, novel processes and catalysts must be developed to achieve efficient processes with high yields. However, designing catalysts and reactors for biomass presents new challenges in catalysis, including catalysis of highly oxygenated biomass feedstocks with diverse functional groups, and accounting for reactions in the condensed phase.

One such process is the "furans platform," in which biomass-derived sugars are dehydrated to form furan derivatives, which can be modified to form a wide variety of useful fuels and chemicals. 5-hydroxymethylfurfural (HMF) is one of these furan derivatives, and can be produced from cellulose through isomerization of glucose to fructose, and dehydration of fructose to HMF. Major issues in HMF production include the high cost of fructose, as well as side reactions in dehydration. To address these concerns, we have leveraged electronic structure calculations to better understand (1) solvent effects relevant to HMF stability, (2) the active sites in catalysts for glucose isomerization, and (3) fructose ketalization reaction that boosts fructose yields from glucose via a new catalyst.

In the acid-catalyzed dehydration of fructose, the stability of the product HMF was found to be dramatically improved by the addition of certain organic co-solvents, but the fundamental reasons were not understood. To develop deeper fundamental understanding into these interactions and their effects on reaction chemistry, electronic structure calculations are integrated with IR spectroscopy and kinetic studies conducted by experimentalists in the Catalysis Center for Energy Innovation (CCEI).

HMF stability and solvation are probed using IR spectroscopy, and an important descriptor of the observed solvent-induced frequency shifts is identified: the Guttman Acceptor Number (AN), a measure of solvent Lewis acidity. Using a model that accurately predicts the solvent-induced frequency shifts, the underlying mechanisms behind the shifts are discovered and the origin of the stability of HMF in co-solvent mixtures is identified.

Glucose isomerization to fructose is a critical step in forming HMF, and the Sn-Beta zeolite is a useful heterogeneous Lewis acid catalyst for isomerization. However, Sn-Beta as-synthesized contains a distribution of active sites, and modifications of the zeolite, for example, with Na-exchange, affect these active sites and their chemistry. To better understand the complex heterogeneous Sn-Beta, three homogeneous analogues (Sn-silsesquioxanes) are synthesized and characterized by CCEI experimentalists to investigate how particular changes in the active site structure affect glucose isomerization to fructose and to mannose, a side product. In addition, reaction networks for glucose isomerization are computed using electronic structure methods. Integrating these experiments with theory leads to new understanding on the catalytic roles of the Sn-O-Si moiety, the acetylacetonate ligands, and the SiOH group, for these sugar chemistries.

To characterize the distribution of active sites in Sn-Beta, an exhaustive survey is performed to probe the relative stability of the possible open site geometries. The T1 and T9 sites are most thermodynamically favored, although substitution at the different T sites yielded fairly similar energies. More importantly, the relative positions of the SnOH and the SiOH in the open site are not adjacent, as reported in prior literature, but the SiOH is opposite the SnOH. This geometry creates unusual Brønsted acidity when strong bases, such as NH3 and pyridine, are adsorbed, because the Sn can stabilize the SiOH oxygen, increasing the acidity of the proton. Characterizing the active site of Sn-Beta, as well as identifying the source of Brønsted acidity inferred by recent experiments, could assist future modeling efforts that utilize this active site geometry.

The highest glucose to fructose yield by Sn-Beta is 33%, but a new catalyst, Sn-SPP (Self-Pillared Pentasil zeolite with framework Sn sites) can achieve a record 65%

yield. In ethanol solvent, Sn-SPP catalyzes a novel reaction: fructose ketalization to ethyl fructoside. When coupled with glucose isomerization to fructose, ketalization removes the fructose product in situ, permitting yields greater than the glucose/fructose equilibrium without ketalization (50%). However, many fundamental questions were unanswered by the experimental work, including how the structure of the active site enables this chemistry, why Sn-SPP performs ketalization while Sn-Beta does not, and why fructose ketalization is catalyzed but not glucose acetalization. These questions are answered using periodic DFT calculations. The most thermodynamically stable active site geometries indicate the active site of Sn-SPP is a "closed" Sn site with three adjacent silanol groups, while the active site of Sn-Beta is a hydrolyzed Sn site with a single, more distant silanol group. Identification of the most favorable ketalization mechanism reveals that the silanols in Sn-SPP facilitate ketalization through key H-bonding interactions at the transition state. However, the silanol in the Sn-Beta active site is not positioned to stabilize the TS, giving a larger barrier and indicating why Sn-Beta is not active for this chemistry. Analyzing glucose acetalization reveals differences in stability of the key oxonium intermediate at the respective transition states, indicating the reason for the remarkable selectivity of this process for fructose ketalization over glucose acetalization.

In summary, this dissertation contributes the first computational study on solvent-induced frequency shifts and their role in solvation and determination of liquid structure, which contributed to understanding of the enhanced stability of HMF by polar aprotic co-solvents. In addition, reaction mechanisms are presented for glucose isomerization on homogeneous Sn-silicate catalysts, and the role of catalyst structure on reactivity and selectivity. Key features of the Sn-Beta active site were identified, explaining the observed Brønsted acidity in Sn-Beta. The first computational study of ketalization and acetalization is also presented here, in the context of explaining the unique reactivity of the mesoporous Sn-SPP due to its unique active site.

Application of computational modeling will continue to improve fundamental understanding of biomass catalysis. Several next steps inspired by the current work

are discussed, including pairing DFT with other spectroscopic techniques to characterize liquid structure, developing water-stable Sn-silsesquioxanes for Sn-Beta active site characterization, and leveraging fructose ketalization as protecting-group chemistry to improve yields in one-pot glucose to HMF reactors.

Chapter 1

INTRODUCTION

1.1 Biomass as a Renewable Chemical Feedstock

For more than a century, petroleum has served as the foundation for the fuel and chemical industries, driving the global economy and enabling our modern transportation, agriculture, and industrial systems. As the world population grows to nearly 10 billion by 2050 [1], and as developing nations raise their standard of living, demand for energy and chemicals is expected to increase [2, 3].

As a fossil resource, petroleum is non-renewable, and an oil-dependent economy is ultimately unsustainable; the "peak oil" hypothesis predicts that as supply becomes scarce, production becomes more expensive until it peaks and declines, with devastating effects on industries dependent on cheap oil [4–6]. While the recent expansion of hydraulic fracturing has revitalized oil production in the United States and reduced oil prices around the world, these unconventional sources are still finite. Moreover, the environmental liabilities of an oil-dependent economy include climate change due to greenhouse gas emissions [7], catastrophic oil spills [8, 9], and earthquakes associated with wastewater disposal from hydraulic fracturing [10].

These concerns have spurred investment in alternative energy sources, including solar, wind, geothermal, and nuclear energy, as well as electric vehicles to harness low-carbon electricity for transportation. Renewable chemicals, however, must still be made of carbon, and biomass is the only feasible source of renewable, fixed carbon for chemicals applications or high-energy density fuels. (CO_2 is another source of carbon for sustainable fuels and chemicals, but all routes for CO_2 valorization require substantial energy inputs.)

A vision for a renewable chemical industry is no new concept. Bio-based fuels have been around even longer than petroleum; in fact, the very first internal combustion engine prototype operated on alcohol fuel in 1826 [11]. Henry Ford considered ethanol to be the "fuel of the future" in 1925, envisioning fuel produced "from apples, weeds, sawdust – almost anything. There is fuel in every bit of vegetable matter that can be fermented." [12] Instead, petroleum-based fuels would dominate in the 20th century, supplying over 95% of transportation fuels [3]. Nonetheless, a strong bio-based product industry has been growing. Currently, worldwide production of corn- and sugar cane-derived ethanol fuel is 26,600 million gallons/year [13], with cellulosic ethanol contributing 190 million gallons in 2016, up from 33 million gallons in 2014, when the first commercial cellulosic ethanol plants came online [14]. Should the lignocellulose-derived fuels industry continue to grow, about 1 billion tons of biomass could be sustainably harvested in the United States – enough to meet 30% of our current transportation fuel demand. [15–17] Lately, this vision has expanded beyond ethanol and fermentation to the concept of the integrated "biorefinery," where the cellulose, hemicellulose, and lignin fractions of biomass are separated, processed, and upgraded into a diverse slate of chemical products, akin to crude oil processing in a refinery [18–22].

The biorefinery is a farm- or cooperative-scale processing plant that uses local biomass to meet local fuel or fertilizer needs, as well as to create value-added chemicals for global markets. Although they do not benefit from traditional economies of scale, small-scale systems require less capital investment and less water, power, and transportation infrastructure than massive chemical plants [20, 22]. Such a technology could be smoothly integrated into existing agricultural enterprises, as well as adopted by small communities or developing nations which have biomass resources, but lack the infrastructure and capital that would be required to harness it. A network of such plants would be a powerful asset for struggling rural economies around the world, as well as a force for sustainability, energy independence, and environmental stewardship. However, for biofuels to be truly sustainable, they must not interfere with food production or contribute to unsustainable water use [23]; utilization of waste biomass often

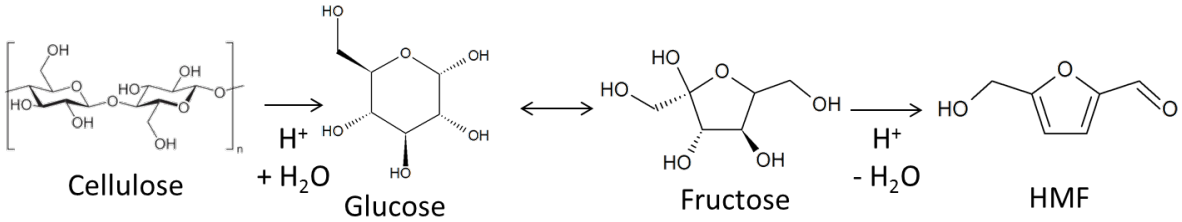

Figure 1.1: Scheme for producing 5-hydroxymethylfurfural (HMF) from the cellulose fraction of lignocellulosic biomass.

offers the greatest environmental benefits [24].

These motivations drove significant research efforts for biorefinery platforms in the late 2000s and early 2010s. A landmark 2004 study by the Department of Energy [25], "Top Value-Added Chemicals from Biomass" identified 12 bio-based molecules with high potential for becoming successful biorefinery platform chemicals. The progress made since then is remarkable: routes to produce all of them have been demonstrated in academic labs, and seven in particular are on their way to commercialization [26].

One category of products highlighted in that study are furan derivatives. Several reviews [27–29] have outlined the vast chemistries possible for these platform chemicals. One furan derivative, 5-hydroxymethylfurfural (HMF), can be produced through dehydration of fructose, which can be derived from glucose, the monomer in cellulose and starch, major components of lignocellulosic biomass (Fig. 1.1). HMF is a versatile platform chemical that can be transformed into a wide variety of useful value-added chemical intermediates (Fig. 1.2), including high-octane fuel additives, such as dimethylfuran [30], p-xylene for PET plastics [31–33], monomers for polyesters [34, 35], and renewable PEF plastics from 2,5-furandicarboxylic acid, which are being commercialized by Avantium [36].

However, there is significant interest in improving efficiency of HMF production. For example, in renewable p-xylene production, technoeconomic [37, 38] and life-cycle analyses [39] have shown the significant energy savings and environmental benefits of renewable p-xylene compared to the petroleum case, but have also shown that the high

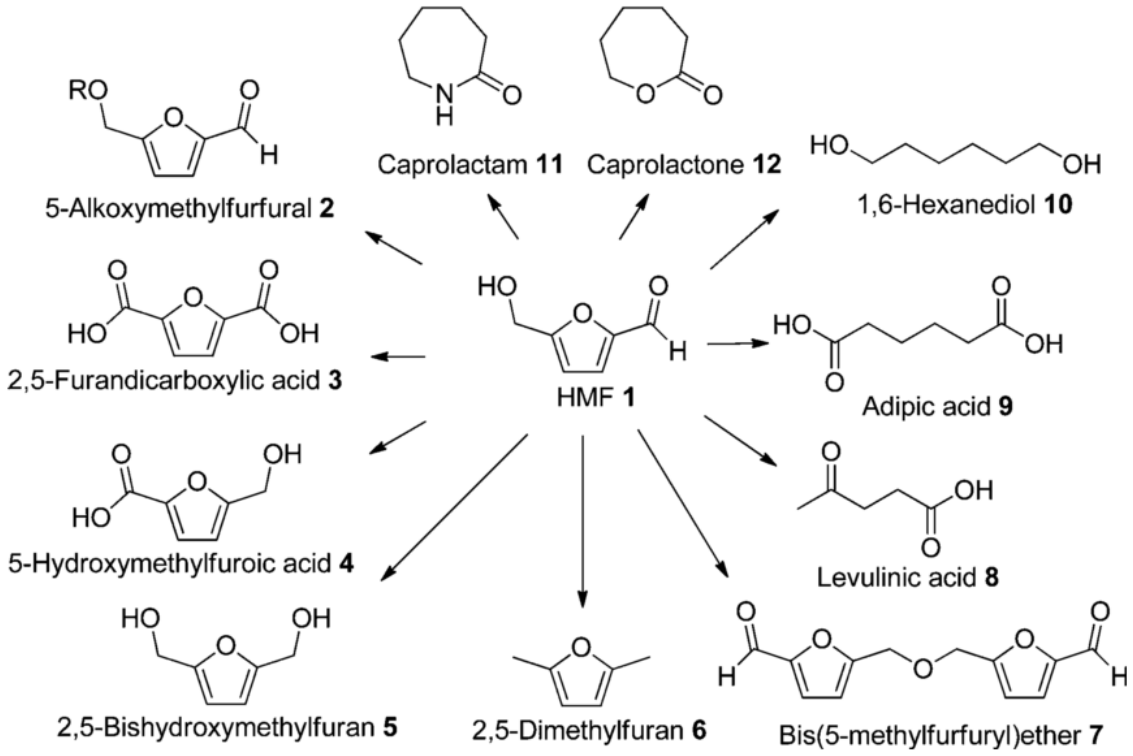

Figure 1.2: HMF as a platform chemical, from van Putten, et al. [29]

cost of HMF is a bottleneck in process viability. Many efforts to improve the efficiency of HMF production from lignocellulosic biomass have targeted improvements to the upstream processes, including cellulose hydrolysis, glucose isomerization, and fructose dehydration, as well as tandem reaction schemes to integrate these processes. Notable success stories involve the use of phase modifiers and co-solvents to improve fructose dehydration to HMF [40], and the Sn-Beta zeolite for enabling glucose isomerization under aqueous, acidic conditions [41], and a one-pot synthesis of HMF from glucose [42].

1.2 Solvation Effects in Biomass Processing

Because most biomass derivatives are not volatile (when heated, sugar decomposes into caramel long before it evaporates), reactions frequently occur in the condensed phase, and the choice of reaction medium is a critical process parameter. Solvents are used to dissolve reagents, extract products, suspend catalysts, and facilitate heat transfer. In addition, complex interactions between solvents, solutes, and catalysts can influence reactivity and selectivity.

Solvent selection has been particularly important in fructose dehydration to HMF. Water is a logical solvent for fructose dehydration – it's cheap, abundant, safe, and even present to some degree whenever biomass is harvested. Sugars are also highly soluble in water, enabling glucose isomerization to fructose in sugar concentrations as high as 45 wt% [41]. Moreover, three molecules of water are produced for every molecule of HMF produced, so it will be present in the reaction medium to some extent. Unfortunately, side reactions during dehydration in water are significant – HMF undergoes rehydration reactions to form levulinic acid, and polymerization reactions consume fructose and HMF forming tar-like humins. Consequently, experimentalists have tested a wide range of solvents through trial-and-error to identify effective processes.

The Dumesic group performed fructose dehydration in the aqueous phase with continuous extraction of the product HMF to an organic phase, to prevent side reactions

of HMF and separate the product [40]. Addition of dimethylsulfoxide (DMSO) to the aqueous phase improved the yields to this reaction even further [40]. The addition of inorganic salts to the aqueous phase can boost HMF selectivity by improving the partition coefficient of HMF into the organic phase [43]. Since then, a wide range of extracting solvents and co-solvents have been tested [43–45], including tetrahydrofuran, acetonitrile, numerous alcohols, numerous ketones, and gamma-valerolactone (GVL), which is a particularly attractive green solvent because it can be produced from fructose in a GVL reaction medium [46–49]. However, the fundamental reasons behind the effect of co-solvents in promoting fructose dehydration and inhibiting HMF side reactions remain unknown.

1.3 Biomass catalysis with zeolites

Zeolites are crystalline, nanoporous aluminosilicate materials with abundant applications in catalysis and separations. Comprised of tetrahedral Si^{4+} and Al^{3+} centers, connected by oxygens, they form 5 – 12 Å wide channels and cavities in networks of 1-, 2-, or 3-dimensional channels. These pore sizes are on the same order of molecule sizes, and tailoring the size and shape of zeolite pores and channels enables precise control over diffusion and adsorption. The size- and shape-selective pore functionality is coupled with catalytic activity, most commonly generated through Al incorporation into the framework to generate Brønsted acid sites.

Synthetic faujasite zeolites were introduced in 1962 for fluid catalytic cracking (FCC) units for gasoline production from crude oil, which were not only orders of magnitude more active than the incumbent amorphous silica-alumina catalysts, but also gave improved yields to gasoline. Faster reactions and reduced coke formation enabled numerous process engineering improvements, adding on the order of $10 billion/year in value through energy savings and increased yields compared to the amorphous silicate materials previously used [50]. Later, zeolites would be introduced for hydrocracking of heavy distillates, isomerization of gasoline to boost octane number, and the synthesis of the high-volume plastic monomers para-xylene and ethyl-benzene [50].

Hoping to leverage the same degree of control in biomass catalysis, many research groups have been studying zeolites for biomass conversion [51, 52]. One particularly promising class of materials is Lewis acidic zeolites, which incorporate Ti, Zr, Nb, Sn, Hf, or Ta into the zeolite framework [52–55]. Lewis acids are electron acceptors, and they are particularly effective for activating electron-rich carbonyl-containing molecules. Corma and coworkers pioneered the synthesis of hydrophobic Lewis acid zeolites, in particular Ti-Beta [56] and Sn-Beta [57], which they found to be active for selective oxidation of ketones [57]. Since then, many studies have shown Sn-Beta to catalyze a diverse range of carbonyl-activating chemistries, including the Baeyer-Villiger oxidation of ketones to lactones [57, 58], Meerwein-Ponndorf-Verley (MPV) reduction of aldehydes and ketones [59, 60], carbon-carbon coupling with aldehydes [61, 62], isomerization of glucose to fructose [41, 63, 64] and to mannose [65], aldol condensation [62, 66], catalytic transfer hydrogenation and etherification [67], and conversion of sugars to lactates [68].

Glucose isomerization to fructose in particular is a critical step for production of HMF. Glucose isomerization is already a mature industrial process, in fact the largest-scale biomanufacturing process, used to produce high-fructose corn syrup (HFCS); worldwide, 8.5 million tons of HFCS were produced in 2015 [69]. Immobilized glucose isomerase enzymes convert glucose in corn syrup into a 42% fructose solution [69–71], a fraction of which is concentrated to 90% using ion-exchange columns, which is then blended back with the 42% to form 55% HFCS, a drop-in sugar replacement with a sweetness matching that of sucrose. Although these have been demonstrated commercially at large scales, for biorefinery applications, these processes are too expensive, as well as less sustainable than processes starting from lignocellulosic biomass instead of food crops [23].

The Sn-Beta zeolite presents many advantages over the enzyme catalysis route: 1) it is more tolerant to impurities in the feed stream that deactivate the enzyme catalysts, 2) it is active at higher temperatures, permitting faster reactions, and 3) it is active under aqueous acidic conditions, permitting tandem reactions of glucose

isomerization with fructose dehydration to HMF43. However, the Sn-Beta zeolite not only catalyzes glucose isomerization to fructose, but epimerization to mannose as well, reducing fructose yields.

Optimizing these reactions and understanding the chemistry fundamentals has been difficult due, in part, to the complex nature of the active sites. When Lewis acids are substituted into the zeolite framework, they may be fully connected to the framework with four Sn-O-Si bonds (closed sites), or with one of these bonds hydrolyzed, forming a $SnOH(O\text{-}Si)_3$ and an adjacent silanol group (open sites). The distribution of these sites, as well as modification of these sites by ion-exchange [64], has been shown to affect reactivity and selectivity [64, 72, 73]. For example, Na-exchange of Sn-Beta or modification by borate salts shifts the product selectivity to mannose [64, 65]. Additional factors affecting catalyst performance include the zeolite framework type, its hydrophobicity and synthesis conditions, and the presence of extra-framework metal oxide clusters. Developing molecular understanding of the nature of these sites and their chemistry would aid in the search for improved catalysts and novel chemistries.

Homogeneous Lewis acids are interesting catalysts to compare to the Sn-Beta zeolite. In fact, the first study combining glucose isomerization with fructose dehydration to HMF was performed with homogeneous $CrCl_2$ in ionic liquids [74]. $CrCl_3$ is also a successful catalyst in water [75], where close examination of the metal salt speciation and the reaction kinetics has revealed $[CrOH]^{2+}$ to be the active species [76]. This active site comprises a Lewis acid (Cr^{3+}) and a Brønsted base (OH^-), both of which play important roles in catalyzing glucose isomerization [77]. The analogy between the homogeneous catalyst and the Sn-Beta open site is striking; Sn-Beta also contains a Lewis acid (Sn^{4+}) and a Brønsted base (OH^-). Although studying homogeneous Lewis acids can reveal important fundamental aspects of this chemistry, such as the influence of ionic radius on selectivity [78], they cannot be used to examine the influence of the zeolite framework, the effects of confinement, and the role of the nearby silanol group in the Sn-Beta open site. Moreover, homogeneous metal salts are less selective for fructose conversion than Sn-Beta [78].

1.4 Modeling with Density Functional Theory

Although commercial reactors are loaded with kilograms of catalyst and fed feedstock by the ton, chemical reactions occur molecule-by-molecule on discrete catalytic active sites. State-of-the-art work in catalysis aims to synthesize effective catalysts, characterize their active sites and their mechanisms of action, and then tailor them to accelerate desired reactions and inhibit side reactions to improve process efficiency. For all of these purposes, computational chemistry is becoming increasingly important to provide insight and guidance in the search for new materials optimized at the molecular level.

In modern science, matter is most fundamentally described using the language of quantum mechanics. The Schrödinger equation [79] is the most general description of quantum systems:

$$i\hbar\frac{\partial}{\partial t}\Psi(\mathbf{r},t) = \hat{H}\Psi(\mathbf{r},t) \tag{1.1}$$

where i is the imaginary unit, $\hbar$ is the reduced Planck constant, $\Psi(\mathbf{r},t)$ is the wavefunction of the quantum system with coordinates $\mathbf{r}$ and at time t, and $\hat{H}$ is the Hamiltonian operator, which characterizes the total energy of the system. For many atomic and molecular systems, the behavior of stationary states is most important, and the simpler time-independent Schrödinger equation can be used:

$$\hat{H}\Psi = E\Psi \tag{1.2}$$

which means, for a stationary state Ψ, when the Hamiltonian operates on the wavefunction Ψ, the result is the energy E of the stationary state multiplied by the wavefunction. The Schrdinger equation can be solved exactly for simple systems, such as the hydrogen atom, He^+, or H_2^+, but for larger systems involving multiple, highly-correlated electrons (most molecular systems of interest to engineers), exact solutions are computationally intractable.

One revolutionary approach for solving the Schrödinger equation is density functional theory (DFT), developed by Walter Kohn, Max Hohenburg, and Lu Jeu Sham [80, 81]. By recasting the Schrdinger equation in terms of the electron density, the computational cost for solving it can be dramatically reduced, enabling reasonably accurate calculations for large systems (up to a few hundred atoms) using modern supercomputers. Given the positions of atomic nuclei, DFT can be used to calculate the electron density and its energy using the self-consistent field calculation developed by Kohn and Sham [81]. Then, an optimization algorithm [82–84] perturbs the coordinates of the nuclei until a local energy minimum or saddle point (for transition states) is reached. Several features of the optimized structure can be compared to experiments, including bond lengths and angles, relative energies between different geometries (often achieving accuracy within 1-2 kcal/mol), and details in the electron density itself. DFT has been used to predict reaction thermochemistry [85–87], barriers of reaction pathways [87, 88], IR [89], Raman [90], NMR [91], and VCD [92] spectra, intramolecular and intermolecular interactions [86], semiconductor band gaps [93], and relative stability of crystal structures and phases [93].

Computational "experiments" like these have the advantages of being able to probe molecular and atomic details that are difficult to measure experimentally, studying unstable or toxic chemicals without risk, and setting up high-throughput screening studies for new materials at a fraction of the time and cost of synthesizing and testing each one. DFT has contributed to scientific understanding in such diverse applications as semiconductors and magnetic materials [94], transition metal catalysis [94–96], electrocatalysis [96, 97], zeolites [98–100], complex fluids [101], proteins and biomaterials [102–105], and drug discovery [106].

Since the 1980s, computer simulation has impacted almost all branches of zeolite research [107, 108], from zeolite synthesis [109–111], structure characterization [98, 112], diffusion [113, 114] and adsorption [115–117] in zeolite pores, chemical reactions at active sites [99, 100, 118, 119], to even prediction of novel frameworks [120] and their performance [121]. Likewise, computational modeling has often been integrated with

experimental work in the discoveries around Lewis acidic zeolites for biomass catalysis. DFT cluster models of Sn-Beta were used with IR spectroscopy of adsorbed CD_3CN to distinguish open and closed sites and first implicate open sites as the active sites [72]. The reaction mechanism for glucose isomerization and its rate-determining step was identified by integrating isotopic labelling and kinetic experiments [122] with reaction profiles computed using DFT [63]. Glucose isomerization reactivity trends among Lewis acids were also predicted using DFT [123]. However, several questions remained unanswered. The precise nature of the Sn-Beta active site is not understood, and there is much debate about the role of the silanol in the Sn-Beta open site, especially the mechanism behind the selectivity shift due to Na-exchange [123–126].

1.5 DFT and Vibrational Spectroscopy to Probe HMF Stability in Solution

Vibrational spectroscopies are powerful methods to characterize solute–solvent interactions. Because the vibrational spectra of solutions can be significantly affected by solvent–solvent, solvent–solute, and solute–solute interactions, they can be used as a tool to probe structure and interactions in the liquid phase [127–129]. Furthermore, understanding the structural and vibrational behavior of catalytic systems can assist in the development of new structure–activity relationships [130, 131].

In addition, DFT is quite accurate at predicting vibrational frequencies and their normal modes for gas-phase species [89]; because other species are quite distant, modeling individual molecules in isolation is a reasonable approximation. However, in the liquid phase, each molecule interacts dynamically with dozens of local neighbors, and as well as with millions of more distant molecules. These interactions can have profound effects on vibrational structure and reaction chemistry, and make modeling vibrational frequencies in solution challenging.

In this dissertation, we integrate vibrational spectroscopy and DFT calculations to elucidate the effects of solvation on HMF stability in DMSO/water mixtures. In Chapter 2, we combine vibrational spectroscopy with electronic structure calculations

to understand the solvation of HMF in DMSO, water, and DMSO/water mixtures and to provide insights into the observed hindrance of HMF side reactions in DMSO/water mixtures. In Chapter 3, we develop a general framework for predicting solvent-induced frequency shifts of carbonyls using DFT, and characterize the influence of local interactions on the electronic structure of HMF in solution.

1.6 Understanding fundamentals of zeolite active sites through DFT

In this dissertation, we apply DFT modeling to probe several fundamental questions about the nature of the Sn-Beta active site, and its activity and selectivity in glucose isomerization. In Chapters 4 and 5, we work to bridge the gap between homogeneous and heterogeneous Lewis acids through model Sn-silsesquioxane catalysts. In Chapter 6, we perform an exhaustive survey of Sn-Beta open site geometries to identify the features of the most thermodynamically stable sites. In Chapter 7, we examine the active site and mechanistic features of a new catalyst, Sn-SPP, which shows dramatically improved glucose isomerization yields through novel ketalization reactions with fructose.

Finally, Chapter 8 provides an overview of the findings from this work, and presents several next steps to continue furthering our understanding of solvation and catalysis.

REFERENCES

[1] J. Melorose, R. Perroy, and S. Careas. World population prospects. *United Nations*, 1(6042):587–92, 2015. ISSN 1098-6596. doi: 10.1017/CBO9781107415324.004.

[2] J. Sulston, N. Biggar, C. Fang, S. Cavenaghi, J. Cleland, J. Cohen, P. Dasgupta, P. M. Eloundou-Enyegue, A. Fitter, H. Demissie, S. Harper, T. Jackson, G. Mace, S. Owens, J. Porrit, M. Potts, J. Pretty, F. Ram, R. Short, S. Spencer, Z. Xiaoying, and E. Zulu. *People and the planet*. Number April. 2012. ISBN 978-0-85403-955-5. doi: Report01/12DES2470.

[3] U.S. Energy Information Administration. *International Energy Outlook 2016*, volume 0484(2016). 2016. ISBN 2025866135. doi: www.eia.gov/forecasts/ieo/pdf/0484(2016).pdf.

[4] M. K. Hubbert. Nuclear Energy and the Fossil Fuels, 1956.

[5] N. A. Owen, O. R. Inderwildi, and D. A. King. The status of conventional world oil reserves-Hype or cause for concern? *Energy Policy*, 38(8):4743–4749, 2010. ISSN 03014215. doi: 10.1016/j.enpol.2010.02.026.

[6] I. Chapman. The end of Peak Oil? Why this topic is still relevant despite recent denials. *Energy Policy*, 64:93–101, 2014. ISSN 03014215. doi: 10.1016/j.enpol.2013.05.010.

[7] IPCC. *Climate Change 2014: Synthesis Report. Contribution of Working Groups I, II and III to the Fifth Assessment Report of the Intergovernmental Panel on Climate Change*. 2014. ISBN 9789291691432. doi: 10.1017/CBO9781107415324.

[8] C. Hoffman. Why the BP Oil Rig Blowout Happened. *Popular Mechanics*, 2010.

[9] J. Latson. Exxon Valdez Oil Spill in Alaska Still Affecting Environment. *Time*, 2015.

[10] M. Wines. Drilling Is Making Oklahoma as Quake Prone as California, 2016.

[11] H. O. Hardenberg. *Samuel Morey and his atmospheric engine*. Society of Automotive Engineers, Warrendale, PA, 1992. ISBN 1560912405.

[12] Ford Predicts Fuel from Vegetation, 1925.

[13] Industry Statistics, 2016.

[14] EPA. Public Data for the Renewable Fuel Standard. Technical report.

[15] R. D. Perlack, L. L. Wright, A. F. Turhollow, R. L. Graham, B. J. Stokes, and D. C. Erbach. Biomass as a Feedstock for a Bioenergy and Bioproducts Industry: The Technical Feasibility of a Billion-Ton Annual Supply. *Agriculture*, DOE/GO-102(April):1–78, 2005.

[16] R. D. R. Perlack, B. B. J. Stokes, L. M. Eaton, and A. F. Turnhollow. U.S. Billion-Ton Update: Biomass Supply for a Bioenergy and Bioproducts Industry. *Renewable Energy*, (August):1–229, 2011.

[17] M. H. Langholtz, B. J. Stokes, and L. Eaton. 2016 Billion-Ton Report. *U.S. Department of Energy*, I(July):411, 2016.

[18] B. Kamm, P. R. Gruber, and Kammm Michael. *Biorefineries Industrial Processes and Products*. Wiley-VCH, 2010. ISBN 3527329536.

[19] E. de Jong, A. Higson, P. Walsh, and M. Wellisch. Biobased Chemicals - Value Added Products from Biorefineries. *A report prepared for IEA Bioenergy-Task 42*, page 36, 2011.

[20] A. J. Ragauskas, C. K. Williams, B. H. Davison, G. Britovsek, J. Cairney, C. A. Eckert, W. J. Frederick Jr., J. P. Hallett, D. J. Leak, C. L. Liotta, J. R. Mielenz, R. Murphy, R. Templer, and T. Tschaplinski. The path forward for biofuels and biomaterials. *Science (New York, N.Y.)*, 311(5760):484–9, 2006. ISSN 1095-9203. doi: 10.1126/science.1114736.

[21] G. W. Huber. Breaking the Chemical and Engineering Barriers to Lignocellulosic Biofuels : Next Generation Hydrocarbon Biorefineries. *NSF*, pages 1–177, 2008.

[22] G. W. Huber and A. Corma. Synergies between bio- and oil refineries for the production of fuels from biomass. *Angewandte Chemie - International Edition*, 46(38):7184–7201, 2007. ISSN 14337851. doi: 10.1002/anie.200604504.

[23] D. Tilman, R. Socolow, J. J. A. Foley, J. Hill, E. Larson, L. Lynd, S. Pacala, J. Reilly, T. Searchinger, C. Somerville, and R. Williams. Beneficial biofuelsthe food, energy, and environment trilemma. *Science*, 325(5938):270–271, 2009. ISSN 00368075. doi: 10.1126/science.1177970.

[24] C. O. Tuck, E. Perez, I. T. Horvath, R. a. Sheldon, and M. Poliakoff. Valorization of Biomass: Deriving More Value from Waste. *Science*, 337(6095):695–699, 2012. ISSN 0036-8075. doi: 10.1126/science.1218930.

[25] T. Werpy and G. Petersen. Top Value Added Chemicals from Biomass. *U.S. Department of Energy*, 1:76, 2004. doi: 10.2172/926125.

[26] J. Lane. The DOE's 12 Top Biobased Molecules what became of them?, 2015.

[27] X. Tong, Y. Ma, and Y. Li. Biomass into chemicals: Conversion of sugars to furan derivatives by catalytic processes. *Appl. Catal., A*, 385(1-2):1–13, 2010. doi: 10.1016/j.apcata.2010.06.049.

[28] A. A. Rosatella, S. P. Simeonov, R. F. M. Frade, and C. A. M. Afonso. 5-Hydroxymethylfurfural (HMF) as a building block platform: Biological properties, synthesis and synthetic applications. *Green Chemistry*, 13(4):754, 2011. ISSN 1463-9262. doi: 10.1039/c0gc00401d.

[29] R. J. Van Putten, J. C. Van Der Waal, E. De Jong, C. B. Rasrendra, H. J. Heeres, and J. G. De Vries. Hydroxymethylfurfural, a versatile platform chemical made from renewable resources. *Chemical Reviews*, 113(3):1499–1597, 2013. ISSN 00092665. doi: 10.1021/cr300182k.

[30] Y. Roman-Leshkov, C. J. Barrett, Z. Y. Liu, and J. A. Dumesic. Production of dimethylfuran for liquid fuels from biomass-derived carbohydrates. *Nature*, 447 (7147):982–985, 2007. doi: 10.1038/nature05923.

[31] T. A. Brandvold. Carbohydrate route to para-xylene and terephthalic acid. *United States Patent Application*, (12/492,182):1–7, 2009.

[32] C. L. Williams, C.-C. Chang, P. Do, N. Nikbin, S. Caratzoulas, D. G. Vlachos, R. F. Lobo, W. Fan, and P. J. Dauenhauer. Cycloaddition of Biomass-Derived Furans for Catalytic Production of Renewablep-Xylene. *ACS Catalysis*, 2(6): 935–939, 2012. doi: 10.1021/cs300011a.

[33] C.-C. Chang, S. K. Green, C. L. Williams, P. J. Dauenhauer, and W. Fan. Ultra-selective cycloaddition of dimethylfuran for renewable p-xylene with H-BEA. *Green Chem.*, 16(2):585–588, 2014. ISSN 1463-9262. doi: 10.1039/C3GC40740C.

[34] Y. Nakagawa, M. Tamura, and K. Tomishige. Catalytic reduction of biomass-derived furanic compounds with hydrogen. *ACS Catalysis*, 3(12):2655–2668, 2013. ISSN 21555435. doi: 10.1021/cs400616p.

[35] J. Tuteja, H. Choudhary, S. Nishimura, and K. Ebitani. Direct synthesis of 1,6-hexanediol from HMF over a heterogeneous Pd/ZrP catalyst using formic acid

as hydrogen source. *ChemSusChem*, 7(1):96–100, 2014. ISSN 18645631. doi: 10.1002/cssc.201300832.

[36] Avantium. Avantium.

[37] Z. Lin, M. Ierapetritou, and V. Nikolakis. Aromatics from Lignocellulosic Biomass: Economic Analysis of the Production of p-Xylene from 5-Hydroxymethylfurfural. *AIChE Journal*, 59(6):2079–2087, 2013. doi: 10.1002/aic.13969.

[38] Z. Lin, V. Nikolakis, and M. Ierapetritou. Alternative Approaches for p Xylene Production from Starch: Techno-Economic Analysis. *Industrial & Engineering Chemistry Research*, 53:10688–10699, 2014. ISSN 0888-5885. doi: 10.1021/ie402469j.

[39] Z. Lin, V. Nikolakis, and M. Ierapetritou. Life cycle assessment of biobased p-xylene production. *Industrial and Engineering Chemistry Research*, 54(8):2366–2378, 2015. ISSN 15205045. doi: 10.1021/ie5037287.

[40] Y. Román-Leshkov, J. N. Chheda, and J. A. Dumesic. Phase modifiers promote efficient production of hydroxymethylfurfural from fructose. *Science*, 312(5782): 1933–1937, 2006. doi: 10.1126/science.1126337.

[41] M. Moliner, Y. Roman-Leshkov, M. E. E. Davis, Y. Román-Leshkov, and M. E. E. Davis. Tin-containing zeolites are highly active catalysts for the isomerization of glucose in water. *Proc Natl Acad Sci U S A*, 107(14):6164–6168, 2010. ISSN 1091-6490. doi: 10.1073/pnas.1002358107.

[42] E. Nikolla, Y. Roman-Leshkov, M. Moliner, and M. E. Davis. "One-pot" synthesis of 5-(hydroxymethyl)furfural from carbohydrates using tin-beta zeolite. *ACS Catalysis*, 1(4):408–410, 2011. ISSN 21555435. doi: 10.1021/cs2000544.

[43] Y. Román-Leshkov and J. A. Dumesic. Solvent Effects on Fructose Dehydration to 5-Hydroxymethylfurfural in Biphasic Systems Saturated with Inorganic Salts. *Topics in Catalysis*, 52(3):297–303, 2009. doi: 10.1007/s11244-008-9166-0.

[44] V. V. Ordomsky, J. Van Der Schaaf, J. C. Schouten, and T. A. Nijhuis. The effect of solvent addition on fructose dehydration to 5-hydroxymethylfurfural in biphasic system over zeolites. *Journal of Catalysis*, 287:68–75, 2012. ISSN 00219517. doi: 10.1016/j.jcat.2011.12.002.

[45] Z. Wang, L. Wang, Y. Jiang, M. Hunger, and J. Huang. Cooperativity of Brønsted and Lewis Acid Sites on Zeolite for Glycerol Dehydration. *ACS Catalysis*, 4(4):1144–1147, 2014. doi: 10.1021/cs401225k.

[46] L. Qi and I. T. Horváth. Catalytic conversion of fructose to γ-valerolactone in γ-valerolactone. *ACS Catalysis*, 2(11):2247–2249, 2012. ISSN 21555435. doi: 10.1021/cs300428f.

[47] L. Qi, Y. F. Mui, S. W. Lo, M. Y. Lui, G. R. Akien, and I. T. Horvath. Catalytic conversion of fructose, glucose, and sucrose to 5-(hydroxymethyl)furfural and levulinic and formic acids in γ- valerolactone as a green solvent. *ACS Catalysis*, 4(5):1470–1477, 2014. ISSN 21555435. doi: 10.1021/cs401160y.

[48] D. M. Alonso, S. G. Wettstein, and J. A. Dumesic. Gamma-valerolactone, a sustainable platform molecule derived from lignocellulosic biomass. *Green Chemistry*, 15(3):584, 2013. ISSN 1463-9262. doi: 10.1039/c3gc37065h.

[49] I. T. Horváth, H. Mehdi, V. Fábos, L. Boda, and L. T. Mika. γ-Valerolactonea sustainable liquid for energy and carbon-based chemicals. *Green Chemistry*, 10 (2):238, 2008. ISSN 1463-9262. doi: 10.1039/b712863k.

[50] J. Weitkamp and L. Puppe. *Catalysis and zeolites: fundamentals and applications*. Springer-Verlag, Berlin, 1999.

[51] E. Taarning, C. M. Osmundsen, X. Yang, B. Voss, S. I. Andersen, and C. H. Christensen. Zeolite-catalyzed biomass conversion to fuels and chemicals. *Energy & Environmental Science*, 4(3):793, 2011. ISSN 1754-5692. doi: 10.1039/c004518g.

[52] H. Y. Luo, J. D. Lewis, and Y. Román-Leshkov. Lewis Acid Zeolites for Biomass Conversion: Perspectives and Challenges on Reactivity, Synthesis, and Stability. *Annu. Rev. Chem. Biomol. Eng*, 7:663–92, 2016. ISSN 19475438. doi: 10.1146/annurev-chembioeng-080615-034551.

[53] P. Y. Dapsens, C. Mondelli, and J. Pérez-Ramírez. Design of Lewis-acid centres in zeolitic matrices for the conversion of renewables. *Chemical Society Reviews*, 44(20):7025–7043, 2015. ISSN 0306-0012. doi: 10.1039/C5CS00028A.

[54] Y. Román-Leshkov and M. E. Davis. Activation of Carbonyl-Containing Molecules with Solid Lewis Acids in Aqueous Media. *ACS Catalysis*, 1(11): 1566–1580, 2011. ISSN 21555435. doi: 10.1021/cs200411d.

[55] M. Moliner. State of the art of Lewis acid-containing zeolites: lessons from fine chemistry to new biomass transformation processes. *Dalton Transactions*, 43: 4197–208, 2014. ISSN 1477-9234. doi: 10.1039/c3dt52293h.

[56] T. Blasco, M. a. Camblor, a. Corma, P. Esteve, J. M. Guil, a. Mart, S. Valencia, a. Martinez, and J. a. Perdigon-Melon. Direct synthesis and characterization of hydrophobic aluminum-free Ti-beta zeolite. *Journal of Physical Chemistry B*, 102(1):75–88, 1998. ISSN 1520-6106. doi: 10.1021/jp973288w.

[57] A. Corma, L. T. Nemeth, M. Renz, and S. Valencia. Sn-zeolite beta as a heterogeneous chemoselective catalyst for Baeyer-Villiger oxidations. *Nature*, 412 (6845):423–425, 2001. ISSN 0028-0836. doi: 10.1038/35086546.

[58] M. Renz, T. Blasco, A. Corma, V. Fornés, R. Jensen, and L. Nemeth. Selective and shape-selective Baeyer-Villiger oxidations of aromatic aldehydes and

cyclic ketones with Sn-beta zeolites and H2O2. *Chemistry*, 8(20):4708–17, 2002. ISSN 0947-6539. doi: 10.1002/1521-3765(20021018)8:20⟨4708::AID-CHEM4708⟩3.0.CO;2-U.

[59] A. Corma, M. E. Domine, and S. Valencia. Water-resistant solid Lewis acid catalysts: Meerwein-Ponndorf-Verley and Oppenauer reactions catalyzed by tin-beta zeolite. *Journal of Catalysis*, 215:294–304, 2003. ISSN 00219517. doi: 10.1016/S0021-9517(03)00014-9.

[60] A. Corma, M. E. Domine, L. Nemeth, and S. Valencia. Al-free Sn-Beta zeolite as a catalyst for the selective reduction of carbonyl compounds (Meerwein-Ponndorf-Verley Reaction). *Journal of the American Chemical Society*, 124:3194–3195, 2002. ISSN 00027863. doi: 10.1021/ja012297m.

[61] A. Corma and M. Renz. Sn-Beta zeolite as diastereoselective water-resistant heterogeneous Lewis-acid catalyst for carbon-carbon bond formation in the intramolecular carbonyl-ene reaction. *Chemical communications (Cambridge, England)*, pages 550–551, 2004. ISSN 1359-7345. doi: 10.1039/b313738d.

[62] S. V. D. Vyver, C. Odermatt, K. Romero, T. Prasomsri, and Y. Román-Leshkov. Solid Lewis Acids Catalyze the Carbon Carbon Coupling between Carbohydrates and Formaldehyde. *ACS Catalysis*, 5:972–977, 2015. doi: 10.1021/cs5015964.

[63] R. Bermejo-Deval, R. S. S. Assary, E. Nikolla, M. Moliner, Y. Roman-Leshkov, S.-J. S.-J. Hwang, A. Palsdottir, D. Silverman, R. F. Lobo, L. A. Curtiss, and M. E. Davis. Metalloenzyme-like catalyzed isomerizations of sugars by Lewis acid zeolites. *Proceedings of the National Academy of Sciences*, 109(25):9727–9732, 2012. ISSN 0027-8424. doi: 10.1073/pnas.1206708109.

[64] R. Bermejo-Deval, M. Orazov, R. Gounder, S. J. Hwang, and M. E. Davis. Active sites in Sn-beta for glucose isomerization to fructose and epimerization to mannose. *ACS Catalysis*, 4(7):2288–2297, 2014. ISSN 21555435. doi: 10.1021/cs500466j.

[65] W. R. Gunther, Y. Wang, Y. Ji, V. K. Michaelis, S. T. Hunt, R. G. Griffin, and Y. Román-Leshkov. Sn-Beta zeolites with borate salts catalyse the epimerization of carbohydrates via an intramolecular carbon shift. *Nature communications*, 3: 1109, 2012. ISSN 2041-1723. doi: 10.1038/ncomms2122.

[66] J. D. Lewis, S. Van De Vyver, and Y. Román-Leshkov. Acid-Base Pairs in Lewis Acidic Zeolites Promote Direct Aldol Reactions by Soft Enolization. *Angewandte Chemie - International Edition*, 54(34):9835–9838, 2015. ISSN 15213773. doi: 10.1002/anie.201502939.

[67] J. D. Lewis, S. Van De Vyver, A. J. Crisci, W. R. Gunther, V. K. Michaelis, R. G. Griffin, and Y. Román-Leshkov. A continuous flow strategy for the coupled transfer hydrogenation and etherification of 5-(hydroxymethyl)furfural using lewis acid zeolites. *ChemSusChem*, 7(8):2255–2265, 2014. ISSN 1864564X. doi: 10.1002/cssc.201402100.

[68] M. S. Holm, S. Saravanamurugan, and E. Taarning. Conversion of sugars to lactic acid derivatives using heterogeneous zeotype catalysts. *Science (New York, N.Y.)*, 328(5978):602–605, 2010. ISSN 0036-8075. doi: 10.1126/science.1183990.

[69] USDA Economic Research Service. Sugars and Sweeteners Background, 2017.

[70] S. H. Bhosale, M. B. Rao, and V. V. Deshpande. Molecular and industrial aspects of glucose isomerase. *Microbiological reviews*, 60(2):280–300, 1996. ISSN 0146-0749.

[71] H. S. Lee and J. Hong. Kinetics of glucose isomerization to fructose by immobilized glucose isomerase : anomeric reactivity of D -glucose in kinetic model. *Journal of Biotechnology*, 84:145–153, 2000.

[72] M. Boronat, P. Concepción, A. Corma, M. Renz, and S. Valencia. Determination of the catalytically active oxidation Lewis acid sites in Sn-beta zeolites, and their optimisation by the combination of theoretical and experimental studies. *Journal of Catalysis*, 234(1):111–118, 2005. ISSN 00219517. doi: 10.1016/j.jcat.2005.05.023.

[73] J. W. Harris, M. J. Cordon, J. R. Di Iorio, J. C. Vega-Vila, F. H. Ribeiro, and R. Gounder. Titration and quantification of open and closed Lewis acid sites in Sn-Beta zeolites that catalyze glucose isomerization. *Journal of Catalysis*, 335: 141–154, 2016. ISSN 00219517. doi: 10.1016/j.jcat.2015.12.024.

[74] H. Zhao, J. E. Holladay, H. Brown, and Z. C. Zhang. Metal Chlorides in Ionic Liquid Solvents Convert Sugars to 5-Hydroxymethylfurfural. *Science*, 113409 (2005), 2006. doi: 10.1126/science.1141199.

[75] V. Choudhary, S. I. Sandler, and D. G. Vlachos. Conversion of xylose to furfural using Lewis and Brønsted acid catalysts in aqueous media. *ACS Catalysis*, 2(9): 2022–2028, 2012. ISSN 21555435. doi: 10.1021/cs300265d.

[76] V. Choudhary, S. H. Mushrif, C. Ho, A. Anderko, V. Nikolakis, N. S. Marinkovic, A. I. Frenkel, S. I. Sandler, and D. G. Vlachos. Insights into the interplay of Lewis and Brønsted acid catalysts in glucose and fructose conversion to 5-(hydroxymethyl)furfural and levulinic acid in aqueous media. *Journal of the American Chemical Society*, 135(10):3997–4006, 2013. ISSN 00027863. doi: 10.1021/ja3122763.

[77] V. Choudhary, S. Caratzoulas, and D. G. Vlachos. Insights into the isomerization of xylose to xylulose and lyxose by a Lewis acid catalyst. *Carbohydrate Research*, 368:89–95, 2013. ISSN 00086215. doi: 10.1016/j.carres.2012.12.019.

[78] H. Nguyen, V. Nikolakis, and D. G. Vlachos. Mechanistic Insights into Lewis Acid Metal Salt-Catalyzed Glucose Chemistry in Aqueous Solution. *ACS Catalysis*, pages 1497–1504, 2016. ISSN 2155-5435. doi: 10.1021/acscatal.5b02698.

[79] E. Schrödinger. An undulatory theory of the mechanics of atoms. *Physical Review*, 28(6):1049–1070, 1926. doi: 10.1103/PhysRev.28.1049.

[80] P. Hohenberg and W. Kohn. Inhomogeneous electron gas. *Physical Review*, 136 (3B):864–871, 1964. ISSN 01631829. doi: 10.1103/PhysRevB.7.1912.

[81] W. Kohn and L. J. Sham. Self-consistent equations including exchange and correlation effects. *Physical Review*, 140(4A):1133–1138, 1965. ISSN 0031899X. doi: 10.1103/PhysRev.140.A1133.

[82] H. B. Schlegel. Optimization of equilibrium geometries and transition structures. *Journal of Computational Chemistry*, 3(2):214–218, 1982. ISSN 1096987X. doi: 10.1002/jcc.540030212.

[83] C. Peng, P. Y. Ayala, H. B. Schlegel, and M. J. Frisch. Using Redundant Internal Coordinates to Optimize Equilibrium Geometries and Transition States. *Journal of Computational Chemistry*, 17(1):49–56, 1996. doi: CCC0192-86511961010049-08.

[84] D. C. Liu and J. Nocedal. On the Limited Memory Method for Large Scale Optimization. *Math. Programming, B*, 45(3):503–528, 1989. ISSN 00255610. doi: 10.1007/BF01589116.

[85] L. A. Curtiss, P. C. Redfern, and K. Raghavachari. Assessment of Gaussian-3 and density-functional theories on the G3/05 test set of experimental energies.

Journal of Chemical Physics, 123(12), 2005. ISSN 00219606. doi: 10.1063/1.2039080.

[86] L. Goerigk and S. Grimme. A thorough benchmark of density functional methods for general main group thermochemistry, kinetics, and noncovalent interactions. *Phys. Chem. Chem. Phys.*, 13:6670–6688, 2011. ISSN 15499618. doi: 10.1039/C0CP02984J.

[87] J. K. Nørskov, M. Scheffler, and H. Toulhoat. Density Functional Theory in Surface Science and Heterogeneous Catalysis Modeling. *MRS Bulletin*, 31 (September):669–674, 2006. ISSN 0883-7694. doi: 10.1557/mrs2006.175.

[88] Y. Zhao, N. González-Garda, and D. G. Truhlar. Benchmark database of barrier heights for heavy atom transfer, nucleophilic substitution, association, and unimolecular reactions and its use to test theoretical methods. *Journal of Physical Chemistry A*, 109(9):2012–2018, 2005. ISSN 10895639. doi: 10.1021/jp045141s.

[89] J. P. Merrick, D. Moran, and L. Radom. An Evaluation of Harmonic Vibrational Frequency Scale Factors. *Journal of Physical Chemistry A*, 111:11683–11700, 2007. doi: 10.1021/jp073974n.

[90] J. R. Cheeseman and M. J. Frisch. Basis set dependence of vibrational Raman and Raman optical activity intensities. *Journal of Chemical Theory and Computation*, 7(10):3323–3334, 2011. ISSN 15499618. doi: 10.1021/ct200507e.

[91] J. R. Cheeseman, G. W. Trucks, T. a. Keith, and M. J. Frisch. A comparison of models for calculating nuclear magnetic resonance shielding tensors. *The Journal of Chemical Physics*, 104(January):5497–5509, 1996. ISSN 00219606. doi: 10.1063/1.471789.

[92] J. R. Cheeseman, M. J. Frisch, F. J. Devlin, and P. J. Stephens. Ab initio calculation of atomic axial tensors and vibrational rotational strengths using

density functional theory. *Chemical Physics Letters*, 252:211–220, 1996. ISSN 0026-8976. doi: 10.1080/002689796173921.

[93] J. Hafner. Ab-initio simulations of materials using VASP: Density-functional theory and beyond. *Journal of Computational Chemistry*, 29(13):2044–2078, 2008. ISSN 01928651. doi: 10.1002/jcc.21057.

[94] A. Logadottir, T. Rod, J. Nørskov, B. Hammer, S. Dahl, and C. Jacobsen. The BrønstedEvansPolanyi Relation and the Volcano Plot for Ammonia Synthesis over Transition Metal Catalysts. *Journal of Catalysis*, 197(2):229–231, 2001. ISSN 00219517. doi: 10.1006/jcat.2000.3087.

[95] M. P. Andersson, T. Bligaard, A. Kustov, K. E. Larsen, J. Greeley, T. Johannessen, C. H. Christensen, and J. K. Nørskov. Toward computational screening in heterogeneous catalysis: Pareto-optimal methanation catalysts. *Journal of Catalysis*, 239(2):501–506, 2006. ISSN 00219517. doi: 10.1016/j.jcat.2006.02.016.

[96] J. Wu and H. Yang. Platinum-based oxygen reduction electrocatalysts. *Accounts of Chemical Research*, 46(8):1848–1857, 2013. ISSN 00014842. doi: 10.1021/ar300359w.

[97] Y. Jiao, Y. Zheng, M. Jaroniec, and S. Zhang Qiao. Origin of the Electrocatalytic Oxygen Reduction Activity of Graphene-Based Catalysts: A Roadmap to Achieve the Best Performance. *Journal of the American Chemical Society*, 136: 4394–4403, 2014. doi: 10.1021/ja500432h.

[98] M. Sierka and A. Joachim Sauer. Structure and reactivity of silica and zeolite catalysts by a combined quantum mechanics[ndash]shell-model potential approach based on DFT. *Faraday Discussions*, 106:41–62, 1997. ISSN 13596640. doi: 10.1039/a701492i.

[99] J. B. Nicholas. Density functional theory studies of zeolite structure, acidity, and reactivity. *Topics In Catalysis*, 4(1-2):157–171, 1997. ISSN 1022-5528. doi: 10.1023/A:1019179903977.

[100] S. Svelle, C. Tuma, X. Rozanska, T. Kerber, and J. Sauer. Quantum chemical modeling of zeolite-catalyzed methylation reactions: Toward chemical accuracy for barriers. *Journal of the American Chemical Society*, 131(2):816–825, 2009. ISSN 00027863. doi: 10.1021/ja807695p.

[101] J. Wu and Z. Li. Density-Functional Theory for Complex Fluids. *Annual Review of Physical Chemistry*, 58(1):85–112, 2007. ISSN 0066-426X. doi: 10.1146/annurev.physchem.58.032806.104650.

[102] R. B. Murphy, D. M. Philipp, and R. A. Friesner. A mixed quantum mechanics/molecular mechanics (QM/MM) method for large-scale modeling of chemistry in protein environments. *Journal Of Computational Chemistry*, 21(16): 1442–1457, 2000. ISSN 1096987X. doi: 10.1002/1096-987X(200012)21:16⟨1442::AID-JCC3⟩3.0.CO;2-O.

[103] S. Grimme, J. Antony, S. Ehrlich, and H. Krieg. A consistent and accurate ab initio parametrization of density functional dispersion correction (DFT-D) for the 94 elements H-Pu. *Journal of Chemical Physics*, 132(15), 2010. ISSN 00219606. doi: 10.1063/1.3382344.

[104] E. M. Sproviero, J. A. Gascon, J. P. McEvoy, G. W. Brudvig, and V. S. Batista. Computational studies of the O2-evolving complex of photosystem II and biomimetic oxomanganese complexes. *Coordination Chemistry Reviews*, 252 (3-4):395–415, 2008. ISSN 00108545. doi: 10.1016/j.ccr.2007.09.006.

[105] R. A. Friesner and V. Guallar. Ab Initio Quantum Chemical and Mixed Quantum Mechanics/Molecular Mechanics (QM/Mm) Methods for Studying Enzymatic

Catalysis. *Ann. Rev. Phys. Chem.*, 56:389–427, 2005. ISSN 0066-426X. doi: 10.1146/annurev.physchem.55.091602.094410.

[106] D. Li, Y. Wang, and K. Han. Recent density functional theory model calculations of drug metabolism by cytochrome P450. *Coordination Chemistry Reviews*, 256 (11-12):1137–1150, 2012. ISSN 00108545. doi: 10.1016/j.ccr.2012.01.016.

[107] J. Newsam. Computational approaches in zeolite structural chemistry. In *Studies in Surface Science and Catalysis*, volume 102, pages 231–265. 1996. doi: 10.1016/S0167-2991(06)81404-7.

[108] V. V. Speybroeck, K. Hemelsoet, L. Joos, M. Waroquier, R. G. Bell, C. Richard, and A. Catlow. Recent advances in zeolite chemistry and catalysis Advances in theory and their application within the field of zeolite chemistry. *Chem. Soc. Rev. Chem. Soc. Rev*, 44(44):7015–7430, 2015. ISSN 0306-0012. doi: 10.1039/C5CS00029G.

[109] D. W. Lewis, D. J. Willock, C. R. A. Catlow, J. M. Thomas, and G. J. Hutchings. De novo design of structure directing agents for the synthesis of microporous solids.pdf, 1996. ISSN 0028-0836.

[110] S. M. Auerbach, M. H. Ford, and P. A. Monson. New insights into zeolite formation from molecular modeling. *Current Opinion in Colloid and Interface Science*, 10(5-6):220–225, 2005. ISSN 13590294. doi: 10.1016/j.cocis.2005.09.012.

[111] G. Sastre. A computational chemistry insight in the role of structure directing agents in the synthesis of zeolites. *Physical chemistry chemical physics : PCCP*, 9(9):1052–1058, 2007. ISSN 1463-9076. doi: 10.1039/b615035g.

[112] M. W. Deem and J. M. Newsam. Determination of 4-connected framework crystal structures by simulated annealing. *Nature*, 342(6247):260–262, 1989. ISSN 0028-0836. doi: 10.1038/342260a0.

[113] E. J. Maginn, A. T. Bell, and D. N. Theodorou. Transport diffusivity of methane in silicalite from equilibrium and nonequilibrium simulations. *The Journal of Physical Chemistry*, 97(16):4173–4181, 1993. ISSN 0022-3654. doi: 10.1021/j100118a038.

[114] F. J. Keil, R. Krishna, and M.-O. Coppens. Modeling of Diffusion in Zeolites. *Reviews in Chemical Engineering*, 16(2), 2000. ISSN 0167-8299. doi: 10.1515/REVCE.2000.16.2.71.

[115] S. P. Greatbanks, I. H. Hillier, N. A. Burton, and P. Sherwood. Adsorption of water and methanol on zeolite Bronsted acid sites: An ab initio, embedded cluster study including electron correlation. *Journal of Chemical Physics*, 105 (9):3770–3776, 1996. ISSN 0021-9606. doi: 10.1063/1.472197.

[116] Y. P. Li, J. Gomes, S. M. Sharada, A. T. Bell, and M. Head-Gordon. Improved force-field parameters for QM/MM simulations of the energies of adsorption for molecules in zeolites and a free rotor correction to the rigid rotor harmonic oscillator model for adsorption enthalpies. *Journal of Physical Chemistry C*, 119(4): 1840–1850, 2015. ISSN 19327455. doi: 10.1021/jp509921r.

[117] G. Piccini, M. Alessio, J. Sauer, Y. Zhi, Y. Liu, R. Kolvenbach, A. Jentys, and J. A. Lercher. Accurate adsorption thermodynamics of small alkanes in zeolites. Ab initio theory and experiment for H-chabazite. *Journal of Physical Chemistry C*, 119(11):6128–6137, 2015. ISSN 19327455. doi: 10.1021/acs.jpcc.5b01739.

[118] T. Demuth, P. Raybaud, S. Lacombe, and H. Toulhoat. Effects of zeolite pore sizes on the mechanism and selectivity of xylene disproportionation - A DFT study. *Journal of Catalysis*, 222(2):323–337, 2004. ISSN 00219517. doi: 10.1016/j.jcat.2003.10.017.

[119] A. J. Jones, R. T. Carr, S. I. Zones, and E. Iglesia. Acid strength and solvation in catalysis by MFI zeolites and effects of the identity, concentration and location of

framework heteroatoms. *Journal of Catalysis*, 312:58–68, 2014. ISSN 00219517. doi: 10.1016/j.jcat.2014.01.007.

[120] R. Pophale, P. a. Cheeseman, and M. W. Deem. A database of new zeolite-like materials. *Physical chemistry chemical physics : PCCP*, 13(27):12407–12412, 2011. ISSN 1463-9076. doi: 10.1039/c0cp02255a.

[121] P. Bai, M. Y. Jeon, L. Ren, C. Knight, M. W. Deem, M. Tsapatsis, and J. I. Siepmann. Discovery of optimal zeolites for challenging separations and chemical transformations using predictive materials modeling. *Nature Communications*, 6:http://dx.doi.org/10.1038/ncomms6912, 2015. ISSN 2041-1723. doi: 10.1038/ncomms6912.

[122] Y. Román-Leshkov, M. Moliner, J. A. Labinger, and M. E. Davis. Mechanism of glucose isomerization using a solid lewis acid catalyst in water. *Angewandte Chemie - International Edition*, 49(47):8954–8957, 2010. ISSN 14337851. doi: 10.1002/anie.201004689.

[123] Y. P. P. Li, M. Head-Gordon, and A. T. T. Bell. Analysis of the reaction mechanism and catalytic activity of metal-substituted beta zeolite for the isomerization of glucose to fructose. *ACS Catalysis*, 4(5):1537–1545, 2014. ISSN 21555435. doi: 10.1021/cs401054f.

[124] N. Rai, S. Caratzoulas, and D. G. Vlachos. Role of silanol group in Sn-beta zeolite for glucose isomerization and epimerization reactions. *ACS Catalysis*, 3 (10):2294–2298, 2013. ISSN 21555435. doi: 10.1021/cs400476n.

[125] G. Yang, E. A. Pidko, and E. J. M. Hensen. The mechanism of glucose isomerization to fructose over Sn-BEA zeolite: A periodic density functional theory study. *ChemSusChem*, 6(9):1688–1696, 2013. ISSN 18645631. doi: 10.1002/cssc.201300342.

[126] J. R. Christianson, S. Caratzoulas, and D. G. Vlachos. Computational Insight into the Effect of Sn-Beta Na Exchange and Solvent on Glucose Isomerization and Epimerization. *ACS Catalysis*, 5(9):5256–5263, 2015. ISSN 2155-5435. doi: 10.1021/acscatal.5b01258.

[127] C. Reichert. *Solvents and Solvent Effects in Organic Chemistry.* Wiley VCH, Weinheim, 2nd edition, 1988.

[128] R. W. Fawcett and A. A. Kloss. Solvent-Induced Frequency Shifts in the Infrared Specturm of Dimethyl Sulfoxide in Organic Solvents. *J. Phys. Chem.*, 100:2019–2024, 1995.

[129] R. A. Nyquist, R. Streck, and G. Jeschek. NMR and IR spectra-structure correlations carbonyl containing compounds in various solvents. *Journal of Molecular Structure (THEOCHEM)*, 377:113–128, 1996.

[130] J. Zakzeski, R. J. H. Grisel, A. T. Smit, and B. M. Weckhuysen. Solid acid-catalyzed cellulose hydrolysis monitored by in situ Atr-Ir spectroscopy. *ChemSusChem*, 5(2):430–437, 2012. ISSN 18645631. doi: 10.1002/cssc.201100631.

[131] G. Tsilomelekis, A. Christodoulakis, and S. Boghosian. Support effects on structure and activity of molybdenum oxide catalysts for the oxidative dehydrogenation of ethane. *Catalysis Today*, 127(1-4):139–147, 2007. ISSN 09205861. doi: 10.1016/j.cattod.2007.03.026.

Chapter 2

ORIGIN OF 5-HYDROXYMETHYLFURFURAL STABILITY IN WATER/DIMETHYL SULFOXIDE MIXTURES

2.1 Abstract

In the present work, we combined vibrational spectroscopy with electronic structure calculations to understand the solvation of HMF in DMSO, water, and DMSO/water mixtures and to provide insights into the observed hindrance of HMF rehydration and aldol condensation reactions if it is dissolved in DMSO/water mixtures. To achieve this goal, the attenuated total reflection FTIR spectra of a wide composition range of binary and ternary mixtures were measured, analyzed, and compared to the findings of ab initio DFT calculations. The effect of solvent on the HMF C=O and O—H vibrational modes reveals significant differences that are ascribed to different intermolecular interactions between HMF and DMSO or water. We also found that DMSO binds to HMF more strongly than water, and interactions with the HMF hydroxyl group are stronger than those with the HMF carbonyl group. We also showed the preferential solvation of HMF C=O groups by DMSO if HMF is dissolved in DMSO/water mixed solvent. Frontier molecular orbital theory was used to examine the influence of the solvent on side reactions. The results show that HMF solvation by DMSO increases its LUMO energy, which reduces its susceptibility to nucleophilic attack and minimizes undesirable hydration and humin-formation reactions. This result, together with the preferential solvation of HMF by DMSO, provide an explanation for the enhanced HMF stability in DMSO/water mixtures observed experimentally.

The IR spectroscopy measurements were conducted by Dr. George Tsilomelekis at the University of Delaware. This chapter was originally published in [1] in a paper

titled "Origin of 5-Hydroxymethylfurfural Stability in Water/Dimethyl Sulfoxide Mixtures." Adapted with permission from John Wiley and Sons. Copyright © 2014, John Wiley and Sons.

2.2 Introduction

The diminishing availability of fossil resources has been the impetus behind the burgeoning research activity to discover and develop technologies that utilize renewable resources for the production of fuels and platform chemicals. Abundant biomass, as the only carbon-containing, renewable, primary-energy carrier, promises to serve as a sustainable alternative that could supply valuable intermediates to the chemical industry. The high functionality of biomass-derived oxygenates, such as carbohydrates, gives us the advantage to convert these molecules into various value-added chemicals through the selective removal of some of their functional groups and the modification of others. For example, carbohydrates are important feedstocks because of their availability, low cost, and the possibility to obtain them from nonedible biomass sources [2–4]. In particular, the dehydration of fructose to 5-hydroxymethylfurfural (HMF) has attracted increasing interest as HMF is considered as a top value-added chemical [5] because it can be transformed to chemicals, polymer precursors, and fuels (e.g., 5-ethoxymethylfurfural (EMF) [6], 2,5-dimethylfuran (DMF) [4, 7] and p-xylene [8–10]). Unfortunately, HMF yields are hampered by side reactions such as further rehydration to levulinic and formic acids [11] as well as polymerization to insoluble humins [12, 13]. Several nonaqueous solvents and ionic liquids in conjunction with homogeneous [7, 14–16] or heterogeneous catalysts [17–21] have been tested in an effort to minimize side reactions. Solvent selection is a topic of great interest because many commonly used solvents in laboratories and the chemical industry are considered unprofitable or environmentally unsafe [22].

It has been reported recently that the use of organic co-solvents in the aqueous reaction medium can enhance HMF stability significantly by minimizing rehydration

and humin-formation reactions [2, 16, 18, 23, 24]. DMSO is an example of such a co-solvent as it is known to enhance HMF yields [2, 23]. However, issues related to HMF separation and recovery from a high-boiling-point, aprotic solvent such as DMSO render this co-solvent unsuitable for large-scale applications and highlight the need to identify other co-solvents with similar benefits to the HMF yield. Unfortunately, how DMSO, as a co-solvent, staves off undesirable reactions remains elusive. With the exception of a recent molecular dynamics simulation study, which suggests the preferential solvation of the HMF carbonyl group by DMSO [25], there is no other theoretical or experimental study on the solvation of HMF in different environments and on the effects of solvation on the stability and reactivity of HMF.

A recent crystallographic study of HMF crystals showed that HMF molecules form an infinite O—H$\cdots$O hydrogen-bonded network. Weak intermolecular C—H$\cdots$O hydrogen bonds (HBs) link these chains into a 3D network structure [26]. Additionally, the HMF (—CHO) formyl group can rotate around the C—C single bond; thus *cis* and *trans* HMF conformations exist (Fig. 2.1). Several studies on the different conformational structures of furans (e.g., furfural or HMF) and their hydration products (e.g., levulinic acid) have been published recently. In the case of furfural, the *cis/trans* conformational equilibrium was found to depend strongly on the solvent [27, 28]. Therefore, one possibility is that the *cis/trans* conformational equilibrium of furans could influence their reactivity in solutions significantly. However, it is not clear whether HMF adopts different conformations in different solvents as well as if conformational equilibrium has any effect on its stability in rehydration reactions.

Vibrational spectroscopies are powerful methods to characterize solute–solvent interactions [22, 27, 29–32]. Furthermore, an understanding of the structural and vibrational behavior of catalytic systems can assist in the development of new structure–activity relationships [22, 33, 34]. It is generally accepted that the vibrational spectra of solute–solvent systems can be affected markedly by solvent–solvent, solute–solute, and solvent–solute interactions, which depend on the physical properties of the solute or solvent such as polarizability and dipole moment [30]. As a result, intermolecular

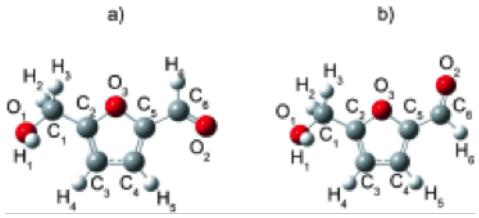

Figure 2.1: a) *trans* and b) *cis* conformations of HMF.

interactions can affect the frequency of a vibrational band, its IR molecular absorptivity coefficient, its Raman scattering cross-section, and its half-width. Thus, it is expected that the molecular structure of HMF should depend strongly on the selected solvent, and such structure transformations/perturbations can easily be detected by Raman and IR spectroscopies.

Raman spectroscopy has been used recently to study the structures of HMF and other furan derivatives; the vibrational assignments of Raman-active HMF modes have also been calculated at the B3LYP/6-31+G(2df,p) level of theory [35, 36]. It has been suggested that solvent and anharmonic effects are the main reasons for the discrepancies between theoretical and experimental frequencies; the relative intensities of the C=O and C=C stretches were also found to be quite sensitive. Experimental spectroscopic studies of the cis/trans conformations of furfural revealed substantial differences between the relative intensities of the C=C and C=O vibrations of the two conformers [27, 28]. However, to the best of our knowledge, Raman and/or IR spectroscopic studies on the effect of different solvents on the molecular structure and chemical stability of HMF have not been performed.

The goal of the present study is to understand the effect of DMSO/water mixtures on the structural and vibrational properties of dissolved HMF and provide insights as to how changes in structure correlate with HMF reactivity. To this end, attenuated total reflection (ATR) FTIR spectroscopy and electronic structure calculations were performed. The vibrational modes of all components were probed for a large number of

binary and ternary mixtures to investigate solvent effects on HMF (e.g., the formation of HBs, competitive solvation around functional groups, and cis/trans conformational equilibrium). To identify intermolecular interactions, changes in bond strength are utilized as they are followed by the red- or blue-shifts of the corresponding vibrational frequencies. A number of possible configurations between HMF and DMSO or water were studied using electronic structure calculations and comparing with ATR-FTIR spectroscopic results. The link between the theoretical/spectroscopic results and the catalytic reactivity of HMF in DMSO/water mixtures is also discussed.

2.3 Results and Discussion

2.3.1 Liquid HMF

The measured IR spectrum of liquid HMF at 40 °C and the calculated IR spectra of its cis and trans conformations are shown in Fig. 2.2a and b. The vibrational assignments in the 800–4000 cm^{-1} range and the corresponding molecular absorptivities for both HMF conformers are shown in Table 2.1. (The atomic coordinates, the 39 normal vibrational modes, and the corresponding displacement vectors of each conformer are presented in Appendix A Tables S1–S5). The following discussion focuses on the C=O and C=C wavenumber region, magnified in Fig. 2.2c. The narrow band at around ∼1670 cm^{-1} is assigned to the carbonyl stretching vibration of liquid HMF. This band has two components instead of one as indicated by the deconvolution shown in Fig. 2.2c. This doublet may be attributed to the HMF cis/trans conformational equilibrium, to the strong coupling between the aldehyde C—H bend and the C=O stretch (which is evident from the magnitudes of the vectors of normal mode 33 shown in Tables S4 and S5 in Appendix A) [37], or it may be a manifestation of two different populations of interactions (primarily HBs) of different magnitude, between carbonyl groups and neighboring HMF molecules. It is generally adopted as a rule of thumb that the vibration of hydrogen-bonded molecules (X—Y$\cdots$H) appears at lower wavenumbers (redshifted) because of the weakening of the X—Y bond [37, 38]. Thus, the high- and low-frequency C=O stretching bands could also be ascribed to non-hydrogen- and

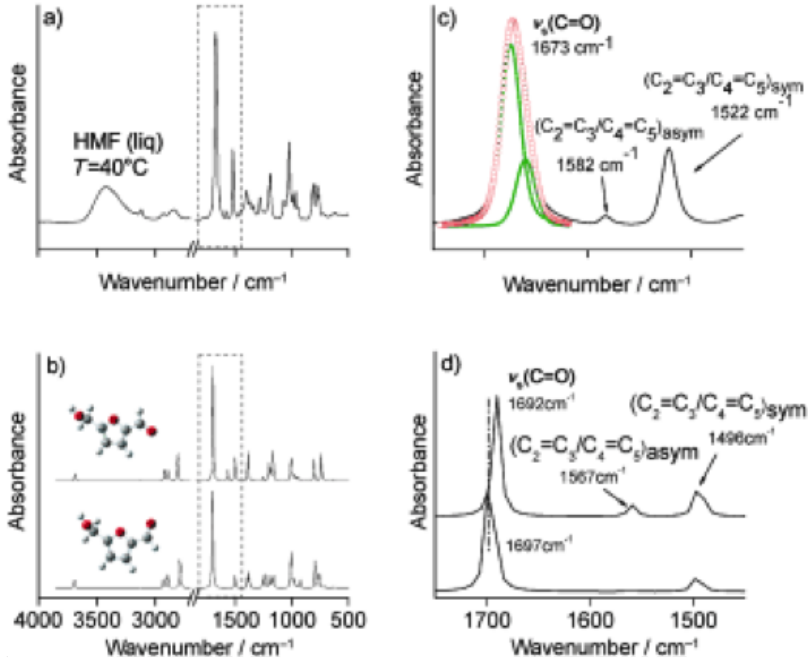

Figure 2.2: a) Experimental IR spectra of liquid HMF at 40°C. b) Calculated IR spectra of the cis and trans HMF conformers. c) and d) show the 1450–1800 cm^{-1} region shown in a) and b), respectively.

hydrogen-bonded carbonyl groups, respectively. Additionally, two other bands at 1583 and ∼1522 cm^{-1} are assigned to the asymmetric and symmetric vibrations of the furan ring C=C bonds.

The major differences between the calculated IR spectra of the two conformers are discussed below. The C=O stretching vibrations of both conformers are at ∼1700 cm^{-1} and differ by ∼8 cm^{-1} [the trans conformer absorbs at the lower wavenumber (Fig. 2.2c; Table 2.1)]. The predicted frequencies of the C=O stretch for both conformers are ∼ 30 cm^{-1} higher than the experimental values. The symmetric and asymmetric stretching of the C=C bonds of both conformers are around ∼1500 and ∼1565 cm^{-1}, respectively. Both of these bands appear at approximately ∼20 cm^{-1} lower wavenumbers than the experimental values. One important difference between the two conformers is the calculated molecular absorptivity (A) ratio of the C=C symmetric/asymmetric stretch. This ratio is 32 for the cis conformer and 3.5 for the trans.

trans-HMF position [cm^{-1}]	intensity [$K\,m\,mol^{-1}$]	*cis*-HMF position [cm^{-1}]	intensity [$K\,m\,mol^{-1}$]	Vibrational assignments[a]
3681	30.29	3682	31.2	O_1–H_1 (s)
3167	0.87	3166	0.252	C_3–H_4/C_4–H_5 sym. (s)
3156	0.06	3146	0.9	C_3–H_4/C_4–H_5 asym. (s)
2971	10.04	2974	8.81	C_1–H_2/C_1–H_3 asym. (s)
2916	34.24	2921	27.2	C_1–H_2/C_1–H_3 sym. (s)
2846	83.15	2827	106	C_6–H_6 (s)
1692	357.45	1697	418.2	C_6=O_2 (s), C_6–H_6 (b)
1567	45.63	1560	2.33	C_2=C_3/C_4=C_5 asym (s)
1496	158.06	1499	87.5	C_2=C_3/C_4=C_5 sym (s)
1446	5.11	1444	6.9	C_1–H_2/C_1–H_3 (sc)
1388	58.35	1394	7.17	C_6–H_6 (r), C_1–H_2/C_1–H_3 (w), C_3–H_4/C_4–H_5 (sc)
1364	41.64	1353	55.8	C_6–H_6 (r), C_1–H_2/C_1–H_3 (w)
1342	35.25	1335	47.5	O_1–H_1/C_1–H_2 (t)
1309	7.14	1308	10.4	O_1–H_1/C_1–H_3 (t)
		1256	52.8	multiple rocking, C_4–C_5–C_6 (b)
1207	10.90	1200	3.77	multiple rocking C_1–C_2–C_3 (b)
1186	78.86			multiple rocking
1180	23.38	1172	46.05	multiple rocking C_4–C_5–C_6 (b)
1143	9.04	1145	8.08	C_1–H_2/C_1–H_3 (t) O_1–H_1 (r)
1047	75.73	1049	91.85	C_1–O_1 (s)
1003	45.02	1008	51.24	C_3–H_4/C_4–H_5 (sc)
974	0.39	966	2.95	C_6–H_6 (r) out of plane
969	2.32	960	10.54	C_2–O_3–C_5 (s) symmetric, multiple rocking
		944	6.94	C_2–O_3–C_5 (s) asymmetric, multiple rocking
940	41.59			C_1–H_2/C_1–H_3 (r) O_1–H_1(r)
		936	28.66	C_1–H_2/C_1–H_3 (r) O_1–H_1(r)
938	1.37			C_2–O_3–C_5 (s) asymmetric, multiple rocking
871	0.75	858	0.38	C_3–H_4/C_4–H_5 (t)
797	47.37	788	52.86	C_3–H_4/C_4–H_5 (w)

[a] (s): Stretching, (r): rocking, (w): wagging, (t): twisting, (sc): scissoring (b): bending.

Table 2.1: IR frequencies and vibrational assignments of *trans*- and *cis*-HMF above 800 cm^{-1}. (The atomic coordinates, the 39 normal vibrational modes and the corresponding displacement vectors of each conformer are presented in Appendix A Tables S1 – S5).

As a result, it can be considered as an indicator of the presence of each conformer. The ratio observed experimentally is close to 6, which suggests that the largest fraction of HMF in the liquid is probably in the trans conformation. This conformer also has the lowest energy in the DFT calculations. Finally, the calculated O—H stretching frequency is overestimated by ∼200 cm^{-1}, whereas its molecular absorptivity compared to that of the carbonyl band at ∼1700 cm^{-1} is underestimated. The reason for these differences is the formation of HBs in which the OH group is the H donor.

This discrepancy between the calculated and experimental C=O stretching frequencies is a result of intermolecular interactions. To account for these interactions, we performed calculations for four trans-HMF dimers. We only used the trans conformer because it was the most stable in the gas-phase calculations. The optimized structures along with the C=O and O—H stretching frequencies are depicted in Fig. 2.3. (The calculated spectra are shown in Appendix A Figure S2). Dimers a and b show HMF molecules that interact through single O—H$\cdots$O—H and O—H$\cdots$O=C HBs, respectively. In dimer c, the monomers interact through their formyl groups, each of which is an HB donor to the O atom of the other. Dimer d shows the two monomers in an antiparallel ring arrangement, which form two O—H$\cdots$O=C HBs, and it is the most stable among the four dimers examined. In dimer d, the in-phase and out-of-phase stretching vibrations of C=O have two discrete IR bands (the asymmetric band has a lower absorbance than the symmetric) with a relative molecular absorptivity ratio of ∼19. The ratio of the two components of the experimental C=O stretching band (Fig. 2.2c) is ∼1.3. Thus, although gas-phase calculations show that dimer d is the most stable, it must be excluded as the dominant species in liquid HMF. Furthermore, based on crystallographic data, dimers a and b should be considered as the most plausible structures [26]. Another important finding from the DFT calculations is that, in contrast to the carbonyl group, the symmetric and asymmetric C=C stretching vibrations are unaffected by the formation of HBs on the carbonyl or hydroxyl groups.

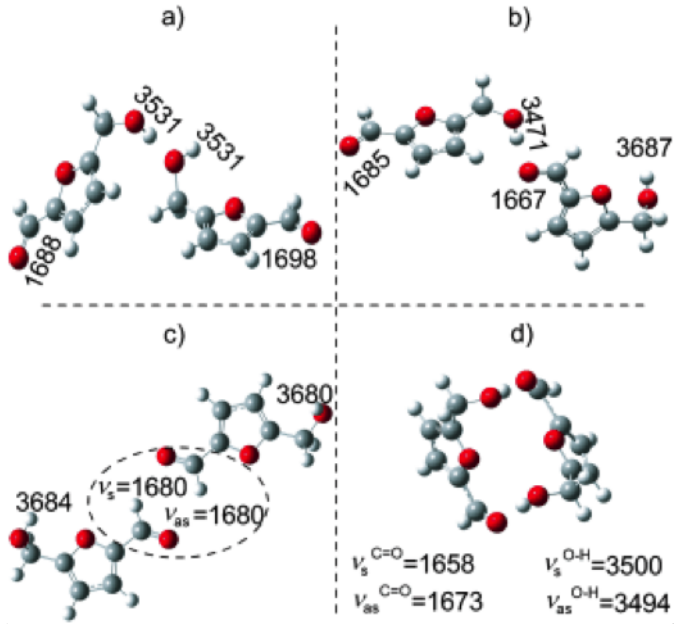

Figure 2.3: Molecular configurations of four trans-HMF dimers and calculated frequencies of the C=O and OH stretching vibrations [cm^{-1}].

2.3.2 HMF in HMF/DMSO and HMF/D_2O binary solutions

The HMF C=C, C=O, and O—H stretching bands in binary HMF/DMSO ($X_{HMF} = 0.3$) and HMF/D_2O ($X_{HMF} = 0.22$) solutions at 25 °C are shown in Fig. 2.4. The positions and shapes of the C=O and O—H bands are sensitive to the solvent, whereas those of the C=C stretches seem to be unaffected. In particular, the following observations, with respect to the bands of liquid HMF, are made:

(i) The HMF C=O stretching band (at ∼1673 cm^{-1} in liquid HMF) slightly shifts to higher wavenumbers if HMF is dissolved in DMSO but redshifts by ∼8 cm^{-1} in D_2O.

(ii) The carbonyl stretch appears as a single, well-defined band in DMSO but remains a doublet in D_2O.

(iii) The HMF O—H vibration is redshifted by ∼100 cm^{-1} in DMSO but no significant shifts were observed for various HMF/D_2O mixtures.

(iv) The $A^{sym}_{C=C}/A^{asym}_{C=C}$ ratio does not change significantly in the two solvents and

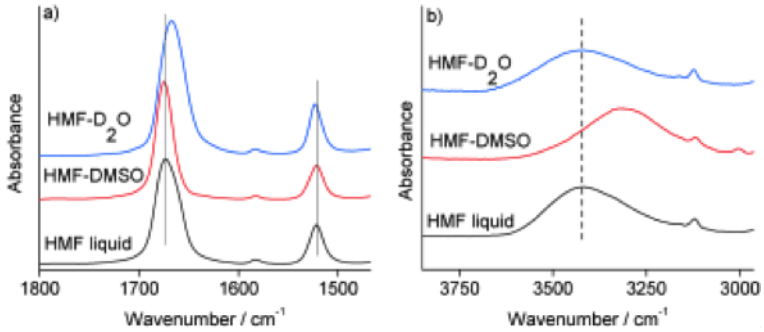

Figure 2.4: ATR-FTIR spectra of liquid HMF, HMF/DMSO, and HMF/D_2O binary mixtures at the a) C=C and C=O and b) OH stretching regions; resolution=4 cm^{-1}, number of scans=32.

the value is ∼6.

The C=O and O—H stretching vibrations do not vary with the concentration of HMF in the range of values examined in this work (Appendix A Figure S3). Thus we infer that the observed changes are not related to HMF–HMF interactions. The experimental observations are discussed and interpreted below.

The frequency of a normal vibration is related strongly to the force constant of the specific bond. Specifically, for simple aldehydes and ketones, the stretching vibration of the carbonyl group gives rise to a strong and distinctive IR absorption band at ∼1700 cm^{-1} that is highly sensitive to bond length and strength perturbations because of intermolecular interactions [30]. Interactions such as HBs result in specific changes to spectroscopic features. It is generally accepted that the classical X—Y$\cdots$H is characterized by the weakening and lengthening of the X—Y bond [39] and, consequently, the IR stretching mode is shifted towards lower wavenumbers (redshifted) [29, 31, 32]. As a result, the observed shifts depend on the nature and strength of the carbonyl or hydroxyl group interactions with their nearest neighbors. Thus, the blueshift of the HMF carbonyl frequency in DMSO indicates that the C=O bond in DMSO is stronger relative to that in neat liquid HMF.

To further investigate the interactions between the C=O bond of HMF and

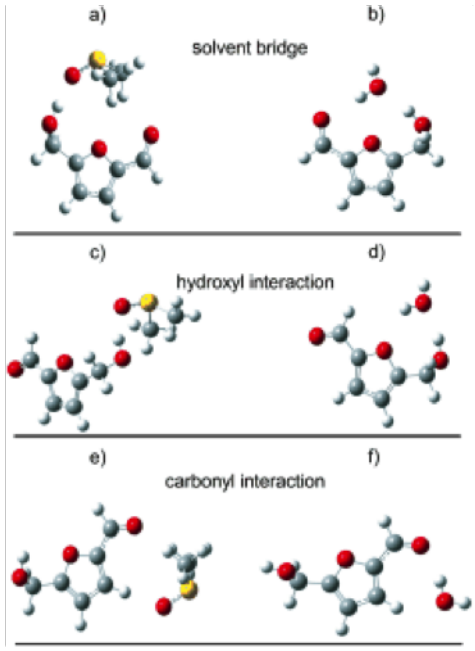

Figure 2.5: Selected configurations of HMF–solvent complexes. Three main types of interaction were observed in the 23 configurations of DMSO/HMF and 10 configurations of H_2O/HMF examined. The solvent interacts with the HMF hydroxyl group (c and d), with the HMF carbonyl group (e and f), and with both moieties to form a bridge with cis-HMF (a and b). The structures shown are the lowest energy configurations for each type of interaction optimized by using the B3LYP/6-31+G(d,p) level of theory.

DMSO or water molecules, DFT calculations were performed for HMF in DMSO and H_2O implicit solvent as well as in a large number of different HMF–DMSO and HMF–water interaction geometries (A). The pairs with the lowest energy (for each interaction) are shown in Fig. 2.5. The binding energies of each complex in the gas phase and in implicit solvent as well as the corresponding carbonyl and hydroxyl frequencies in the gas phase in implicit and explicit solvent are shown in Table 2.2.

The calculations show that DMSO binds more strongly to HMF than water and that interactions with the HMF hydroxyl group are stronger than with the HMF carbonyl group. The calculated $A^{sym}_{C=C}/A^{asym}_{C=C}$ ratio of trans-HMF/DMSO is ∼4, whereas that of cis-HMF/DMSO is ∼90. The experimental value of this ratio is 6, which

Configuration	$\nu_{C=O}$[a] [cm^{-1}]	ν_{O-H}[a] [cm^{-1}]	Binding energy[b] [kcal mol^{-1}] vacuum B3LYP/ 6-31+G(d,p)	implicit B3LYP/ 6-31+G(d,p)	vacuum MP2/ aug-cc-pVDZ	implicit MP2/ aug-cc-pVDZ	vacuum MP2/ aug-cc-pVTZ	implicit MP2/ aug-cc-pVTZ
a[b]	1675.4	3346.7	−13.93	−19.38	−19.22	−10.41	−17.24	−19.40
b	1660.8	3468.4	−12.63	−17.65	−12.39	−18.49	−12.12	−17.78
c	1688.8	3291.8	−10.98	−17.86	−18.33	−23.87	−15.91	−20.21
d	1694.1	3525.4	−8.34	−15.44	−9.01	−17.31	−8.75	−16.66
e	1672.7	3687.6	−8.06	−11.87	−11.58	−15.36	−10.18	−12.67
f	1670.4	3691.0	−7.68	−8.92	−8.12	−15.77	−7.75	−15.10
implicit solvent								
cis–DMSO	1656	3656						
cis–H_2O	1598.6	3657.1						
trans–DMSO	1660	3638						
trans–H_2O	1602.8	3656.1						

[a] Frequencies were calculated at the B3LYP/6-31+G(d,p) level and scaled by 0.9648.[29] [b] Binding energies in vacuum calculated from $E_{complex,vacuum}-E_{HMF,vacuum}-E_{solvent,vacuum}$. Implicit binding energies calculated from $E_{complex,implicit}-E_{HMF,vacuum}-E_{solvent,implicit}$. Structures were optimized at the B3LYP/6-31+G(d,p) level, reoptimized at the MP2/aug-cc-pVDZ level, and then single-point energy calculations were performed at the MP2/aug-cc-pVTZ level. [c] the MP2/aug-cc-pVDZ optimization pushes the DMSO away from the carbonyl, so it ends up being just a DMSO/HMF OH interaction rather than a bridge.

Table 2.2: Frequencies and electronic binding energies of the configurations presented in Fig. 2.5.[a]

indicates that the trans conformer is the dominant species in DMSO. Although all the solvent molecules of the first solvation cell are not typically considered explicitly, electronic structure calculations combined with spectroscopic data can provide sound indications of the strength of interactions and help us to reach conclusions on plausible configurations [40]. For example, our DFT calculations show that if the O atom of the HMF carbonyl group is hydrogen bonded with solvent molecules, the ν_s(C=O) of HMF appears at higher wavenumbers in DMSO (1672–1674 cm^{-1}) than in water (1660 cm^{-1}). These results are in excellent agreement with our experiments.

In the case of HMF/D_2O solutions, the shape of ν_s(C=O) manifests hydrogen bonding of C=O with D_2O, with a broad distribution of binding strengths. The DFT calculations indeed confirm that HBs between water and HMF around the C=O group of varying binding strength can cause different shifts in the ν_s(C=O) vibrational mode. Thus, the addition of more than one D_2O molecule around HMF may lead to interactions that could influence the location, intensity, and width of the C=O band significantly. Similar findings have been reported for other systems with carbonyl groups. In the case of acetone/methanol mixtures, the location of the C=O frequency

of non-hydrogen-bonded acetone monomers is quite different from that of singly and doubly hydrogen-bonded acetone molecules [31]. Additionally, multiple carbonyl bands have also been reported for camphor in various solvents [41]. There, the double C=O band in protic solvents such as methanol has been attributed to the presence of both nonspecifically solvated camphor ($\nu_{C=O}$ = 1745.4 cm^{-1}) and a specific equimolar 1:1 camphor/methanol complex ($\nu_{C=O}$ = 1732.2 cm^{-1}). Contrary to the double shape of the C=O band in water, only a single, well-defined peak appears in DMSO. In view of our earlier analysis of the C=O band in pure liquid HMF, the single C=O peak in DMSO could be ascribed either to the stabilization of one of the two conformers (we propose trans-HMF because of the low $A^{sym}_{C=C}/A^{asym}_{C=C}$ ratio) or to weaker coupling with the bending mode of the formyl C—H group.

We also paid particular attention to the effect of solvent on the O—H stretching band as it is very sensitive to hydrogen bonding. The very broad O—H band reflects a broad distribution of HB strengths; and changes in the shape of the band shape suggest a redistribution of binding strengths. Deconvolution of the O—H region, by using Voigt profiles, revealed one (in the case of DMSO) or two (in the case of D_2O) components centered at ∼3320 and ∼3430 cm^{-1}. The low frequency part of the O—H stretching band at ∼3300 cm^{-1} is caused by the vibrations of O—H groups with stronger HBs than those that have their O—H stretching band in the vicinity of ∼3400 cm^{-1}. It is obvious that, contrary to the C=O group, the O—H group of HMF forms stronger HBs (as H donor) with DMSO than D_2O. Based on our calculations, the HMF O—H stretching vibration appears at lower wavenumbers (∼3290–3350 cm^{-1}) if it is an HB donor to a DMSO molecule than to a water O atom (∼3470–3520 cm^{-1}), which indicates stronger binding with DMSO. These findings are in excellent agreement with our experimental results. Furthermore, it is also accepted that the HB strength and the O—H shifts depend on the Lewis basicity of the solvent, which can be quantified by the solvent donor number (DN) [22]. DMSO has a higher DN (DN_{DMSO}=29.8) than water (DN_{water}=18), which further confirms our findings.

Before we analyze the data for the ternary mixtures, we will comment on the

changes in the vibrational bands of each solvent as a function of HMF concentration. In the case of HMF/D_2O solutions, we observed differences in the relative intensities of the symmetric and asymmetric bands of D_2O that could be ascribed either to redistribution of water HBs, which result from intermolecular interactions with HMF, or to reorganization of the self-association of the water molecules. The IR spectra of the binary HMF/DMSO solutions in the 600–1200 cm^{-1} region are shown in Fig. 2.6. The spectra have been normalized with respect to the band at 950 cm^{-1}, which has been assigned to the rocking of the DMSO methyl groups and is routinely used in the literature as a reference owing to its low sensitivity to intermolecular interactions. With the increasing HMF concentration, the S=O stretching vibration (1057 cm^{-1}) remains fixed but its absorbance decreases, and a well-defined band at ∼1025 cm^{-1} increases in intensity. This can be ascribed to the formation of hydrogen-bonded HMF–DMSO complexes at the expense of DMSO–DMSO clusters. In the past, these bands have been used to correlate Raman spectra with the coordination number of DMSO around glucose [42] and fructose [40]. Unfortunately, because of overlaps with the C3—H4/C4—H5 scissoring vibrational mode of HMF in the same region (predicted at ∼1009 cm^{-1} by DFT), it is difficult to further analyze the S=O spectral envelope and thus use the spectra to estimate coordination numbers. However, it is well established in the literature that important information about the DMSO structure can be obtained from analyzing the changes in the DMSO C—S—C symmetric and asymmetric vibrations at 667 and 697 cm^{-1}, respectively. In the case of DMSO/water mixtures, the charge transfer between DMSO and water leads to elongation of the S=O bond and to an increase in the electron density around the S nucleus and, consequently, to a strengthening of the C—S bond [43, 44]. Thus, we observe a blueshift in the C—S—C symmetric and asymmetric vibrations and a redshift in the S=O stretching vibration. We also observed identical shifts in the case of DMSO/D_2O binary mixtures. In contrast, in the case of HMF/DMSO mixtures, the C—S—C stretches do not shift with the HMF concentration. This behavior is reported here for the first time and it is quite surprising because a blueshift was expected. It reflects that the C—S bond length and

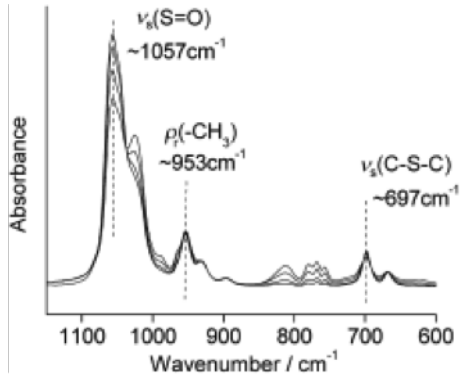

Figure 2.6: IR spectra of binary HMF/DMSO solutions in the 600–1800 cm^{-1} region; T=25 °C, resolution=4 cm^{-1}, Number of scans=32.

C—S—C angle do not change significantly as DMSO interacts with HMF. Analysis of the DFT-derived spectra showed that the only DMSO–HMF complex geometry that did not induce changes in the C—S—C band is that shown in Fig. 2.5e, in which the *trans*-HMF C=O group interacts with the DMSO methyl groups and S=O interacts with the C—H of the HMF ring. All the other configurations have blueshifted C—S—C bands. Thus, if we consider that *trans*-HMF is the most stable conformer and the excellent agreement between the calculated and experimental spectra, we suggest that the dominant interaction between HMF and DMSO in solution is that implied by the structure shown in Fig. 2.5e.

2.3.3 HMF in HMF/DMSO/D_2O ternary solutions

The carbonyl region of the IR spectra of ternary mixtures are shown in Fig. 2.7a and S4. In all cases, the HMF/DMSO molar ratio was kept constant at a value of 0.3. No significant changes in the positions of the C=O and OH bands of HMF were observed as the HMF concentration was varied at constant D_2O/DMSO molar fractions. In the following discussion, the D_2O mol fraction (X_{D_2O}) will refer to the D_2O molar faction in the D_2O/DMSO binary solvent and not in the ternary mixture. As can be seen, the position of the C=O stretch seems to be unaffected up to X_{D_2O} ~0.3–0.4. However, at higher water contents, the C=O stretch redshifts with increasing X_{D_2O}. This effect is

ascribed to a weakening of the C=O bond, caused by the formation of C=O$\cdots$D HBs. Therefore, it becomes quite clear that at high X_{D_2O} fractions, the water molecules displace the DMSO that is coordinated around the HMF C=O group.

As mentioned in the previous section, C=O functionalities could interact with the H atoms of DMSO methyl groups. Thus, one would expect that both C=O$\cdots$H and C=O$\cdots$D HBs with DMSO and D_2O, respectively, could exist simultaneously, and that their spectral signatures should be similar to those observed in the corresponding binary mixtures. The C=O bands of all the spectra were deconvoluted by using Voigt functions based on the Levenberg–Marquardt algorithm. A representative analysis is presented in Figure S5 in Appendix A. The results showed that up to X_{D_2O}~0.3, only one Voigt profile is sufficient to fit the C=O stretching vibration at ~1674 cm^{-1}. For higher X_{D_2O}, two additional Voigt profiles were used at ~1667 and 1658 cm^{-1} to account for the doublet that is observed if HMF interacts with water. The deconvolution was performed by keeping the frequency position and peak width constant. We ascribe the high-frequency peak to carbonyl bonds that interact with DMSO and the lower frequency peaks to one or more C=O$\cdots$D HBs with D_2O. Therefore, the broadening of the C=O band at a higher D_2O content reflects a wide distribution of HB strengths. Additionally, the integrated absorbance of the bands that correspond to interactions of the HMF carbonyl group with DMSO or D_2O as a function of X_{D_2O} is shown in Fig. 2.7b. This analysis indicates that DMSO preferentially solvates the HMF C=O bond if X_{D_2O} is less than ~0.4. This finding is in agreement with a molecular dynamics (MD) study that showed the preferential solvation of DMSO around the HMF carbonyl group even in the presence of a significant amount of water [25].

Finally, we address the effect of solvent on the OH stretching vibration of HMF that appears in the 3200–3500 cm^{-1} range (Fig. 2.8a). In contrast to the carbonyl group, significant changes in the O—H stretching vibration occur even if small amounts of D_2O are added to DMSO. As mentioned earlier, in the course of the analysis of the experimental and calculated frequencies of the binary mixtures, the O—H vibration of HMF occurs at lower wavenumbers in DMSO than in water. Deconvolution of

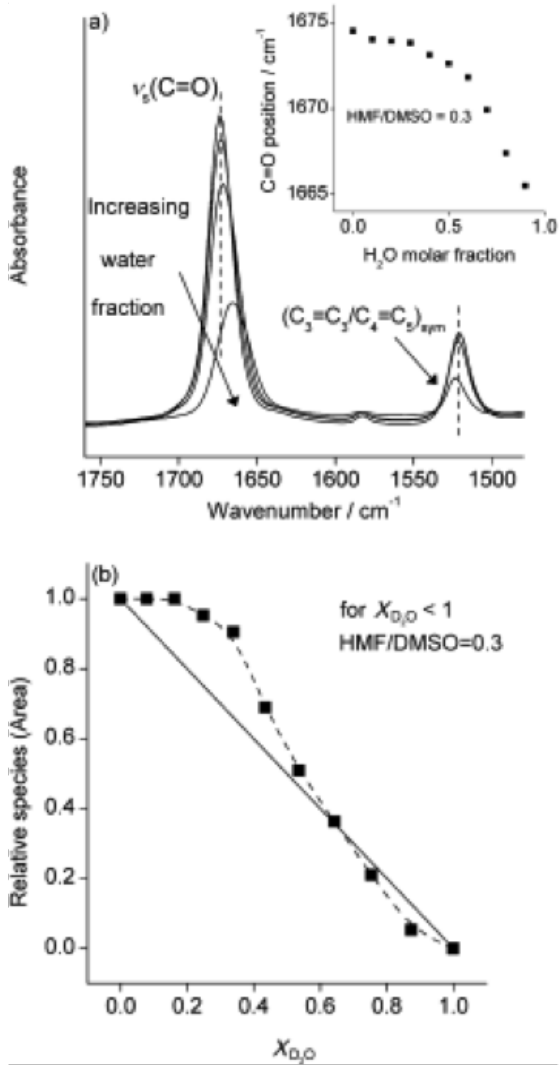

Figure 2.7: a) Effect of D_2O on the C=C and C=O stretching vibrations of HMF in HMF/DMSO/D_2O and constant HMF/DMSO=0.3 molar ratio (if $X_{D_2O} < 1$); T=25 °C, resolution=4 cm^{-1}, number of scans=32. b) Relative integrated areas of HMF species hydrogen bonded through C=O with DMSO or D_2O molecules.

representative spectra has been performed for the O—H band by using Voigt functions. Two Voigt profiles are necessary for the deconvolution, which are located at ∼3300 and 3400 cm^{-1}. In the case of DMSO, the band at ∼3300 cm^{-1} is assigned to the OH groups that are hydrogen bonded with the O atom of DMSO, whereas the bands at ∼3300 and 3400 cm^{-1} in the case of D_2O are ascribed to HMF OH groups with different HB strengths with the O atom of D_2O (Figure S6). The integrated areas of these bands are shown in Fig. 2.8b. It is obvious that a high-frequency band is observed that increases with the molar fraction of D_2O even at a low D_2O content. This observation clearly shows that D_2O preferentially coordinates around the HMF hydroxyl groups in ternary mixtures, in agreement with an earlier MD study [25].

2.3.4 Link with HMF reactivity

Rehydration and aldol condensation reactions are implicated in the formation of HMF side products [12, 13, 45]. These reactions involve the nucleophilic attack of water or of an enol on HMF. Frontier molecular orbital theory was used to examine the influence of the solvent on these reactions. Changes in the energy of the LUMO influence the reactivity of a molecule: the higher (or lower) the LUMO energy the higher (or lower) the barrier for a nucleophilic attack.

The LUMO topologies of selected configurations are shown in Fig. 2.9. The major features of the LUMO topology, such as the significant amplitude on the carbonyl and ring antibonding orbitals and the small amplitude on the hydroxyl group, are essentially unchanged between isolated HMF and HMF in the presence of solvent. Although the LUMO topology does not change significantly in the presence of solvent, the LUMO energy does. For isolated HMF in implicit solvent (Fig. 2.10a), DMSO increases the LUMO and water decreases the LUMO relative to gas-phase HMF. This finding agrees with experimental observations that DMSO inhibits side reactions of HMF, and it suggests that DMSO increases the LUMO energy of HMF, which protects it from nucleophilic attack by water. An examination of the bimolecular complexes shown in Fig. 2.5 in implicit solvent (Fig. 2.10b) corroborates this observation. In

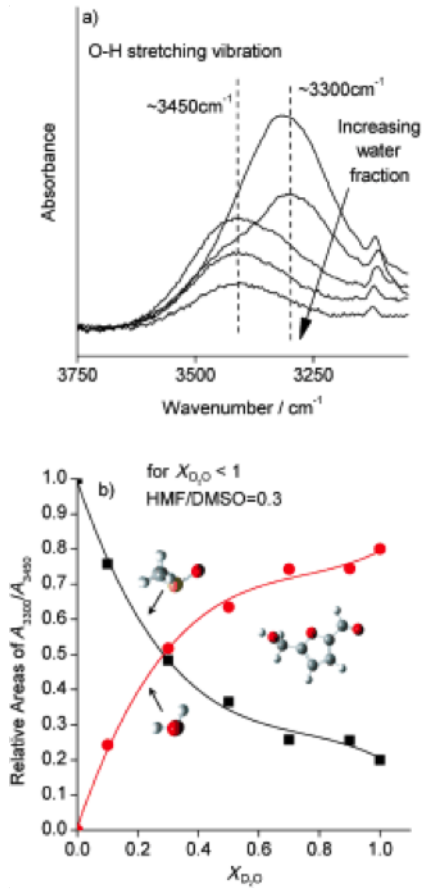

Figure 2.8: a) Effect of D_2O on the O—H stretching vibrations of HMF in HMF/DMSO/D_2O and constant HMF/DMSO=0.3 molar ratio (if $X_{D_2O} < 1$); T=25 °C, resolution=4 cm^{-1}, number of scans=32. b) Relative integrated areas of the OH bands at 3300 and 3460 cm^{-1}.

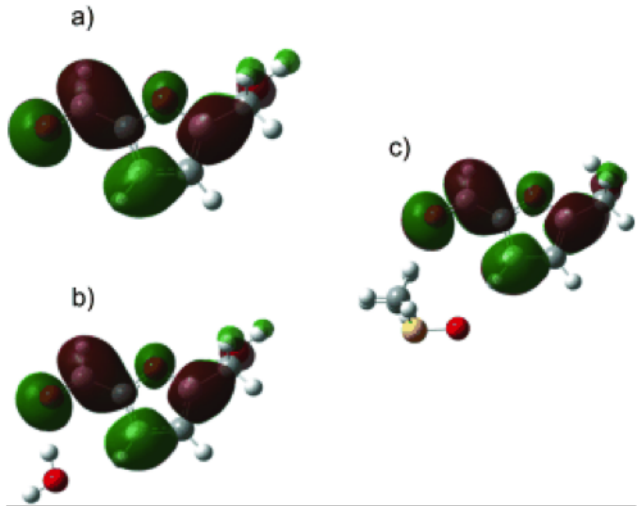

Figure 2.9: The topology of the LUMO of a) isolated *trans*-HMF, b) *trans*-HMF that interacts with water through the C=O group, and c) *trans*-HMF that interacts with DMSO through the C=O group. The LUMO topology is not strongly affected by interaction with solvent.

addition, the influence of individual hydrogen-bonding interactions can be examined. If the specific DMSO–carbonyl interaction is accounted for, the LUMO energy is unchanged relative to HMF in implicit DMSO, but this specific interaction with water further decreases the LUMO of HMF. The specific DMSO–hydroxyl interaction further increases the LUMO energy, whereas the specific interaction of water does not perturb the HMF LUMO energy relative to that in implicit water. This underscores the importance of preferential solvent interactions. The interaction of DMSO with the HMF hydroxyl group protects HMF from nucleophilic attack, and the interaction of water with the HMF carbonyl group increases the susceptibility of HMF to nucleophilic attack. Recent work by Aziz et al. showed that it is possible to measure the HOMO and LUMO energies of the constituents of DMSO/water and acetone/water binary mixtures by using soft X-ray spectroscopy and resonant inelastic X-ray scattering [46, 47]. This approach might eventually be used to validate our calculations and gain further understanding of this system.

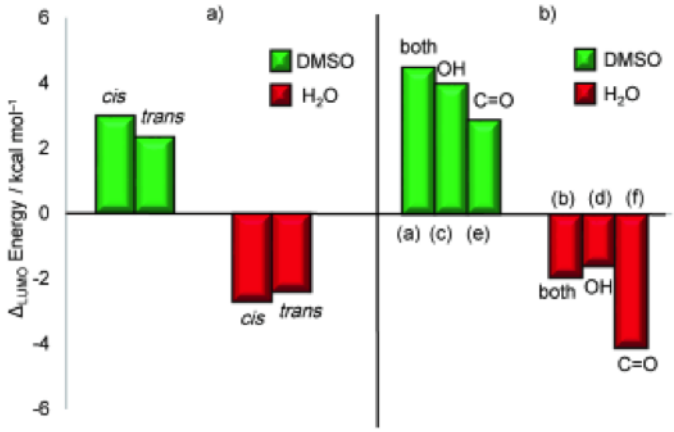

Figure 2.10: a) Change in LUMO energy of isolated HMF in implicit solvent and b) representative configurations of HMF–solvent complexes in implicit solvent (see Fig. 2.5 for structures). The reference LUMO energy in all systems is that of isolated HMF in a vacuum. DMSO increases the LUMO energy on HMF, which reduces its susceptibility to nucleophilic attack, whereas water decreases the LUMO, which increases its susceptibility to nucleophilic attack

2.4 Conclusions

The solvation of 5-hydroxymethylfurfural (HMF) in DMSO, D_2O, and DMSO/D_2O mixtures was investigated by using attenuated total reflectance (ATR) FTIR spectroscopy and DFT calculations. The position, width, and shape of the HMF carbonyl, hydroxyl, and C=C bands were analyzed and compared with calculated spectra from a large number of configurations to explore the formation of hydrogen bonds with the solvent and understand the effect of solvation on the cis/trans HMF conformational equilibrium. We found that the trans conformer appears to be the most dominant for all samples examined. Analysis of the data from binary mixtures revealed that DMSO binds more strongly than water to both the hydroxyl and carbonyl groups of HMF. The influence of solvent on the energy of the LUMO was examined by using frontier molecular orbital theory. The energy of the LUMO influences the reactivity of a molecule in the case of nucleophilic attack. In all cases examined, the LUMO energy of HMF is higher if it is solvated with DMSO than with water, which indicates

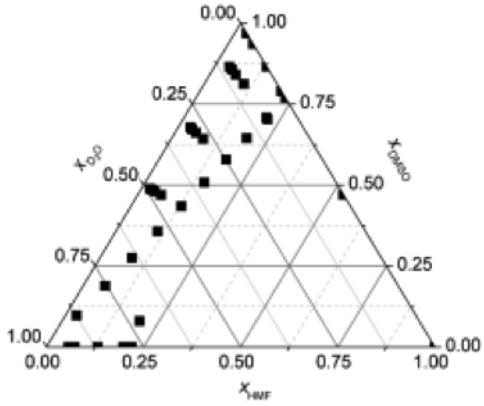

Figure 2.11: Ternary diagram of sample compositions.

that solvation by DMSO reduces its susceptibility to nucleophilic attack. Analysis of the ATR-FTIR data of HMF/DMSO/D_2O ternary mixtures revealed that DMSO preferentially solvates the HMF carbonyl group. This finding, in conjunction with the effect of DMSO on the HMF LUMO energy, provides an explanation for the enhanced stability of HMF if DMSO is used as a co-solvent in fructose dehydration reactions.

2.5 Experimental Section

2.5.1 Materials

High purity HMF (>99 % purity, Sigma), DMSO (≥99.5 %, Sigma), and D_2O (>99.9 %, Sigma) were used without any further purification. For the binary HMF/DMSO and HMF/D_2O solutions, appropriate amounts of HMF were added to DMSO or D_2O (0.5 mL). Samples with a varying HMF concentration were prepared by diluting the initial mixtures with appropriate amounts of each solvent. For the preparation of HMF/DMSO/D_2O ternary mixtures, appropriate amounts of HMF were added to binary DMSO/D_2O solutions in the range of X_{D_2O}=0.1–0.9. A series of measurements were also performed for mixtures with constant HMF/DMSO and DMSO/D_2O molar ratios. The compositions of all samples tested are shown in a ternary diagram in Fig. 2.11 and summarized in Table S6 in Appendix A.

2.5.2 ATR-IR Spectroscopy

A Nicolet 8700 FTIR spectrometer equipped with a deuterated, L-alanine-doped triglycine sulfate (DLaTGS) detector, and a Golden Gate single-reflection diamond ATR was used for all spectroscopic studies. The instrument was equipped with a purge gas of dehumidified air to remove water vapor. The resolution of the instrument was set at 4 cm^{-1} for the whole set of measurements and the number of scans varied from 16 to 32. To account for the effect of wavenumber on the penetration depth, the spectra were corrected by using the following equations as implemented by the OMNIC v8 software:

$$Absorbance(\nu)_{corrected} = \frac{Absorbance(\nu)_{ATR}}{d_p} \tag{2.1}$$

$$d_p = \frac{10000}{2\pi\nu(n_p^2 sin^2\theta - n_s^2)^{1/2}} \tag{2.2}$$

in which d_p is the penetration depth, ν is the wavenumber [cm^{-1}], n_p is the refractive index of diamond (2.47), n_s is the refractive index of the sample, and θ is the angle of incidence of the IR beam at the surface of the diamond (45 °). The refractive index of each sample was measured by using a Bausch & Lomb Abbe-3L refractometer. The refractive indices of the binary DMSO/D_2O and ternary HMF/DMSO/D_2O mixtures are presented in Appendix A Figure S1.

2.5.3 Computational methods

Electronic structure calculations were performed by using Gaussian 09, Revision A.02 software [48], at the B3LYP/6-31+G(d,p), MP2/aug-cc-pVDZ, and MP2/aug-cc-pVTZ levels of theory. Bimolecular complexes of HMF that interact with HMF, DMSO, and H_2O were studied to examine the local hydrogen-bonding interactions between the solvent and the HMF hydroxyl and carbonyl groups. These systems were studied in the gas phase as well as using the SMD implicit solvation model [49] for water and DMSO.

Vibrational frequencies were calculated at the B3LYP/6-31+G(d,p) level and scaled by 0.9648 [50]. Structures were optimized and frequencies calculated at the B3LYP level. These structures were optimized again at the MP2/aug-cc-pVDZ level, and single-point energy calculations were performed on the latter at the MP2/aug-cc-pVTZ level to obtain interaction energies between hydrogen-bonded molecules.

2.6 Acknowledgements

The work was financially supported by the Catalysis Center for Energy Innovation, an Energy Frontier Research Center funded by the U.S. Department of Energy, Office of Science, Office of Basic Energy Sciences under Award Number DE-SC0001004.

REFERENCES

[1] G. Tsilomelekis, T. R. Josephson, V. Nikolakis, and S. Caratzoulas. Origin of 5-hydroxymethylfurfural stability in water/dimethyl sulfoxide mixtures. *ChemSusChem*, 7(1):117–126, 2014. doi: 10.1002/cssc.201300786.

[2] J. N. Chheda, Y. Román-Leshkov, and J. A. Dumesic. Production of 5-hydroxymethylfurfural and furfural by dehydration of biomass-derived mono- and poly-saccharides. *Green Chemistry*, 9(4):342, 2007. doi: 10.1039/b611568c.

[3] J. N. Chheda, G. W. Huber, and J. A. Dumesic. Liquid-phase catalytic processing of biomass-derived oxygenated hydrocarbons to fuels and chemicals. *Angewandte Chemie - International Edition*, 46(38):7164–7183, 2007. ISSN 14337851. doi: 10.1002/anie.200604274.

[4] Y. Roman-Leshkov, C. J. Barrett, Z. Y. Liu, and J. A. Dumesic. Production of dimethylfuran for liquid fuels from biomass-derived carbohydrates. *Nature*, 447 (7147):982–985, 2007. doi: 10.1038/nature05923.

[5] A. a. Rosatella, S. P. Simeonov, R. F. M. Frade, and C. a. M. Afonso. 5-Hydroxymethylfurfural (HMF) as a building block platform: Biological properties, synthesis and synthetic applications. *Green Chemistry*, 13(4):754, 2011. ISSN 1463-9262. doi: 10.1039/c0gc00401d.

[6] M. Balakrishnan, E. R. Sacia, and A. T. Bell. Etherification and reductive etherification of 5-(hydroxymethyl)furfural: 5-(alkoxymethyl)furfurals and 2,5-bis(alkoxymethyl)furans as potential bio-diesel candidates. *Green Chemistry*, 14 (6):1626–1634, 2012. ISSN 1463-9262. doi: 10.1039/C2GC35102A.

[7] J. M. R. Gallo, D. M. Alonso, M. A. Mellmer, J. H. Yeap, H. C. Wong, and J. A. Dumesic. Production of furfural from lignocellulosic biomass using beta zeolite and biomass-derived solvent. *Topics in Catalysis*, 56(18-20):1775–1781, 2013. ISSN 10225528. doi: 10.1007/s11244-013-0113-3.

[8] C. L. Williams, C.-C. Chang, P. Do, N. Nikbin, S. Caratzoulas, D. G. Vlachos, R. F. Lobo, W. Fan, and P. J. Dauenhauer. Cycloaddition of Biomass-Derived Furans for Catalytic Production of Renewablep-Xylene. *ACS Catalysis*, 2(6):935–939, 2012. doi: 10.1021/cs300011a.

[9] N. Nikbin, P. T. Do, S. Caratzoulas, R. F. Lobo, P. J. Dauenhauer, and D. G. Vlachos. A DFT study of the acid-catalyzed conversion of 2,5-dimethylfuran and ethylene to p-xylene. *Journal of Catalysis*, 297:35–43, 2013. ISSN 00219517. doi: 10.1016/j.jcat.2012.09.017.

[10] P. T. M. Do, J. R. McAtee, D. A. Watson, and R. F. Lobo. Elucidation of Diels-Alder reaction network of 2,5-dimethylfuran and ethylene on HY zeolite catalyst. *ACS Catalysis*, 3(1):41–46, 2013. ISSN 21555435. doi: 10.1021/cs300673b.

[11] T. D. Swift, C. Bagia, V. Nikolakis, D. G. Vlachos, G. Peklaris, P. Dornath, and W. Fan. Reactive adsorption for the selective dehydration of sugars to furans: Modeling and experiments. *AIChE Journal*, 59(9):3378–3390, 2013. ISSN 00011541. doi: 10.1002/aic.14090.

[12] S. K. R. Patil and C. R. F. Lund. Formation and Growth of Humins via Aldol Addition and Condensation during Acid-Catalyzed Conversion of 5-Hydroxymethylfurfural. *Energy Fuels*, 25(10):4745–4755, 2011. doi: 10.1021/ef2010157.

[13] S. K. R. Patil, J. Heltzel, and C. R. F. Lund. Comparison of structural features of humins formed catalytically from glucose, fructose, and 5-hydroxymethylfurfuraldehyde. *Energy and Fuels*, 26(8):5281–5293, 2012. ISSN 08870624. doi: 10.1021/ef3007454.

[14] M. Chidambaram and A. T. Bell. A two-step approach for the catalytic conversion of glucose to 2,5-dimethylfuran in ionic liquids. *Green Chemistry*, 12(7):1253, 2010. ISSN 1463-9262. doi: 10.1039/c004343e.

[15] B. Liu, Z. Zhang, K. Huang, and Z. Fang. Efficient conversion of carbohydrates into 5-ethoxymethylfurfural in ethanol catalyzed by AlCl3. *Fuel*, 113:625–631, 2013. doi: 10.1016/j.fuel.2013.06.015.

[16] Y.-Y. Lee and K. C.-W. Wu. Conversion and kinetics study of fructose-to-5-hydroxymethylfurfural (HMF) using sulfonic and ionic liquid groups bi-functionalized mesoporous silica nanoparticles as recyclable solid catalysts in DMSO systems. *Phys. Chem. Chem. Phys.*, 14:13914–13917, 2012. ISSN 1463-9084. doi: 10.1039/c2cp42751f.

[17] Y. Y. Gorbanev, S. K. Klitgaard, J. M. Woodley, C. H. Christensen, and A. Riisager. Gold-catalyzed aerobic oxidation of 5-hydroxymethylfurfural in water at ambient temperature. *ChemSusChem*, 2(7):672–675, 2009. ISSN 18645631. doi: 10.1002/cssc.200900059.

[18] V. V. Ordomsky, J. Van Der Schaaf, J. C. Schouten, and T. A. Nijhuis. The effect of solvent addition on fructose dehydration to 5-hydroxymethylfurfural in biphasic system over zeolites. *Journal of Catalysis*, 287:68–75, 2012. ISSN 00219517. doi: 10.1016/j.jcat.2011.12.002.

[19] R. Weingarten, W. C. Conner, and G. W. Huber. Production of levulinic acid from cellulose by hydrothermal decomposition combined with aqueous phase dehydration with a solid acid catalyst. *Energy & Environmental Science*, 5(6):7559–7574, 2012. ISSN 1754-5692. doi: 10.1039/c2ee21593d.

[20] R. Kourieh, V. Rakic, S. Bennici, and A. Auroux. Relation between surface acidity and reactivity in fructose conversion into 5-HMF using tungstated zirconia catalysts. *Catalysis Communications*, 30:5–13, 2013. ISSN 15667367. doi: 10.1016/j.catcom.2012.10.005.

[21] F. Wang, H. Z. Wu, C. L. Liu, R. Z. Yang, and W. S. Dong. Catalytic dehydration of fructose to 5-hydroxymethylfurfural over Nb 2O5 catalyst in organic solvent. *Carbohydrate Research*, 368:78–83, 2013. ISSN 00086215. doi: 10.1016/j.carres.2012.12.021.

[22] C. Reichardt. *Solvents and Solvent Effects in Organic Chemistry.* Wiley VCH, Weinheim, 2nd edition, 1988.

[23] Y. Román-Leshkov, J. N. Chheda, and J. A. Dumesic. Phase modifiers promote efficient production of hydroxymethylfurfural from fructose. *Science*, 312(5782): 1933–1937, 2006. doi: 10.1126/science.1126337.

[24] Y. Román-Leshkov and J. A. Dumesic. Solvent Effects on Fructose Dehydration to 5-Hydroxymethylfurfural in Biphasic Systems Saturated with Inorganic Salts. *Topics in Catalysis*, 52(3):297–303, 2009. doi: 10.1007/s11244-008-9166-0.

[25] S. H. Mushrif, S. Caratzoulas, and D. G. Vlachos. Understanding solvent effects in the selective conversion of fructose to 5-hydroxymethyl-furfural: a molecular dynamics investigation. *Phys. Chem. Chem. Phys.*, 14(8):2637–2644, 2012. doi: 10.1039/c2cp22694d.

[26] T. Shalumova and J. M. Tanski. 5-(Hydroxymethyl)furan-2-carbaldehyde. *Acta Crystallographica Section E: Structure Reports Online*, 66(9):0–5, 2010. ISSN 16005368. doi: 10.1107/S1600536810031119.

[27] M. Rogojerov, G. Keresztury, and B. Jordanov. Vibrational spectra of partially oriented molecules having two conformers in nematic and isotropic solutions: Furfural and 2-chlorobenzaldehyde. *Spectrochimica Acta - Part A: Molecular and Biomolecular Spectroscopy*, 61(7):1661–1670, 2005. ISSN 13861425. doi: 10.1016/j.saa.2004.11.043.

[28] R. Rivelino, S. Canuto, and K. Coutinho. Conformational stability of furfural in aqueous solution: The role of hydrogen bonding. *Brazilian Journal of Physics*, 34 (1):84–89, 2004. ISSN 0103-9733.

[29] R. W. Fawcett and A. A. Kloss. Solvent-Induced Frequency Shifts in the Infrared Specturm of Dimethyl Sulfoxide in Organic Solvents. *J. Phys. Chem.*, 100:2019–2024, 1995.

[30] R. A. Nyquist, R. Streck, and G. Jeschek. NMR and IR spectra-structure correlations carbonyl containing compounds in various solvents. *Journal of Molecular Structure (THEOCHEM)*, 377:113–128, 1996.

[31] J. J. Max and C. Chapados. Infrared spectroscopy of acetone-methanol liquid mixtures: Hydrogen bond network. *Journal of Chemical Physics*, 122(1), 2005. ISSN 00219606. doi: 10.1063/1.1790431.

[32] A. G. Kalampounias, G. Tsilomelekis, and S. Boghosian. Short-time microscopic dynamics of aqueous methanol solutions. *Molecular Physics*, 110(24):3095–3102, 2012. ISSN 00268976. doi: Doi10.1080/00268976.2012.697586.

[33] J. Zakzeski, R. J. H. Grisel, A. T. Smit, and B. M. Weckhuysen. Solid acid-catalyzed cellulose hydrolysis monitored by in situ Atr-Ir spectroscopy. *ChemSusChem*, 5(2):430–437, 2012. ISSN 18645631. doi: 10.1002/cssc.201100631.

[34] G. Tsilomelekis, A. Christodoulakis, and S. Boghosian. Support effects on structure and activity of molybdenum oxide catalysts for the oxidative dehydrogenation of ethane. *Catalysis Today*, 127(1-4):139–147, 2007. ISSN 09205861. doi: 10.1016/j.cattod.2007.03.026.

[35] T. Kim, R. S. Assary, L. A. Curtiss, C. L. Marshall, and P. C. Stair. Vibrational properties of levulinic acid and furan derivatives: Raman spectroscopy and theoretical calculations. *Journal of Raman Spectroscopy*, 42(12):2069–2076, 2011. doi: 10.1002/jrs.2951.

[36] T. Kim, R. S. Assary, C. L. Marshall, D. J. Gosztola, L. A. Curtiss, and P. C. Stair. Studies of the Raman spectra of cyclic and acyclic molecules: Combination and prediction spectrum methods. *Chemical Physics Letters*, 531:210–215, 2012. doi: 10.1016/j.cplett.2012.02.002.

[37] K. Nakamoto. *Infrared and Raman Spectra of Inorganic and Coordination Compounds*. Wiley-Interscience, Hoboken, 6th ed. edition, 2009.

[38] J. Joseph and E. D. Jemmis. Red-, Blue-, or No-Shift in Hydrogen Bonds: A Unifed Explanation. *J Am Chem Soc*, 129:4620–4632, 2007. doi: 10.1021/ja067545z.

[39] T. Steiner. The hydrogen bond in the solid state. *Angew. Chem. Int. Ed.*, 41(1): 49–76, 2002. ISSN 1433-7851. doi: 10.1002/1521-3773(20020104)41:1⟨48::AID-ANIE48⟩3.0.CO;2-U.

[40] V. Nikolakis, S. H. Mushrif, B. Herbert, K. S. Booksh, and D. G. Vlachos. Fructose-water-dimethylsulfoxide interactions by vibrational spectroscopy and molecular dynamics simulations. *The journal of physical chemistry. B*, 116(36): 11274–83, 2012. ISSN 1520-5207. doi: 10.1021/jp3056703.

[41] C. Laurence, M. Berthelot, M. Lucon, M. Helbert, D. G. Morris, and J.-F. Gal. The influence of solvent on the inductive order of substituents from infrared measurements on 4-substituted camphors: a new model of inductive effects. *Journal of the Chemical Society, Perkin Transactions 2*, (4):705, 1984. ISSN 0300-9580. doi: 10.1039/p29840000705.

[42] M. Paolantoni, M. E. Gallina, P. Sassi, and A. Morresi. Structural properties of glucose-dimethylsulfoxide solutions probed by Raman spectroscopy. *Journal of Chemical Physics*, 130(16):1–9, 2009. ISSN 00219606. doi: 10.1063/1.3116250.

[43] Q. Li, X. An, B. Gong, and J. Cheng. Spectroscopic and theoretical evidence for the cooperativity between red-shift hydrogen bond and blue-shift hydrogen bond in DMSO aqueous solutions. *Spectrochimica Acta - Part A: Molecular and Biomolecular Spectroscopy*, 69(1):211–215, 2008. ISSN 13861425. doi: 10.1016/j.saa.2007.03.034.

[44] K. Noack, J. Kiefer, and A. Leipertz. Concentration-dependent hydrogen-bonding effects on the dimethyl sulfoxide vibrational structure in the presence of water, methanol, and ethanol. *ChemPhysChem*, 11(3):630–637, 2010. ISSN 14394235. doi: 10.1002/cphc.200900691.

[45] I. van Zandvoort, Y. Wang, C. B. Rasrendra, E. R. van Eck, P. C. Bruijnincx, H. J. Heeres, and B. M. Weckhuysen. Formation, molecular structure, and morphology of humins in biomass conversion: influence of feedstock and processing conditions. *ChemSusChem*, 6(9):1745–1758, 2013. doi: 10.1002/cssc.201300332.

[46] K. Atak, N. Engel, K. M. Lange, R. Golnak, M. Gotz, M. Soldatov, J. E. Rubensson, N. Kosugi, and E. F. Aziz. The chemical bond in carbonyl and sulfinyl groups studied by soft X-ray spectroscopy and ab initio calculations. *ChemPhysChem*, 13 (13):3106–3111, 2012. ISSN 14394235. doi: 10.1002/cphc.201200314.

[47] K. M. Lange, R. K??nnecke, S. Ghadimi, R. Golnak, M. A. Soldatov, K. F. Hodeck, A. Soldatov, and E. F. Aziz. High resolution X-ray emission spectroscopy of water and aqueous ions using the micro-jet technique. *Chemical Physics*, 377(1-3):1–5, 2010. ISSN 03010104. doi: 10.1016/j.chemphys.2010.08.023.

[48] M. J. Frisch, G. W. Trucks, H. B. Schlegel, G. E. Scuseria, M. A. Robb, J. R. Cheeseman, G. Scalmani, V. Barone, B. Mennucci, G. A. Petersson, H. Nakatsuji, M. Caricato, X. Li, H. P. Hratchian, A. F. Izmaylov, J. Bloino, G. Zheng, J. L. Sonnenberg, M. Hada, M. Ehara, K. Toyota, R. Fukuda, J. Hasegawa, M. Ishida, T. Nakajima, Y. Honda, O. Kitao, H. Nakai, T. Vreven, J. A. Montgomery Jr., J. E. Peralta, F. Ogliaro, M. J. Bearpark, J. Heyd, E. N. Brothers, K. N. Kudin, V. N. Staroverov, R. Kobayashi, J. Normand, K. Raghavachari, A. P. Rendell, J. C. Burant, S. S. Iyengar, J. Tomasi, M. Cossi, N. Rega, N. J. Millam, M. Klene, J. E. Knox, J. B. Cross, V. Bakken, C. Adamo, J. Jaramillo, R. Gomperts, R. E. Stratmann, O. Yazyev, A. J. Austin, R. Cammi, C. Pomelli, J. W. Ochterski, R. L. Martin, K. Morokuma, V. G. Zakrzewski, G. A. Voth, P. Salvador, J. J. Dannenberg, S. Dapprich, A. D. Daniels, Ö. Farkas, J. B. Foresman, J. V. Ortiz, J. Cioslowski, and D. J. Fox. Gaussian 09, 2009.

[49] A. V. Marenich, C. J. Cramer, D. G. Truhlar, and A. V. Marenich Cramer, Christopher J., and Truhlar, Donald G. Universal Solvation Model Based on Solute Electron Density and on a Continuum Model of the Solvent Defined by the Bulk Dielectric Constant and Atomic Surface Tensions. *Journal of Physical Chemistry B*, 113:6378–6396, 2009. doi: 10.1021/jp810292n.

[50] J. P. Merrick, D. Moran, and L. Radom. An Evaluation of Harmonic Vibrational Frequency Scale Factors. *Journal of Physical Chemistry A*, 111:11683–11700, 2007. doi: 10.1021/jp073974n.

Chapter 3

SOLVENT-INDUCED FREQUENCY SHIFTS OF 5-HYDROXYMETHYLFURFURAL DEDUCED VIA INFRARED SPECTROSCOPY AND *AB INITIO* CALCULATIONS

3.1 Abstract

Solvent-induced frequency shifts (SIFS) of the carbonyl stretching vibration ν(C=O) of 5-hydroxymethylfurfural were measured in protic, polar aprotic, and non-polar solvents. The Gutmann acceptor number (AN) was found to correlate with the measured frequency shifts. The SIFS in six solvents were investigated using *ab initio* electronic structure calculations, treating the solvent implicitly and with an explicit solvent ligand interacting with the carbonyl. The conductor-polarizable continuum model (CPCM) of solvation predicted that ν(C=O) shifted according with the dielectric constant as (ϵ-1)/(2ϵ+1), in agreement with the analytical predictions of the Kirkwood-Bauer-Magat (KBM) theory for a dipole in a dielectric continuum, but in disagreement with the experimental trend. The experimental SIFS were best predicted using gas-phase complexes of HMF and explicit solvent-ligand. Natural bond orbital (NBO) analysis and Bader's atoms in molecules theory were used to investigate the electronic structure of these complexes. Strong SIFS were found to arise from stronger H-bonding interactions, as observed in delocalization of carbonyl lone-pair electrons by H-bonding solvent σ*(X—H) orbitals, and an increase in charge density and a decrease in local potential energy at the H-bond (3,-1) critical point. Consequently, by predicting the experimental SIFS and examining the electronic structure, we find the first theoretical evidence for treating Gutmann's solvent AN as a measure of solvent Lewis acidity.

The IR spectroscopy measurements were conducted by Dr. George Tsilomelekis and Dr. Christina Bagia at the University of Delaware. This chapter is adapted

with permission from [1] in a paper titled "Solvent-Induced Frequency Shifts of 5-Hydroxymethylfurfural Deduced via Infrared Spectroscopy and ab Initio Calculations." Reprinted with permission from the American Chemical Society. Copyright © 2014, American Chemical Society.

3.2 Introduction

Due to environmental, economic, and political concerns, research into alternative sources for petroleum-based fuels and chemicals has garnered considerable interest. As the only source of renewable, fixed carbon, biomass holds significant potential for displacing nonrenewable crude oil as a feedstock for the chemical industry. One promising biomass-derived platform chemical is 5-hydroxymethyl furfural (HMF) [2]. HMF is produced through sugar dehydration in aqueous solution, but process yields are low due to side product formation, including humins and organic acids (Fig. 3.1). To improve yields to HMF, many groups have investigated alternative solvents and solvent mixtures (see reviews [2–6]), but the fundamental role of the reaction medium is not yet understood, for two main reasons. First, mechanistic details of HMF degradation are not known. A recent, gas-phase, theoretical study has explored the thermochemistry of a possible pathway to levulinic and formic acids, but transition states were not identified and it was suggested that the acid catalyst attacks the HMF hydroxyl group and not the carbonyl group, whose affinity for the proton is higher [7]. Even less is known about the formation of humins [8, 9]. Second, it is quite unclear how local solvent-substrate interactions affect the electronic and vibrational structure of HMF and its intermediates to degradation products, especially the stability and structure of the rate-determining transition states.

We have previously reported on the interactions of HMF with DMSO and water [10, 11]. In binary HMF/solvent mixtures, the HMF C=O stretching vibration slightly shifts to higher wavenumbers in DMSO, but redshifts in water due to C=O $\cdots$ H-O hydrogen bonds. In ternary HMF/DMSO/water mixtures, DMSO preferentially coordinates the carbonyl in solutions with less than 40 mol % water; at high water

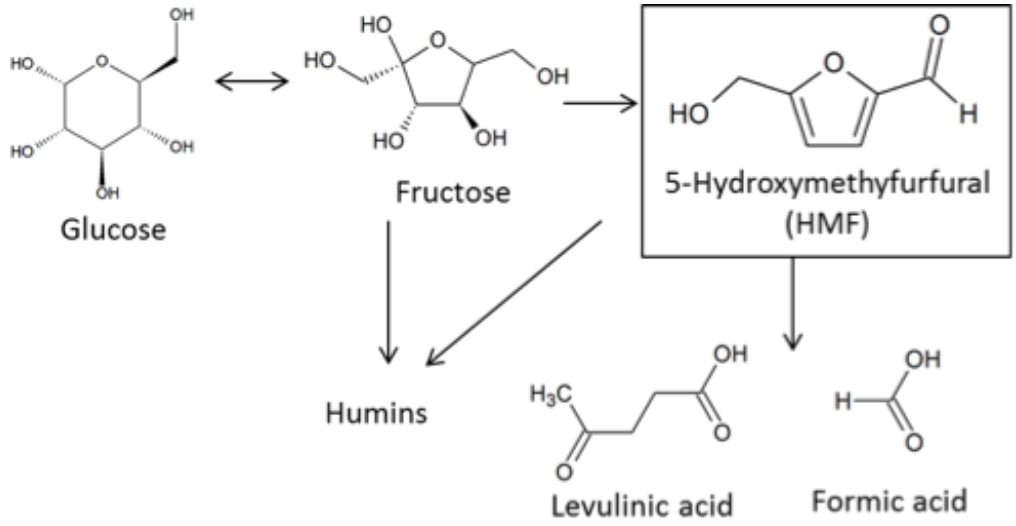

Figure 3.1: Reaction pathways for producing HMF from sugar dehydration, along with routes to major side products.

concentration, hydrogen bonding interactions with water displace the DMSO from the HMF carbonyl. To better understand these frequency shifts, it is important to understand the physics of these interactions, and to investigate their behavior across a range of solvents.

Infrared (IR) spectroscopy is a fast, non-destructive technique for characterizing the vibrational properties of materials. The numerous intermolecular interactions in a liquid mixture influence molecular vibrations, and these solvent-induced frequency shifts (SIFS) have been correlated to pure-solvent properties to investigate solvent-solute and solvent-solvent interactions [12–15]. For example, Nyquist et al. reported that SIFS of carbonyls can be correlated to the Gutmann acceptor number [16] (AN), suggesting that solvents act as Lewis acids that withdraw electron density away from the solute carbonyl, causing ν(C=O) to redshift [15]. They observed less redshift for alcohol solvents, and attributed the deviation to be a consequence of competitive solvent-solvent H-bonding interactions. The earliest theoretical model treating frequency shifts, the Kirkwood-Bauer-Magat (KBM) model [17], describes the frequency

shift $\Delta\nu$ as a function of dielectric constant ϵ_s with the following relationship

$$\frac{\Delta\nu}{\nu} = C\frac{\epsilon_s - 1}{2\epsilon_s + 1} \tag{3.1}$$

where C is a complex parameter specific to each solute – a function of the cavity radius, the mass and frequency of the molecular vibrator, the effective charge of one of the poles of the dipole, and a anharmonicity constant. This model was successful for correlating SIFS of HCl in non-polar solvents [18] but has been proved inadequate for describing carbonyl frequency shifts [13, 14, 19]. The KBM model was derived using Onsager's treatment of a solute as a dipole in a spherical cavity solvated by a dielectric continuum, a model too simple for application to real solutes and solvents.

Electronic structure calculations have been successful in predicting IR spectra for molecules in the gas phase. For this purpose, hybrid functionals, such as B3LYP, have been found to give better frequency predictions than Hartree-Fock and even more computationally expensive methods, such as MP2, QCISD, and CCD, when linear scaling factors are applied to empirically correct for known limitations of these methods [20]. To predict the behavior of a molecule in solution, the solvent is brought into the model implicitly or explicitly. Implicit solvent models of varying complexity treat the solvent as a dielectric continuum that surrounds a solute cavity [21], while an explicit solvation model involves adding a "shell" of one or more explicit solvent molecules to interact with sites on the solute. Kubelka et al. studied the carbonyl stretch of N-methylacetamide in water using DFT, and studied models with both implicit and explicit solvation, concluding that the SIFS are most accurately predicted when both explicit solvent ligands and the implicit dielectric continuum are incorporated into the model [22]. Jalkanen and coworkers have studied IR spectra of the aqueous zwitterion L-alanine by examining the solute with four [23], nine [24], and twenty [25] explicit water molecules, and with the Onsager, CPCM, and PCM implicit solvation models [25]. They concluded that implicit solvation is necessary, though different implicit models lead to different results. Explicit solvation is also necessary, because hydrogen

bonding is significant, and increasing the number of explicit solvent molecules from four to nine was found to improve the fit. Chowdhry et al. found that implicit (IEF-PCM) and explicit solvent was necessary for calculating accurate spectra of L-alanine and glycine in aqueous solution [26]. Nobrega et al. studied α-alanine in numerous implicit solvents, acetonitrile, ethanol, carbon tetrachloride, as well as in the gas-phase, but did not consider explicit solvent ligands [27].

We previously reported the experimental and calculated IR spectra of HMF in mixtures of DMSO and H2O [10]. In the present work, we specifically investigate SIFS of the carbonyl of HMF in a broader selection of pure protic and aprotic solvents. We show that the carbonyl stretching frequency of HMF is correlated to the solvent AN. Using *ab initio* calculations with implicit and explicit solvation models, we predict these frequency shifts and, using Natural Bond Orbital analysis (NBO) and Bader's atoms in molecules (AiM) theory, we demonstrate that the strength of the SIFS is indeed associated with the ability of the solvent to withdraw electron density and polarize the HMF carbonyl.

3.3 Methods

3.3.1 Experimental

IR spectra were measured for low fraction of HMF in several solvents. High purity 5-hydroxymethyl furfural (> 99% purity, Sigma) was mixed with tetrahydrofuran (THF) (anhydrous, $\geq$ 99.9%, Sigma), toluene($\geq$ 99.5%, Fisher Scientific), ethyl acetate ($\geq$ 99.5%, Fisher Scientific), acetone ($\geq$ 99.9%, HPLC Grade, Sigma), acetonitrile (ACN) (99.9%, Fischer Scientific), DMSO ($\geq$ 99.5%, Sigma), methanol (MeOH) (99.9%, Fisher Scientific), ethanol (99.9%, Fisher Scientific), 1-propanol (99.9%, Fisher Scientific), 2-propanol (99.9%, Fisher Scientific), D_2O (> 99.8 atom % D, Acros), acetic acid ($\geq$ 99.99%, Sigma), and formic acid (FA) ($\geq$ 95%, Sigma). Appropriate amounts of HMF were added in 0.5 ml of each solvent and stirred for 10 minutes for complete HMF dissolution. The final concentration of HMF in all samples was kept constant at 5%w/v.

A Nicolet 8700 FTIR spectrometer equipped with a DTG detector and a Golden Gate single-reflection diamond ATR was used for all spectroscopic studies. The instrument was equipped with a purge gas of dehumidified air. The resolution of the instrument was set at 4 cm^{-1} for all measurements and the number of scans varied from 16 to 32 scans, depending on the signal/noise ratio of each sample. All the spectroscopic measurements were conducted at 25 °C.

To account for the effect of wavenumber on the penetration depth, the spectra were corrected using the following equations as implemented by the OMNIC v8 software:

$$Absorbance(\nu)_{corrected} = \frac{Absorbance(\nu)_{ATR}}{d_p} \tag{3.2}$$

$$d_p = \frac{10000}{2\pi\nu(n_p^2 sin^2\theta - n_s^2)^{1/2}} \tag{3.3}$$

where d_p is the penetration depth, ν is the wavenumber in cm^{-1}, n_p is the refractive index of diamond (2.47), n_s is the refractive index of the sample, and θ is the angle of incidence of the IR beam at the surface of the diamond (45 °). The refractive index of each pure solvent was used for the spectra correction.

3.3.2 Computational

Electronic structure calculations were performed with Gaussian 09, revision A.02 [28]. Structures were optimized and vibrational frequencies were calculated at the B3LYP/6-31+G(d,p) level. Gas-phase frequencies were scaled by a uniform scaling factor 0.9648 [20]. These structures were optimized again at the MP2/aug-cc-pVDZ level, and single point energy calculations were performed on these structures with MP2/aug-cc-pVTZ. Zero-point energy corrections were estimated from the B3LYP results. Natural Bond Orbital (NBO) analysis was performed to study the electron

density distribution among atoms and the energy stabilization due to orbital mixing and electron delocalization (NBO Version 3.1) [29]. The topology of the electron density was characterized using Bader's AiM theory [30]. Critical points were located and analyzed using the AiM2000 software [31].

Isolated HMF in both the s-cis and s-trans conformation was studied in vacuum and in the CPCM solvation models [32]. Six solvents were investigated computationally: THF, DMSO, ACN, MeOH, H2O, and FA. To investigate the effects of H-bonding, explicit solvent molecules were introduced, and bimolecular HMF-solvent complexes were studied in numerous configurations in which the solvent participated in hydrogen bonding with the HMF carbonyl. These explicit solvent systems were studied both in the implicit solvents and in vacuum.

3.4 Results

3.4.1 Experimental SIFS of HMF C=O and Descriptors

The experimental IR frequencies of the HMF carbonyl are reported in Table S1 in Appendix B. In alcohol solvents and acetic acid, the carbonyl frequency was split into two peaks. Correlations of ν(C=O) of the HMF carbonyl with several solvent properties were investigated, including the Gutmann acceptor (AN) and donor (DN) numbers as measures of solvent basicity and acidity [16], static dielectric constant (ϵ_s), refractive index (n_{op}), and dipole moment [33]. Solvent polarity (Y) and the KBM parameter (KBM) were estimated from the dielectric constant using Eq. (4) and (5), respectively, and solvent polarizability (P) was calculated from the refractive index using Eq. (6).

$$Y = \frac{\epsilon_s - 1}{\epsilon_s + 2} \tag{3.4}$$

$$KBM = \frac{\epsilon_s - 1}{2\epsilon_s + 1} \tag{3.5}$$

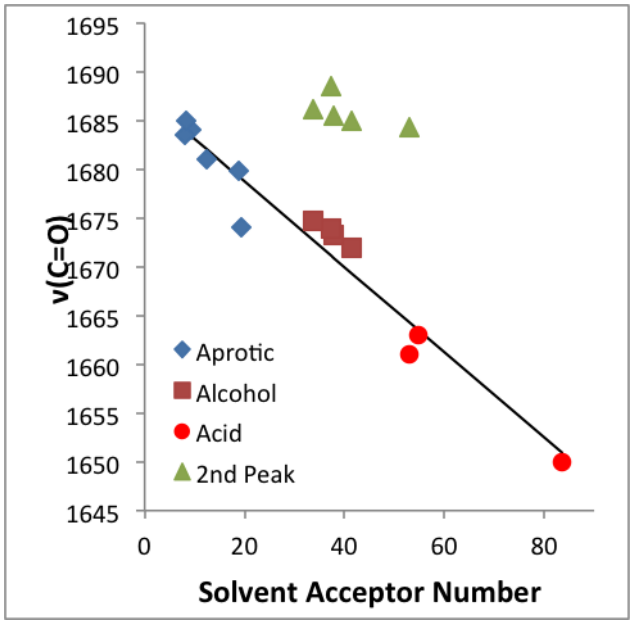

Figure 3.2: Correlation of experimental ν(C=O) with solvent acceptor number (R^2 = 0.94). In several solvents, ν(C=O) was split into two peaks. In these cases, the lower frequency was used in the correlation, and the higher frequency is reported as the 2nd peak.

$$P = \frac{n_{op}^2 - 1}{n_{op}^2 + 2} \tag{3.6}$$

Of these properties, the solvent AN was identified as the strongest descriptor of the carbonyl frequency shift, with correlation coefficient R^2=0.9436, as shown in Fig. 3.2. Correlations with the other properties were weaker than with the solvent AN, ranging from R^2=0.0072 for the DN to R^2=0.3152 for the dielectric constant.

Because the Gutmann AN is the best descriptor of the ν(C=O) shift, we hypothesize that Lewis acidic solvents withdraw electron density from the carbonyl, weakening the carbonyl double bond, giving it more single bond character, hence, causing a redshift in frequency. This also may correspond to an increase in polarization of

	CPCM Solvent	B3LYP/6-31+G(d,p) Solvation Energy (kcal/mol)	mp2/aug-cc-pVDZ Solvation Energy (kcal/mol)	mp2/aug-cc-pVTZ Solvation Energy (kcal/mol)	HMF Dipole Moment (debye)	ΔDipole Moment	Calc. ν(C=O) [cm^{-1}]	Δν(C=O) [cm^{-1}]	C=O bond length [Å]	Δ C=O bond length [Å]
Trans HMF	Vacuum	0.00	0.00	0.00	3.111		1753.8		1.2225	
	THF	-6.71	-5.66	-5.76	4.539	1.428	1712.1	-41.7	1.2302	0.0077
	ACN	-7.68	-6.43	-6.54	4.798	1.688	1704.7	-49.1	1.2316	0.0091
	DMSO	-7.74	-6.48	-6.59	4.815	1.704	1704.2	-49.6	1.2317	0.0092
	MeOH	-7.65	-6.41	-6.52	4.792	1.681	1704.9	-48.9	1.2316	0.0090
	H2O	-7.82	-6.54	-6.65	4.837	1.726	1703.5	-50.2	1.2318	0.0093
	FA	-7.76	-6.49	-6.60	4.820	1.709	1704.1	-49.7	1.2317	0.0092
Cis HMF	Vacuum	0.00	0.00	0.00	3.661		1759.2		1.2208	
	THF	-7.71	-6.19	-6.14	5.183	1.522	1709.5	-49.7	1.2300	0.0092
	ACN	-8.86	-7.12	-7.05	5.456	1.795	1700.6	-58.6	1.2316	0.0109
	DMSO	-8.94	-7.18	-7.10	5.474	1.813	1700.0	-59.2	1.2317	0.0110
	MeOH	-8.83	-7.10	-7.02	5.449	1.788	1700.8	-58.4	1.2316	0.0108
	H2O	-9.04	-7.26	-7.18	5.497	1.836	1699.3	-59.9	1.2319	0.0111
	FA	-8.96	-7.19	-7.12	5.479	1.818	1699.9	-59.3	1.2317	0.0110

Table 3.1: HMF in Implicit Solvent. Properties of the HMF carbonyl as predicted by CPCM implicit solvent with no solvent ligand. Changes are reported with gas phase trans HMF as the reference state. The solvation energies are zero-point corrected.

the carbonyl bond. To test these hypotheses, we use electronic structure calculations to predict the IR spectra of HMF in different solution models, and NBO analysis to investigate changes in the distribution of electron density.

3.4.2 Calculated SIFS of HMF C=O

3.4.2.1 Implicit Solvent Calculations

First, cis and trans HMF were optimized in the gas-phase and in the CPCM implicit solvation model [32]. Solvation energies, frequencies, and C=O bond length are shown in Table 3.1. Predictions for gas-phase HMF are shown; no experimental spectra are available for gas-phase HMF due to its low vapor pressure.

As shown in Fig. 3.3, the CPCM model closely agrees with the KBM relationship

for predicting the frequency shift. The HMF dipole moment increases with increasing solvent dielectric constant, proportionally to (ϵ-1)/(2ϵ+1), and the ν(C=O) commensurately redshifts from the gas-phase value – this is a mathematical property of the solvation model, so $R^2 = 1$. When plotted against the dielectric constant, the frequency rapidly decreases as the dielectric constant increases from unity in vacuum (ν_{HMF} = 1753.8 cm^{-1}) to 7.4 in THF (ν_{HMF} = 1712.1 cm^{-1}). Selecting different solvents with a higher ϵ than THF has a negligible effect on the frequency, because (ϵ-1)/(2ϵ+1) asymptotically approaches the value of 1/2. Methanol (ϵ =32.7) is the first solvent in the "plateau" region, and water, methanol, acetonitrile, and formic acid give calculated frequencies within 2 cm^{-1} of each other (Fig. 3.3). No such plateau region is observed in the experimental frequencies (Fig. 3.2), so electrostatics alone (i.e., reaction field and charge density induced on the surface of the polarized dielectric) cannot account for those changes in the distribution of the electron density responsible for the shift in the ν(C=O) vibration; local interactions between the first solvation shell and the solute must be considered.

3.4.2.2 Addition of Explicit Solvent Ligand

Implicit solvation models cannot account for either hydrogen bonding interactions or the electron density delocalization between solute and solvent molecules. An explicit solvent molecule was introduced to gas-phase HMF, and several conformations of the HMF-solvent complex were optimized with the solvent interacting with the carbonyl group. These complexes were also reoptimized in implicit solvent. Zero-point corrected binding (or in the case of implicit solvent, solvation) energies, frequencies, NBO, and Bader analysis were calculated at the B3LYP/6-31+G(d,p) level. For calculating electronic binding energies, structures were reoptimized at the MP2/aug-cc-pVDZ level, along with single-point energy calculations at the MP2/aug-cc-pVTZ//MP2/aug-cc-pVDZ level. The lowest energy structures at the MP2/aug-cc-pVDZ level for cis and trans HMF are shown in Fig. 3.4 with their accompanying binding energies, ν(C=O) and C=O bond length in Table 3.2. For each solvent, the most stable conformation is

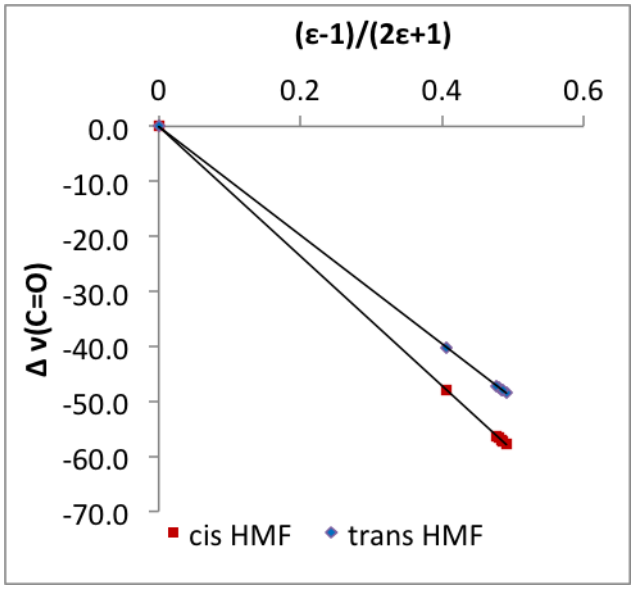

Figure 3.3: In the CPCM implicit solvent, the calculated SIFS of HMF carbonyl from gas-phase gives a perfect fit ($R^2 = 1$) to the KBM solvation parameter and passes through the origin. This agrees with the behavior predicted by Onsager and Kirkwood.

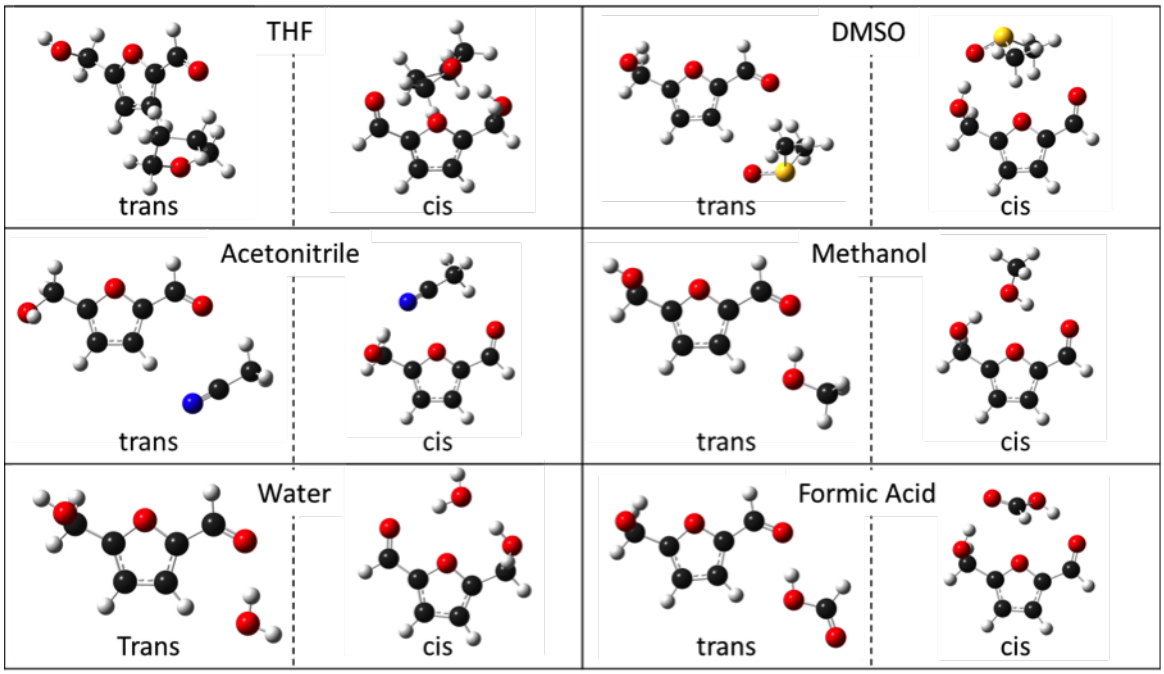

Figure 3.4: Lowest energy structures optimized with MP2/aug-cc-pVDZ in vacuum. To examine a variety of HMF – solvent interactions, several conformations of HMF and 1 solvent molecule were optimized with the solvent interacting with both cis and trans HMF. The lowest energy structures in which the solvent is interacting with the carbonyl are shown here.

cis HMF with a solvent "bridge" interacting with both the HMF hydroxyl and carbonyl.

The HMF carbonyl forms one H-bond with most solvent ligands, except up to two H-bonds (one for each lone pair of oxygen) with DMSO (Table S2 in Appendix B). In some configurations of THF and DMSO, the O $\cdots$ H distance is greater than or nearly 2.7 Å, indicating weak H-bonding (if any at all). For the protic solvents and DMSO, the carbonyl O $\cdots$ methyl H hydrogen bonds in the cis-bridge structure are slightly longer than those in the carbonyl-only interaction structure (by 0.072 Å in FA to 0.310 Å in MeOH), due to a competing attraction of the solvent by the HMF hydroxyl as well. The protic solvents exhibit proper H-bonds with the HMF carbonyl (the solvent O—H bond length increases), DMSO and THF exhibit improper H-bonds (the H—C bond length decreases), and acetonitrile exhibits both.

Explicit Solvent		B3LYP/6-31+G(d,p) Binding E (kcal/mol)	mp2/aug-cc-pVDZ Binding E (kcal/mol)	mp2/aug-cc-pVTZ Binding E (kcal/mol)	Calc. ν(C=O) [cm^{-1}]	Δν(C=O) [cm^{-1}]	Scaled ν(C=O) [cm^{-1}]	C=O bond length [Å]	Δ C=O bond length [Å]
Vacuum	cis				1759.2		1697.3	1.2318	
	trans				1753.8		1692.1	1.2308	
THF	cis	-10.04	-12.25	-12.88	1747.0	-12.2	1685.5	1.2318	0.0009
	trans	-4.73	-9.00	-9.37	1746.4	-7.4	1684.9	1.2341	0.0024
ACN	cis	-7.75	-9.14	-10.07	1739.7	-14.1	1678.5	1.2349	0.0041
	trans	-3.57	-4.80	-5.38	1740.4	-18.8	1679.1	1.2345	0.0027
DMSO	cis	-10.49	-13.29	-13.60	1736.5	-22.7	1675.4	1.2353	0.0044
	trans	-5.67	-7.49	-7.72	1733.7	-20.1	1672.7	1.2365	0.0047
MeOH	cis	-8.59	-9.31	-10.02	1722.8	-36.4	1662.2	1.2378	0.0070
	trans	-4.79	-5.49	-6.06	1730.1	-23.6	1669.2	1.2369	0.0051
H2O	cis	-6.93	-7.81	-8.45	1721.4	-32.4	1660.8	1.2375	0.0067
	trans	-4.37	-4.55	-5.06	1731.3	-27.9	1670.4	1.2365	0.0048
FA	cis	-11.28	-12.03	-13.34	1710.5	-48.7	1650.3	1.2398	0.0090
	trans	-9.17	-8.94	-9.73	1715.3	-38.5	1654.9	1.2393	0.0076

Table 3.2: Binding energies and properties of the HMF carbonyl interacting with explicit solvent ligand in the gas phase. Binding energies in kcal/mol for structures shown in Fig. 3.4: (Complex in vacuum – Trans HMF in vacuum – Solvent in vacuum). The Z-P correction calculated at the B3LYP level was used to estimate that at the MP2 levels. Counterpoise corrections were added to all binding energies in vacuum. Changes are reported with gas phase cis or trans HMF as the reference state. Frequencies were calculated with B3LYP/6-31+G(d,p) and geometry with mp2/aug-cc-pVDZ. Frequencies scaled by uniform scaling factor 0.9648 [20].

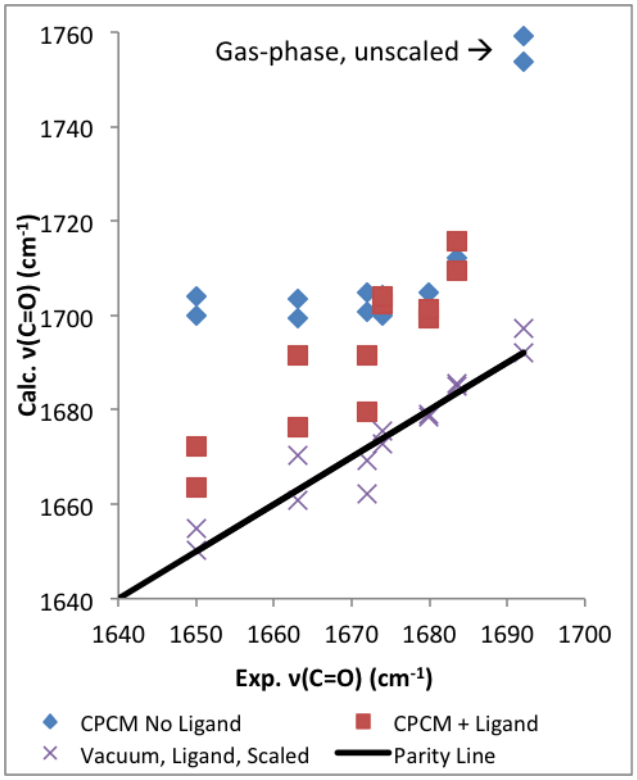

Figure 3.5: Parity plot comparing experimental HMF ν(C=O) with calculated HMF ν(C=O) for CPCM solvation model with and without solvent ligand. Frequencies calculated with implicit solvent are unscaled, while frequencies were scaled by 0.9648 for gas-phase calculations [20].

The frequencies calculated for these complexes in vacuo are higher relative to experiment, but after applying a uniform frequency scaling factor of 0.9648, [20] they agree closely with the experimental ν(C=O) (Fig. 3.5 and Table 3.2). All solvent interactions with the carbonyl redshift the stretching frequency relative to vacuum, but polar aprotic solvents shift the carbonyl frequency much less (10-20 cm^{-1}) compared to the protic solvents (25-40 cm^{-1}). All solvents give frequency shifts close to experiment, except water and methanol, where experimentally, HMF ν(C=O) in methanol is higher than in water by 9 cm^{-1} – the calculated frequencies are within 2 cm^{-1} of each other for cis and trans. For all solvents, the length of the carbonyl bond increases in proportion to the carbonyl frequency.

When the HMF-solvent complex is immersed in CPCM solvent (structures shown in Figure S1 in Appendiex B), aprotic solvents give frequencies quite close to the no-ligand results, with the THF ligand increasing the trans HMF ν(C=O) by 3.5 cm^{-1} and acetonitrile ligand decreasing it by 3.4 cm^{-1} relative to the calculated frequency in these implicit solvents without the ligand (Table 3.3). These small changes indicate that the weak local interactions do not dramatically shift ν(C=O). However, adding protic solvent ligands leads to significant changes, with additional redshifts of 12 cm^{-1} (water) and 36 cm^{-1} (formic acid) due to H-bonding with the ligand (Table S3 in Appendix B). These shifts indicate that adding explicit solvent ligands improves the model prediction relative to the HMF in implicit solvent (Fig. 3.5), however omitting the implicit solvent and using a linear scaling factor produces better agreement with experiment. Studies of the aqueous-phase spectra of carbonyl-containing species have also found that calculated spectra of a solute in implicit water are improved by the addition of explicit solvent molecules [22, 24]. In contrast to these works, however, we find that explicit solvent without a reaction field produces better agreement with experiment than explicit solvent with a reaction field.

3.4.3 NBO Analysis

3.4.3.1 Implicit Solvent

The implicit solvents induce changes in the dipole moment of HMF (Table 3.1), which leads to several changes in electronic structure, and the KBM parameter (ϵ-1)/(2ϵ+1) is the descriptor for such changes. As the dielectric constant increases and the frequency redshifts, the carbonyl bond increases in length and becomes more polarized. The partial charge on the oxygen becomes more negative, decreasing from -0.547 in vacuum to -0.616 in water for trans HMF (cis HMF shows the same trends), while the NBO partial charge on C1 becomes more positive, increasing from 0.338 to 0.344 for trans HMF in water (Table S4 in Appendix B). The partial charges of C3 and C5 also increase (by as much as 0.012 and 0.028) while the partial charges of C2 and C4 decrease (by as much as 0.014 and 0.004), in accordance with the resonance structures

Explicit Solvent		B3LYP/6-31+G(d,p) Solvation Energy (kcal/mol)	MP2/aug-cc-pVDZ Solvation Energy (kcal/mol)	MP2/aug-cc-pVDZ // MP2/aug-cc-pVTZ Solvation Energy (kcal/mol)	Calc. ν(C=O) [cm^{-1}]	Δν(C=O) [cm^{-1}]	C=O bond length [Å]	Δ C=O bond length [Å]
Vacuum	cis				1759.2		1.2308	
	trans				1753.8		1.2318	
THF	cis	-15.92	-18.38	-15.98	1709.5	-49.7	1.2358	0.0050
	trans	-10.61	-12.65	-11.06	1715.6	-38.1	1.2362	0.0044
ACN	cis	-11.81	-15.21	-14.08	1699.3	-59.9	1.2378	0.0070
	trans	-7.71	-9.32	-8.94	1701.2	-52.5	1.2373	0.0055
DMSO	cis	-14.35	-19.57	-17.78	1702.5	-56.7	1.2371	0.0063
	trans	-8.75	-12.78	-11.45	1704.0	-49.8	1.2383	0.0065
MeOH	cis	-13.69	-16.31	-15.00	1679.7	-79.5	1.2399	0.0091
	trans	-10.52	-11.79	-11.43	1691.5	-62.2	1.2399	0.0080
H2O	cis	-12.97	-13.48	-13.13	1676.3	-82.9	1.2408	0.0100
	trans	-10.24	-10.84	-10.42	1691.6	-62.2	1.2395	0.0077
FA	cis	-15.35	-17.89	-17.37	1663.5	-95.7	1.2436	0.0128
	trans	-14.03	-14.57	-14.36	1672.3	-81.5	1.2429	0.0111

Table 3.3: Properties of the HMF carbonyl interacting with explicit solvent ligand and in implicit solvent. Solvation energies calculated ($E_{complex,CPCM} - E_{solute,vacuum} - E_{solvent,CPCM}$). The Z-P correction calculated at the B3LYP level was used to estimate that at the MP2 levels. Changes are reported with gas phase cis or trans HMF as the reference state. Frequencies and NBO partial charges calculated with B3LYP/6-31+G(d,p), and geometry with mp2/aug-cc-pVDZ.

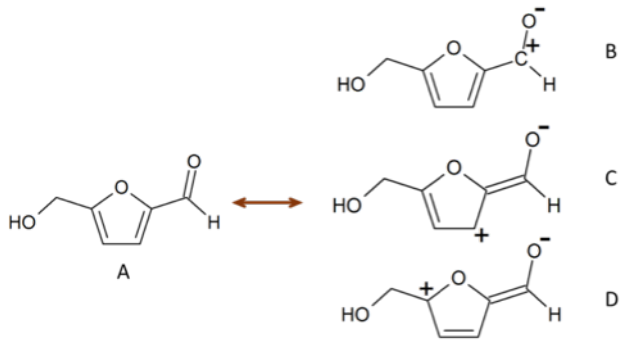

Figure 3.6: Resonance scheme. High-dielectric solvent increases contribution of resonance structures in which polarized C=O bond has more single bond character, and redshifts in frequency.

C and D in (Fig. 3.6). Examination of the NBO occupancies, tabulated in Table S4 and Table S5 in Appendix B, shows that π(C=O) increases very slightly (0.0027 at most), which would result in a slight strengthening of the carbonyl bond. This is offset by the more significant increase in π*(C=O) (as much as 0.0357), which weakens the bond, as observed. This, along with the increase in occupancy of the lone-pair orbitals on oxygen, particularly the more p-type lone pair, (up 0.0117) contributes to the increase in oxygen partial charge. The π(C2=C3), π(C4=C5), and π*(C4=C5) in the furan ring decrease in occupancy (as much as 0.0135, 0.0248, and 0.0062, respectively, for trans HMF in water), while π*(C2=C3) increases (by 0.0141). The partial charges and orbital occupancies change more significantly between vacuum and THF than among the protic solvents, again because the KBM parameter reaches a plateau at high ϵ.

The relative importance of the alternative Lewis structures B, C, and D was evaluated in comparison to the default Lewis structure A (Fig. 3.6). The default Lewis structure A for trans HMF in vacuum has 1.847% non-Lewis electrons. Lewis structures B, C, and D have 2.898%, 3.523%, and 3.808% non-Lewis electrons, respectively, as a greater separation of charge is less favorable. Interestingly, adding an implicit solvent reduces the importance of Lewis structure A (increasing the percentage of non-Lewis electrons by as much as 0.034%) relative to structures B, C, and D (decreasing the

percentage of non-Lewis electrons by 0.015%, 0.093%, and 0.127%, respectively) (Table S6 in Appendix B). Again, the quantitative changes of % non-Lewis electrons are directly proportional to the KBM parameter. This agrees with our hypothesis linking the polarization of the carbonyl to stabilization of the resonance structures shown in Fig. 3.6, increasing the single-bond character of the carbonyl, leading to bond length increase and ν(C=O) redshift.

3.4.3.2 Explicit Solvent Ligand in the Gas-Phase

Just as with the implicit solvent, explicit solvent makes the carbonyl bond more polarized, with the oxygen charge becoming more negative, decreasing as much as 0.065, and the carbon charge becoming more positive, increasing as much as 0.023 (Table S7 in Appendix B). The occupancy trends observed with the implicit solvent are also seen here in vacuum with just one explicit solvent molecule. The π(C=O) increases slightly, π^*(C=O) and π^*(C2=C3) increase, and π(C2=C3), π(C4=C5), and π^*(C4=C5) decrease (Table S7 in Appendix B). The π^*(C=O) changes the most, and is most directly correlated with the carbonyl frequency shift (Fig. 3.7 and Table S8 in Appendix B).

According to second-order perturbation theory delocalization analysis, the solvent does not directly interact with the carbonyl bond. The π^*(C=O) mixes with the nearby π(C2=C3) and is not interacting with any solvent orbitals (Table S9 in Appendix B). This delocalization stabilization energy is correlated to the strength of the ν(C=O) frequency shift (Fig. 3.8), increasing from 21-23 kcal/mol for HMF in vacuum, to 27-29 kcal/mol for HMF with formic acid. The primary interaction between solvent and HMF is via the carbonyl oxygen lone pairs, which are delocalized by the σ^*(O—H) of the solvent in the protic solvents and σ^*(C-H) in the aprotic solvents (Fig. 3.11). Of the two lone pairs on the oxygen, the more p-type lone pair interacts more strongly with the H-bond donor, in agreement with the observations of Reed et al.[34] This leads to a decrease in lone pair occupancy (Fig. 3.10) and an increase in σ^*(X—H) (X = C, O) occupancy that depends on ν(C=O) (Fig. 3.9). In THF, σ^*(C—H) occupancy

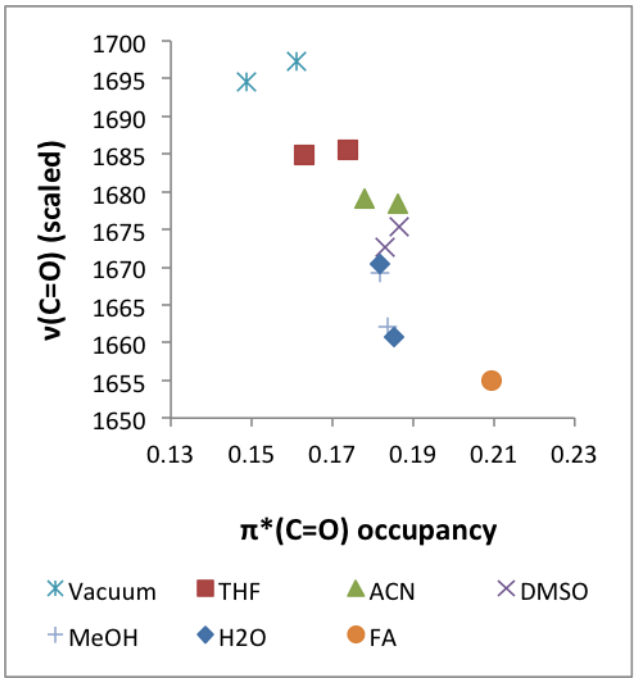

Figure 3.7: Calculated ν(C=O) for gas phase HMF/solvent complexes shown in Figure 4 (both cis and trans conformations) are compared to the occupancy of the π*(C=O) antibonding orbital. Increase in occupancy of the π*(C=O) orbital leads to a weaker bond, and ν(C=O) redshifts.

increases by only 0.018 when interacting with the HMF carbonyl, and the stabilization energy of the LP(O)→ σ*(C—H) delocalization is less than 1 kcal/mol, giving evidence of very weak H-bonding (if at all). In formic acid, the σ*(O—H) occupancy increases by as much as 0.060, and the LP(O) → σ*(O—H) stabilization energy is as much as 18.44 kcal/mol (Table S9 in Appendix B). In the protic solvents, this leads to a red-shift in ν(O—H) of the solvent (as much as 405 cm^{-1} for FA) (Fig. 3.12). However, shifts in ν(C—H) could not be elucidated owing to strong coupling and changes in coupling between the donating C—H and other C—H bonds. In the implicit solvent, the lone pairs increased in occupancy as the carbonyl frequency was redshifted, but in the presence of hydrogen bonding, the lone pairs donate electron density to the solvent σ*(X—H) and the change in lone pair occupancy is less significant. Fig. 3.13 highlights the major changes in occupancy due to H-bonding which lead to frequency shifts in ν(C=O).

3.4.3.3 Atoms in Molecules Analysis

The binding energy of the solvent to the solute is not a good measure of the H-bond strength due to additional interactions between the solvent molecule and the HMF hydroxyl or the furan ring H. So, we use Bader's Atoms AiM theory[30] to examine the electron density, the Laplacian of the density, and the kinetic and potential energy at the H-bond critical points in the gas-phase solvent-HMF complexes. Molecular graphs of all the HMF/solvent complexes optimized with B3LYP/6-31+G(d,p) are shown in Fig. 3.14, and the properties of the bond critical points (BCP) between the solvent H and the HMF carbonyl are given in Table S10 in Appendix B.

As can be seen in Fig. 3.14, HMF interacts with each of the solvents at multiple sites, defined by (3,-1) BCPs in the electron density. In the trans conformation, the carbonyl accepts one or two H-bonds from each solvent molecule, while the hydrogen on C3 donates a hydrogen bond to O in the protic solvents, THF, and DMSO, and to the N in acetonitrile, as seen by the formation of (3,-1) BCPs in the density. (3,+1) ring critical points (RCP) appear in the plane enclosed by these hydrogen bonds and

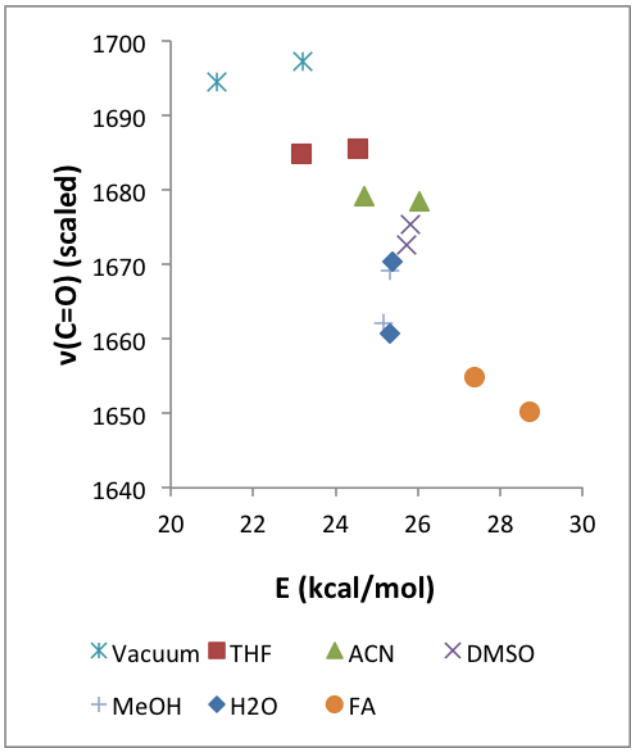

Figure 3.8: Calculated ν(C=O) for gas phase HMF/solvent complexes shown in Fig. 3.4 (both cis and trans conformations) are compared to the delocalization stabilization energy between π(C2=C3) $\rightarrow$ π^*(C=O). As the principal delocalization for the carbonyl, π(C2=C3) $\rightarrow$ π^*(C=O), increases in strength, π^*(C=O) increases in occupancy (see Fig. 3.7), the bond becomes weaker, and ν(C=O) redshifts.

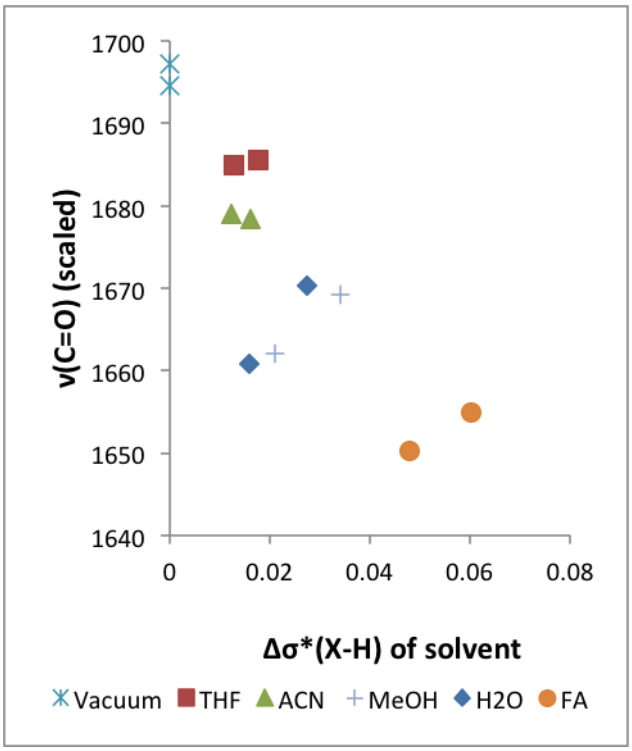

Figure 3.9: Calculated ν(C=O) for gas phase HMF/solvent complexes shown in Fig. 3.4 (both cis and trans conformations) are compared to the change in occupancy of the σ*(X—H) (X = C or O) of the solvent H which is nearest to the HMF carbonyl O. While all solvents had an increase in σ*(X-H) occupancy upon interaction with the HMF carbonyl, the solvents which significantly shifted ν(C=O) experienced the greatest increase in occupancy of this orbital. Cis-bridge configurations of MeOH and H_2O fall outside the trend, likely due to cooperative H-bonding with the HMF hydroxyl, or due to interaction with the furan O. DMSO participated in multiple H-bonds with the HMF carbonyl, and so is excluded on this plot.

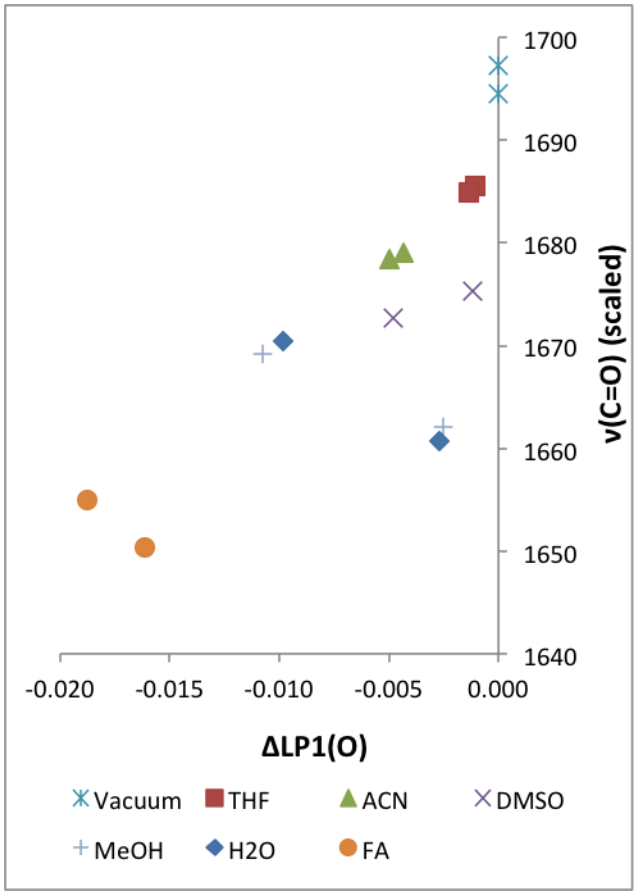

Figure 3.10: The occupancy of the lone pair on the carbonyl oxygen (LP1) is a descriptor for the SIFS of ν(C=O), decreasing with decreasing ν(C=O). The cis-bridge configs of MeOH and H_2O fall outside the trend, possibly due to cooperative H-bonding with the HMF hydroxyl or interaction with the furan O.

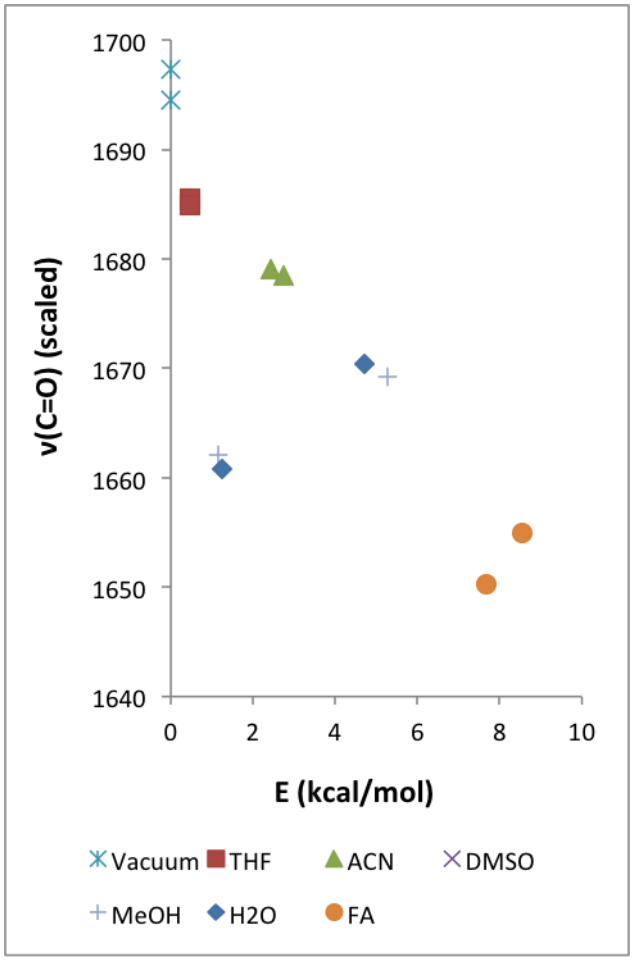

Figure 3.11: Calculated ν(C=O) for gas phase HMF/solvent complexes shown in Fig. 3.4 (both cis and trans conformations) are compared to the delocalization stabilization energy between the HMF carbonyl O lone pair and solvent σ^*(X-H) (X=C or O) which is H-bonded to the carbonyl. Delocalization stabilization energy increases from negligible with THF to several kcal/mol as frequency redshifts. The cis-bridge configs of MeOH and H_2O fall outside the trend, likely due to cooperative H-bonding with the HMF hydroxyl or interaction with the furan O. DMSO is not included because multiple solvent H interact with the carbonyl O.

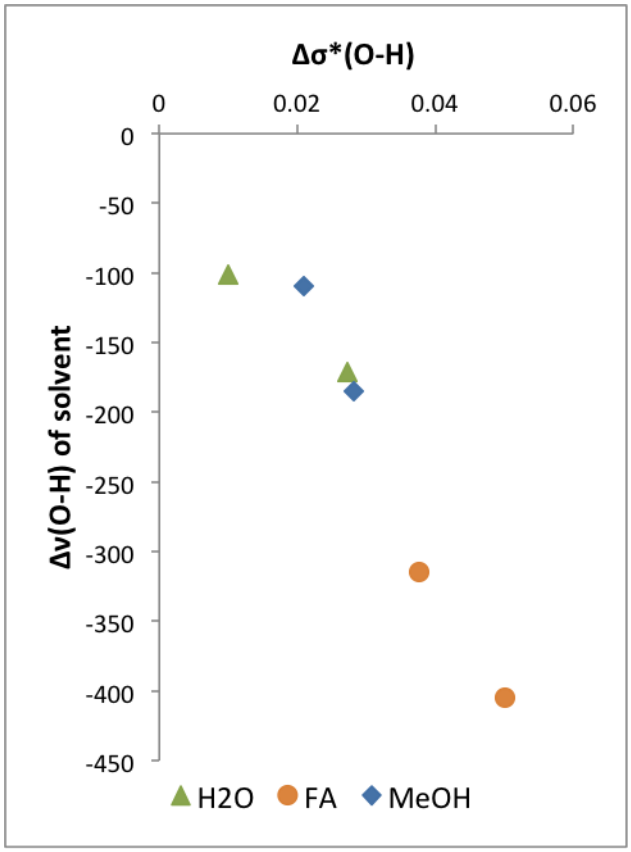

Figure 3.12: The redshift in protic solvent ν(O—H) is compared to change in solvent σ*(O—H) (solvent molecule in complex - solvent molecule in vacuum).Protic solvents exhibit H-bonding with HMF carbonyl, and ν(O—H) decreases as occupancy of σ*(O-H) increases. Aprotic solvents are not shown here because C—H stretching is not an isolated vibration, being coupled to other modes.

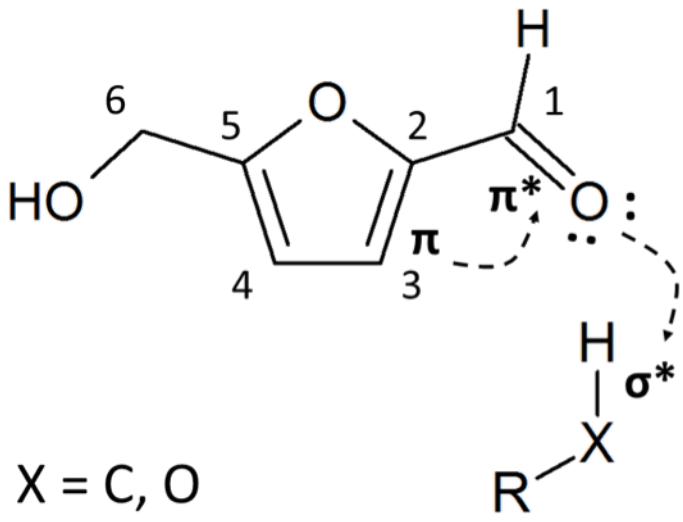

Figure 3.13: Scheme indicating transfer of electrons due to solvent interaction.

the covalent bonds of HMF and the solvent. In the cis conformations, the carbonyl of HMF accepts one or two H-bonds from the solvent, and the hydroxyl of HMF donates an H-bond to the solvent O in the protic solvents, DMSO, and THF, and to the N in acetonitrile. However, instead of forming a single (3,+1) RCP in the plane between the hydroxyl and carbonyl H-bond paths, the furan O also forms a (3,-1) BCP with the solvent, to form at least two rings and RCPs (Fig. 3.14). In water, methanol, and THF, the furan O is also engaged in a bond with the same solvent hydrogen that interacts with HMF. Because of the highly acute X-H—O bond angle (107.1, 109.5, and 124.0 respectively), this is likely not a persistent interaction, but it may be influencing the H-bonding between the solvent and the HMF carbonyl. The furan O interacts with the C of formic acid with the N in acetonitrile. DMSO shows complex behavior with cis HMF, with two hydrogens each engaged in two bonds with furan O and carbonyl O, such that four (3,+1) RCPs and one (3,+3) cage critical point are observed.

The hydrogen bonds associated with the carbonyl of HMF are most likely to influence ν(C=O), so the properties of the electron density at the H-bond critical

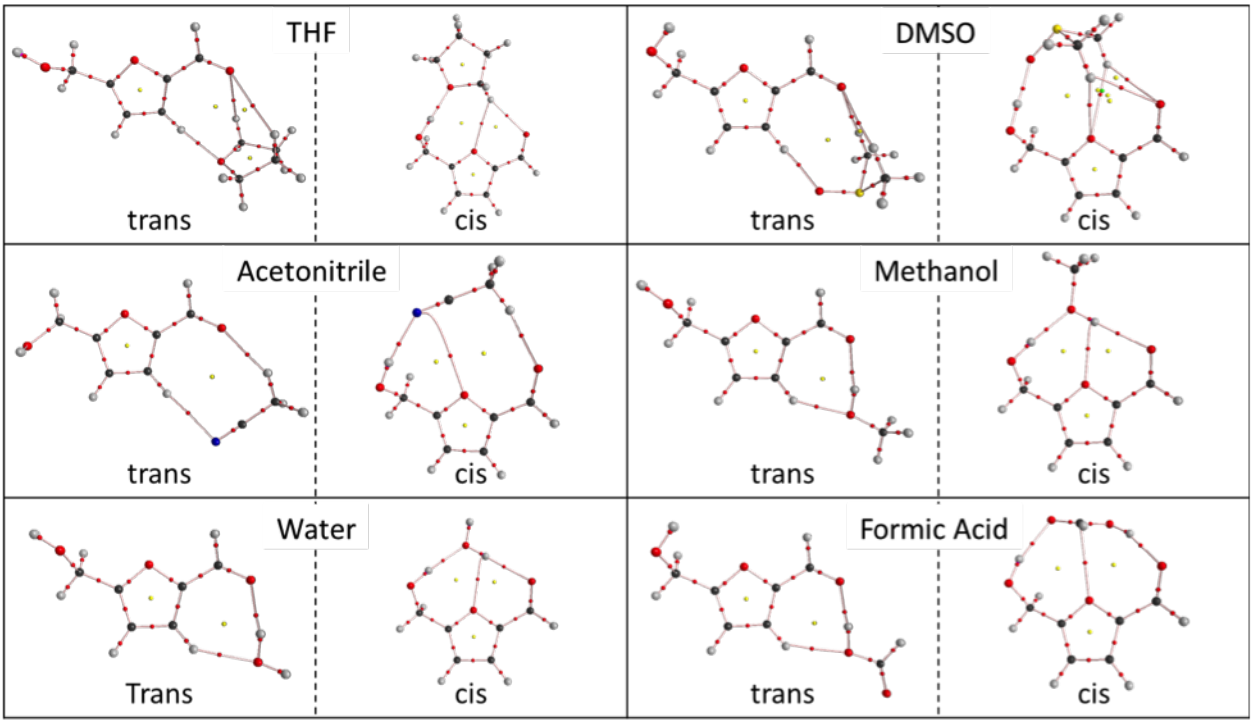

Figure 3.14: Molecular graphs of the solvent/HMF complexes in vacuum. Red points are (3,-1) critical points in the density, and yellow points are (3,+1) critical points in the density.

points have been catalogued (Table S10 in Appendix B). For all H-bonds, the local virial theorem is satisfied

$$2T(\mathbf{r}) + V(\mathbf{r}) - \hbar^2/4m)\nabla^2\rho(\mathbf{r}) = 0 \tag{3.7}$$

where T is the Lagrangian kinetic energy, V is the potential energy, and $\nabla^2\rho$ is the Laplacian of the charge density[30]. $\nabla^2\rho$ is positive at the BCP for all solvents, indicating a region of charge depletion and a generally weak, closed-shell, non-covalent interaction, consistent with literature findings for H-bonded systems [35–39]. HMF forms stronger H-bonds with solvents that redshift ν(C=O) more, as evidenced by high electron density (as much as 0.0403 au for trans HMF with formic acid) and low (more negative) potential energy (-0.0294 au for trans HMF with formic acid) at the BCP relative to solvents which shift ν(C=O) less. As the H-bond strength increases, one would expect $\nabla^2\rho$ to decrease, which would indicate more local charge concentration with a stronger bond. Grabowski and coworkers observed a decrease in $\nabla^2\rho$ with increasing H-bond strength in HF H-bonding with various electron donors [40]. However, we find $\nabla^2\rho$ is larger for stronger H-bonds (0.0298 au for trans HMF with formic acid), and this is because the kinetic energy is larger (0.0296 au). This occurs because stronger H-bonds have shorter bond lengths (Table S2 in Appendix B) which leads to a compression of the wave function, i.e., charge localization, and thus a higher local kinetic energy at the H-bond critical point. In crystal structures with H-bonds to carbonyl groups, shorter H-bond lengths were found to correspond to longer C=O bonds [41], corroborating our observation of longer C=O bonds (leading to a frequency redshift) associated with a decrease in H-bond length and an increase in kinetic energy.

The above observations are nearly monotonic across the range of solvents studied (Fig. 3.15). Outliers include the DMSO and THF conformations, in addition to the cis HMF with water and MeOH. Cis HMF with DMSO and trans HMF with THF and DMSO appear to involve bifurcated H-bonds (where two solvent hydrogens simultaneously bond with the HMF carbonyl). For THF, DMSO, methanol, and water, the

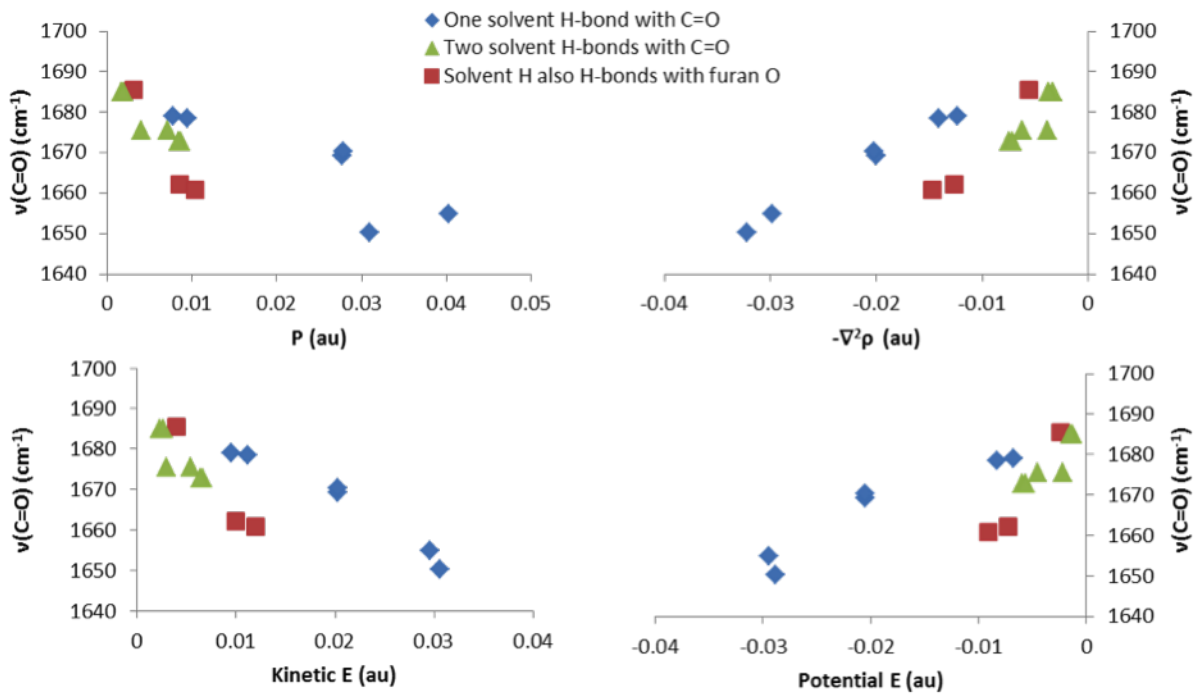

Figure 3.15: Properties of the solvent-HMF carbonyl hydrogen bond from Bader Analysis. For the simple systems with 1 H-bond, the trends stretch across protic and aprotic solvents. But, if a protic solvent hydrogen H-bonds with both the carbonyl O and the furan O, or, if the HMF carbonyl O is H-bonded to multiple solvent H, then the BCP lies outside the general behavior, with a smaller magnitude density, KE, PE, Lap, and curvature than one would expect from the observed frequency shift.

furan O of cis-HMF appears to form a bond with the solvent H that is H-bonded to the carbonyl. In these cases with non-simple H-bond connectivity, the individual H-bonds with the HMF carbonyl become weaker than expected, giving a lower ρ and a less negative V for a given frequency shift compared to the rest of the solvent set. Bader analysis in literature involving bifurcated H-bonds[39] and a single hydrogen forming bonds with three atoms[42] is fairly unexplored and has not yet been examined in relation to IR frequencies.

3.5 Discussion

The CPCM solvation model by itself does not agree with experiment because it relies on a methodology akin to the KBM theory for SIFS, and the frequency shift plateaus for high dielectric solvents. In this high-dielectric regime, solvent molecules are usually polar, and local interactions become significant. However, at low dielectric, the local interactions seem to be less significant, and the CPCM model continues to predict strong frequency shifts due to the solvent dielectric. It would appear that there are two regimes of frequency shifts – an "optical regime," where the frequency shift is dominated by the dielectric constant of the medium departing from $\epsilon = 1$ in the gas phase, and a "local regime," where the KBM parameter has reached a plateau and local interactions are responsible for any further frequency shift (Fig. 3.5).

The use of frequency scaling factors raises important issues. Quantum mechanical harmonic frequencies deviate from experimental frequencies because of anharmonicity, finite basis sets, and partial accounting for electron correlation [20]. Because these effects are generally uniform, linear scaling factors specific to theory level and basis set have been successful in empirically correcting for these effects in gas-phase spectra. However, applying the same scaling factors to structures in implicit solvent will result in over-correcting the frequencies. We see this for HMF in the solvents studied here, and it has also been reported to be the case for L-alanine [24] and N-methylacetamide [22] in implicit water. In these studies, the authors report unscaled frequencies, and find the best agreement with both implicit and explicit solvent. We find that for solvents with a high dielectric constant (the KBM parameter has plateaued), the implicit-plus-explicit solvation model gives unscaled frequencies in reasonable agreement with our experiments and in agreement with literature [22, 24]. However, for solvents in the low-ϵ regime, this procedure is inappropriate because the CPCM model makes ν(C=O) too sensitive to the solvent dielectric, and it quickly diverges to the gas-phase frequency as ϵ approaches unity. The most successful method we found was to treat the solute plus explicit solvent in the gas-phase, and scale the frequencies with the empirical scale factors developed for gas-phase structures. For this system, the subtle differences

in local interactions (whether weak or strong H-bonding with O—H or C—H of the solvent, and possibly other local interactions present in the model) account for the differences in ν(C=O), and the strength of the SIFS is not dependent on differences in the dielectric of the bulk solution. Because measures of H-bond strength (whether from NBO or Bader analysis) do not perfectly correlate with the frequency shift, H-bonding interactions alone are not responsible for the SIFS. Solvent atoms other than the H-bond donor also interact with HMF, especially with the furan ring oxygen, and these do affect the frequency shift, but only as minor corrections to the major effects of H-bonding with the carbonyl.

The frequency shifts of isolated HMF in implicit solvent correlate with several changes in electronic structure. As ν(C=O) redshifts, the occupancy of π^*(C1=O1) increases as π(C2=C3) is delocalized, the partial charges of the carbon and oxygen become more polarized, and resonance structures with a single-bond C^+—O^- become more stable. These effects also appear in the explicit solvation model, including the shift of electron density from π(C2=C3) to π^*(C1=O1) and the polarization of the carbonyl, but these are induced by a different mechanism: electron transfer from the lone pairs on the carbonyl oxygen to the hydrogen-bond donor σ^*(X—H). Because the explicit solvation model agrees better with experiment, we attribute the source of the frequency shifts in experiment to lie in the solvent's ability to withdraw electron density from the carbonyl (in other words, its Lewis acidity), rather than by the dielectric of the medium inducing a change in the dipole moment of the solute. The same scaling factor used to correct for anharmonicity in gas-phase calculations of other molecules was found to be suitable for bringing the ν(C=O) of HMF in these solute/solvent clusters in the gas-phase into agreement with experimental measurements of liquid-phase solutions. But whichever mechanism is at work in the experiment, these calculations predict similar consequences in the electronic structure in terms of changes in partial charges and orbital occupancies, which generally correlate with the SIFS of the carbonyl.

Since we relate the SIFS to the Lewis acidity of the solvent, our calculations agree with the experimental observation that SIFS of carbonyls are correlated with

the Gutmann AN of the solvent. Several works have treated the AN as an index of solvent Lewis acidity and correlated it with SIFS of carbonyl [12, 15, 43, 44] or sulfoxide[45] functional groups of solutes. The AN was originally defined on a scale for the ^{31}P NMR shift of triethylphosphine oxide in different solvents[16], and as such, is an empirical descriptor. By reproducing SIFS that correlate with the Gutmann AN and investigating their electronic structure, we find the first theoretical evidence for treating the empirical AN as a measure of Lewis acidity, because the observed frequency shift indeed coincides with the ability of the solvent to withdraw electron density from the carbonyl.

3.6 Conclusions

We have performed IR measurements of the ν(C=O) of 5-hydroxymethyl furfural (HMF) in various solvents and performed *ab initio* calculations in implicit, explicit, and implicit+explicit solvents in order to understand why different solvents shift the frequency differently. We have shown that the carbonyl stretching frequency of HMF is correlated with the Gutmann acceptor number of the solvent, a measure of solvent Lewis acidity, and we have reproduced these frequency shifts in *ab initio* calculations. The dielectric constant of the medium does not affect ν(C=O) as predicted by Bauer or the CPCM model due to the importance of H-bonding interactions and deviation of this model from experiment in solvents with low dielectric constant. Through NBO analysis, we have demonstrated that ν(C=O) redshifts as the carbonyl bond is polarized and weakened due to increased occupancy of the π*(C=O) orbital, transferred from the adjacent π(C2=C3) orbital. The solvent does not directly interact with π*(C=O), but with the lone pairs on the carbonyl via H-bonding interactions. Bader analysis shows that strong SIFS of ν(C=O) are associated with increased charge density and potential energy at the bond critical point of the solvent/HMF carbonyl H-bond, providing another indication of the importance of solvent-HMF interaction strength. Through electronic structure calculations, we confirm that the empirical Gutmann acceptor number is a descriptor of the solvent?s ability to withdraw electron

density.

3.7 Acknowledgements

This work was supported from the Catalysis Center for Energy Innovation, an Energy Frontier Research Centre funded by the U. S. Department of Energy, Office of Science and Office of Basic Energy Sciences under award number DE-SC0001004, and by the National Science Foundation Graduate Research Fellowship Program #0750966. This research used resources of the National Energy Research Scientific Computing Center, a DOE Office of Science User Facility supported by the Office of Science of the U.S. Department of Energy under Contract No. DE-AC02-05CH11231.

REFERENCES

[1] T. R. Josephson, G. Tsilomelekis, C. Bagia, V. Nikolakis, D. G. Vlachos, and S. Caratzoulas. Solvent-induced frequency shifts of 5-hydroxymethylfurfural deduced via infrared spectroscopy and ab initio calculations. *Journal of Physical Chemistry A*, 118(51):12149–12160, 2014. ISSN 1089-5639. doi: 10.1021/jp508340p.

[2] X. Tong, Y. Ma, and Y. Li. Biomass into chemicals: Conversion of sugars to furan derivatives by catalytic processes. *Appl. Catal., A*, 385(1-2):1–13, 2010. doi: 10.1016/j.apcata.2010.06.049.

[3] M. E. Zakrzewska, E. Bogel-Lukasik, and R. Bogel-Lukasik. Ionic Liquid-Mediated Formation of 5-Hydroxymethylfurfural: A Promising Biomass-Derived Building Block. *Chemical Reviews*, 111:397–417, 2011. doi: 10.1021/cr100171a.

[4] T. Stahlberg, W. Fu, J. M. Woodley, and A. Riisager. Synthesis of 5-(hydroxymethyl)furfural in ionic liquids: paving the way to renewable chemicals. *ChemSusChem*, 4(4):451–458, 2011. doi: 10.1002/cssc.201000374.

[5] Z. Wang, L. Wang, Y. Jiang, M. Hunger, and J. Huang. Cooperativity of Brønsted and Lewis Acid Sites on Zeolite for Glycerol Dehydration. *ACS Catalysis*, 4(4): 1144–1147, 2014. doi: 10.1021/cs401225k.

[6] L. Hu, G. Zhao, W. Hao, X. Tang, Y. Sun, L. Lin, and S. Liu. Catalytic conversion of biomass-derived carbohydrates into fuels and chemicals via furanic aldehydes. *RSC Adv.*, 2(30):11184, 2012. doi: 10.1039/c2ra21811a.

[7] G. Yang, E. A. Pidko, and E. J. M. Hensen. Mechanism of Brønsted acid-catalyzed conversion of carbohydrates. *Journal of Catalysis*, 295:122–132, 2012. doi: 10.1016/j.jcat.2012.08.002.

[8] S. K. R. Patil and C. R. F. Lund. Formation and Growth of Humins via Aldol Addition and Condensation during Acid-Catalyzed Conversion of 5-Hydroxymethylfurfural. *Energy Fuels*, 25(10):4745–4755, 2011. doi: 10.1021/ef2010157.

[9] I. van Zandvoort, Y. Wang, C. B. Rasrendra, E. R. van Eck, P. C. Bruijnincx, H. J. Heeres, and B. M. Weckhuysen. Formation, molecular structure, and morphology of humins in biomass conversion: influence of feedstock and processing conditions. *ChemSusChem*, 6(9):1745–1758, 2013. doi: 10.1002/cssc.201300332.

[10] G. Tsilomelekis, T. R. Josephson, V. Nikolakis, and S. Caratzoulas. Origin of 5-hydroxymethylfurfural stability in water/dimethyl sulfoxide mixtures. *ChemSusChem*, 7(1):117–126, 2014. doi: 10.1002/cssc.201300786.

[11] S. H. Mushrif, S. Caratzoulas, and D. G. Vlachos. Understanding solvent effects in the selective conversion of fructose to 5-hydroxymethyl-furfural: a molecular dynamics investigation. *Phys. Chem. Chem. Phys.*, 14(8):2637–2644, 2012. doi: 10.1039/c2cp22694d.

[12] D. Kun Cha, A. A. Kloss, A. C. Tikanen, and W. Ronald Fawcett. Solvent-induced frequency shifts in the infrared spectrum of acetone in organic solvents. *Phys. Chem. Chem. Phys.*, 1(20):4785–4790, 1999. doi: 10.1039/a905776e.

[13] N. Tekin, H. Namli, and O. Turhan. Solvents effect on infrared spectra of 1,3-indanedione in organic solvents. *Vib. Spectrosc.*, 39(2):214–219, 2005. doi: 10.1016/j.vibspec.2005.03.006.

[14] N. Tekin, H. Pir, and S. Sagdinc. Study of the solvent effects on the molecular structure and CO stretching vibrations of flurbiprofen. *Spectrochimica Acta, Part*

A: Molecular and Biomolecular Spectroscopy, 98:122–131, 2012. doi: 10.1016/j.saa.2012.08.069.

[15] R. A. Nyquist, R. Streck, and G. Jeschek. NMR and IR spectra-structure correlations carbonyl containing compounds in various solvents. *Journal of Molecular Structure (THEOCHEM)*, 377:113–128, 1996.

[16] V. Gutmann. Solvent Effects on the Reactivities of Organometallic Compounds. *Coord. Chem. Rev.*, 18:225–255, 1976.

[17] E. M. Bauer and M. Magat. Sur La Deformation Des Molecules Et Leurs Spectres de Vibration Dans Les Etats Condenses. *Physica*, 5(8):718–724, 1938.

[18] W. West and R. T. Edwards. The Infrared Absorption Spectrum of Hydrogen Chloride in Solution. *Journal of Chemical Physics*, 5(1):14, 1937. doi: 10.1063/1.1749924.

[19] N. S. Bayliss, A. R. H. Cole, and L. H. Little. Solvent Effects in Infra-red spectra: C=O, C-H, and C-C vibrations. *Aust. J. Chem.*, 8(1):26–38, 1955. doi: 10.1071/CH9550026.

[20] J. P. Merrick, D. Moran, and L. Radom. An Evaluation of Harmonic Vibrational Frequency Scale Factors. *Journal of Physical Chemistry A*, 111:11683–11700, 2007. doi: 10.1021/jp073974n.

[21] J. Tomasi, B. Mennucci, and C. Roberto. Quantum Mechanical Continuum Solvation Models. *Chemical Reviews*, 105:2999–3093, 2005. doi: 10.1021/cr9904009.

[22] J. Kubelka and T. A. Kiederling. Ab Initio Calculation of Amide Carbonyl Stretch Vibrational Frequencies in Solution with Modified Basis Sets. 1. N-Methyl Acetamide. *Journal of Phyical Chemistry A*, 105:10922–10928, 2001. doi: 10.1021/jp013203y.

[23] E. Tajkhorshid, K. J. Jalkanen, and S. Suhai. Structure and Vibrational Spectra of the Zwitterion L-Alanine in the Presence of Explicit Water Molecules: A Density Functional Analysis. *Journal of Physical Chemistry B*, 102(30):5899–5913, 1998. doi: 10.1021/jp9803135.

[24] K. Frimand, H. Bohr, K. J. Jalkanen, and S. Suhai. Structures, vibrational absorption and vibrational circular dichroism spectra of L-alanine in aqueous solution: a density functional theory and RHF study. *Chem. Phys.*, 255:165–194, 2000.

[25] K. J. Jalkanen, I. M. Degtyarenko, R. M. Nieminen, X. Cao, L. A. Nafie, F. Zhu, and L. D. Barron. Role of hydration in determining the structure and vibrational spectra of L-alanine and N-acetyl L-alanine N-methylamide in aqueous solution: a combined theoretical and experimental approach. *Theor. Chem. Acc.*, 119(1-3): 191–210, 2007. doi: 10.1007/s00214-007-0361-z.

[26] B. Z. Chowdhry, T. J. Dines, S. Jabeen, and R. Withnall. Vibrational Spectra of α-Amino Acids in the Zwitterionic State in Aqueous Solution and the Solid State: DFT Calculations and the Influence of Hydrogen Bonding. *Journal of Phyical Chemistry A*, 112:10333–10347, 2008. doi: 10.1021/jp8037945.

[27] G. F. Nobrega, J. R. Sambrano, A. R. de Souza, J. J. Queralt, and E. Longo. DFT study of α-alanine as a function of the medium polarity. *Journal of Molecular Structure (THEOCHEM)*, 544:151–157, 2001. doi: 10.1016/S0166-1280(01)00374-8.

[28] M. J. Frisch, G. W. Trucks, H. B. Schlegel, G. E. Scuseria, M. A. Robb, J. R. Cheeseman, G. Scalmani, V. Barone, B. Mennucci, G. A. Petersson, H. Nakatsuji, M. Caricato, X. Li, H. P. Hratchian, A. F. Izmaylov, J. Bloino, G. Zheng, J. L. Sonnenberg, M. Hada, M. Ehara, K. Toyota, R. Fukuda, J. Hasegawa, M. Ishida, T. Nakajima, Y. Honda, O. Kitao, H. Nakai, T. Vreven, J. A. Montgomery Jr., J. E. Peralta, F. Ogliaro, M. J. Bearpark, J. Heyd, E. N. Brothers, K. N. Kudin, V. N. Staroverov, R. Kobayashi, J. Normand, K. Raghavachari, A. P. Rendell,

J. C. Burant, S. S. Iyengar, J. Tomasi, M. Cossi, N. Rega, N. J. Millam, M. Klene, J. E. Knox, J. B. Cross, V. Bakken, C. Adamo, J. Jaramillo, R. Gomperts, R. E. Stratmann, O. Yazyev, A. J. Austin, R. Cammi, C. Pomelli, J. W. Ochterski, R. L. Martin, K. Morokuma, V. G. Zakrzewski, G. A. Voth, P. Salvador, J. J. Dannenberg, S. Dapprich, A. D. Daniels, Ö. Farkas, J. B. Foresman, J. V. Ortiz, J. Cioslowski, and D. J. Fox. Gaussian 09, 2009.

[29] E. D. Glendening, A. E. Reed, J. E. Carpenter, and F. Weinhold. NBO Version 3.1.

[30] R. F. W. Bader. *Atoms in Molecules: A Quantum Theory.* Clarendon, Oxford, England, 1990. ISBN 0198558651.

[31] F. Biegler-Konig, J. Schonbohm, and D. Bayles. Software news and updates - AIM2000 - A program to analyze andvisualize atoms in molecules. *J. Comput. Chem.*, 22(5):545–559, 2001.

[32] V. Barone and M. Cossi. Quantum Calculation of Molecular Energies and Energy Gradients in Solution by a Conductor Solvent Model. *Journal of Phyical Chemistry A*, 102:1995–2001, 1998.

[33] W. M. Haynes, T. J. Bruno, and D. Lide R. CRC Handbook of Chemistry and Physics, 2014.

[34] A. E. Reed Curtiss, Larry A., and Weinhold, Frank. Intermolecular Interactions from a Natural Bond Orbital, Donor-Acceptor Viewpoint. *Chemical Reviews*, 88: 899–926, 1988. doi: 0009-2665/88/0788-0899.

[35] G. L. Sosa, N. Peruchena M., R. H. Contreras, and E. A. Castro. Topological and NBO analysis of hydrogen bonding interactions involving C-H—O bonds. *Journal of Molecular Structure (THEOCHEM)*, 577:219–228, 2002.

[36] P. Kolandaivel and V. Nirmala. Study of proper and improper hydrogen bonding using Bader's atoms in molecules (AIM) theory and NBO analysis. *Journal of Molecular Structure (THEOCHEM)*, 694(1-3):33–38, 2004. doi: 10.1016/j.molstruc.2004.01.030.

[37] S. Wojtulewski and S. J. Grabowski. Blue-shifting CH. . . Y intramolecular hydrogen bonds DFT and AIM analyses. *Chem. Phys.*, 309(2-3):183–188, 2005. doi: 10.1016/j.chemphys.2004.09.008.

[38] J. R. Cheeseman, M. T. Carroll, and R. F. W. Bader. The Mechanics of Hydrogen Bond Formation in Conjugated Systems. *Chem. Phys. Lett.*, 143(5):450–458, 1988.

[39] L. Checinska, S. J. Grabowski, and M. Malecka. An analysis of bifurcated H-bonds: crystal and molecular structures of O,O-diphenyl 1-(3-phenylthioureido)-pentanephosphonate and O,O-diphenyl 1-(3-phenylthioureido)butanephosphonate. *J. Phys. Org. Chem.*, 16(4):213–219, 2003. doi: 10.1002/poc.596.

[40] S. J. Grabowski. Hydrogen bonding strengthmeasures based on geometric and topological parameters. *Journal of Physical Organic Chemistry*, 17(1):18–31, 2004. doi: 10.1002/poc.685.

[41] S. J. Grabowski. Analysis of C=O...H-O Interaction in Organic Crystal Structures. *Tetrahedron*, 54:10153–10160, 1998.

[42] B. A. Vastine and M. B. Hall. The molecular and electronic structure of carbon-hydrogen bond activation and transition metal assisted hydrogen transfer. *Coord. Chem. Rev.*, 253(7-8):1202–1218, 2009. doi: 10.1016/j.ccr.2008.07.015.

[43] G. Desimoni, G. Faita, P. P. Righetti, and L. Toma. V(l). Diels-Alder with Heterodienophiles: a Unified Approach to the Solvent Effect of the Diels-Alder Reaction. *Tetrahedron*, 46(23):7951–7970, 1990.

[44] A. Matsumoto and Y. Mohri. Effects of Solvent as an Electron-Pair Acceptor on Propagation Reactions During Radical Polymerization and Copolymerization of Polar Vinyl Monomers. *J. Polym. Sci., Part A: Polym. Chem.*, 37:2803–2814, 1999.

[45] R. W. Fawcett and A. A. Kloss. Solvent-Induced Frequency Shifts in the Infrared Specturm of Dimethyl Sulfoxide in Organic Solvents. *J. Phys. Chem.*, 100:2019–2024, 1995.

Chapter 4

METHYL-LIGATED TIN SILSESQUIOXANE CATALYZED REACTIONS OF GLUCOSE

4.1 Abstract

Tin-containing zeolite Beta (Sn-Beta) has been investigated as a catalyst for isomerizing aldohexoses into ketohexoses through a Lewis acid mediated hydride shift. Recent studies on the reactivities of Lewis base-doped and alkali-exchanged Sn-Beta samples have conclusively demonstrated that the "open" tin site performs the glucose isomerization reaction. With Lewis base doped Sn-Beta, glucose conversion is almost completely eliminated and product selectivity is shifted predominantly to mannose. These data suggest that glucose reactions may occur through pathways that do not involve the "open" site in Sn-Beta; albeit at significantly lower rates. To examine this possibility, reactions of glucose catalyzed by a homogeneous model of Sn-Beta that does not contain "open" sites, methyl-ligated tin silsesquioxane 1a, is experimentally and theoretically examined. 1a is an active glucose conversion catalyst selectively producing mannose, although the rates of reaction are far below those obtained from Sn-Beta. A hybrid quantum mechanical/molecular mechanics model is constructed, and the complete catalytic cycle is computationally examined, considering ring-opening, three distinct pathways for each hydride- and carbon-shift reaction, and ring-closing. The combined experimental and computational results suggest that there could be reaction pathways that involve Si-O-Sn cleavage that give much slower reaction rates than the open tin site in Sn-Beta.

The synthesis, characterization, and kinetic experiments were conducted by Kramer Brand at CalTech. This chapter is adapted with permission from [1] in a paper

titled "Methyl-ligated tin silsesquioxane catalyzed reactions of glucose" Reprinted with permission from the *Journal of Catalysis*. Copyright © 2016, Elsevier.

4.2 Introduction

Microporous solids containing Lewis acid sites have garnered considerable interest for their ability to selectively convert highly functionalized, carbonyl-containing molecules such as glucose [2–4]. Interest in carbonyl-based chemistry has been driven by the attractiveness of producing transportation fuels and fine chemicals from biomass-derived sources [5–7]. A tin-containing molecular sieve with the zeolite beta topology (Sn-Beta) has emerged as a useful solid Lewis acid catalyst to perform highly selective reactions with carbohydrates, such as the isomerization of glucose to fructose [8]. Sn-Beta, initially synthesized by Corma et al. [9, 10], has been demonstrated to catalyze the Baeyer-Villiger oxidation of ketones to lactones [10, 11], Meerwein-Ponndorf-Verley (MPV) reduction of aldehydes and ketones [12, 13], epimerization of glucose [8, 14–16], carbon-carbon bond coupling reactions [17, 18], and Diels-Alder reactions [19].

The efficacy of Sn-Beta has stimulated research on resolving the active catalytic site and mechanism for the glucose isomerization reaction. Metal-containing zeolites like Sn-Beta, contain a distribution of "closed" sites (a $(SiO)_4Sn$ center) and "open" sites (a $(SiO)_3SnOH$ center with an adjacent silanol group) that occur when the framework is partially hydrolyzed [20]. In a recent study, Harris et al. demonstrated that the number of open and closed sites in Sn-Beta may be quantitatively determined utilizing Lewis bases as titrants [21]. In the same report, an inverse linear correlation between the initial rate of glucose isomerization with the amount of pyridine dosed was demonstrated, implying that isomerization activity should be fully suppressed when all open sites are titrated. Bermejo-Deval et al. sodium-exchanged the silanol groups adjacent to the open tin site and observed a complete shift in selectivity from fructose to mannose, providing the first experimental evidence that the open site was the most active tin site, as well as emphasizing the significance of the silanol moiety in the reaction

mechanism [16]. This work also revealed that titration of the open site with NH_3 (Sn-Beta-NH_3) attenuated the activity of the catalyst indicating that the open and closed sites do not interconvert under reaction conditions.

Several different reaction mechanisms involving a catalytically active open site have been proposed. Work from Li et al. [22] suggests that glucose first binds to the open site through coordination of the basic C1 carbon hydroxyl, with subsequent transfer of the acidic proton to the framework lattice followed by a 1,2-intramolecular hydride shift. This results in a monodentately bound fructose stabilized by the adjacent silanol group through the O1 oxygen. Yang et al. [23]consider a similar type of mechanism involving the closed site. Rai et al. [24] and Christianson et al. [25] propose similar pathways, however, their calculations involve the acidic C2 hydroxyl proton transferring to the stannanol group, forming a water molecule. Rai et al. also demonstrated that in the absence of a silanol group adjacent to the tin center, the glucose binds to the tin bidentately and selectively produces mannose through a 1,2-intramolecular carbon shift. Experimental results support this prediction [16]. The Davis lab has also shown the effect of the silanol moiety in directing the selectivity of glucose conversion to either fructose or mannose using a pair of silsesquioxanes retaining an octahedral tin site with and without an adjacent silanol substituent [26].

The observation of some glucose activity despite poisoning (Sn-Beta-NH_3) implies that there may be other reaction pathways with rates slower than those catalyzed by the open site in Sn-Beta. One possible pathway could involve the protonation of a framework Sn-O-Si bond by glucose to facilitate binding to the Lewis acidic site. To test this case, we synthesized a methyl-ligated tin silsesquioxane (1a), and investigated its glucose reaction pathways, both experimentally and theoretically. Compound 1a contains a tin atom terdentately bound to a silsesquioxane ligand through three Sn-O-Si bridging bonds, as schematically shown in Fig. 4.1. Here, we demonstrate that 1a is an active catalyst (but with low rates of reaction) for the conversion of glucose to mannose and fructose via 1,2-intramolecular carbon and hydride shifts, respectively. Additionally, a hybrid quantum mechanics/molecular mechanics (QM/MM) electronic

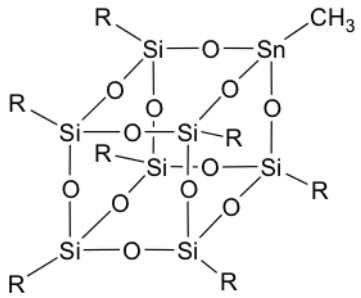

Figure 4.1: Schematic representation of the structure of 1a. R = cyclohexyl

structure model is used to compare pathways in the production of fructose and mannose. The catalytic cycle model consists of three distinct operations: 1) deprotonation and ring-opening of glucose, 2) hydride- or carbon-shift (Blik) reactions, and 3) ring-closing and reprotonation of the mannose or fructose products.

4.3 Experimental Methods

All glassware was dried at 433 K prior to all syntheses, and purged with argon while cooling. All syntheses, purification procedures, and reaction tests were carried out under argon using standard air- and water-free techniques. Benzene (99.8%, anhydrous, Sigma-Aldrich), hexane (95%, anhydrous, Sigma-Aldrich), tetrahydrofuran (THF, ≥99.9%, anhydrous, Sigma-Aldrich), dimethyl sulfoxide (DMSO, ≥99.9%, anhydrous, Sigma-Aldrich) and acetonitrile (99.8%, anhydrous, Sigma-Aldrich) were used as received. Triethylamine (99.5%, Sigma-Aldrich) was distilled from 3A molecular sieves. Methyltin trichloride (97%, Sigma-Aldrich) was used without further purification. Heptacyclohexyl trisilanol silsesquioxane (1) was obtained from Hybrid Plastics and recrystallized by slow diffusion of acetonitrile into a concentrated THF solution of; its purity was confirmed by ^{1}H, ^{13}C, and ^{29}Si NMR [27].

4.3.1 Synthesis of 1a

1a was synthesized by the reaction of methyltin trichloride with the incompletely condensed trisilanol silsesquioxane 1, as reported by Feher et al. [27] To ensure that all triethylamine (used as a scavenger base, and reported to be a highly selective catalyst in the conversion of glucose to fructose [28]) was removed from the product, acetonitrile was layered onto a concentrated solution of 1a in benzene. The resultant white powder was filtered and dried for 12 hours under a dynamic vacuum of <50 mTorr.

4.3.2 Material Characterization

Nuclear magnetic resonance (NMR) spectra of 1a were collected either on a Varian Inova 500 (^{1}H, 499.7; ^{13}C, 125.7 MHz) equipped with a broadband probe or on a Varian Inova 400 (^{29}Si, 79.4; ^{119}Sn, 149.1 MHz). ^{29}Si and ^{119}Sn NMR were referenced to $SiMe_4$ and $SnMe_4$, respectively. Chromium(III) acetylacetonate ($Cr(acac)_3$) was added to samples for ^{29}Si and ^{119}Sn NMR characterization as a shiftless relaxation agent.

^{1}H NMR (500 MHz, $CDCl_3$, 298 K): 1.60-1.90 (vbr m, 35 H, CH_2), 1.10-1.33 (vbr m, 35 H, CH_2), 0.94 (s, 3 H, CH_3), 0.65-0.81 (vbr m, 7 H, CH). ^{13}C NMR (125.7 MHz, $CDCl_3$, 298 K): 27.70, 27.56, 27.18, 26.95, 26.73, 26.67 (s, CH_2); 24.35, 23.44, 23.24 (s, 3:3:1 for CH); -3.13 (s, CH_3). ^{29}Si NMR (79.4 MHz, $CDCl_3$, 298 K, 0.02 M $Cr(acac)_3$): -65.01, -68.24, -69.55 (s, 3:1:3). ^{119}Sn NMR (149.1 MHz, $CDCl_3$, 298 K, 0.02 M $Cr(acac)_3$): -247.60.

4.3.3 Reaction Procedures

Reactions of D-glucose (Sigma-Aldrich, anhydrous, ≥99.5%) were conducted under anhydrous conditions in 10 mL thick-walled glass reactors (VWR) that were heated in a temperature-controlled oil bath placed on top of a digital stirring hot plate (Fisher Scientific). Both glucose and 1a were separately dried under vacuum (<50 mTorr) for at least 12 hours prior to the addition of anhydrous DMSO and benzene solvents, respectively. Glass reactors (with their stir bars) were dried for at least 3

hours at 433 K, capped with Teflon septa, and purged with argon while cooling. In a typical reaction, the dried reactors were charged with 6 mL of a 1:1 volumetric ratio of the catalyst and glucose stock solutions, resulting in a 2% (w/w) initial glucose solution, with a glucose:Sn molar ratio of 75. Reactors were placed in the oil bath at a predetermined temperature, and approximately 125 mg aliquots were extracted at regular time intervals. These reaction aliquots were mixed with 125 mg of a 2% (w/w) aqueous D-mannitol (Sigma-Aldrich, ≥98%) solution, which was used as an internal standard for quantification. To ensure thorough catalyst removal from the aliquot solution prior to quantification, 0.3 mL of H2O was added, and the solution was filtered using a 0.2 μm PTFE syringe filter.

Reaction aliquots were analyzed by high performance liquid chromatography (HPLC) using an Agilent 1200 system (Agilent) equipped with refractive index (RI) and evaporative light scattering (ELS) detectors. The glucose, fructose, mannose, and mannitol fractions were separated with a Hi-Plex Ca column (6.5 x 300 mm, 8 μm particle size, Agilent) held at 353 K. Ultrapure water was used as the mobile phase at a flow rate of 0.6 mL min^{-1}.

Glucose conversion and product yields were calculated by

$$X_{Gluc}(t) = \frac{n_{Gluc}(t=0) - n_{Gluc}(t)}{n_{Gluc}(t=0)} x100[\%] \tag{4.1}$$

$$Y_i(t) = \frac{n_i(t)}{n_{Gluc}(t=0)} x100[\%] \tag{4.2}$$

where $X_{gluc}(t)$ is the glucose conversion at time t; $Y_i(t)$ is the yield of product i at time t; $n_{gluc}(t=0)$ is the initial moles of glucose in the reactor; and $n_i(t)$ is the moles of product i at time t.

Reactions using singly- and doubly-labeled glucose at the C1 position (1-13C glucose, 98-99%, Cambridge Isotope Laboratories; 2-^{2}H; 1-^{13}C glucose, 99% ^{13}C, 98% ^{2}H, Omicron Biochemicals) were performed utilizing the same conditions outlined for

D-glucose, but were quenched in cold water after a set duration. To separate the catalyst from the reaction solution, approximately 6 mL of ultrapure water was added and the resultant biphasic solution was filtered. Solvent was removed from the catalyst-free fraction by rotary evaporation; the recovered solids were dissolved in D_2O and analyzed by ^1H and ^{13}C NMR. These NMR spectra were referenced to 3-(trimethylsilyl)-1-propanesulfonic acid sodium salt (DSS).

4.3.4 Computational Methods

Hybrid quantum mechanics/molecular mechanics (QM/MM) electronic structure calculations were used to examine the interactions between the sugars and the catalyst and also to compute various reaction pathways for glucose isomerization and epimerization. All 167 atoms of the catalyst/sugar complex were included in all of the calculations. Within the framework of the ONIOM approach to QM/MM calculations [29, 30], the M062X functional [31] was implemented to model the quantum mechanical domain of the system. Specifically, the cyclohexyl ligands terminating the Si corners of 1a were parameterized using the universal molecular mechanics force field (UFF). The complexing sugar, methyl substituent, and the silicon and oxygen atoms of the complex were modeled with the 6-31G(d,p) basis set, while the Sn atom was described using the LANL2DZ effective core basis set [32]. All calculations were performed in the gas phase using Gaussian 09 version A.09 [33].

4.4 Results and Discussion

4.4.1 Catalytic Behavior of 1a

Conversion and yield data for glucose reactions catalyzed by 1a are given in Fig. 4.2 and Fig. 4.3, respectively. Reaction profiles were collected between 363 – 393 K at 10 K intervals. As with Sn-Beta-NH_3, 1a converts glucose more selectively to mannose than fructose. Fructose is detected as a primary product. As the reaction temperature is increased, formation of by-products becomes increasingly significant, as indicated by the deterioration in carbon balance (Appendix C: Figure S.1). An initial

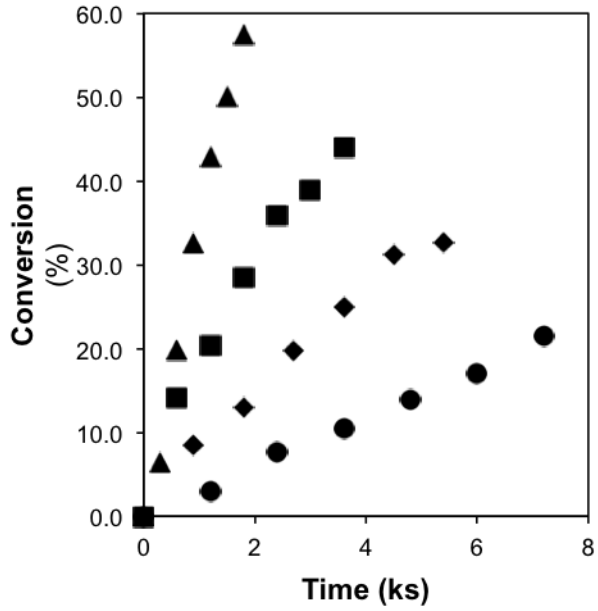

Figure 4.2: Glucose conversion as a function of time from the reaction of 2% (w/w) glucose in 1:1 DMSO:benzene solution with 1a (1:75 Sn/glucose molar ratio) at 363 K (●), 373 K (♦), 383 K (■), 393 K (▲).

investigation into identifying these products indicates that numerous retro-aldol and aldol products are formed. Retro-aldol and aldol reactions have been reported to be catalyzed by tin-containing molecular sieves, although under different reaction conditions, e.g., at high temperatures (>433 K) and through the use of tandem catalysts [34, 35].

Table 1 summarizes the initial rate data for as-made and modified Sn-Beta, 1a, and for two other tin silsesquioxanes capable of binding glucose without necessarily protonating the Sn-O-Si bond [26]. These silsesquioxanes retain octahedrally coordinated tin sites with an adjacent siloxy group capped by either a proton (2a), analogous to the open site in Sn-Beta, or a trimethylsilyl substituent (2b), representative of sodium-exchanged zeolite Beta (Na-Sn-Beta) (structures for 2a and 2b are given in Fig. 4.4).

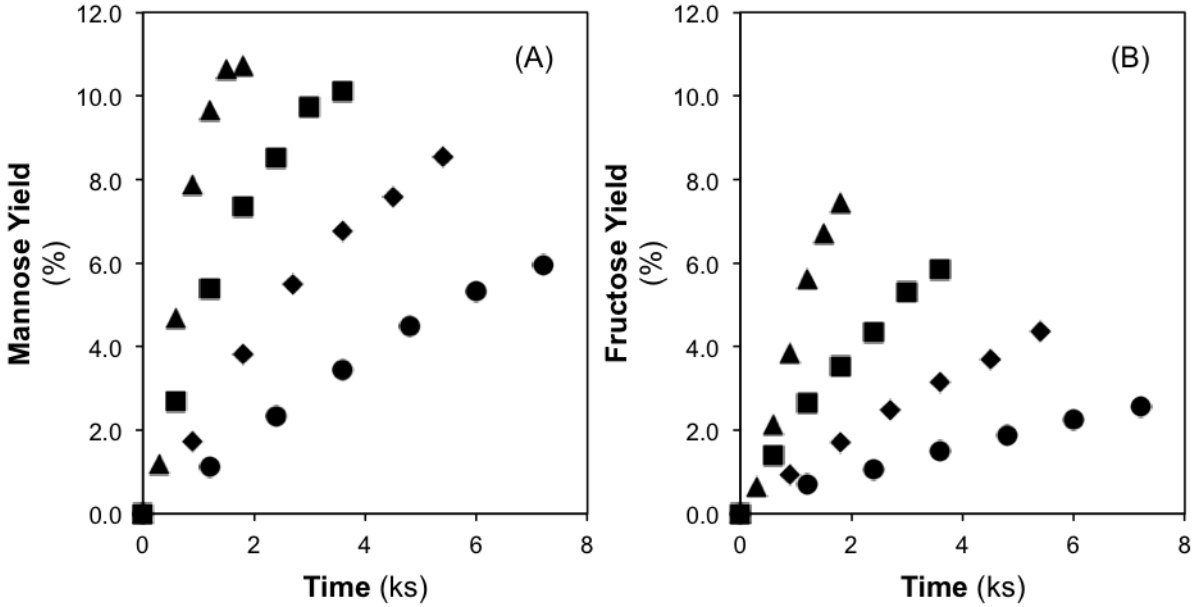

Figure 4.3: Mannose (A) and fructose (B) yields as a function of time from the reaction of 2% (w/w) glucose in 1:1 DMSO:benzene solution with 1a (1:75 Sn/glucose molar ratio) at 363 K (•), 373 K (♦), 383 K (■), 393 K (▲).

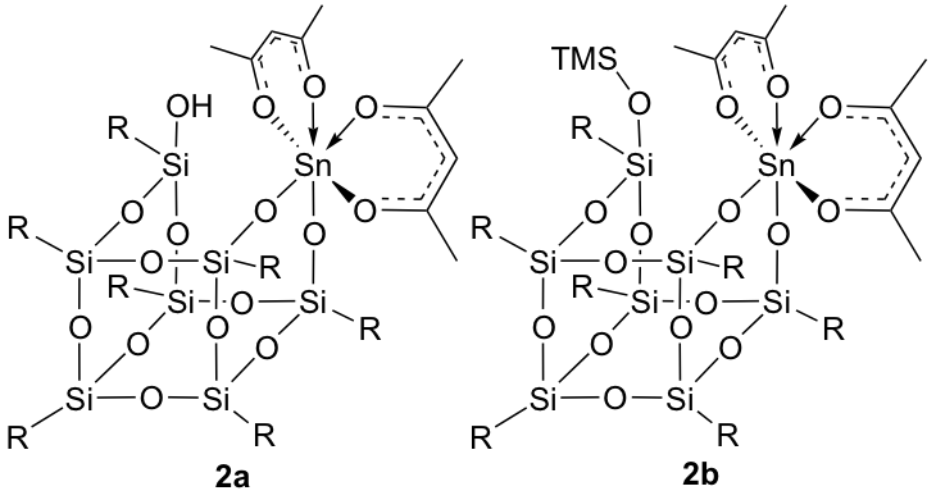

Figure 4.4: Schematic representation of the structures of 2a and 2b. "R" denotes a cyclohexyl ligand.

Initial Rate, mol/(s-L-total mol Sn)	Catalytic Material						
	1a[a]	1a[b]	2a	2b	Sn-Beta	Na-Sn-Beta	Sn-Beta-NH_3
Glucose Consumption	2.69×10^{-1}	1.02×10^{-1}	1.42	8.23×10^{-1}	2.10	1.64	2.99×10^{-1}
Mannose Production	1.01×10^{-1}	4.43×10^{-2}	5.49×10^{-1}	3.80×10^{-1}	3.52×10^{-1}	1.04	1.89×10^{-1}
Fructose Production	6.28×10^{-2}	2.55×10^{-2}	7.56×10^{-1}	1.34×10^{-1}	9.30×10^{-1}	0	0

Table 4.1: Initial rate data for as-made and modified Sn-Beta, as well as tin silsesquioxanes considered here and in other work [16, 26]. All initial rate data were calculated from reactions performed at 353 K unless otherwise noted. All heterogeneous reactions were performed in methanol. [a]At 363K. [b]Initial rates at 353 K determined from activation energy data. Heterogeneous materials were normalized by total tin content, which may underestimate the actual initial rates at the open site in Sn-Beta.

From these data, 1a and Sn-Beta-NH_3 have the lowest initial rates, approximately an order of magnitude slower than Sn-Beta. The decreased activity for Sn-Beta titrated with NH_3 (to effectively block the open framework site), in conjunction with that for 1a, corroborates the hypothesis that reactions at closed sites are slow and selective to mannose. An alternative hypothesis consistent with the experimental data is that the "open" sites remain active for NH_3-Sn-Beta, while the modification reduces their activity and fructose selectivity. However, limited activity of the closed site is a simpler explanation: it does not require assuming the coincidence of two distinct modifications similarly affecting both rate and selectivity of the open site.

Apparent activation energies for the simultaneous production of mannose and fructose by 1a are calculated from the data shown in Fig. 4.5 (Arrhenius plots are given in Appendix C: Figures S.2-S.3, and the calculated rate constants are listed in Appendix C: Table S.1). The concentrations of the mannose and fructose products were used to calculate the values of apparent first-order rate constants, k. High conversion values, wherein catalyst deactivation and equilibrium effects become significant, were ignored in the analysis. The epimerization of glucose to mannose has a calculated

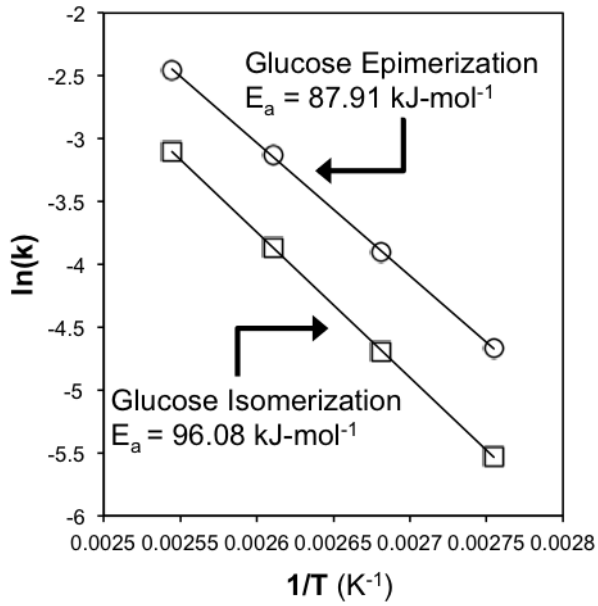

Figure 4.5: Arrhenius plot for the first-order epimerization and isomerization of glucose catalyzed by 1a.

apparent activation energy of 87.9 kJ-mol^{-1}, while the isomerization of glucose to fructose has a modestly higher apparent activation energy of 96.1 kJ-mol^{-1}. For Sn-Beta, an experimentally determined apparent activation energy of 93 $\pm$ 15 kJ-mol^{-1} has been reported for fructose production in H_2O, and 70 $\pm$ 14 kJ-mol^{-1} for mannose production in CH_3OH [15]. The similarity of these activation energies, however, does not take into account any variations in non-rate-limiting, pre-equilibrium step energies that may be responsible for the observed differences in activity between 1a and Sn-Beta.

4.4.2 Glucose Reaction Pathways

Fig. 4.6 depicts possible routes to fructose and mannose from glucose. A C_2 to C_1 hydride transfer converts glucose into fructose (F1), and a secondary hydride transfer from C_1 to C_2 transforms fructose (F1) to mannose (M1). A 1,2-intramolecular carbon shift directly transforms glucose into mannose (M2). A subsequent hydride transfer also produces fructose (F2). The formation of these products may be distinguished

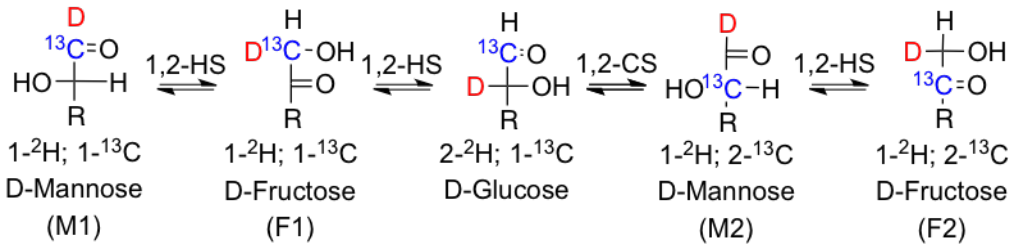

Figure 4.6: Possible reaction pathways involving hydride and carbon shifts at C_1 and C_2. Sugars are depicted using Fischer projections. Abbreviations F1, M1, M2, and F2 indicate location of ^{13}C on first or second carbon of sugar, when C_1 of glucose reactant is labeled. R = $C_4H_9O_4$.

through the use of isotopically labeled starting compounds.

4.4.2.1 ^{13}C- and ^{2}H-labeling experiments

To investigate the reaction pathways promoted by 1a, 10% (w/w) glucose enriched with ^{13}C at the C_1 position (1-^{13}C glucose) or with ^{13}C at the C_1 position and ^{2}H at the C_2 position (2-^{2}H; 1-^{13}C glucose) solutions were reacted for 60 minutes at 373 K in 1:1 DMSO:benzene, maintaining a glucose:Sn molar ratio of 75. ^{13}C spectra (Fig. 4.7) show strong resonances at $\delta = 98.7$ and 94.8, corresponding to the β- and α-glucopyranose starting material labeled with ^{13}C at the C_1 position, respectively. Additionally, both spectra have resonances at $\delta = 74.0$ and 73.5, corresponding to β- and α-mannopyranose labeled with ^{13}C at the C_2 position, respectively (M2 in Fig. 4.6). These results, coupled with the reaction data, suggest that 1a preferentially catalyzes the 1,2-intramolecular carbon shift of glucose to mannose, analogous to the Blik reaction [36].

In addition to the formation of mannose, fructose is produced in lower yields. For the singly labeled 1-^{13}C glucose experiment, two ^{13}C resonances at $\delta = 66.7$ and 65.5 are observed, corresponding to the β and α forms of fructofuranose, respectively. These resonances are not observed in the spectra obtained from 2-^{2}H; 1-^{13}C glucose. This result is likely a consequence of a 1,2-intramolecular hydride shift that negates the

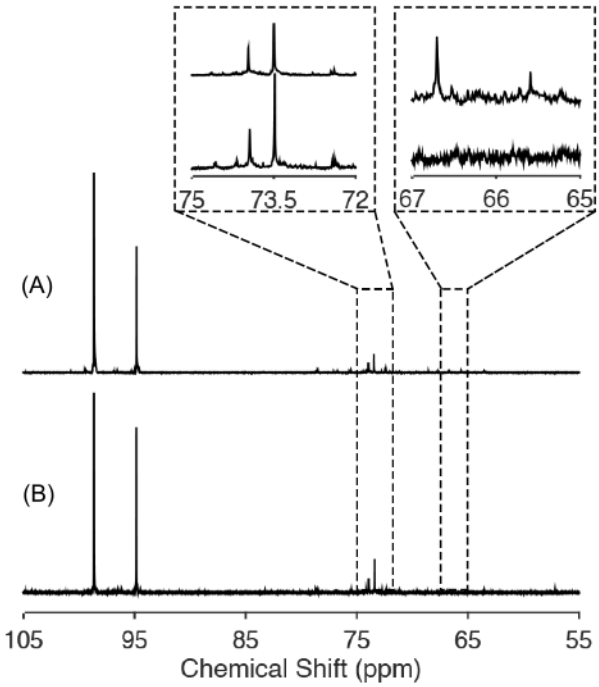

Figure 4.7: ^{13}C NMR spectra for reactant and products with 1a (1:75 Sn/glucose molar ratio) in a 10% (w/w) at 373 K for 60 minutes with: (A) 1-^{13}C glucose and (B) 2-^{2}H; 1-^{13}C glucose in a 1:1 DMSO:benzene solvent system.

nuclear Overhauser enhancement (NOE), an effect that amplifies ^{13}C resonances for directly bonded ^{13}C-^{1}H pairs; no such amplification occurs for ^{13}C-^{2}H pairs, resulting in substantial attenuation of the ^{13}C resonances and the subsequent production of triplets from coupling to ^{2}H (spin 1) [37]. The low intensity triplets that would be expected in ^{13}C spectra for ^{13}C-^{2}H pairs are not observable in Figure 6, reflecting the low yield of fructose as a consequence of the kinetic isotope effect. The ^{1}H NMR spectra from the reaction of 2-^{2}H; 1-^{13}C glucose, shown in Fig. 4.8, may also be used to confirm that the 1,2-intramolecular hydride shift is the prevailing fructose-forming mechanism. As discussed by Roman-Leshkov et al., the base-catalyzed conversion of 2-^{2}H glucose to fructose results in scrambling of the deuterons between the glucose and solvent system, resulting in unlabeled glucose exhibiting a peak corresponding to a proton in the C_2 position at $\delta = 3.2$ [38]. The spectra shown in Fig. 4.8 do not demonstrate this behavior, indicating the glucose remains deuterated at the C_2 position, further suggesting that the 1,2-intramolecular hydride shift mechanism occurs. Moreover, this spectrum exhibits no C_1 position mannose proton at $\delta = 5.17$, indicating the deuteron shifts from the C_2 to C_1 position during the intramolecular carbon shift reaction, and that the F1 to M1 hydride shift does not occur in significant yield. In general, the mannose to fructose hydride shift is not detectable under the reaction conditions utilized. These reaction pathways are analogous to what has been observed with Sn-Beta [16, 38].

4.4.3 Identification of the Catalytic Species

Experiments were performed to confirm that the observed catalysis was due solely to 1a, and not a consequence of starting reagents or leached tin species formed by degradation of the catalyst under reaction conditions. Control experiments were performed with 1 exposed to all synthesis procedures, but without the addition of CH_3SnCl_3. In this instance, no glucose conversion was observed. A solution of CH_3SnCl_3 in benzene catalyzed formation of fructose, but in yields lower than that observed with 1a; no mannose formation was observed.

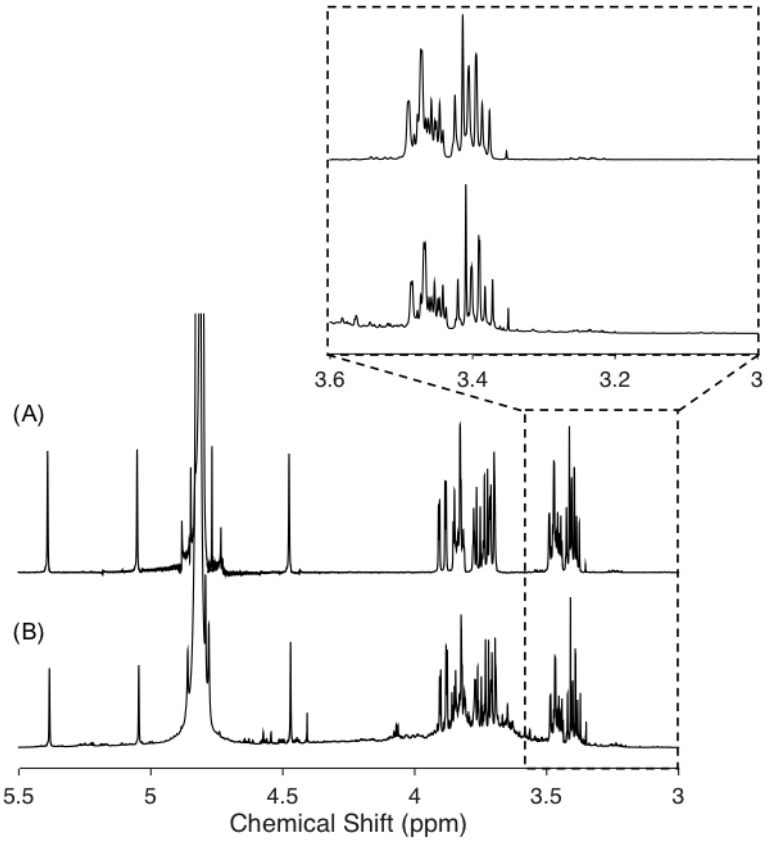

Figure 4.8: ^{1}H NMR spectra for: (A) unreacted 2-^{2}H; 1-^{13}C glucose, and (B) reactant and products with 1a (1:75 Sn/glucose molar ratio) in a 10% (w/w) at 373 K for 60 minutes with 2-^{2}H; 1-^{13}C glucose in a 1:1 DMSO:benzene solvent system.

To examine the structural integrity of 1a post reaction, the catalyst was separated from a reaction performed at 393 K for 1 hour, utilizing the same parameters and procedures outlined previously. These conditions were chosen to ensure a large excess of glucose relative to 1a, so that statistically all Lewis acid sites should participate in the catalysis. In order to separate the catalyst from the crude reaction solution, an excess of hexane was added to the mixture while the reaction vessel was maintained at 393 K. This resulted in the formation of an immiscible two-phase system, consisting of the dense polar DMSO phase containing the carbohydrates and the less dense non-polar catalyst-containing phase. The two phases were separated, and the hexane solution was allowed to cool, then washed with an excess of acetonitrile. The hexane phase was again separated, the volatiles were removed, and the resultant white powder was dried under vacuum for 12 hours. NMR analysis of this material (Appendix C: Figures S.4-S.7) is in very good agreement with spectra obtained of the material prior to reaction, and data presented in the literature [27]. Taken together, these results suggest that the structure of 1a likely remains intact over the course of the reaction, and is the origin of the catalytically active species.

4.4.3.1 Computational Chemistry

For Sn-Beta, the open site has been postulated to be the active catalytic site, whereby a stannanol group facilitates the initial binding step of the glucose molecule to the Lewis acid site [15, 23, 24, 38]. This reaction mechanism is not possible for 1a, however, due to the absence of the stannanol. In order for 1a to catalyze the conversion of glucose, we hypothesize that the Sn-O-Si bridging bonds must be involved to allow the glucose C_1 hydroxy proton to transfer to one of the three Si-O-Sn bridging bonds, analogous to pathways proposed by Li et al. [22] and Yang et al. [23] In a very recent study, Beletskiy et al. provide evidence that this type of proton shift may occur for 2-propanol (adsorbed as 2-propoxide) on silica-immobilized tin silsesquioxane complexes [39]. Similar lattice protonation mechanisms have been proposed for metal-containing zeolites [17, 40]. This proton transfer results in the formation of an adjacent silanol

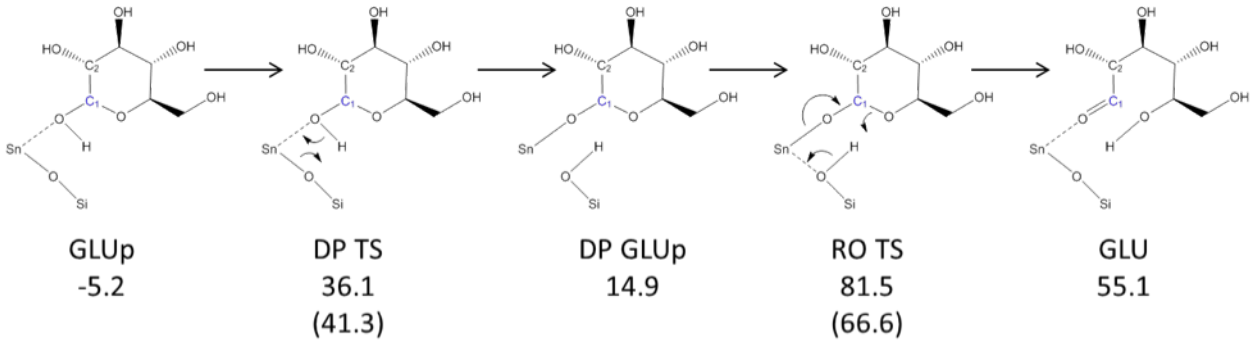

Figure 4.9: Glucose ring-opening mechanism. Gas-phase free energies (in kJ-mol^{-1}) at 373 K for intermediates and transition states are reported relative to isolated glucose and catalyst. Intrinsic barriers reported in parentheses. GLUp: glucopyranose; DP: deprotonation; RO: ring opening; GLU: open-chain glucose.

group to the tin site, as well as glucose bound to the tin site. In situ NMR spectroscopy characterization was attempted by exposing the catalyst to reaction conditions and collecting spectra at 373 K; unfortunately, no evidence for proton transfer to one of the Sn-O-Si bond was obtained. In order to garner further insight into the glucose reaction mechanisms for 1a, a theoretical approach was taken.

Fig. 4.9 depicts the previously described proposed glucose ring-opening mechanism on 1a and compares the relative gas-phase free energies. The calculations estimate that deprotonation and ring-opening are endothermic, with intrinsic free energy barriers of 41.3 and 66.6 kJ-mol^{-1}, respectively. Bermejo-Deval et al. [15] report an activation energy of 37.3 kJ-mol^{-1} for ring-opening at an open site. Work by Yang et al. [23] also suggests that the initial glucose deprotonation step at the open site is thermodynamically more stable than at the closed site. These data suggest that binding to and performing ring opening at a site without a hydroxyl moiety present (as with 1a and the closed site in Sn-Beta) is less favorable. As considered by Li et al. [22], this variation and subsequent difference in energies is likely a function of geometric distortion and deviations in Lewis acidity between the two sites.

After ring-opening, hydride transfer or Blik reactions convert glucose into fructose or mannose, respectively. Generally, there are three possible pathways in converting glucose, which we categorize as "O_1 Binding," "O_2 Binding," and "Bidentate," identified according to whether the open glucose binds to the Sn Lewis acid site via the O_1 position, O_2 position, or both during the reaction. The mechanistic details and energetics of these pathways are compared in Fig. 4.10 and 4.11.

The bidentate mechanism involves: 1) coordination of both O_1 and O_2 to the Sn center in an octahedral geometry, 2) deprotonation, forming a silanol and binding O_2 to the Sn, 3) a H/C-shift with a chelate-like transition state, and 4) reprotonation in sequential steps. For both isomerization and epimerization, the bidentate pathway is predicted to be the most favorable, with intrinsic free energy barriers of 79.6 kJ-mol^{-1} and 101.0 kJ-mol^{-1}, respectively.

The O_1 binding pathway begins by coordination of the aldehyde oxygen to the Sn, maintaining a hydrogen bonding interaction between O_2 and the Sn-O-Si bridge. The first step binds O_1 to the Sn during a concerted deprotonation of O_2 alongside the H/C-shift. Intrinsic barriers for the H/C-shift are 115.5 kJ-mol^{-1} and 110.9 kJ-mol^{-1}, respectively. Reprotonation of O_1 follows in a subsequent step.

The O_2 binding pathway starts with a deprotonation forming a silanol and binding O_2 to the Sn. This deprotonation is endothermic, with an intrinsic barrier of 50 kJ-mol^{-1} and a free energy of reaction of 26.9 kJ-mol^{-1}. O_1 then forms a hydrogen bond with the silanol formed in situ, which subsequently reprotonates the sugar during the concerted H/C-shift reaction. Intrinsic barriers for the H/C-shift are 61.1 kJ-mol^{-1} and 93.5 kJ-mol^{-1}, respectively.

To our knowledge, this is the first time a systematic approach has been considered for glucose isomerization and epimerization reaction mechanisms, which frequently consider only the bidentate [15, 23–25, 41, 42], O_1 binding [15], or O_2 binding [23–25, 42].

To finish the catalytic cycle, the ring closing reactions of deprotonated fructose, open fructose, and open mannose were examined. Deprotonated open fructose

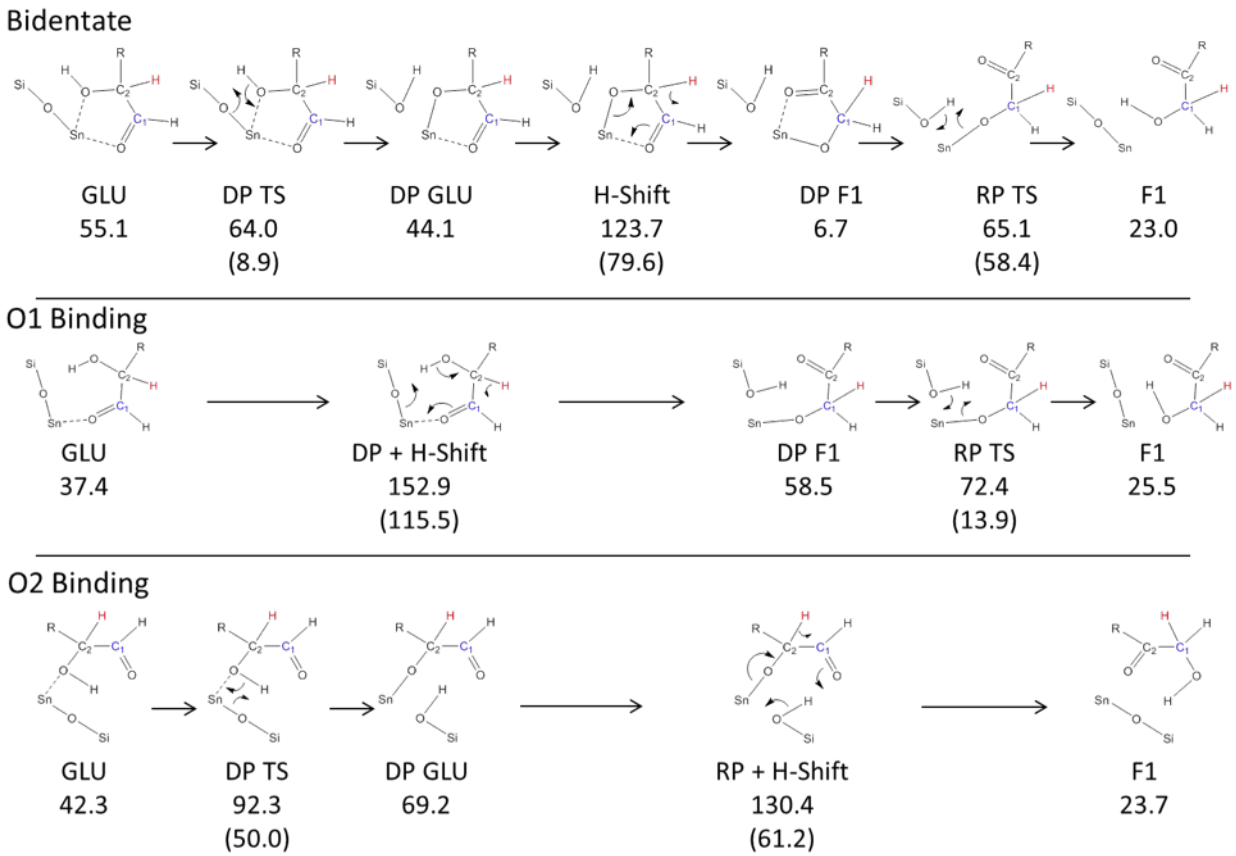

Figure 4.10: H-Shift Pathways. Three pathways are shown for transforming open-chain glucose (GLU) into open-chain fructose (F1), via deprotonation (DP), reprotonation (RP), and H-shift reactions. The bidentate transition state gives the lowest barrier for reaction, with a slightly more stable transition state than the O_2 binding pathway. Gas-phase free energies (in kJ-mol^{-1}) at 373 K for intermediates and transition states are reported relative to isolated glucose and catalyst, with intrinsic barriers reported in parentheses.

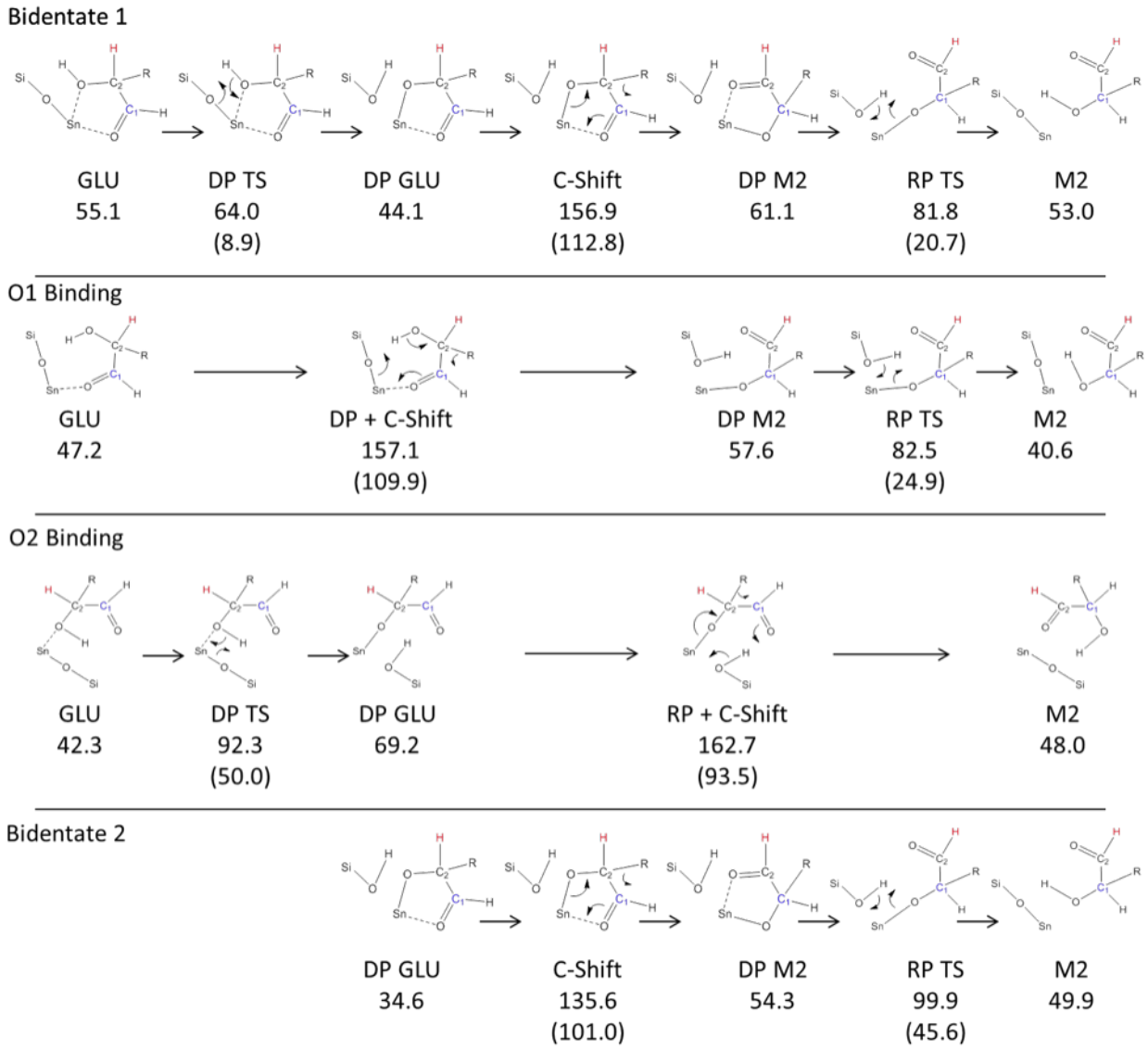

Figure 4.11: C-Shift Pathways. Open-chain glucose (GLU) transforms directly into open-chain mannose (M2) through deprotonation (DP), reprotonation (RP), and C-shift reactions. Four pathways are shown: three starting from the initial geometries of the H-shift reactions (bidentate, O_1 binding, and O_2 binding) and an additional bidentate pathway starting from a different geometry to facilitate O_3 hydroxyl interaction with 1a. Gas-phase free energies (in kJ-mol^{-1}) at 373 K for intermediates and transition states are reported relative to isolated glucose and catalyst, with intrinsic barriers reported in parentheses.

ring-closes to produce O_1-deprotonated fructofuranose. A slightly different pathway for open fructose ring closing produces O_2-deprotonated fructofuranose. Subsequent reprotonation regenerates the catalyst and produces fructofuranose. Similarly, open mannose ring-closes to form O_1-deprotonated mannopyranose, and subsequent reprotonation regenerates the catalyst and produces mannopyranose. These pathways have relatively low barriers compared to H/C-shift reactions, and their details are in Appendix C. Also included in Appendix C are the bidentate, O_1 binding, and O_2 binding pathways for interconverting fructose and mannose (F1 to M1), which have higher barriers than the competing fructose ring-closing pathways. Products M1 and F2 are not observed because ring-closing is facile relative to additional H/C-shift reactions.

We analyzed the selectivity trends using the energy span model [43] (see Supporting Information). The gas-phase transition state free energies for the mannose (135.6 kJ-mol^{-1}) and fructose (123.7 kJ-mol^{-1}) pathways slightly favor fructose as the major product. In experiment, the difference in apparent activation energy is 8.2 kJ-mol^{-1} in favor of mannose production – a difference too small to be expected to be resolved by QM/MM calculations which do not take into account the complex solvation environment of the experiments.

4.4.3.2 Electronic structure analysis of the H/C-shift reactions

The character of the H/C-shift reactions was also analyzed according to the Natural Bond Orbital (NBO) method (see Tables S.3 – S.8). In general, four overall mechanisms govern a hydride transfer: (a) electron-proton-electron pathway (e^- – H^+ – e^-); (b) electron-hydrogen atom transfer; (c) hydrogen atom-electron transfer; and (d) one-step hydride ion transfer [44]. Choudhary et al. analyzed the hydride transfer in the bidentate mechanism for xylose to xylulose on the Sn-Beta zeolite [41]. They proposed that the H-shift mechanism involves the rate-limiting transfer of a neutral hydrogen atom from C_2 to C_1, concerted with a rapid electron transfer from O_2 to O_1. Following a similar methodology, we conclude that the bidentate mechanism for the H-shift on 1a follows the same mechanism: a neutral hydrogen atom transfers from C_2

to C_1 concertedly with an adiabatic electron transfer from O_2 to O_1, facilitated by a C_2—O_2 and C_1—O_1 anti-bonding π system at the transition state. The O_1-binding H-shift is a test case for observing the H-shift reaction without the prior deprotonation of O_2. Without deprotonation prior to the hydride transfer, the H—C_2 bond is less polarized and thus charge separation comes at a higher energy cost. Comparison with the bidentate pathway shows how the sugar deprotonation step activates the C_2 donor fragment for the subsequent H-shift. The electronic structure of the bidentate C-shift was also analyzed. The results demonstrate that this pathway's electronic composition is remarkably analogous to that of the H-shift, including the C_2—O_2 and C_1—O_1 π system for transferring an electron and a neutral C_3 fragment as a transferring group. A detailed analysis may be found in Appendix C.

4.5 Conclusions

We have synthesized and tested methyl-ligated tin silsesquioxane as a catalyst for glucose reactivity to examine the activity and structure of tin species that are analogous to the closed tin site in Sn-Beta. The catalytic nature of 1a suggests that there are glucose conversion pathways that involve the breaking of the Si-O-Sn linkage at some point in the reaction cycle and that such pathways may be possible from the closed sites in Sn-Beta. We have not conclusively proven this point here, and since the bond angles in 1a are significantly different from Sn-Beta, these pathways may not occur in the latter. However, if they do, they participate in catalyzing the reaction of glucose at a rate significantly slower than the open site. Isotopic labeling experiments demonstrate that these reactions occur via 1,2-intramolecular carbon and hydrogen shift pathways for mannose and fructose, respectively, yielding products that are indistinguishable from those obtained by catalysis at the open site. The full catalytic cycle has been theoretically investigated considering three distinct pathways for the hydride- and carbon-shift reaction reactions. It has been calculated that the most favorable pathway to produce both fructose and mannose over 1a is by glucose binding

bidentately to the tin center, deprotonation to one of the Sn-O-Si bridges, and performing either a hydride- or carbon-shift reaction. We propose that a similar mechanism occurs at the closed site in Sn-Beta.

4.6 Acknowledgements

Research was supported as part of the Catalysis Center for Energy Innovation, an Energy Frontier Research Center funded by the U.S. Department of Energy (DOE), Office of Science, Basic Energy Sciences (BES), under Award number DE-SC0001004. S.K.B. wishes to acknowledge funding from the National Science Foundation Graduate Research Fellowship Program under Grant No. DGE-1144469. T.R.J. also wishes to acknowledge funding from the National Science Foundation Graduate Research Fellowship Program under Grant No. 0750966, as well as the George W. Laird Merit Fellowship. Any opinions, findings, and conclusions or recommendations expressed in this material are those of the author(s) and do not necessarily reflect the views of the National Science Foundation. The authors would like to thank Marat Orazov and Jeff Christianson for numerous useful conversations.

REFERENCES

[1] S. K. Brand, T. R. Josephson, J. A. Labinger, S. Caratzoulas, D. G. Vlachos, and M. E. Davis. Methyl-Ligated Tin Silsesquioxane Catalyzed Reactions of Glucose. *Journal of Catalysis*, 341:62–71, 2016.

[2] Y. Román-Leshkov and M. E. Davis. Activation of Carbonyl-Containing Molecules with Solid Lewis Acids in Aqueous Media. *ACS Catalysis*, 1(11):1566–1580, 2011. ISSN 21555435. doi: 10.1021/cs200411d.

[3] M. Moliner. State of the art of Lewis acid-containing zeolites: lessons from fine chemistry to new biomass transformation processes. *Dalton Transactions*, 43: 4197–208, 2014. ISSN 1477-9234. doi: 10.1039/c3dt52293h.

[4] A. Corma and H. Garc. Lewis Acids as Catalysts in Oxidation Reactions : From Homogeneous to Heterogeneous Systems. *Chemical Reviews*, 102:3837–92, 2002. ISSN 0009-2665. doi: 10.102/cr010333.

[5] J. C. Serrano-Ruiz and J. A. Dumesic. Catalytic routes for the conversion of biomass into liquid hydrocarbon transportation fuels. *Energy & Environmental Science*, 4:83, 2011. ISSN 1754-5692. doi: 10.1039/c0ee00436g.

[6] D. M. Alonso, J. Q. Bond, and J. A. Dumesic. Catalytic conversion of biomass to biofuels. *Green Chemistry*, 12:1493, 2010. ISSN 1463-9262. doi: 10.1039/c004654j.

[7] A. J. Ragauskas, C. K. Williams, B. H. Davison, G. Britovsek, J. Cairney, C. A. Eckert, W. J. Frederick Jr., J. P. Hallett, D. J. Leak, C. L. Liotta, J. R. Mielenz, R. Murphy, R. Templer, and T. Tschaplinski. The path forward for biofuels and

biomaterials. *Science (New York, N.Y.)*, 311(5760):484–9, 2006. ISSN 1095-9203. doi: 10.1126/science.1114736.

[8] M. Moliner, Y. Roman-Leshkov, M. E. E. Davis, Y. Román-Leshkov, and M. E. E. Davis. Tin-containing zeolites are highly active catalysts for the isomerization of glucose in water. *Proc Natl Acad Sci U S A*, 107(14):6164–6168, 2010. ISSN 1091-6490. doi: 10.1073/pnas.1002358107.

[9] A. Corma and S. Valencia. (UOP LLC.) US Patent 5,968,463. 1999.

[10] A. Corma, L. T. Nemeth, M. Renz, and S. Valencia. Sn-zeolite beta as a heterogeneous chemoselective catalyst for Baeyer-Villiger oxidations. *Nature*, 412(6845): 423–425, 2001. ISSN 0028-0836. doi: 10.1038/35086546.

[11] M. Renz, T. Blasco, A. Corma, V. Fornés, R. Jensen, and L. Nemeth. Selective and shape-selective Baeyer-Villiger oxidations of aromatic aldehydes and cyclic ketones with Sn-beta zeolites and H2O2. *Chemistry*, 8(20):4708–17, 2002. ISSN 0947-6539. doi: 10.1002/1521-3765(20021018)8:20⟨4708::AID-CHEM4708⟩3.0.CO;2-U.

[12] A. Corma, M. E. Domine, and S. Valencia. Water-resistant solid Lewis acid catalysts: Meerwein-Ponndorf-Verley and Oppenauer reactions catalyzed by tin-beta zeolite. *Journal of Catalysis*, 215:294–304, 2003. ISSN 00219517. doi: 10.1016/S0021-9517(03)00014-9.

[13] A. Corma, M. E. Domine, L. Nemeth, and S. Valencia. Al-free Sn-Beta zeolite as a catalyst for the selective reduction of carbonyl compounds (Meerwein-Ponndorf-Verley Reaction). *Journal of the American Chemical Society*, 124:3194–3195, 2002. ISSN 00027863. doi: 10.1021/ja012297m.

[14] R. Bermejo-Deval, R. Gounder, and M. E. Davis. Framework and extraframework tin sites in zeolite beta react glucose differently. *ACS Catalysis*, 2(12):2705–2713, 2012. ISSN 21555435. doi: 10.1021/cs300474x.

[15] R. Bermejo-Deval, R. S. S. Assary, E. Nikolla, M. Moliner, Y. Roman-Leshkov, S.-J. S.-J. Hwang, A. Palsdottir, D. Silverman, R. F. Lobo, L. A. Curtiss, and M. E. Davis. Metalloenzyme-like catalyzed isomerizations of sugars by Lewis acid zeolites. *Proceedings of the National Academy of Sciences*, 109(25):9727–9732, 2012. ISSN 0027-8424. doi: 10.1073/pnas.1206708109.

[16] R. Bermejo-Deval, M. Orazov, R. Gounder, S. J. Hwang, and M. E. Davis. Active sites in Sn-beta for glucose isomerization to fructose and epimerization to mannose. *ACS Catalysis*, 4(7):2288–2297, 2014. ISSN 21555435. doi: 10.1021/cs500466j.

[17] S. V. D. Vyver, C. Odermatt, K. Romero, T. Prasomsri, and Y. Román-Leshkov. Solid Lewis Acids Catalyze the Carbon Carbon Coupling between Carbohydrates and Formaldehyde. *ACS Catalysis*, 5:972–977, 2015. doi: 10.1021/cs5015964.

[18] A. Corma and M. Renz. Sn-Beta zeolite as diastereoselective water-resistant heterogeneous Lewis-acid catalyst for carbon-carbon bond formation in the intramolecular carbonyl-ene reaction. *Chemical communications (Cambridge, England)*, pages 550–551, 2004. ISSN 1359-7345. doi: 10.1039/b313738d.

[19] J. J. Pacheco and M. E. Davis. Synthesis of terephthalic acid via Diels-Alder reactions with ethylene and oxidized variants of 5-hydroxymethylfurfural. *Proceedings of the National Academy of Sciences of the United States of America*, 111(15): 8363–7, 2014. ISSN 1091-6490. doi: 10.1073/pnas.1408345111.

[20] M. Boronat, P. Concepción, A. Corma, M. Renz, and S. Valencia. Determination of the catalytically active oxidation Lewis acid sites in Sn-beta zeolites, and their optimisation by the combination of theoretical and experimental studies. *Journal of Catalysis*, 234(1):111–118, 2005. ISSN 00219517. doi: 10.1016/j.jcat.2005.05.023.

[21] J. W. Harris, M. J. Cordon, J. R. Di Iorio, J. C. Vega-Vila, F. H. Ribeiro, and R. Gounder. Titration and quantification of open and closed Lewis acid sites in

Sn-Beta zeolites that catalyze glucose isomerization. *Journal of Catalysis*, 335: 141–154, 2016. ISSN 00219517. doi: 10.1016/j.jcat.2015.12.024.

[22] Y. P. P. Li, M. Head-Gordon, and A. T. T. Bell. Analysis of the reaction mechanism and catalytic activity of metal-substituted beta zeolite for the isomerization of glucose to fructose. *ACS Catalysis*, 4(5):1537–1545, 2014. ISSN 21555435. doi: 10.1021/cs401054f.

[23] G. Yang, E. A. Pidko, and E. J. M. Hensen. The mechanism of glucose isomerization to fructose over Sn-BEA zeolite: A periodic density functional theory study. *ChemSusChem*, 6(9):1688–1696, 2013. ISSN 18645631. doi: 10.1002/cssc.201300342.

[24] N. Rai, S. Caratzoulas, and D. G. Vlachos. Role of silanol group in Sn-beta zeolite for glucose isomerization and epimerization reactions. *ACS Catalysis*, 3 (10):2294–2298, 2013. ISSN 21555435. doi: 10.1021/cs400476n.

[25] J. R. Christianson, S. Caratzoulas, and D. G. Vlachos. Computational Insight into the Effect of Sn-Beta Na Exchange and Solvent on Glucose Isomerization and Epimerization. *ACS Catalysis*, 5(9):5256–5263, 2015. ISSN 2155-5435. doi: 10.1021/acscatal.5b01258.

[26] S. K. Brand, J. A. Labinger, and M. E. Davis. Tin Silsesquioxanes as Models for the "Open" Site in Tin-Containing Zeolite Beta. *ChemCatChem*, 8(1):121–124, 2016. ISSN 18673899. doi: 10.1002/cctc.201501067.

[27] F. J. Feher, D. A. Newman, and J. F. Walzer. Silsesquioxanes as models for silica surfaces. *Journal of the American Chemical Society*, 111(5):1741–1748, 1989. ISSN 0002-7863. doi: 10.1021/ja00187a028.

[28] C. Liu, J. M. Carraher, J. L. Swedberg, C. R. Herndon, C. N. Fleitman, and J.-P. Tessonnier. Selective Base-Catalyzed Isomerization of Glucose to Fructose. *ACS Catalysis*, 4:4295–4298, 2014. ISSN 2155-5435. doi: 10.1021/cs501197w.

[29] T. Vreven, K. S. Byun, I. Komaromi, S. Dapprich, J. A. Montgomery Jr., K. Morokuma, and M. J. Frisch. Combining Quantum Mechanics Methods with Molecular Mechanics Methods in ONIOM. *Journal of Chemical Theory and Computation*, 2(3):815–826, 2006. ISSN 1549-9618. doi: 10.1021/ct050289g.

[30] S. Dapprich, I. Komáromi, K. S. Byun, K. Morokuma, and M. J. Frisch. A new ONIOM implementation in Gaussian98. Part I. The calculation of energies, gradients, vibrational frequencies and electric field derivatives. *Journal of Molecular Structure: THEOCHEM*, 461-462:1–21, 1999. ISSN 01661280. doi: 10.1016/S0166-1280(98)00475-8.

[31] Y. Zhao and D. G. Truhlar. The M06 suite of density functionals for main group thermochemistry, thermochemical kinetics, noncovalent interactions, excited states, and transition elements: Two new functionals and systematic testing of four M06-class functionals and 12 other function. *Theoretical Chemistry Accounts*, 120(1-3):215–241, 2008. ISSN 1432881X. doi: 10.1007/s00214-007-0310-x.

[32] W. R. Wadt and P. J. Hay. Ab initio effective core potentials for molecular calculations. Potentials for main group elements Na to Bi. *The Journal of Chemical Physics*, 82(1):284–298, 1985. ISSN 00219606. doi: 10.1063/1.448799.

[33] M. J. Frisch, G. W. Trucks, H. B. Schlegel, G. E. Scuseria, M. A. Robb, J. R. Cheeseman, G. Scalmani, V. Barone, B. Mennucci, G. A. Petersson, H. Nakatsuji, M. Caricato, X. Li, H. P. Hratchian, A. F. Izmaylov, J. Bloino, G. Zheng, J. L. Sonnenberg, M. Hada, M. Ehara, K. Toyota, R. Fukuda, J. Hasegawa, M. Ishida, T. Nakajima, Y. Honda, O. Kitao, H. Nakai, T. Vreven, J. A. Montgomery Jr., J. E. Peralta, F. Ogliaro, M. J. Bearpark, J. Heyd, E. N. Brothers, K. N. Kudin, V. N. Staroverov, R. Kobayashi, J. Normand, K. Raghavachari, A. P. Rendell, J. C. Burant, S. S. Iyengar, J. Tomasi, M. Cossi, N. Rega, N. J. Millam, M. Klene, J. E. Knox, J. B. Cross, V. Bakken, C. Adamo, J. Jaramillo, R. Gomperts, R. E. Stratmann, O. Yazyev, A. J. Austin, R. Cammi, C. Pomelli, J. W. Ochterski,

R. L. Martin, K. Morokuma, V. G. Zakrzewski, G. A. Voth, P. Salvador, J. J. Dannenberg, S. Dapprich, A. D. Daniels, Ö. Farkas, J. B. Foresman, J. V. Ortiz, J. Cioslowski, and D. J. Fox. Gaussian 09, 2009.

[34] M. S. Holm, S. Saravanamurugan, and E. Taarning. Conversion of sugars to lactic acid derivatives using heterogeneous zeotype catalysts. *Science (New York, N.Y.)*, 328(5978):602–605, 2010. ISSN 0036-8075. doi: 10.1126/science.1183990.

[35] M. Orazov and M. E. Davis. Tandem catalysis for the production of alkyl lactates from ketohexoses at moderate temperatures. *Proceedings of the National Academy of Sciences*, 112(38):201516466, 2015. ISSN 0027-8424. doi: 10.1073/pnas.1516466112.

[36] M. L. Hayes, N. J. Pennings, A. S. Serianni, and R. Barker. Epimerization of aldoses by molybdate involving a novel rearrangement of the carbon skeleton. *Journal of the American Chemical Society*, 104(24):6764–6769, 1982. ISSN 0002-7863. doi: 10.1021/ja00388a047.

[37] D. Neuhaus and W. M. P. *The nuclear Overhauser effect in structural and conformational analysis*. 1989. ISBN 0-89573-343-9; 3-527-26639-9.

[38] Y. Román-Leshkov, M. Moliner, J. A. Labinger, and M. E. Davis. Mechanism of glucose isomerization using a solid lewis acid catalyst in water. *Angewandte Chemie - International Edition*, 49(47):8954–8957, 2010. ISSN 14337851. doi: 10.1002/anie.201004689.

[39] E. V. Beletskiy, X. Hou, Z. Shen, J. R. Gallagher, J. T. Miller, Y. Wu, T. Li, M. C. Kung, and H. H. Kung. Supported Tetrahedral Oxo-Sn Catalyst: Single Site, Two Modes of Catalysis. *Journal of the American Chemical Society*, 138(13): 4294–4297, 2016. ISSN 15205126. doi: 10.1021/jacs.5b13436.

[40] J. D. Lewis, S. Van De Vyver, and Y. Román-Leshkov. Acid-Base Pairs in Lewis Acidic Zeolites Promote Direct Aldol Reactions by Soft Enolization. *Angewandte*

Chemie - International Edition, 54(34):9835–9838, 2015. ISSN 15213773. doi: 10.1002/anie.201502939.

[41] V. Choudhary, S. H. Mushrif, C. Ho, A. Anderko, V. Nikolakis, N. S. Marinkovic, A. I. Frenkel, S. I. Sandler, and D. G. Vlachos. Insights into the interplay of Lewis and Brønsted acid catalysts in glucose and fructose conversion to 5-(hydroxymethyl)furfural and levulinic acid in aqueous media. *Journal of the American Chemical Society*, 135(10):3997–4006, 2013. ISSN 00027863. doi: 10.1021/ja3122763.

[42] R. S. Assary and L. A. Curtiss. Theoretical study of 1,2-hydride shift associated with the isomerization of glyceraldehyde to dihydroxy acetone by Lewis acid active site models. *Journal of Physical Chemistry A*, 115(31):8754–8760, 2011. ISSN 10895639. doi: 10.1021/jp204371g.

[43] S. Kozuch. Steady State Kinetics of Any Catalytic Network: Graph Theory, the Energy Span Model, the Analogy between Catalysis and Electrical Circuits, and the Meaning of Mechanism. *ACS Catalysis*, 5(9):5242–5255, 2015. ISSN 2155-5435. doi: 10.1021/acscatal.5b00694.

[44] O. Tapia, J. Andres, J. M. Aullo, and C.-I. Branden. Electronic aspects of the hydride transfer mechanism. Ab initio analytical gradient studies of the cyclopropenyl-cation/lithium hydride model reactant system. *The Journal of Chemical Physics*, 83(9):4673, 1985. ISSN 00219606. doi: 10.1063/1.449039.

Chapter 5

1,2-H VERSUS 1,2-C-SHIFT ON SN-SILSESQUIOXANES

5.1 Abstract

Lewis-acidic zeolites such as Sn-Beta catalyze glucose isomerization to fructose via an intramolecular 1,2-H-shift reaction, a key step for converting lignocellulosic biomass into renewable chemicals. Na-exchange of Sn-Beta titrates the neighboring SiOH group in the open Sn site, and shifts catalyst selectivity to mannose formed by a 1,2-C-shift reaction. To probe structure/activity relationships in the zeolite, tin-containing silsesquioxanes with (1a) and without (1b) a neighboring SiOH group were recently synthesized and tested. These molecular catalysts are active for glucose conversion, and the presence (absence) of the SiOH favors fructose (mannose) selectivity by intramolecular H(C)-shift reactions. Using density functional theory, we investigated numerous H/C-shift pathways on these tin-silsesquioxane catalysts. On both 1a and 1b, the H-shift reaction occurs through a bidentate binding mode without participation of the SiOH, while the bidentate binding mode is not favored for the C-shift due to steric hindrance. Instead, the C-shift reaction occurs through different concerted reaction pathways, in which an acetylacetonate (acac) ligand interacts with the substrate in the transition state complexes. Favorable H-shift pathways without SiOH participation and acac ligand promotion of the C-shift pathway explain why 1a produces mannose from C-shift reactions instead of exclusively catalyzing H-shift reactions, as the Sn-Beta open site does.

5.2 Introduction

Utilization of lignocellulosic biomass as a renewable chemical feedstock is a promising path to a more sustainable chemical industry [2–6]. Lewis-acidic zeolites, Sn-Beta in particular, have emerged as useful catalysts for a wide range of transformations in biomass conversion, including Baeyer-Villiger oxidation of ketones to lactones [7], the Meerwein-Ponndorf-Verley (MPV) reduction of carbonyls [8], the 1,2-H-shift of glucose [9] and xylose [10], retro-aldol and esterification of sugars to lactates [11], the 1,2-carbon shift of glucose [12] and arabinose [13], and dehydration reactions in the production of renewable aromatics from furans [14].

The isomerization of glucose to fructose is of particular interest due to the abundance of cellulose as a glucose feedstock and the value of fructose for production of 5-hydroxymethylfurfural (HMF) [15] and lactic acid [16, 17]. ^{119}Sn NMR [12] and acetonitrile adsorption and spectroscopy [18] have identified two types of Sn sites in Sn-Beta: a "closed" framework Sn site, $Sn(OSi)_4$, and a hydrolyzed "open" site, $Sn(OSi)_3OH$ with a neighboring SiOH. Open sites are stronger Lewis acids than closed sites [18–20] and more active for glucose isomerization [19, 20]. Fig.5.1 shows a reaction scheme for different glucose transformation reactions catalyzed by Sn-Beta. Sn-Beta selectively produces fructose F1 via a 1,2-H-shift reaction from glucose, and mannose M1 as a side product via a subsequent 1,2-H-shift reaction from fructose [19]. Modification of the open site by Na+ titration [19] or with borate salts [13] shifts selectivity from fructose to mannose, but this mannose is produced via a 1,2-C-shift (M2), or Bilik reaction [21]. Moreover, different synthesis methods produce catalysts with different ratios of open and closed sites [18, 20]. Understanding these structure-activity and structure-selectivity relationships is important for optimizing Sn-Beta synthesis and deployment in future biorefineries.

Beginning with Assary and Curtiss' examination of glyceraldehyde isomerization to dihydroxyacetone on open and closed sites of Sn-Beta[22], several computational studies have investigated the glucose isomerization mechanism on the Sn-Beta zeolite [23–28]. These have found that the open site is more active than the closed site,

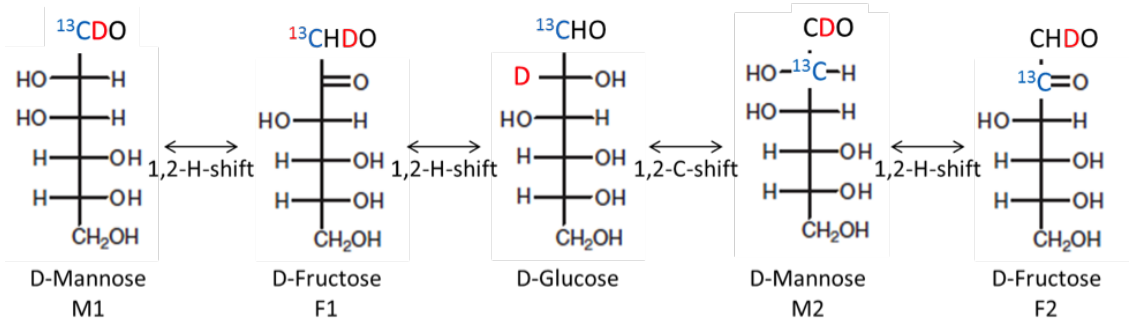

Figure 5.1: Glucose transformation products via 1,2-H-shift and 1,2-C-shift reactions. Experiments with ^{13}C- and D-labeled glucose enable distinction of mannose and fructose from different pathways.

whether examined as a 5T (five tetrahedral atoms) cluster [22, 24], or an extended 208T QM/MM model [27], implicating the stronger Brønsted basicity of SnOH relative to SnOSi [27]. However, a study using periodic DFT found little difference between closed and open sites [25]. Using a 9T open site cluster, Rai et al. found that glucose in a bidentate coordination to the Sn favored a C-shift reaction, while glucose coordinated to the Sn and neighboring SiOH favored the H-shift reaction, suggesting the neighboring SiOH enabling fructose selectivity by participating in a concerted reaction [26]. However, a more complete analysis of this 9T cluster [28] with and without Na-exchange identified a more favorable bidentate binding geometry that favored the H-shift without SiOH participation, instead finding that Na^+ provides electrostatic stabilization of the C-shift TS more than the H-shift TS. A larger, less flexible zeolite cluster favored a concerted, rather than bidentate, mechanism for both Sn-Beta and Na-Sn-Beta, and observed the same electrostatic effect on the H/C-shift transition states.

These studies highlight several challenges associated with modeling Sn-Beta. In addition, there is no experimental consensus for the crystallographic location of the Sn atom. Consequently, computational studies have used either the T2 substitution [25, 27], as it is most thermodynamically stable closed site [29], or the T9 substitution

[26, 28, 30], in agreement with acetonitrile adsorption and spectroscopic evidence [18, 31]. The T5/T6 sites exhibited similar agreement with acetonitrile adsorption [18], and have also been proposed on account of EXAFS experiments [32], but haven't been examined computationally.

Silsesquioxanes have been useful for reducing the heterogeneous-homogeneous gap in catalysis by providing single-site molecular analogues for evaluating structure-property relationships [33]. Recently, several Sn silsesquioxanes have been synthesized and tested to evaluate the active sites in Sn-Beta [34–37]. Beletskiy et al., synthesized a tetrahedral Sn-silsesquioxane [35], grafted it onto silica [34], and demonstrated its activity for epoxide ring-opening and MPV reduction, comparable to Sn-Beta. This catalyst was also active for glucose isomerization to fructose, but formed significant side products, possibly due to surface silanol groups. Brand et al. have synthesized and tested three tin silsesquioxanes [36, 37] (Fig. 5.2)with structural differences designed to model the open (1a), Na-exchanged (1b), and closed (2) sites in Sn-Beta. All catalysts are active for glucose isomerization and epimerization. Analysis of initial rate data for these three tin silsesquioxanes and Sn-Beta, Na-Sn-Beta, and NH_3-Sn-Beta reveals several structure-property correlations among the catalysts [37]. Sn-Beta and 1a are most active, and selective towards fructose (although mannose formed from Sn-Beta is from a 2,1-H-shift from fructose, while 1a forms mannose through the 1,2-C-shift of glucose). Na-Sn-Beta and 1b, each of which have had the neighboring SiOH replaced, showed reduced activity in glucose conversion and a shift in product selectivity to mannose formed by 1,2-C-shift of glucose, implicating the SiOH as an important feature for promoting selectivity to fructose. NH_3-Sn-Beta, CH_3-Sn-Beta, and 2 exhibited an order of magnitude reduction in activity relative to Sn-Beta, with mannose as major product, providing evidence for some residual activity on closed Sn sites. Taken together, these silsesquioxane experiments have decoupled the functions of the open, closed, and Na-exchanged sites, which cannot be done explicitly in the heterogeneous case due to challenges in synthesizing zeolites with exclusively one kind of Sn site.

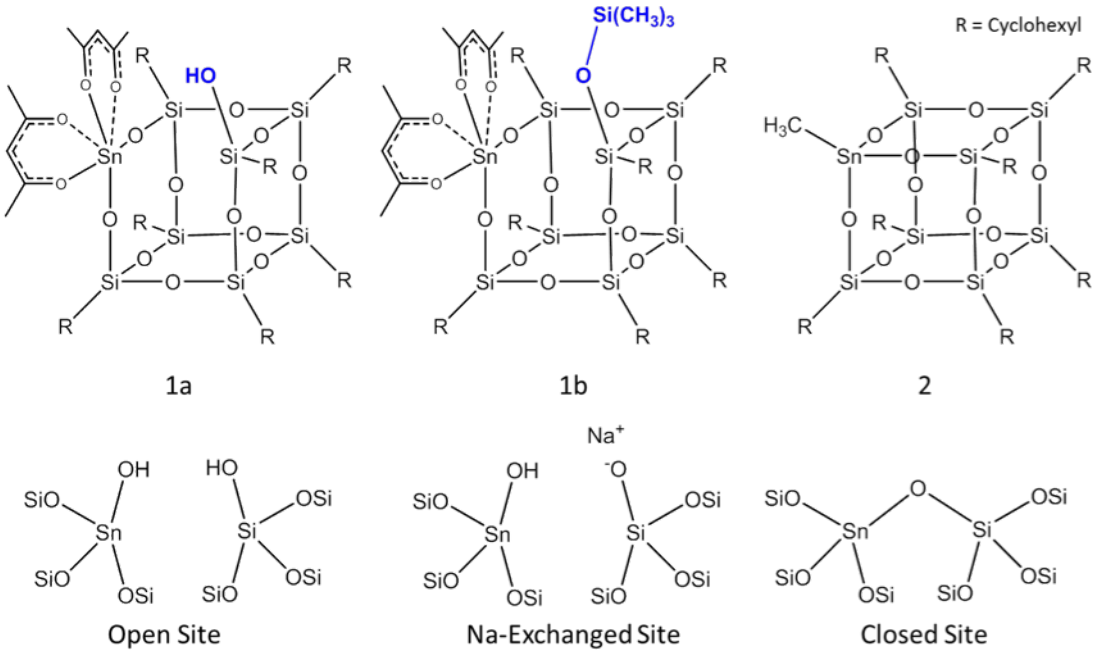

Figure 5.2: Tin-silsesquioxanes synthesized and tested for glucose isomerization by Brand et al.[36, 37] 1a and 1b contain an octahedral Sn site, coordinated by two acetylacetonate ligands, and 2 contains a tetrahedral Sn site ligated by a methyl group. These are structural models of the Sn-Beta open, Na-exchanged, and closed sites.

In our previous paper, we calculated several pathways for glucose ring-opening, conversion to fructose and mannose, and product ring-closing on 2 [37]. In this work, we report glucose transformation mechanisms for 1a and 1b, focusing on the rate-determining steps of the 1,2-H-shift and 1,2-C-shift.

5.3 Computational Methods

Electronic structure calculations were performed using density functional theory to calculate reaction pathways and examine catalyst/substrate interactions. Geometry optimizations and frequency calculations were performed using the M062X functional [38] with the LANL2DZ effective core basis set [39] for the Si and Sn atoms, 3-21G for the cyclohexyl ligands, and 6-31G(d,p) basis set for the sugar, acac ligands, framework O atoms, and the H or CH_3 groups on the SiOH (1a) or SiOTMS (1b) moieties (basis set A). After geometry optimization, single-point electronic energy calculations with larger basis sets were performed to refine the calculated electronic energies, using LANL2DZ for Si and Sn, 6-31G(d,p) for the cyclohexyl ligands, and 6-31G(2df,pd) for the sugars, acac ligands, framework O atoms, and H/TMS (basis set B). Transition states were verified by identifying a single imaginary frequency, and reactants and products were connected to transition states by following the intrinsic reaction coordinate. Calculations were performed in the gas phase using Gaussian 09 version A.09 [40]; Natural Bond Orbital (NBO) analysis was performed with NBO version 6.0 [41]; and analysis using Bader's Atoms-In-Molecules theory (QTAIM)[42] was performed using Critic2 [43].

5.4 Results

5.4.1 Catalyst Structure

To investigate the stability of the Sn-O interactions with the acac ligands, we examined several possible conformations of 1a and 1b (Fig. 5.3). Both 1a and 1b were most stable with both acac ligands in the cis orientation; significant energy penalties ($>$ 20 kcal/mol) are incurred by pulling one or both ligands into the trans orientation.

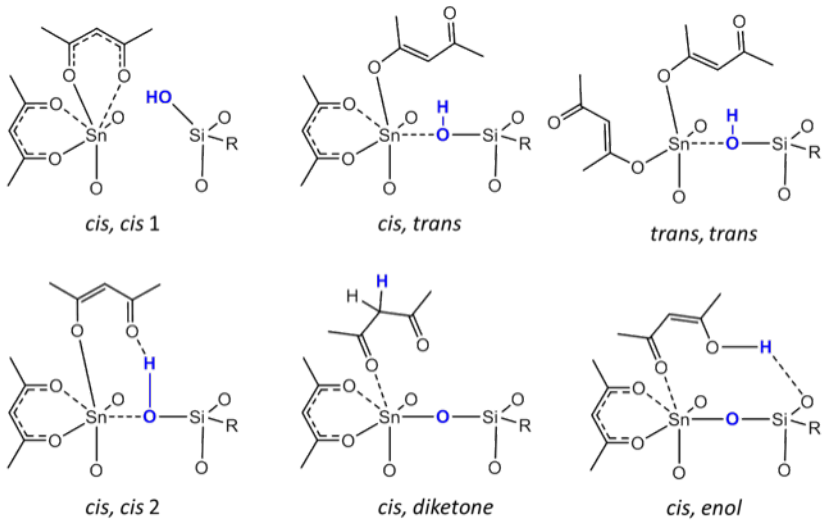

Conformation	1a	1b
cis, cis 1	0.0	0.0
cis, trans	25.2	24.7
trans, trans	54.9	49.9
cis, cis 2	8.44	N/A
cis, diketone	24.9	N/A
cis, enol	8.78	N/A

Figure 5.3: Different orientations of acac ligands on Sn in 1a and 1b, with relative free energies at 353 K reported in kcal/mol.

Several alternative conformations for 1a were considered by deprotonating the SiOH to a ligand and forming a third Sn-O-Si bridge. When the proton was transferred to C3 of the acac (forming a diketone) or to an acac O (forming an enol), the resulting structures were significantly less stable than the original structure, because the SiOH is not strongly acidic and the acac ligand is not a strong proton acceptor (see below). An additional configuration was 3.7 kcal/mol less stable than the original structure. In this, the SiOH coordinates to the Sn and H-bonds to the displaced cis acac ligand. The dominant Lewis structure of the Sn site in the most stable configuration, according to NBO analysis, is presented in Figure S1 in Appendix D.

5.4.2 Proton Affinities

Both the 1,2 H-shift and 1,2 C-shift reactions are activated by an initial deprotonation of the substrate [22]. In addition, the Brønsted basicity of the SnOH in Lewis-acidic zeolites has been proposed as a descriptor for the 1,2 H-shift barrier [27]. To probe the relative strength of candidate Brønsted bases, proton affinities were calculated for several sites on the catalyst (Fig. 5.4). The Sn-O-Si bridge oxygens bound

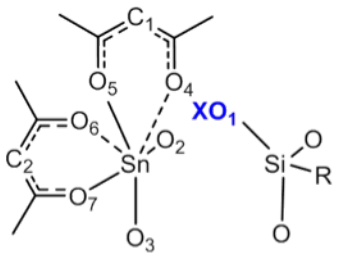

Protonation Site	1a Proton Affinity (kcal/mol)	1b Proton Affinity (kcal/mol)
O_1 [c]	239.8 [a]	237.2 [c]
O_2	240.2	241.9
O_3	235.3	239.5
O_4	242.0 [a]	220.3
O_5	219.9	217.6
O_6	217.0	222.3
O_7 [b]	239.0 [b]	238.4 [b]
C_1	217.7	220.5
C_2	224.7	229.7

Figure 5.4: Proton affinities of candidate Brønsted bases in 1a (X = H) and 1b (X = $Si(CH_3)_3$). [a] Proton migrated to bridge O2 during optimization; shared with SiOH. [b] Proton migrated to Si-O-Si bridge; shared with ligand O7 [c] Proton on OTMS; shared with ligand O7.

the proton most strongly, with proton affinities of 242 kcal/mol for both 1a and 1b. In 1a, a proton placed on the SiOH migrated to the Sn-O-Si bridge during optimization, while in 1b, a proton placed on the SiOTMS was shared with a ligand oxygen. The proton affinities of the ligand oxygens (O4-O7) were considerably less favorable – ranging from 217.0 to 222.3 kcal/mol – and in several cases, the proton migrated away from the ligand O to another O during optimization. The third carbon of each acac ligand also had weaker proton affinities (ranging from 217.7 to 229.7 kcal/mol). We therefore rule out the acac ligands as proton acceptors in sugar deprotonation.

5.4.3 Reaction Pathways

To reduce configurational complexity, accelerate calculations, and focus on the salient features of the reaction mechanism, we approximated glucose as glyceraldehyde (GLY), the smallest aldose which allows for comparison of the 1,2-H-shift and 1,2-C-shift reactions, producing dihydroxyacetone (DHA) and GLY with opposite chirality to the reactant, respectively.

The 1,2 hydride/carbon shift reaction on a bifunctional Lewis acid/Brønsted

base active site can be generalized to three possible mechanisms, depending on the binding geometry to the site [37]. The "bidentate binding" pathway, so-named for the bidentate coordination of the sugar at the transition state, involves three steps: 1) deprotonation of O2 to the Brønsted base and binding of O2 to the Lewis acid, 2) the H/C-shift reaction in a chelate-like transition state, and 3) reprotonation of O1. The "O1 binding" pathway is two steps: concerted deprotonation with the H/C-shift, followed by reprotonation. The "O2 binding" pathway is also two steps: deprotonation of O2 to the Brønsted base and subsequent H/C-shift concerted with reprotonation. Only 6 pathways are needed to examine a catalyst with a single Lewis-acid/Brønsted base site, the methyl-tin silsesquioxane 2, with only the Sn-O-Si bridge moiety. While 1b has only Sn-O-Si bridges as Brønsted bases, allowing for 6 distinct pathways, 1a has Sn-O-Si bridges as well as a SiOH, which may facilitate proton transfers to the Sn-O-Si bridges or to the acac ligands, as has been proposed for Sn-Beta [26, 28].

5.4.3.1 Pathways on Sn-O-Si bridges

Fig. 5.5 depicts the pathways on the Sn-O-Si bridges, and Table S1 and Figures S2-S4 in Appendix D contain the energetics for these pathways on 1a and 1b. Fig. 5.8 gives the highest TS free energy for all pathways to facilitate their comparison. For a 1,2-H-shift reaction, the product is DHA, and R_1 and R_2 designate H and CH_2OH, respectively. For a 1,2-C-shift reaction, the product is GLY of opposite chirality, and R_1 and R_2 designate CH_2OH and H, respectively.

The bidentate binding pathway begins by deprotonating GLY to a Sn-O-Si bridge, binding O2 of GLY to the Sn and forming a new silanol by virtue of the opening of the Sn-O-Si bridge. At intermediate B-3, 1a has two SiOH groups, while 1b has this new SiOH and the original SiOTMS. The highest transition state in these pathways was B-4, with the H-shift being favored over the C-shift on both 1a (TS free energies of 28.3 and 32.8 kcal/mol, respectively) and 1b (27.5 and 38.1 kcal/mol). The higher barrier for the C-shift is due to greater steric hindrance by the acac ligands on the transferring CH_2OH group compared to the H atom. Christianson et al., also

found the bidentate-binding C-shift TS to be less stable than that for the H-shift on Sn-Beta [28].

The bidentate binding pathways contain configurations unique to this work in their unusually crowded 7-coordinated Sn. In Sn-Beta, both closed and open sites are tetrahedral when all water ligands have been removed, 5-coordinated with NH_3 adsorbed, and octahedral when water is adsorbed [19]. In aqueous solution, the coordination of Sn(IV) is 6 [44], as $[Sn(OH_2)^6]^{4+}$, but higher coordination has not been observed. Furthermore, while bidentate binding is possible in relatively flexible zeolite clusters [23, 26, 28], it is unfavorable in larger, less flexible clusters and periodic zeolite models [27, 28] in which the open site is formed by hydrolyzing a Sn-O-Si. For these reasons, we were not expecting to find a favorable bidentate binding mode in 1a and 1b, yet it is not only possible, but most favorable for H-shift pathways. In order to accommodate the sugar oxygens at the TS, the ligand and framework oxygens are displaced, and the average Sn-O(acac) distance increases slightly from 2.052 Å in isolated 1a to 2.122 Å at the bidentate H-shift TS on 1a. An octahedral Sn ideally contains O-Sn-O angles of 90°, and 1a and 1b have angles ranging from 84.5° between oxygens on the same ligand, and 101.2° between a framework and ligand O. However, in the bidentate H-shift TS, for example, the coordinated oxygens form a pentagonal bipyramid with O-Sn-O angles ranging from 70.4° to 76.4° in the plane of the pentagon – near the ideal value of 72°. While the bidentate H-shift is the most stable H-shift pathway, the bidentate C-shift is unfavorable due to its bulkier transition state; the steric hindrance imposed by the acac ligands results in more favorable monodentate binding for the C-shift.

The O1-binding pathway begins by coordinating O1 to the Sn and the O2 hydroxyl into an H-bond with a Sn-O-Si bridge. This either requires bringing Sn into a 7-coordinated arrangement (O1 H/C-shift on 1a, and O1 H-shift on 1b) or displacing an O of the acac ligand (O1 C-shift on 1b). O2 is then deprotonated to form a silanol in a concerted reaction with the H/C-shift. The final step is reprotonation of O1 from the newly formed silanol. On 1a, both the H-shift and C-shift TS were considerably

less stable than in the bidentate binding mode (16 and 9 kcal/mol higher energy, respectively), but on 1b, the O1-binding C-shift TS was more stable than the bidentate binding TS by 10 kcal/mol). This stabilization occurs due to reduced crowding around the Sn site and interactions between the O3 hydroxyl and acac ligand oxygens (see Discussion and Appendix D).

The O2-binding pathway begins by deprotonating the O2 hydroxyl to a Sn-O-Si bridge and opening of the latter. The formyl O1 forms an H-bond with the newly-formed silanol, and in the next step, the silanol transfers its proton to O1 in a concerted step with the H/C-shift, forming the final product. None of the O2 binding pathways were found to be the most favorable on 1a or 1b.

The Sn-O-Si bridge pathways comprise the possible pathways on 1b, and we can identify an important effect of the SiOH replacement with SiOTMS. On 1a, the bidentate H-shift is favored over the C-shift by 4.5 kcal/mol, while on 1b, the H-shift is even more favored, by 7.6 kcal/mol; in this case, the bulky TMS crowds the ligands, which cannot displace as much to accommodate the bulky C-shift TS. On the other hand, the O1-binding pathway on 1b significantly stabilizes the C-shift, while it does not on 1a. This brings the difference between the most favorable pathways on 1b, the bidentate H-shift and the O1 binding C-shift, to less than 1 kcal/mol, within typical DFT errors.

5.4.3.2 Pathways unique to 1a

The silanol function on 1a enables additional reaction pathways by facilitating proton transfers during the H/C-shift steps and by permitting the *cis,cis 2* configuration of 1a, allowing participation of a ligand oxygen. We identified O1 and O2 binding pathways with the SiOH acting as the proton acceptor/donor, facilitating a proton transfer with either a Sn-O-Si bridge or with a ligand O, as well as a pathway in which a displaced acac ligand stabilizes the H/C-shift transition state by interacting with the transferring moiety. These pathways are shown in Fig. 5.6 and Fig. 5.7; energetics are

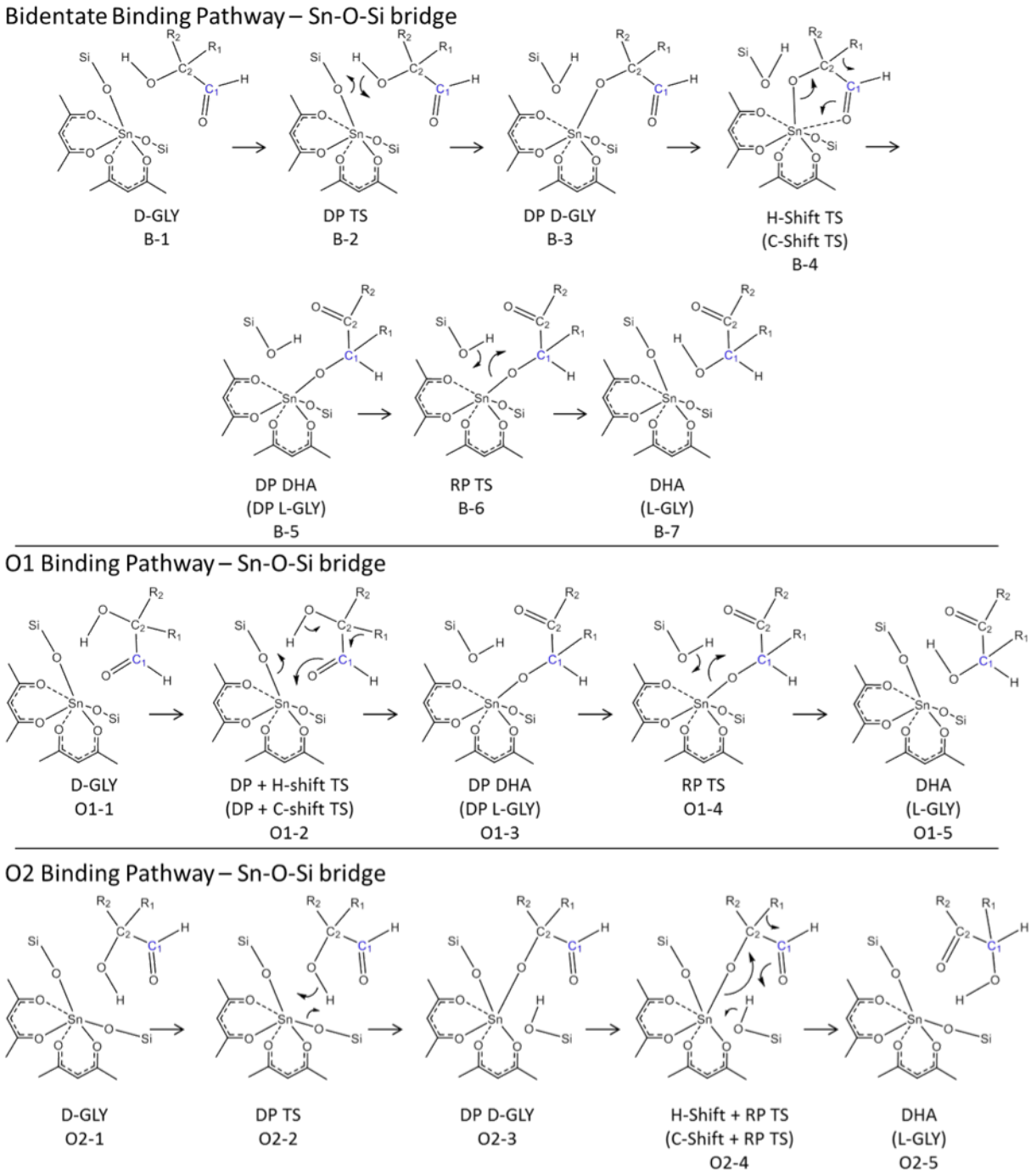

Figure 5.5: Reaction pathways for H/C-shift on Sn-O-Si bridge in 1a and 1b. GLY = glyceraldehyde, DHA = dihydroxyacetone, DP = deprotonation, RP = reprotonation. When R_1 = H, R_2 = CH_2OH, the rate-determining step contains a H-shift, and the product is DHA. When R_1 = CH_2OH, R_2 = H, the rate-determining step contains a C-shift, and the product is glyceraldehyde of opposite chirality to the reactant.

reported in Table S2 and Figures S5 and S6 in Appendix D, and the highest TS energy for each pathway is shown in Fig. 5.8.

In the O1sb and O2sb pathways, GLY approaches the Sn site on the same side as the SiOH, and the SiOH participates by shuttling a proton to a Sn-O-Si bridge. In the O1sb pathways, the SiOH donates an H-bond across a face of the silicate cube to an opposite Sn-O-Si bridge, and when the GLY undergoes a concerted H-shift and deprotonation, the SiOH acts as a proton "wire," receiving the O2 hydroxyl proton and passing its own proton to the Sn-O-Si bridge. In the O2sb pathways, GLY deprotonates to a Sn-O-Si bridge and binds to the Sn as in the O2 pathways, but the subsequent concerted H-shift/reprotonation uses the SiOH to shuttle the proton to O1. TS energies for all of these pathways were unfavorable, being over 10 kcal/mol greater than H/C-shift TS energies for the bidentate binding mode on 1a.

Two variations on these pathways were also explored. In these pathways, catalyst 1a first rearranges to the *cis,cis 2* configuration (see Fig. 5.3). When the sugar binds, the displaced acac ligand O interacts with the O3 hydroxyl of GLY, and HC2, which will undergo the H-shift, is either far from (O1sb-la) or near to (O1sb-lb) the acac O. The H-shift proceeds in a concerted reaction with the SiOH shuttling a proton from O2 to the Sn-O-Si bridge, but the ligand interaction reduces the barrier. In O1sb-la, the ligand oxygen is H-bonded to O3 at the TS, bringing the TS free energy to 38.8 kcal/mol, and in O1sb-lb, the ligand oxygen is coordinated to the transferring H atom, reducing the TS free energy to 32.7 kcal/mol. Having a ligand O stabilizing the transferring H does reduce the barrier, but the bidentate pathway, with a TS energy of 28.3 kcal/mol) remains favored by 4.4 kcal/mol.

We also identified pathways involving the SiOH shuttling a proton to an acac ligand oxygen. These also begin with the catalyst in the *cis,cis 2* configuration, except when the sugar binds, the displaced acac ligand oxygen retains its H-bond with the SiOH. In these pathways, the sugar undergoes an O1-binding pathway, a concerted C-shift with deprotonation to the SiOH, which passes its proton to the ligand O, forming an enol. Reversing this proton shuttle back to the O1 oxygen completes the cycle to

produce the product sugar. In both the H- and C-shift reactions, the O3 hydroxyl is interacting with the ligand acac (or enol at O2sl-3), which dramatically reduces the C-shift TS free energy to 28.2 kcal/mol. This is the most favorable C-shift pathway on 1a, which is comparable in energy to the H-shift, although varying significantly in structure.

5.5 Discussion

Overall, the most favorable H-shift TS for both 1a and 1b is the bidentate binding mode, with TS free energies of 28.3 and 27.5 kcal/mol, respectively (Fig. 5.8). Fig. 5.9 shows images of these geometries. We find that, while the SiOH permits numerous additional pathways on 1a, none of these are more energetically favorable than the bidentate binding mode, which both 1a and 1b can accommodate. Likewise, the most favorable C-shift TS for both 1a and 1b have remarkably similar free energies, 28.2 and 28.3 kcal/mol, respectively, even though 1a involves a concerted proton shuttle from O2 to SiOH to an acac ligand, while 1b involves a concerted proton transfer to a Sn-O-Si bridge. The common feature in both of these pathways is a strong interaction between acac ligand oxygen(s) and the O3 hydroxyl at the transition state. Despite the structural diversity among these reaction pathways, the TS energies are indistinguishable, within typical DFT errors.

One common feature among the most favorable C-shift reactions is an H-bonding interaction between the C3 hydroxyl and an oxygen atom of the catalyst. To examine this more closely, we analyzed several H/C-shift transition states using Bader's Atoms In Molecules (QTAIM) theory [42]. Table S3 in Appendix D provides key information about the (3, -1) bond critical points (BCPs) involved in the H/C-shift elementary steps.

The key interaction identified in the Bader analysis for the C-shift is the contraction of the C3—O3 bond at the TS, which is accompanied by an increase in electron density and charge concentration as the single bond takes on more double-bond character. The lowest-barrier C-shift TS exhibits the most dramatic contraction of the

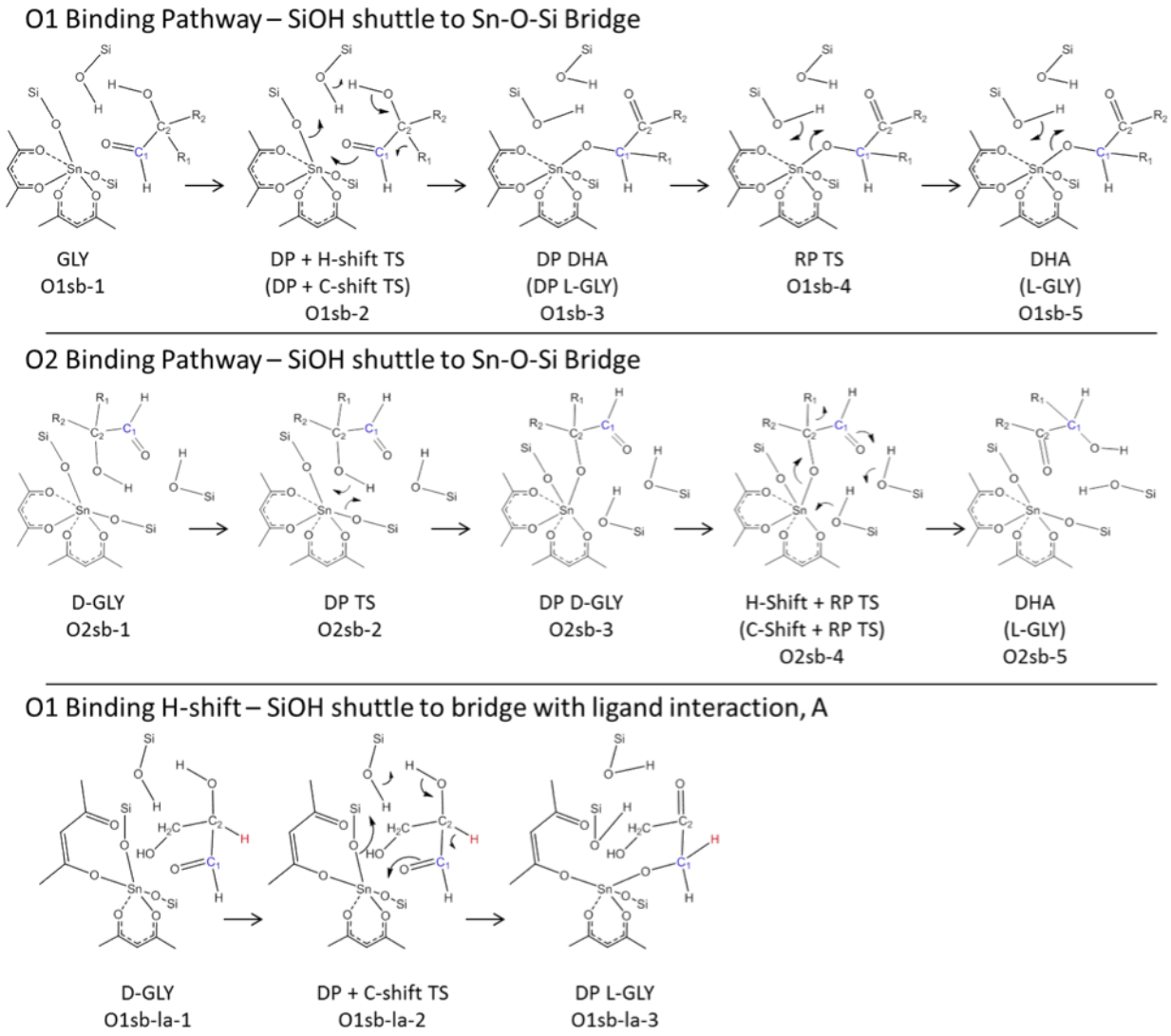

Figure 5.6: Pathways unique to 1a, invoking the SiOH in proton transfer to a Sn-O-Si bridge. GLY = glyceraldehyde, DHA = dihydroxyacetone, DP = deprotonation, RP = reprotonation. When R_1 = H, R_2 = CH_2OH, the rate-determining step contains a H-shift, and the product is DHA. When R_1 = CH_2OH, R_2 = H, the rate-determining step contains a C-shift, and the product is glyceraldehyde of opposite chirality to the reactant.

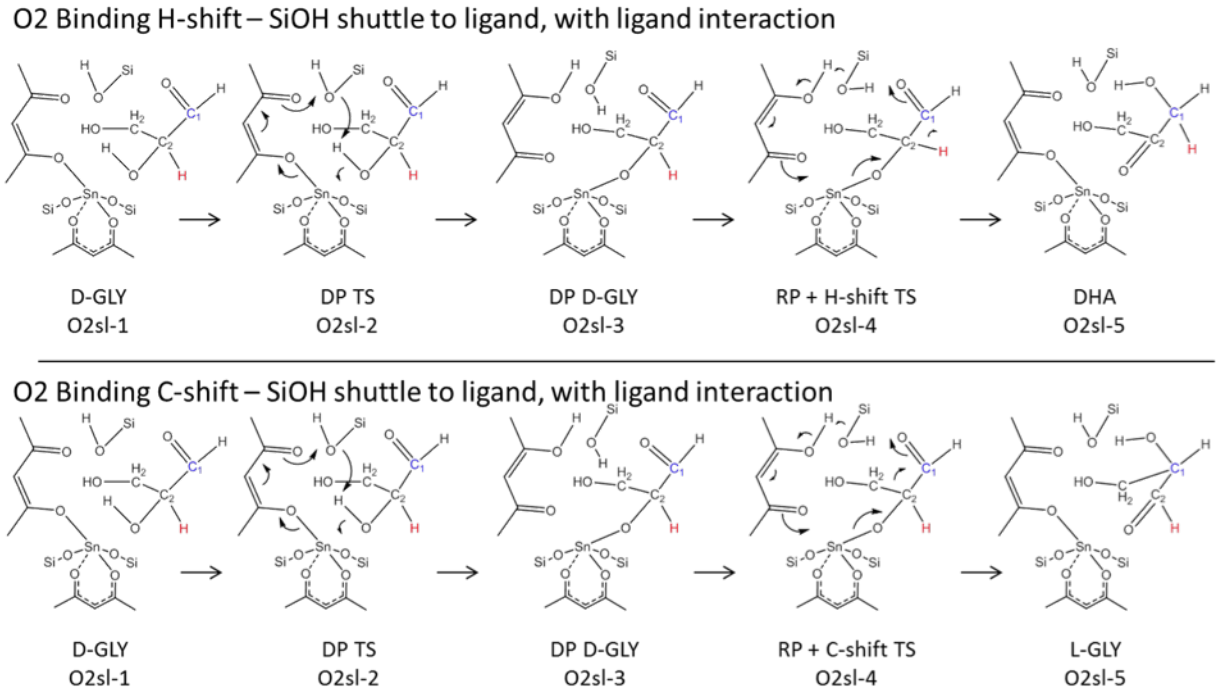

Figure 5.7: Pathways unique to 1a, continued, invoking the SiOH in proton transfer to an acac ligand O. GLY = glyceraldehyde, DHA = dihydroxyacetone, DP = deprotonation, RP = reprotonation

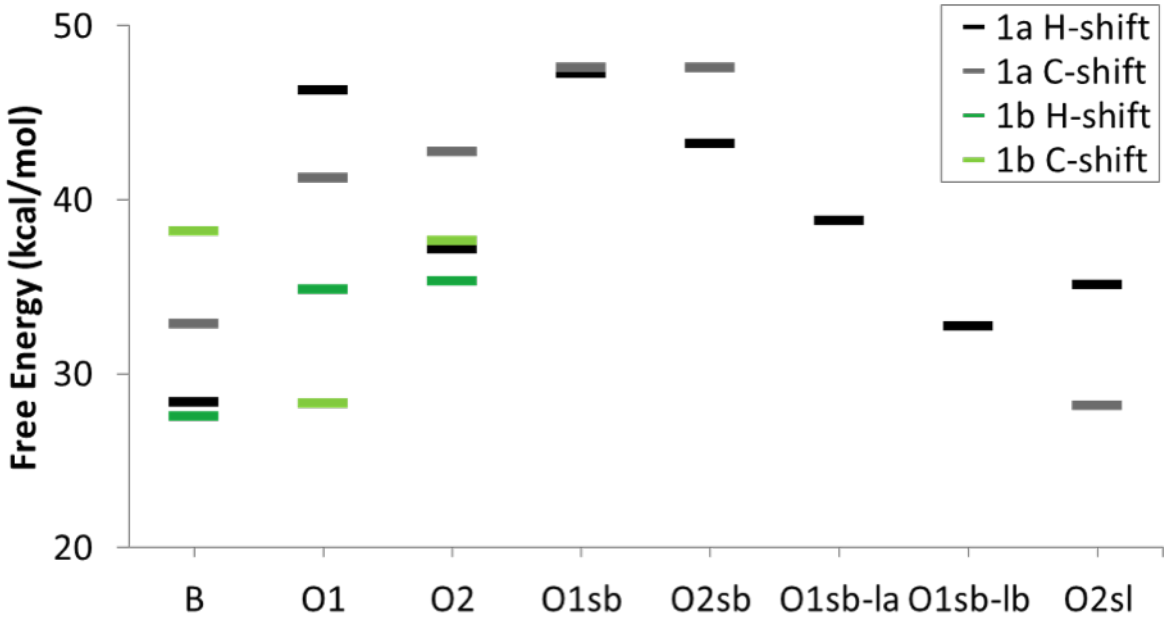

Figure 5.8: Highest TS free energy of all reaction pathways, calculated at 353 K. Full reaction profiles are reported in Tables S1 and S2 and in Figures S2-S6 in Appendix D.

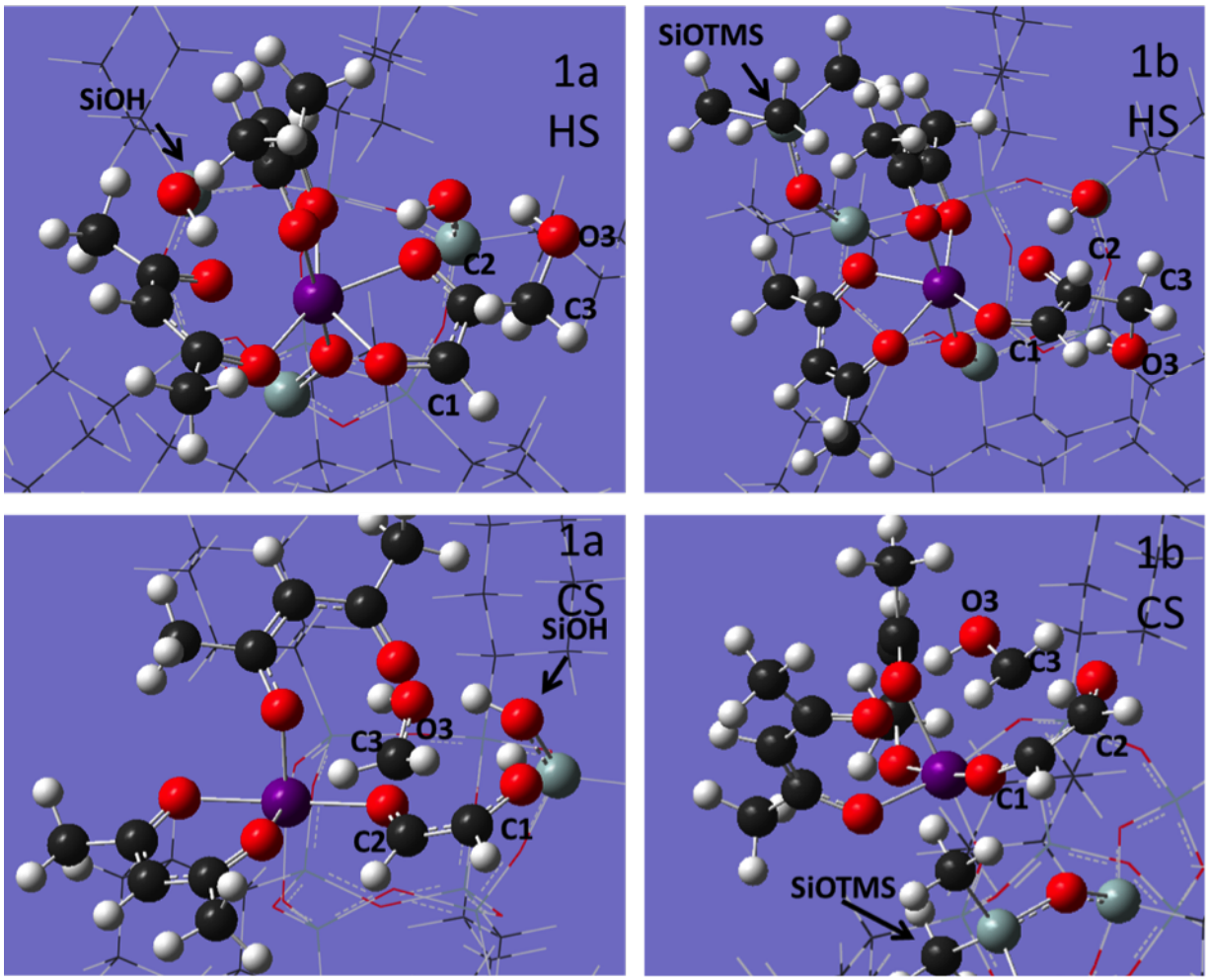

Figure 5.9: Lowest-barrier transition state geometries for the H/C-shift reaction on 1a and 1b. The sugar, acac ligands, Sn-O-Si bridge atoms, and SiOH/SiOTMS are shown as ball and stick to clarify the active site geometry and to highlight the sugar/catalyst interactions. Coordinates may be found in the online Supporting Information as OH_H_B-5, OH_C_O2sl-4, TMS_H_B-5, and TMS_C_O1-2.

C3—O3 bond, from 1.403 Å in gas phase to 1.333 Å at the O2sl-4 C-shift TS, while the highest-barrier C-shift exhibits less contraction, with a C3—O3 bond length of 1.361 Å at the C-shift TS. This contraction is accompanied by an increase in charge density ρ, an increase in local charge concentration (marked by a sign change in $\nabla^2(\rho)$), and an increase in bond ellipticity – all signatures of increased double-bond character. This is facilitated by H-bond interactions between the O3 hydroxyl and SiOH, SiOSi, or ligand O in the catalyst, depending on the pathway. In the most favorable C-shift on both 1a and 1b, the O3 hydroxyl is interacting with two ligand oxygens, which stabilize a weakened O3—H bond and a strengthened C3—O3 bond. The activity for both of these catalysts for the C-shift pathway is therefore a consequence of the acac ligands.

According to the Energy Span Model[45] and the Curtin-Hammett Principle[46], the selectivity of a simple reaction network with measured turn-over frequencies (TOF) to two products can be expressed as

$$S = \frac{TOF_A}{TOF_B} \approx e^{\Delta G_{TS}} = e^{(G_{TS,B} - G_{TS,A})/RT} \tag{5.1}$$

where ΔG_{TS} is the difference in Gibbs free energy of the selectivity-determining TS for products A and B [45]. From the experimental data at 353 K, with 1a, $G_{TS,MAN}$ – $G_{TS,FRU}$ = 0.22 kcal/mol, while with 1b, $G_{TS,MAN}$ – $G_{TS,FRU}$ = -0.73 kcal/mol (see Table 5.1). Both of these free energy differences are less than typical DFT error of $\tilde{2}$ kcal/mol.

Using the energy span model, we also calculated the TOF at 353 K for the lowest-barrier H/C-shift pathways on 1a and 1b. The calculated TOF on 1a are 1.98 x 10^{-7} mol sugar/s mol Sn for H-shift and 2.48 x 10^{-7} for C-shift; on 1b, these are 6.01 x 10^{-7} and 2.07 x 10^{-7} respectively. Resolving the difference between experimental and theoretical rates would require reducing the theoretical barriers by about 7 kcal/mol. Such an energy difference can readily be attributed to hydrogen bonding between the hexose substrate and the surrounding solvent molecules (specifically, DMSO), which

	1a	1b
Fructose TOF (mol/s L mol Sn)	0.756	0.134
Mannose TOF (mol/s L mol Sn)	0.549	0.38
TOF_{Fru}/TOF_{Man}	1.38	0.353
ΔG_{TS}	0.320	-1.04
$G_{TS,MAN} - G_{TS,FRU}$ at 353 K (kcal/mol)	0.224	-0.731

Table 5.1: Experimental initial rate data on 1a and 1b from Brand et al.[36, 37] and the Gibbs free energy differences between the TOF-determining transition states for fructose and mannose formation assuming constant pre-exponential terms.

were not accounted for in this study with the model triose in the gas phase.

Our calculations are consistent with experiment in identifying H-shift and C-shift pathways of comparable barriers on each catalyst. More importantly, we can rule out the hypothesis that SiOH participation in the rate-determining step is critical for fructose selectivity, because H-shift pathways involving SiOH participation (O1sb, O2sb, O1sb-la, O1sb-lb, and O2sl) consistently gave higher barriers than the bidentate H-shift pathway (4.4 kcal/mol higher for O1sb-lb and > 6.9 kcal/mol higher for the others). We also identify the importance of ligand O atom interactions with the O3 for stabilizing the C-shift TS; pathways without this ligand interaction gave higher barriers (4.7 kcal/mol higher for bidentate on 1a and >9 kcal/mol higher for the others).

1a and 1b are therefore limited models of the open sites of Sn-Beta and Na-Sn-Beta, in particular due to the presence of the acac ligands, which stabilize the C-shift transition state whether or not a SiOH is present. Sn-Beta is so selective to H-shift reactions that mannose from C-shift is undetected; mannose is instead produced via a double H-shift. Consequently, the activation of the C-shift pathway by Na-Sn-Beta is a dramatic change. Because 1a is already active for the C-shift, the shift in selectivity to mannose with the TMS substitution is more incremental. We have identified why this is the case: the acac ligands can stabilize the C-shift TS so that it has comparable barriers

to the H-shift on both 1a and 1b. As Quadrelli and Basset conclude in their review of silsesquioxanes as analogues to heterogeneous catalysts [33], *"The analogy [between heterogeneous and silsesquioxane chemistry] mostly breaks down when silsesquioxane can access a chemistry that heterogeneous catalysts cannot,"* which we find to be the case in catalysts 1a and 1b due to the presence of the acac ligands.

5.6 Conclusions

Several pathways were investigated for H-shift and C-shift pathways on the tin-silsesquioxanes 1a and 1b. The H-shift proceeds through a bidentate binding pathway on both 1a and 1b, and the C-shift proceeds through concerted pathways that invoke the acac ligand. The most favorable H/C-shift pathways on 1a and 1b have comparable barriers, consistent with both fructose (from H-shift) and mannose (from C-shift) produced in significant quantities on both catalysts. Our calculations show that the selectivity of the Sn-silsesquioxanes is not determined by the presence (in Sn-silsesquioxane 1a) or absence (from Sn-silsesquioxane 1b) of a silanol group SiOH. We find that there is nothing inherent about the silanol group that would tilt the outcome either in the direction of the 1,2-H-shift channel or in the direction of the 1,2-C-shift. Both channels are activated by an initial proton transfer (from the C2—OH) which can take place quite effectively via a Sn-O-Si bridge or an acac ligand. Both channels, in the gas phase, are almost equally accessible. This conclusion should be independent of the theory level, in the sense that it is independent of the error inherent in DFT, since all pathways were computed at the same level. Further, it is in reasonable agreement with the experiments (carried out in mixed, 50/50 v/v benzene/DMSO solvent), according to which isomerization is preferred to epimerization with a TOF ratio of 1.4 on 1a, while epimerization is preferred to isomerization with a TOF ratio of 2.5 on 1b. Our calculations suggest that the modest differences in selectivity between the Sn-silsesquioxanes 1a and 1b must be due to micro-solvation phenomena: the trimethylsilyl-capped 1b is locally less polar in the vicinity of the active site compared to the SiOH-bearing 1a.

5.7 Acknowledgements

Research was supported as part of the Catalysis Center for Energy Innovation, an Energy Frontier Research Center funded by the U.S. Department of Energy (DOE), Office of Science, Basic Energy Sciences (BES), under Award number DE-SC0001004. This research used resources of the National Energy Research Scientific Computing Center, a DOE Office of Science User Facility supported by the Office of Science of the U.S. Department of Energy under Contract No. DE-AC02-05CH11231. T.R.J. wishes to acknowledge funding from the National Science Foundation Graduate Research Fellowship Program under Grant No. 0750966, as well as the George W. Laird Merit Fellowship. S.K.B. wishes to acknowledge funding from the National Science Foundation Graduate Research Fellowship Program under Grant No. DGE-1144469. Any opinions, findings, and conclusions or recommendations expressed in this material are those of the author(s) and do not necessarily reflect the views of the National Science Foundation. The authors would like to thank Professor Mark Davis and Dr. Jeff Christianson for numerous useful conversations.

REFERENCES

[1] T. R. Josephson, S. K. Brand, S. Caratzoulas, and D. G. Vlachos. 1,2-H- versus 1,2-C-Shift on Sn-Silsesquioxanes. *ACS Catalysis*, pages 25–33, 2016. ISSN 2155-5435. doi: 10.1021/acscatal.6b03128.

[2] T. Werpy and G. Petersen. Top Value Added Chemicals from Biomass. *U.S. Department of Energy*, 1:76, 2004. doi: 10.2172/926125.

[3] A. J. Ragauskas, C. K. Williams, B. H. Davison, G. Britovsek, J. Cairney, C. A. Eckert, W. J. Frederick Jr., J. P. Hallett, D. J. Leak, C. L. Liotta, J. R. Mielenz, R. Murphy, R. Templer, and T. Tschaplinski. The path forward for biofuels and biomaterials. *Science (New York, N.Y.)*, 311(5760):484–9, 2006. ISSN 1095-9203. doi: 10.1126/science.1114736.

[4] D. Tilman, R. Socolow, J. J. A. Foley, J. Hill, E. Larson, L. Lynd, S. Pacala, J. Reilly, T. Searchinger, C. Somerville, and R. Williams. Beneficial biofuelsthe food, energy, and environment trilemma. *Science*, 325(5938):270–271, 2009. ISSN 00368075. doi: 10.1126/science.1177970.

[5] R. D. R. Perlack, B. B. J. Stokes, L. M. Eaton, and A. F. Turnhollow. U.S. Billion-Ton Update: Biomass Supply for a Bioenergy and Bioproducts Industry. *Renewable Energy*, (August):1–229, 2011.

[6] P. C. A. Bruijnincx and B. M. Weckhuysen. Shale gas revolution: An opportunity for the production of biobased chemicals? *Angewandte Chemie - International Edition*, 52(46):11980–11987, 2013. ISSN 14337851. doi: 10.1002/anie.201305058.

[7] A. Corma, L. T. Nemeth, M. Renz, and S. Valencia. Sn-zeolite beta as a heterogeneous chemoselective catalyst for Baeyer-Villiger oxidations. *Nature*, 412(6845): 423–425, 2001. ISSN 0028-0836. doi: 10.1038/35086546.

[8] A. Corma, M. E. Domine, L. Nemeth, and S. Valencia. Al-free Sn-Beta zeolite as a catalyst for the selective reduction of carbonyl compounds (Meerwein-Ponndorf-Verley Reaction). *Journal of the American Chemical Society*, 124:3194–3195, 2002. ISSN 00027863. doi: 10.1021/ja012297m.

[9] M. Moliner, Y. Roman-Leshkov, M. E. E. Davis, Y. Román-Leshkov, and M. E. E. Davis. Tin-containing zeolites are highly active catalysts for the isomerization of glucose in water. *Proc Natl Acad Sci U S A*, 107(14):6164–6168, 2010. ISSN 1091-6490. doi: 10.1073/pnas.1002358107.

[10] V. Choudhary, A. B. Pinar, S. I. Sandler, D. G. Vlachos, and R. F. Lobo. Xylose isomerization to xylulose and its dehydration to furfural in aqueous media. *ACS Catalysis*, 1(12):1724–1728, 2011. ISSN 21555435. doi: 10.1021/cs200461t.

[11] M. S. Holm, S. Saravanamurugan, and E. Taarning. Conversion of sugars to lactic acid derivatives using heterogeneous zeotype catalysts. *Science (New York, N.Y.)*, 328(5978):602–605, 2010. ISSN 0036-8075. doi: 10.1126/science.1183990.

[12] R. Bermejo-Deval, R. Gounder, and M. E. Davis. Framework and extraframework tin sites in zeolite beta react glucose differently. *ACS Catalysis*, 2(12):2705–2713, 2012. ISSN 21555435. doi: 10.1021/cs300474x.

[13] W. R. Gunther, Y. Wang, Y. Ji, V. K. Michaelis, S. T. Hunt, R. G. Griffin, and Y. Román-Leshkov. Sn-Beta zeolites with borate salts catalyse the epimerization of carbohydrates via an intramolecular carbon shift. *Nature communications*, 3: 1109, 2012. ISSN 2041-1723. doi: 10.1038/ncomms2122.

[14] C. L. Williams, C.-C. Chang, P. Do, N. Nikbin, S. Caratzoulas, D. G. Vlachos, R. F. Lobo, W. Fan, and P. J. Dauenhauer. Cycloaddition of Biomass-Derived

Furans for Catalytic Production of Renewablep-Xylene. *ACS Catalysis*, 2(6):935–939, 2012. doi: 10.1021/cs300011a.

[15] R. J. Van Putten, J. C. Van Der Waal, E. De Jong, C. B. Rasrendra, H. J. Heeres, and J. G. De Vries. Hydroxymethylfurfural, a versatile platform chemical made from renewable resources. *Chemical Reviews*, 113(3):1499–1597, 2013. ISSN 00092665. doi: 10.1021/cr300182k.

[16] M. Orazov and M. E. Davis. Tandem catalysis for the production of alkyl lactates from ketohexoses at moderate temperatures. *Proceedings of the National Academy of Sciences*, 112(38):201516466, 2015. ISSN 0027-8424. doi: 10.1073/pnas.1516466112.

[17] M. Dusselier, P. Van Wouwe, A. Dewaele, E. Makshina, and B. F. Sels. Lactic acid as a platform chemical in the biobased economy: the role of chemocatalysis. *Energy & Environmental Science*, 6(5):1415, 2013. ISSN 1754-5692. doi: 10.1039/c3ee00069a.

[18] M. Boronat, P. Concepción, A. Corma, M. Renz, and S. Valencia. Determination of the catalytically active oxidation Lewis acid sites in Sn-beta zeolites, and their optimisation by the combination of theoretical and experimental studies. *Journal of Catalysis*, 234(1):111–118, 2005. ISSN 00219517. doi: 10.1016/j.jcat.2005.05.023.

[19] R. Bermejo-Deval, M. Orazov, R. Gounder, S. J. Hwang, and M. E. Davis. Active sites in Sn-beta for glucose isomerization to fructose and epimerization to mannose. *ACS Catalysis*, 4(7):2288–2297, 2014. ISSN 21555435. doi: 10.1021/cs500466j.

[20] J. W. Harris, M. J. Cordon, J. R. Di Iorio, J. C. Vega-Vila, F. H. Ribeiro, and R. Gounder. Titration and quantification of open and closed Lewis acid sites in Sn-Beta zeolites that catalyze glucose isomerization. *Journal of Catalysis*, 335: 141–154, 2016. ISSN 00219517. doi: 10.1016/j.jcat.2015.12.024.

[21] M. L. Hayes, N. J. Pennings, A. S. Serianni, and R. Barker. Epimerization of aldoses by molybdate involving a novel rearrangement of the carbon skeleton. *Journal of the American Chemical Society*, 104(24):6764–6769, 1982. ISSN 0002-7863. doi: 10.1021/ja00388a047.

[22] R. S. Assary and L. A. Curtiss. Theoretical study of 1,2-hydride shift associated with the isomerization of glyceraldehyde to dihydroxy acetone by Lewis acid active site models. *Journal of Physical Chemistry A*, 115(31):8754–8760, 2011. ISSN 10895639. doi: 10.1021/jp204371g.

[23] R. Bermejo-Deval, R. S. S. Assary, E. Nikolla, M. Moliner, Y. Roman-Leshkov, S.-J. S.-J. Hwang, A. Palsdottir, D. Silverman, R. F. Lobo, L. A. Curtiss, and M. E. Davis. Metalloenzyme-like catalyzed isomerizations of sugars by Lewis acid zeolites. *Proceedings of the National Academy of Sciences*, 109(25):9727–9732, 2012. ISSN 0027-8424. doi: 10.1073/pnas.1206708109.

[24] V. Choudhary, S. H. Mushrif, C. Ho, A. Anderko, V. Nikolakis, N. S. Marinkovic, A. I. Frenkel, S. I. Sandler, and D. G. Vlachos. Insights into the interplay of Lewis and Brønsted acid catalysts in glucose and fructose conversion to 5-(hydroxymethyl)furfural and levulinic acid in aqueous media. *Journal of the American Chemical Society*, 135(10):3997–4006, 2013. ISSN 00027863. doi: 10.1021/ja3122763.

[25] G. Yang, E. A. Pidko, and E. J. M. Hensen. The mechanism of glucose isomerization to fructose over Sn-BEA zeolite: A periodic density functional theory study. *ChemSusChem*, 6(9):1688–1696, 2013. ISSN 18645631. doi: 10.1002/cssc.201300342.

[26] N. Rai, S. Caratzoulas, and D. G. Vlachos. Role of silanol group in Sn-beta zeolite for glucose isomerization and epimerization reactions. *ACS Catalysis*, 3 (10):2294–2298, 2013. ISSN 21555435. doi: 10.1021/cs400476n.

[27] Y. P. P. Li, M. Head-Gordon, and A. T. T. Bell. Analysis of the reaction mechanism and catalytic activity of metal-substituted beta zeolite for the isomerization of glucose to fructose. *ACS Catalysis*, 4(5):1537–1545, 2014. ISSN 21555435. doi: 10.1021/cs401054f.

[28] J. R. Christianson, S. Caratzoulas, and D. G. Vlachos. Computational Insight into the Effect of Sn-Beta Na Exchange and Solvent on Glucose Isomerization and Epimerization. *ACS Catalysis*, 5(9):5256–5263, 2015. ISSN 2155-5435. doi: 10.1021/acscatal.5b01258.

[29] S. Shetty, S. Pal, D. G. Kanhere, and A. Goursot. Structural, electronic, and bonding properties of zeolite Sn-beta: A periodic density functional theory study. *Chemistry - A European Journal*, 12(2):518–523, 2005. ISSN 09476539. doi: 10.1002/chem.200500487.

[30] T. D. Courtney, C.-C. Chang, R. J. Gorte, R. F. Lobo, W. Fan, and V. Nikolakis. Effect of water treatment on Sn-BEA zeolite: Origin of 960cm1 FTIR peak. *Microporous and Mesoporous Materials*, 210:69–76, 2015. ISSN 13871811. doi: 10.1016/j.micromeso.2015.02.012.

[31] M. Boronat, P. Concepción, A. Corma, M. T. Navarro, M. Renz, and S. Valencia. Reactivity in the confined spaces of zeolites: the interplay between spectroscopy and theory to develop structure-activity relationships for catalysis. *Physical chemistry chemical physics : PCCP*, 11:2876–2884, 2009. ISSN 1463-9076. doi: 10.1039/b821297j.

[32] S. R. Bare, S. D. Kelly, W. Sinkler, J. J. Low, S. Valencia, A. Corma, L. T. Nemeth, F. S. Modica, S. Valencia, A. Corma, and L. T. Nemeth. Uniform catalytic site in Sn-β-zeolite determined using X-ray absorption fine structure. *J. Am. Chem. Soc.*, 127(37):12924–12932, 2005. doi: 10.1021/ja052543k.

[33] E. A. Quadrelli and J. M. Basset. On silsesquioxanes' accuracy as molecular models for silica-grafted complexes in heterogeneous catalysis. *Coordination Chemistry Reviews*, 254(5-6):707–728, 2010. ISSN 00108545. doi: 10.1016/j.ccr.2009.09.031.

[34] E. V. Beletskiy, X. Hou, Z. Shen, J. R. Gallagher, J. T. Miller, Y. Wu, T. Li, M. C. Kung, and H. H. Kung. Supported Tetrahedral Oxo-Sn Catalyst: Single Site, Two Modes of Catalysis. *Journal of the American Chemical Society*, 138(13): 4294–4297, 2016. ISSN 15205126. doi: 10.1021/jacs.5b13436.

[35] E. V. Beletskiy, Z. Shen, M. V. Riofski, X. Hou, J. R. Gallagher, J. T. Miller, Y. Wu, H. H. Kung, and M. C. Kung. Tetrahedral Sn-silsesquioxane: Synthesis, characterization and catalysis. *Chemical Communications*, 50(100):15699–15701, 2014. ISSN 1359-7345. doi: 10.1039/c4cc07897g.

[36] S. K. Brand, J. A. Labinger, and M. E. Davis. Tin Silsesquioxanes as Models for the "Open" Site in Tin-Containing Zeolite Beta. *ChemCatChem*, 8(1):121–124, 2016. ISSN 18673899. doi: 10.1002/cctc.201501067.

[37] S. K. Brand, T. R. Josephson, J. A. Labinger, S. Caratzoulas, D. G. Vlachos, and M. E. Davis. Methyl-Ligated Tin Silsesquioxane Catalyzed Reactions of Glucose. *Journal of Catalysis*, 341:62–71, 2016.

[38] Y. Zhao and D. G. Truhlar. The M06 suite of density functionals for main group thermochemistry, thermochemical kinetics, noncovalent interactions, excited states, and transition elements: Two new functionals and systematic testing of four M06-class functionals and 12 other function. *Theoretical Chemistry Accounts*, 120(1-3):215–241, 2008. ISSN 1432881X. doi: 10.1007/s00214-007-0310-x.

[39] W. R. Wadt and P. J. Hay. Ab initio effective core potentials for molecular calculations. Potentials for main group elements Na to Bi. *The Journal of Chemical Physics*, 82(1):284–298, 1985. ISSN 00219606. doi: 10.1063/1.448799.

[40] M. J. Frisch, G. W. Trucks, H. B. Schlegel, G. E. Scuseria, M. A. Robb, J. R. Cheeseman, G. Scalmani, V. Barone, B. Mennucci, G. A. Petersson, H. Nakatsuji, M. Caricato, X. Li, H. P. Hratchian, A. F. Izmaylov, J. Bloino, G. Zheng, J. L. Sonnenberg, M. Hada, M. Ehara, K. Toyota, R. Fukuda, J. Hasegawa, M. Ishida, T. Nakajima, Y. Honda, O. Kitao, H. Nakai, T. Vreven, J. A. Montgomery Jr., J. E. Peralta, F. Ogliaro, M. J. Bearpark, J. Heyd, E. N. Brothers, K. N. Kudin, V. N. Staroverov, R. Kobayashi, J. Normand, K. Raghavachari, A. P. Rendell, J. C. Burant, S. S. Iyengar, J. Tomasi, M. Cossi, N. Rega, N. J. Millam, M. Klene, J. E. Knox, J. B. Cross, V. Bakken, C. Adamo, J. Jaramillo, R. Gomperts, R. E. Stratmann, O. Yazyev, A. J. Austin, R. Cammi, C. Pomelli, J. W. Ochterski, R. L. Martin, K. Morokuma, V. G. Zakrzewski, G. A. Voth, P. Salvador, J. J. Dannenberg, S. Dapprich, A. D. Daniels, Ö. Farkas, J. B. Foresman, J. V. Ortiz, J. Cioslowski, and D. J. Fox. Gaussian 09, 2009.

[41] E. D. Glendening, C. R. Landis, and F. Weinhold. NBO 6.0: Natural bond orbital analysis program. *Journal of Computational Chemistry*, 34(16):1429–1437, 2013. ISSN 01928651. doi: 10.1002/jcc.23266.

[42] R. F. W. Bader. *Atoms in Molecules: A Quantum Theory*. Clarendon, Oxford, England, 1990. ISBN 0198558651.

[43] A. Otero-De-La-Roza, E. R. Johnson, and V. Luaña. Critic2: A program for real-space analysis of quantum chemical interactions in solids. *Computer Physics Communications*, 185(3):1007–1018, 2014. ISSN 00104655. doi: 10.1016/j.cpc.2013.10.026.

[44] M. J. Taylor and J. M. Coddington. The constitution of aqueous tin(IV) chloride and bromide solutions and solvent extracts studied by 119Sn NMR and vibrational spectroscopy. *Polyhedron*, 11(12):1531–1544, 1992. ISSN 02775387. doi: 10.1016/S0277-5387(00)83148-4.

[45] S. Kozuch. Steady State Kinetics of Any Catalytic Network: Graph Theory, the Energy Span Model, the Analogy between Catalysis and Electrical Circuits, and the Meaning of Mechanism. *ACS Catalysis*, 5(9):5242–5255, 2015. ISSN 2155-5435. doi: 10.1021/acscatal.5b00694.

[46] D. Curtin. Stereochemical Control of Organic Reaction Differences in Behavior of Diastereomers. *Rec. Chem. Prog.*, 15:111–128, 1954.

Chapter 6

DISTRIBUTION OF OPEN SITES IN SN-BETA ZEOLITE

6.1 Abstract

A survey of the open site geometries in Sn-Beta has been completed. Comparing the relative energies of 144 distinct open site structures identifies both T9 and T1 sites as the most stable open sites. However, a key feature of these sites is that the Sn-O-Si bridge which is hydrolyzed is opposite the SnOH, rather than adjacent. This results in geometries in which the SiOH in the open site is significantly more acidic than a surface SiOH or a SiOH defect in the zeolite, as found in adsorption calculations of NH_3, pyridine, and acetonitrile. Frequency shifts calculated for acetonitrile are consistent with experimental frequency shifts, and the proposed open site geometry suggests a new assignment for a peak observed experimentally by Harris, et al.[1] and Otomo, et al.[2] The stabilization of the open site silanol by the nearby Sn generates this unusual Brønsted acidity in the Sn-Beta open site, which highlights the need to consider new reaction mechanisms in the Sn-Beta literature.

6.2 Introduction

Sn-substituted zeolites have found applications in a wide range of carbonyl-activating chemistries, including Baeyer-Villiger oxidation of ketones to lactones [4], Meerwein-Ponndorf-Verley (MPV) reduction of carbonyls [5], 1,2-H-shift of glucose [6] and xylose [7], retro-aldol and esterification of sugars to lactates [8, 9], the 1,2-carbon shift of glucose [10] and arabinose [11], dehydration reactions in the production of

renewable aromatics from furans [12], and the catalytic transfer hydrogenation and etherification of 5-hydroxymethylfurfural [13]. Sn-Beta is particularly relevant for converting biomass derivatives derived from sugars – C5 and C6 compounds that are accommodated by its 12-member ring pores.

Several techniques have been employed to characterize the structure, activity, and selectivity of the active sites in Sn-Beta. Experiments with ^{119}Sn NMR on isotopically-enriched catalysts identified two distinct Sn sites: the closed site $Sn(OSi)_4$ and a hydrolyzed open site $Sn(OSi)_3OH$ [4, 14, 15]. Infrared spectroscopy of adsorbed CD_3CN has been used to quantify the relative amounts of open and closed sites [1, 2, 15, 16]. Boronat, et al. identified a correlation between the amount of CD_3CN adsorbed to open sites in different Sn-Beta samples and the zeolite activity for Baeyer-Villiger Oxidation, providing evidence for open sites as the active sites [16]. Bermejo-Deval, et al. showed that Na^+-exchange of Sn-Beta shifts glucose selectivity from fructose to mannose, shutting down the intramolecular 1,2-H-shift and activating the intramolecular 1,2-C-shift. In addition, NH_3 adsorption shuts down catalyst activity by blocking open sites [15]. Otomo, et al. identified weak Brønsted acidic silanols in Sn-Beta using IR spectroscopy of adsorbed CD_3CN, and showed that Li^+-, Na^+-, and NH_4^+-exchange passivates these silanols and reduces side reactions in Baeyer-Villiger Oxidation [2]. Recently, Harris, et al. demonstrated the use of pyridine as a selective titrant for these open sites, demonstrating a concomitant reduction in turn-over-frequency for glucose isomerization as open sites are blocked by increasing amounts of pyridine adsorption [1]. Brønsted acids have been hypothesized in Sn-Beta due to its activity in etherification [13], however pyridine adsorption has not given evidence of Brønsted acids in Sn-, Zr-, or Ti-Beta [17, 18].

Because individual Sn-Beta active sites are difficult to isolate and test in experiment, the Davis group has synthesized and tested silsesquioxane models of the Sn-Beta active sites [19, 20]. These have shown that while the open site model catalysts are significantly more active, the closed site model does have a small amount of glucose isomerization activity. However, the acac ligands present on the open site models stabilize

the C-shift reaction [21] and several differences between the heterogeneous and homogeneous systems, including solvent and confinement effects, conflated the comparison with Sn-Beta.

To attribute ν(C≡N) = 2316 cm^{-1} to the open site, and ν(C≡N) = 2308 cm^{-1} to the closed site, Boronat, et al. also performed DFT calculations using cluster models of Sn-Beta with Sn substituted at the T1, T5, and T9 sites[1]. Both T5 and T9 open sites gave comparable ν(C≡N) shifts to experimental ν(C≡N) shifts, and all open sites more strongly bound CH_3CN than the closed sites [16]. In the same year, Shetty, et al. used periodic-DFT to compare the relative stability of the Sn substitution at all nine T sites, finding T2 to be most stable [23] for closed sites – but open sites were not investigated. Also in the same year, Bare et al. used X-ray absorption fine structure (EXAFS) to characterize Sn-Beta, concluding that Sn is substituted as pairs into the T1 and T2 positions [24]. Since then, a number of theoretical mechanistic studies have used the T2 site [25, 26], the T7 site [27, 28], or T9 site [29] in investigations of the mechanism for glucose isomerization.

However, no systematic study of the relative stability of Sn-Beta open sites has been performed using periodic-DFT, to enable a comparison of open site stability on equal footing. This communication closes that gap by comparing the energies of 144 distinct Sn-Beta open sites, as well as the binding and spectroscopic features of the most stable sites that are identified.

6.3 Electronic structure methods

Periodic density function theory calculations were performed using the GPAW software [30, 31] in the ASE framework [32]. The core electrons were represented with the PAW formalism [33, 34], while the valence electrons were represented with the Perdew-Burke-Ernzerhof (PBE) exchange-correlation functional [35]. Optimizations

[1] Note about T site nomenclature: Here, we use the nomenclature originating in the work by Newsam, et al. [22]. An alternative nomenclature is used by the International Zeolite Associate Structure Commission website. We have included a note in Appendix E for clarification.

were performed using the quasi-Newton limited memory Broyden-Fletcher-Goldfarb-Shanno (LBFGS) optimizer [36]. Initial optimizations used a double-ζ plus polarization (DZP) linear combination of atomic orbitals (LCAO) basis set [37], and final optimizations were performed using the finite difference approach with a grid spacing of 0.2 Å. Electronic energies were optimized to a precision to 10^{-6} eV, with a Fermi-Dirac smearing of 0.1 eV, and nuclear degrees of freedom were optimized to a force convergence threshold of 0.05 eV Å^{-1}. Dispersion corrections were estimated using Grimme's DFT-d3 method [38], with structures reoptimized to 0.05 eV Å^{-1}. Frequencies and entropic corrections were calculated using LCAO, after re-optimizing with tighter electronic (10^{-8} eV) and force (0.01 eV Å^{-1}) convergence thresholds. All calculations were performed at the Γ-point.

6.4 Results and Discussion

6.4.1 Relative stability of closed sites

The geometry of polymorph A of the BEA zeolite framework was obtained from the International Zeolite Association online database [39]. Experimental unit cell parameters 12.632 x 12.632 x 26.186 Å were used. Sn atoms were substituted into the framework once at each of the nine T sites, with a Si/Sn ratio of 63 for all structures. The relative stability using PBE and PBE-d3 is reported in Table 6.1, in addition to those reported by Shetty, et al. [23]

We find several stable sites for Sn substitution, with T9, T1, and T6 within 1 kcal/mol. In fact, 7 of the sites are within 2.5 kcal/mol of the most stable T9, suggesting there may be a broad distribution of Sn substitutions at multiple sites. These calculations are considerably different from Shetty, et al., who found T2 and T8 to be relatively stable, but found higher energies ($>$ 3 kcal/mol) for the rest of the sites [23]. Differences between these works arise from employing ultrasoft Vanderbilt pseudopotentials instead of the PAW pseudopotentials used in our study.

	ΔE, PBE, kcal/mol	ΔE, PBE-d3, kcal/mol	ΔE from Shetty, et al.[20] (kcal/mol)
T1	0.459	1.074	6.762
T2	2.198	2.767	0
T3	1.386	1.347	4.899
T4	1.761	2.162	3.634
T5	4.013	4.338	6.348
T6	0.866	1.172	5.750
T7	2.802	3.086	5.152
T8	2.273	1.876	1.380
T9	0	0	8.234

Table 6.1: Relative stability of closed Sn-Beta sites

6.4.2 Relative stability of open sites

The open site of Sn-Beta occurs through the hydrolysis of the closed Sn site, producing a SnOH and a neighboring SiOH. As depicted in Figure 1, the closed Sn site is tetrahedral, with four framework bonds (1-4), and four "gaps" opposite each framework bond (A-D). Binding an OH to one of the "gaps" and binding an H to one of the bridges generates an open site. Each of the nine T sites has four "gaps" and four bridges, generating 144 unique geometries. For the most stable geometries, the SiOH and SnOH were rotated and reoptimized to search for the most stable configuration.

The BEA framework has two 12-ring cylindrical channels along the a and b directions, and a helical channel intersecting these along the c direction. Smaller 4, 5, and 6-ring channels also extend through the a and b directions, forming small (4 and 5-ring) and medium (6-ring) pockets between the 12-ring channels. For this study, we have organized the sites according to the location of each "gap" for the OH in a channel, medium cage, or small cage, and the connectivity of each bridge for the H

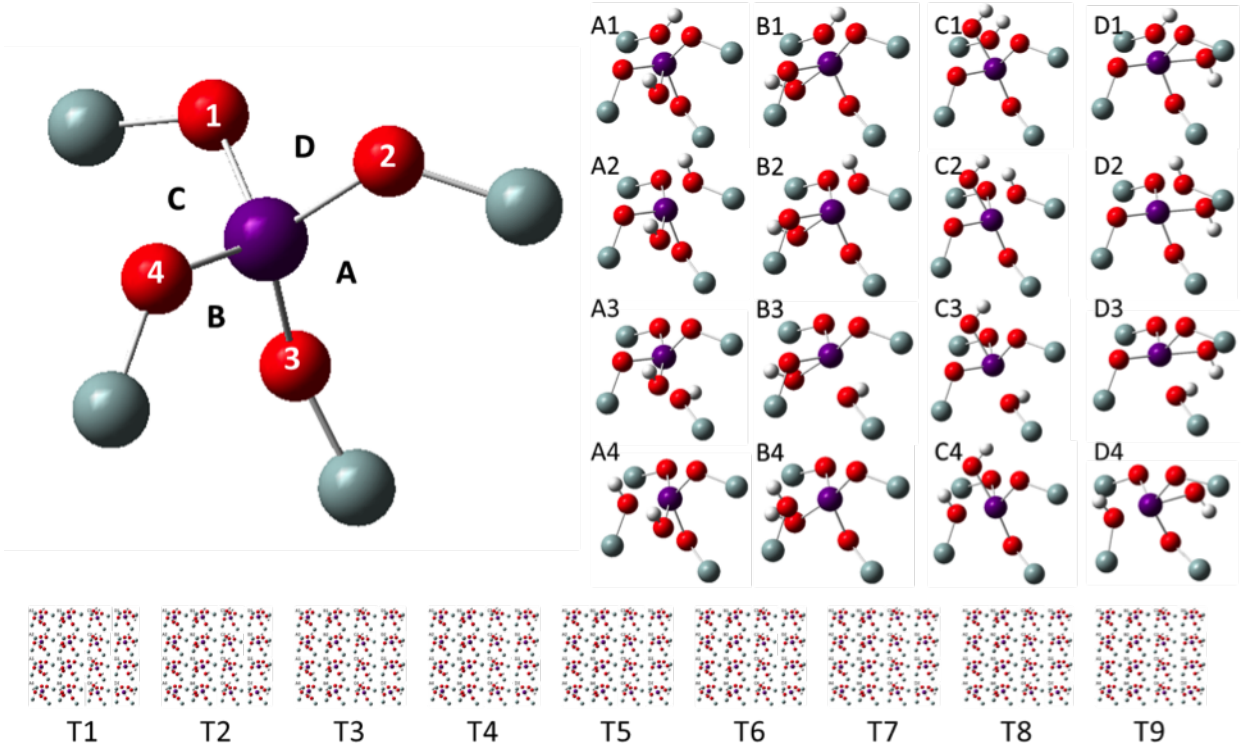

Figure 6.1: Diagram depicting tetrahedral Sn site, and four framework bonds (1-4) and four "gaps" opposite each framework bond (A-D). To form an open site, one H is placed on a framework bond and one OH is placed in a "gap," providing 16 unique bonding patterns for each T site. Repeating this procedure on all nine T sites generates 144 candidate open sites.

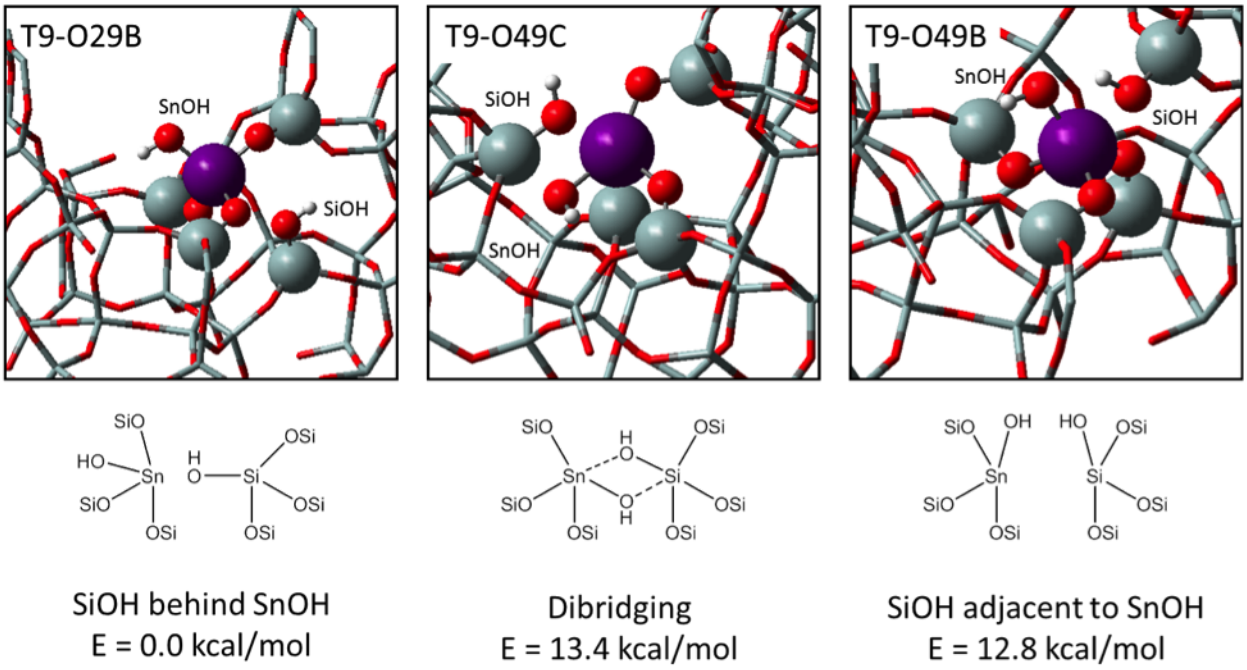

Figure 6.2: Selected geometries of different open site configurations. T9-O29B is the most stable open site geometry, and the SiOH is positioned behind the SnOH. Two additional geometries, T9-O49C and T9-O49B are shown to illustrate examples of less stable dibridging and H-bonded open sites, respectively. Energies are reported with respect to the most stable T9-O29B geometry.

(details available in Appendix E). In our geometry nomenclature, T1-O12A indicates a Sn at position T1, with the hydrogen on the oxygen of the T1-T2 bridge, and with the OH in gap A, a channel according to Table S1.

From this survey, we find the most stable open site to be T9-O29B, depicted in Fig. 6.2 along with a couple less stable alternative geometries. This site is characterized by a SnOH protruding into a channel, and the hydrolyzed bridge opposite the SnOH, so the SiOH oxygen is stabilized by the Sn. In fact, the most stable geometry for each site (highlighted in bold in Table S2 in Appendix E), is always characterized in the same way – the SnOH in a channel and the SiOH behind the SnOH.

In Fig. 6.3 the full data is plotted against a geometric descriptor: the distance

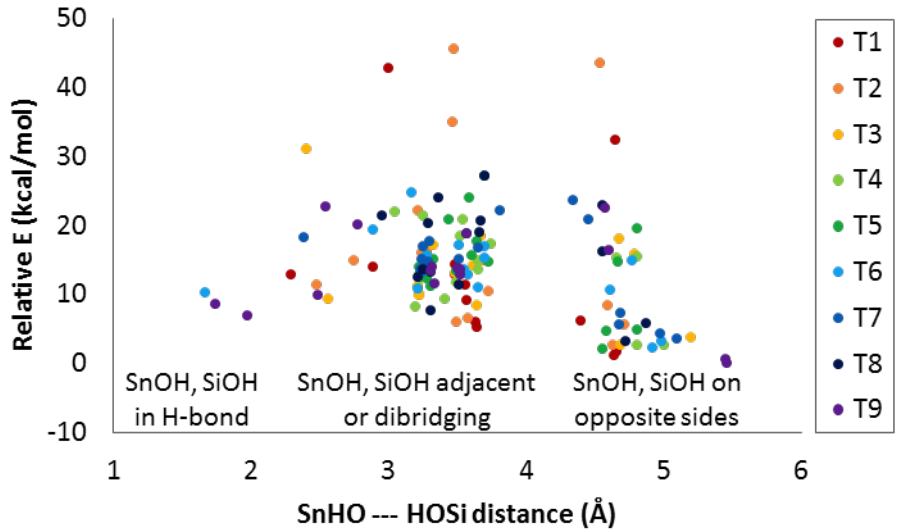

Figure 6.3: Relative PBE energy (kcal/mol) of open sites with respect to the distance between the oxygen of SnOH and the hydrogen of SiOH. The largest O—H distances (> 4 Å) correspond to geometries in which the SnOH and SiOH are on opposite sides, the shortest distances (< 2 Å) are approximate H-bonds between SiOH and SnOH, and the intermediate distances include the other structures, including the dibridging geometries.

between the oxygen atom of SnOH and the hydrogen atom of SiOH. This reveals a distinct pattern in the possible geometries: when the SiOH is behind the SnOH, the O$\cdots$H distance is greater than 4 Å; hydrolyzing any of the other three bridges results in a shorter O$\cdots$H distance. Moreover, the relative stability of the long-distance geometries over the short-distance ones is clear by comparing energies of structures within the same T site.

6.4.3 Possible mechanisms for open site formation

Sn-Beta synthesis starts from dealuminated H-Beta. Removing aluminum leaves behind silanol "nests," which react with $SnCl_4$ as it is incorporated into the framework. Incomplete condensation of all the silanols could generate open sites. The dynamics of this process are outside the scope of this chapter, but one can imagine the possibility

of open sites with either "adjacent" or "opposite" configurations after condensation. As we have shown, open sites with the SiOH adjacent to the SnOH are typically thermodynamically less stable than those with the SiOH opposite the SnOH. In some of these cases (but not all), the adjacent SiOH can transfer its proton to the opposite Sn-O-Si bridge and form the corresponding opposite open site. We tested this for converting T9-O49A (adjacent SiOH) into T9-O29A (opposite SiOH) and found the proton transfer to have a negligible barrier (11 kcal/mol) for relaxing to the more stable open site geometry. Alternatively, water can assist the proton transfer through the Grotthuss mechanism, reducing this already-small barrier to 1 kcal/mol (Table S3 in Appendix E).

Another hypothesized route is through the hydrolysis of closed sites. After adsorption to a closed site, water deprotonates to a Sn-O-Si bridge, forming an "adjacent" open site. Rotation of the H atom about the Si-O bond can then direct it toward the Sn-O-Si bridge that is opposite the SnOH. Transfer of the proton from the SiOH to the bridge could then generate the "opposite" open site. For converting the T9 closed site into T9-O29A in the gas phase, we found the overall barrier to be 24.6 kcal/mol. Details of the reaction are provided in Table S3 in Appendix E.

6.4.4 Adsorption of Lewis Bases

Adsorption energies of the Lewis bases NH_3, pyridine, and acetonitrile were also calculated for the most stable closed (T9) and open site (T9-O29B) geometries (Table 6.2 and Fig. 6.4). Because the Sn site is at the intersection of two channels, adsorbates can coordinate to two locations on the Sn closed and open sites, as well as to the SnOH and the SiOH for the open site. Different features of the active sites strongly affect adsorption behavior. For all systems, with the exception of NH_3 with PBE-d3, the open site binds 2.5–8 kcal/mol more strongly than the closed site, in agreement with prior work [16].

Acetonitrile binds more weakly to the sites than NH_3 and pyridine. It binds most strongly to the Sn Lewis acid of the open site, binding 2–4 kcal/mol more weakly

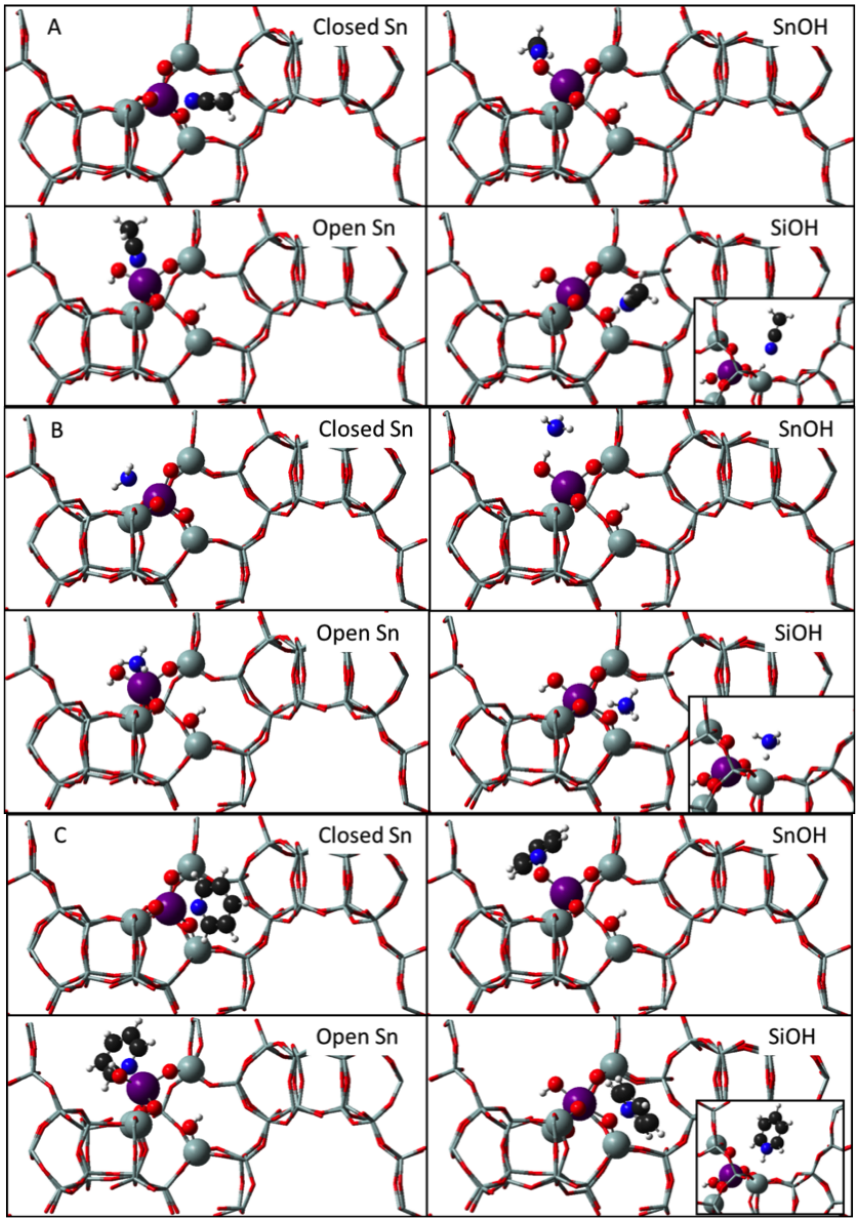

Figure 6.4: Most stable adsorption geometries of acetonitrile (A), NH_3 (B), and pyridine (C) on the T8 Sn-Beta closed Sn site, open Sn site, open SnOH, and open SiOH. Inset image shows side view of adsorbate bound to the SiOH. Adsorbates and first coordination shell around Sn site are depicted using ball-and-stick model, while rest of zeolite framework is depicted using tube model.

PBE ΔE	Closed Sn 1	Closed Sn 2	Open Sn 1	Open Sn 2	SnOH	SiOH
Acetonitrile	-7.00	-6.98	-9.56	-10.43	-8.55	-6.13
NH3	-15.54	-16.11	-15.72	-18.49	-10.36	-15.45
Pyridine	-12.47	-12.06	-13.90	-20.91	-9.12	-18.40

PBE-d3 ΔE	Closed Sn 1	Closed Sn 2	Open Sn 1	Open Sn 2	SnOH	SiOH
Acetonitrile	-15.98	-16.01	-17.39	-16.01	-14.33	-14.40
NH3	-21.46	-22.20	-21.09	-21.85	-13.82	-22.24
Pyridine	-27.73	-27.36	-29.21	-32.35	-22.41	-34.34

PBE ΔG	Closed Sn 1	Closed Sn 2	Open Sn 1	Open Sn 2	SnOH	SiOH
Acetonitrile	6.33		1.01	-2.55	0.08	4.13

Table 6.2: Binding energies in kcal/mol calculated with PBE for various bases on the Sn sites, with gas phase adsorbate and bare catalyst as reference.

to the Sn closed site or to the SnOH or SiOH. For the stronger bases, NH_3 and pyridine, the SnOH is weakly binding, while the Sn Lewis acid binds comparably to the SiOH; for PBE, the Sn Lewis acid binds 2–3 kcal/mol more strongly that the SiOH, while for PBE-d3, the SiOH binds 1–2 kcal/mol more strongly than the Sn Lewis acid. IR spectroscopy of Sn-Beta with adsorbed pyridine has not shown evidence of pyridinium, possibly indicating that pyridine adsorption to the Lewis site is favored over adsorption to the SiOH, in agreement with the PBE binding energies, but not the PBE-d3 [18].

Adsorption geometries (PBE) are shown in Fig. 6.4. These highlight the unusually acidic nature of the SiOH in the Sn-Beta open site. For NH_3 and pyridine, the SiOH deprotonates to the adsorbate, and the SiO binds to the Sn. In the open site, the Sn$\cdots$O(H)Si distance is 3.23 Å, while the SiO$\cdots$H distance is 0.98 Å. When NH_3 or pyridine bind to the SiOH, the Sn—OSi distances shrinks to 2.16 Åand 2.14 Å, respectively, and the SiO$\cdots$H distance increases to 1.60 and 1.80 Å, respectively. Acetonitrile does not abstract the proton, leaving the SiO—H distance at 1.02 Å, but the Sn$\cdots$O(H)Si distance still decreases to 2.48 Å, indicating some stabilization of the SiOH by the Sn.

6.4.5 Acetonitrile Vibrations

We calculated vibrational frequencies for adsorbed acetonitrile to compare with prior work. The ν(C≡N) frequency blueshifts as acetonitrile binds to the catalyst, and it shifts by 35.5 cm^{-1} on the closed Sn site, and 41.2 cm^{-1} on the open Sn site, the same trend observed in cluster models of closed and open sites [16], and in agreement with experimental shifts of the peaks assigned to these two types of Lewis sites [1, 15, 16]. Acetonitrile can also bind to the SnOH and the SiOH in the open site. Adsorption to the SnOH shifts ν(C≡N) by 13 cm^{-1}, while adsorption to the SiOH shifts ν(C≡N) significantly more; by 29.6 cm^{-1}. To compare this to SiOH defects and surface SiOH, we created a SiOH defect in the Sn-Beta framework by replacing the Sn in the open site with a Si, and also by removing the Sn atom. Acetonitrile binds less strongly to these SiOH groups, with ν(C≡N) shifting by an average of 18.2 cm^{-1}. The trend in these shifts on these typical SiOH groups is consistent with experimental ν(C≡N) shift of 10 cm^{-1}, as well as calculated ν(C≡N) shift for a bare SiOH cluster [16]. Boronat, et al. found the calculated frequency for SnOH binding to be comparable to that of SiOH, in agreement with our calculated ν(C≡N) shift on the SnOH. However, the open site SiOH next to the Sn is significantly more acidic, with a dramatically stronger ν(C≡N) compared to a surface SiOH, indicative of its unique character because of its interaction with the Sn. This Brønsted acidity, arising from the Sn$\cdots$O(H)Si interaction in the hydrolyzed open site, is consistent with experimental IR spectroscopy of adsorbed CD_3CN [1, 2], and with observations of etherification activity in Sn-Beta [13].

6.5 Conclusions

Using periodic DFT, we have completed a survey of open site geometries in the Sn-Beta zeolite. At every T site, the most stable geometry is characterized by a SnOH protruding into a channel, and an SiOH behind the SnOH. The most stable site is the T9, although several T sites have energies within 2 kcal/mol of the most stable geometry. Adsorption of strong bases such as NH_3 and pyridine is favored at the open Sn Lewis site; however adsorption to the SiOH has comparable binding strength to

	Closed Sn	Open Sn	Open Sn SiOH (acidic)	Open Sn SiOH	SnOH	SiOH	Gas Phase
Calc. ν(C≡N) (cm^{-1}) Δν(C≡N) (cm^{-1})	2281.9 33.3	2287.6 39	2278.2 29.6	2261.7 13.1	2261.6 13.0	2266.8 18.2	2248.6 0
Exp.[15] ν(C≡N) (cm^{-1}) Δν(C≡N) (cm^{-1})	2308 43	2316 51				2276 11	2265 0
Calc.[15] Δν(C≡N) (cm^{-1}) Average of T1, T5, T9	43	53			17	16	
Exp.[14] ν(C≡N) (cm^{-1}) Δν(C≡N) (cm^{-1})	2307	2315				2276	
Exp.[1,2] ν(C≡N) (cm^{-1}) Δν(C≡N) (cm^{-1})	2308 43	2316 51	2287 * 22 *			2275 10	2265 0

Table 6.3: Vibrational frequencies of acetonitrile adsorbed onto different Sn sites, and comparison with literature. * Harris, et al.[1] assigned this frequency to a speculated doubly-hydrolyzed Sn site and Otomo, et al.[2] observed this peak, but did not assign it; we list it here with our proposed assignment.

the Lewis site, and resulted into abstraction of the SiOH proton. Calculated frequency shifts of acetonitrile are in agreement with prior experimental and theoretical work. The primary finding is evidence for unusual Brønsted acidity in the Sn-Beta open site, which may enable new reaction mechanisms not yet considered in the literature.

6.6 Acknowledgements

Research was supported as part of the Catalysis Center for Energy Innovation, an Energy Frontier Research Center funded by the U.S. Department of Energy (DOE), Office of Science, Basic Energy Sciences (BES), under Award number DE-SC0001004. This research used resources of the National Energy Research Scientific Computing Center, a DOE Office of Science User Facility supported by the Office of Science of the U.S. Department of Energy under Contract No. DE-AC02-05CH11231. T.R.J. wishes to acknowledge funding from the National Science Foundation Graduate Research Fellowship Program under Grant No. 0750966, as well as the George W. Laird Merit Fellowship. Any opinions, findings, and conclusions or recommendations expressed in

this material are those of the author(s) and do not necessarily reflect the views of the National Science Foundation. The authors would like to thank Zhiqiang Zhang for numerous useful conversations.

REFERENCES

[1] J. W. Harris, M. J. Cordon, J. R. Di Iorio, J. C. Vega-Vila, F. H. Ribeiro, and R. Gounder. Titration and quantification of open and closed Lewis acid sites in Sn-Beta zeolites that catalyze glucose isomerization. *Journal of Catalysis*, 335: 141–154, 2016. ISSN 00219517. doi: 10.1016/j.jcat.2015.12.024.

[2] R. Otomo, R. Kosugi, Y. Kamiya, T. Tatsumi, and T. Yokoi. Modification of Sn-Beta zeolite: characterization of acidic/basic properties and catalytic performance in BaeyerVilliger oxidation. *Catal. Sci. Technol.*, 6(8):2787–2795, 2016. ISSN 2044-4753. doi: 10.1039/C6CY00532B.

[3] T. R. Josephson, G. R. Jenness, D. G. Vlachos, and S. Caratzoulas. Distribution of open sites in Sn-Beta zeolite. *Microporous and Mesoporous Materials*, 245:45–50, 2017. ISSN 13871811. doi: 10.1016/j.micromeso.2017.02.065.

[4] A. Corma, L. T. Nemeth, M. Renz, and S. Valencia. Sn-zeolite beta as a heterogeneous chemoselective catalyst for Baeyer-Villiger oxidations. *Nature*, 412(6845): 423–425, 2001. ISSN 0028-0836. doi: 10.1038/35086546.

[5] A. Corma, M. E. Domine, L. Nemeth, and S. Valencia. Al-free Sn-Beta zeolite as a catalyst for the selective reduction of carbonyl compounds (Meerwein-Ponndorf-Verley Reaction). *Journal of the American Chemical Society*, 124:3194–3195, 2002. ISSN 00027863. doi: 10.1021/ja012297m.

[6] M. Moliner, Y. Roman-Leshkov, M. E. E. Davis, Y. Román-Leshkov, and M. E. E. Davis. Tin-containing zeolites are highly active catalysts for the isomerization of glucose in water. *Proc Natl Acad Sci U S A*, 107(14):6164–6168, 2010. ISSN 1091-6490. doi: 10.1073/pnas.1002358107.

[7] V. Choudhary, A. B. Pinar, S. I. Sandler, D. G. Vlachos, and R. F. Lobo. Xylose isomerization to xylulose and its dehydration to furfural in aqueous media. *ACS Catalysis*, 1(12):1724–1728, 2011. ISSN 21555435. doi: 10.1021/cs200461t.

[8] M. S. Holm, S. Saravanamurugan, and E. Taarning. Conversion of sugars to lactic acid derivatives using heterogeneous zeotype catalysts. *Science (New York, N.Y.)*, 328(5978):602–605, 2010. ISSN 0036-8075. doi: 10.1126/science.1183990.

[9] M. Orazov and M. E. Davis. Tandem catalysis for the production of alkyl lactates from ketohexoses at moderate temperatures. *Proceedings of the National Academy of Sciences*, 112(38):201516466, 2015. ISSN 0027-8424. doi: 10.1073/pnas.1516466112.

[10] R. Bermejo-Deval, R. Gounder, and M. E. Davis. Framework and extraframework tin sites in zeolite beta react glucose differently. *ACS Catalysis*, 2(12):2705–2713, 2012. ISSN 21555435. doi: 10.1021/cs300474x.

[11] W. R. Gunther, Y. Wang, Y. Ji, V. K. Michaelis, S. T. Hunt, R. G. Griffin, and Y. Román-Leshkov. Sn-Beta zeolites with borate salts catalyse the epimerization of carbohydrates via an intramolecular carbon shift. *Nature communications*, 3: 1109, 2012. ISSN 2041-1723. doi: 10.1038/ncomms2122.

[12] C. L. Williams, C.-C. Chang, P. Do, N. Nikbin, S. Caratzoulas, D. G. Vlachos, R. F. Lobo, W. Fan, and P. J. Dauenhauer. Cycloaddition of Biomass-Derived Furans for Catalytic Production of Renewablep-Xylene. *ACS Catalysis*, 2(6):935–939, 2012. doi: 10.1021/cs300011a.

[13] J. D. Lewis, S. Van De Vyver, A. J. Crisci, W. R. Gunther, V. K. Michaelis, R. G. Griffin, and Y. Román-Leshkov. A continuous flow strategy for the coupled transfer hydrogenation and etherification of 5-(hydroxymethyl)furfural using lewis acid zeolites. *ChemSusChem*, 7(8):2255–2265, 2014. ISSN 1864564X. doi: 10.1002/cssc.201402100.

[14] R. Bermejo-Deval, R. S. S. Assary, E. Nikolla, M. Moliner, Y. Roman-Leshkov, S.-J. S.-J. Hwang, A. Palsdottir, D. Silverman, R. F. Lobo, L. A. Curtiss, and M. E. Davis. Metalloenzyme-like catalyzed isomerizations of sugars by Lewis acid zeolites. *Proceedings of the National Academy of Sciences*, 109(25):9727–9732, 2012. ISSN 0027-8424. doi: 10.1073/pnas.1206708109.

[15] R. Bermejo-Deval, M. Orazov, R. Gounder, S. J. Hwang, and M. E. Davis. Active sites in Sn-beta for glucose isomerization to fructose and epimerization to mannose. *ACS Catalysis*, 4(7):2288–2297, 2014. ISSN 21555435. doi: 10.1021/cs500466j.

[16] M. Boronat, P. Concepción, A. Corma, M. Renz, and S. Valencia. Determination of the catalytically active oxidation Lewis acid sites in Sn-beta zeolites, and their optimisation by the combination of theoretical and experimental studies. *Journal of Catalysis*, 234(1):111–118, 2005. ISSN 00219517. doi: 10.1016/j.jcat.2005.05.023.

[17] Y. Zhu, G. K. Chuah, and S. Jaenicke. Selective Meerwein-Ponndorf-Verley reduction of α, β-unsaturated aldehydes over Zr-zeolite beta. *Journal of Catalysis*, 241(1):25–33, 2006. ISSN 00219517. doi: 10.1016/j.jcat.2006.04.008.

[18] B. Tang, W. Dai, G. Wu, N. Guan, L. Li, and M. Hunger. Post-synthesis of Sn-Beta zeolites as Lewis acid catalysts for the ring-open hydration of epoxides. *ACS Catalysis*, 4:2801–2810, 2014.

[19] S. K. Brand, J. A. Labinger, and M. E. Davis. Tin Silsesquioxanes as Models for the "Open" Site in Tin-Containing Zeolite Beta. *ChemCatChem*, 8(1):121–124, 2016. ISSN 18673899. doi: 10.1002/cctc.201501067.

[20] S. K. Brand, T. R. Josephson, J. A. Labinger, S. Caratzoulas, D. G. Vlachos, and M. E. Davis. Methyl-Ligated Tin Silsesquioxane Catalyzed Reactions of Glucose. *Journal of Catalysis*, 341:62–71, 2016.

[21] T. R. Josephson, S. K. Brand, S. Caratzoulas, and D. G. Vlachos. 1,2-H- versus 1,2-C-Shift on Sn-Silsesquioxanes. *ACS Catalysis*, pages 25–33, 2016. ISSN 2155-5435. doi: 10.1021/acscatal.6b03128.

[22] J. Newsam, M. Treacy, W. Koetsier, and C. de Gruyter. Structural characterization of zeolite beta. *Proc R Soc Lond A*, 420:375–405, 1988. ISSN 1364-5021. doi: 10.1098/rspa.1983.0054.

[23] S. Shetty, S. Pal, D. G. Kanhere, and A. Goursot. Structural, electronic, and bonding properties of zeolite Sn-beta: A periodic density functional theory study. *Chemistry - A European Journal*, 12(2):518–523, 2005. ISSN 09476539. doi: 10.1002/chem.200500487.

[24] S. R. Bare, S. D. Kelly, W. Sinkler, J. J. Low, S. Valencia, A. Corma, L. T. Nemeth, F. S. Modica, S. Valencia, A. Corma, and L. T. Nemeth. Uniform catalytic site in Sn-β-zeolite determined using X-ray absorption fine structure. *J. Am. Chem. Soc.*, 127(37):12924–12932, 2005. doi: 10.1021/ja052543k.

[25] G. Yang, E. A. Pidko, and E. J. M. Hensen. The mechanism of glucose isomerization to fructose over Sn-BEA zeolite: A periodic density functional theory study. *ChemSusChem*, 6(9):1688–1696, 2013. ISSN 18645631. doi: 10.1002/cssc.201300342.

[26] Y. P. P. Li, M. Head-Gordon, and A. T. T. Bell. Analysis of the reaction mechanism and catalytic activity of metal-substituted beta zeolite for the isomerization of glucose to fructose. *ACS Catalysis*, 4(5):1537–1545, 2014. ISSN 21555435. doi: 10.1021/cs401054f.

[27] T. D. Courtney, C.-C. Chang, R. J. Gorte, R. F. Lobo, W. Fan, and V. Nikolakis. Effect of water treatment on Sn-BEA zeolite: Origin of 960cm1 FTIR peak. *Microporous and Mesoporous Materials*, 210:69–76, 2015. ISSN 13871811. doi: 10.1016/j.micromeso.2015.02.012.

[28] J. R. Christianson, S. Caratzoulas, and D. G. Vlachos. Computational Insight into the Effect of Sn-Beta Na Exchange and Solvent on Glucose Isomerization and Epimerization. *ACS Catalysis*, 5(9):5256–5263, 2015. ISSN 2155-5435. doi: 10.1021/acscatal.5b01258.

[29] N. Rai, S. Caratzoulas, and D. G. Vlachos. Role of silanol group in Sn-beta zeolite for glucose isomerization and epimerization reactions. *ACS Catalysis*, 3 (10):2294–2298, 2013. ISSN 21555435. doi: 10.1021/cs400476n.

[30] J. Mortensen, L. Hansen, and K. Jacobsen. Real-space grid implementation of the projector augmented wave method. *Physical Review B*, 71(3):035109, 2005. ISSN 1098-0121. doi: 10.1103/PhysRevB.71.035109.

[31] J. Enkovaara, C. Rostgaard, J. J. Mortensen, J. Chen, M. Dułak, L. Ferrighi, J. Gavnholt, C. Glinsvad, V. Haikola, H. a. Hansen, H. H. Kristoffersen, M. Kuisma, a. H. Larsen, L. Lehtovaara, M. Ljungberg, O. Lopez-Acevedo, P. G. Moses, J. Ojanen, T. Olsen, V. Petzold, N. a. Romero, J. Stausholm-Møller, M. Strange, G. a. Tritsaris, M. Vanin, M. Walter, B. Hammer, H. Häkkinen, G. K. H. Madsen, R. M. Nieminen, J. K. Nørskov, M. Puska, T. T. Rantala, J. Schiøtz, K. S. Thygesen, and K. W. Jacobsen. Electronic structure calculations with GPAW: a real-space implementation of the projector augmented-wave method. *Journal of physics. Condensed Matter*, 22(25):253202, 2010. ISSN 0953-8984. doi: 10.1088/0953-8984/22/25/253202.

[32] S. R. Bahn and K. W. Jacobsen. An object-oriented scripting interface to a legacy electronic structure code. *Computing in Science and Engineering*, 4(3):56–66, 2002. ISSN 15219615. doi: 10.1109/5992.998641.

[33] P. E. Blöchl. Projector augmented-wave method. *Physical Review B*, 50(24): 17953–17979, 1994. ISSN 01631829. doi: 10.1103/PhysRevB.50.17953.

[34] G. Kresse. From ultrasoft pseudopotentials to the projector augmented-wave method. *Physical Review B*, 59(3):1758–1775, 1999. ISSN 1098-0121. doi: 10.1103/PhysRevB.59.1758.

[35] J. P. Perdew, K. Burke, and M. Ernzerhof. Generalized Gradient Approximation Made Simple. *Physical Review Letters*, 77(18):3865–3868, 1996. ISSN 0031-9007. doi: 10.1103/PhysRevLett.77.3865.

[36] D. C. Liu and J. Nocedal. On the Limited Memory Method for Large Scale Optimization. *Math. Programming, B*, 45(3):503–528, 1989. ISSN 00255610. doi: 10.1007/BF01589116.

[37] A. H. Larsen, M. Vanin, J. J. Mortensen, K. S. Thygesen, and K. W. Jacobsen. Localized atomic basis set in the projector augmented wave method. *Physical Review B - Condensed Matter and Materials Physics*, 80(19):1–10, 2009. ISSN 10980121. doi: 10.1103/PhysRevB.80.195112.

[38] S. Grimme, J. Antony, S. Ehrlich, and H. Krieg. A consistent and accurate ab initio parametrization of density functional dispersion correction (DFT-D) for the 94 elements H-Pu. *Journal of Chemical Physics*, 132(15), 2010. ISSN 00219606. doi: 10.1063/1.3382344.

[39] C. Baerlocher and L. B. McCusker. Database of Zeolite Structures.

Chapter 7

SELECTIVE FRUCTOSE ETHERIFICATION ON HIERARCHICAL SN-SPP ZEOLITE

7.1 Abstract

While Lewis-acid zeolites such as Sn-Beta catalyze glucose isomerization in an alcoholic medium, mesoporous Sn-SPP catalyzes both glucose isomerization to fructose and fructose etherification (formally ketalization) to ethyl fructoside, enabling fructose yields in excess of the glucose/fructose equilibrium. Using periodic DFT calculations and Monte Carlo simulations, the ketalization reaction mechanism and adsorption behavior were examined. The silanols in Sn-SPP facilitate the ketalization reaction through H-bonding interactions at the transition state, only possible via a Sn-O-Si-OH moiety, present in Sn-SPP but not in Sn-Beta. Fructose ketalization is favored over glucose acetalization due to differences in stability of the oxonium intermediates, which are stabilized by the Sn-SPP active site. The open site of hydrophobic Sn-Beta cannot perform these reactions, because its active site does not contain the requisite silanol.

7.2 Introduction

In the integrated "biorefinery" concept, the cellulose, hemicellulose, and lignin fractions of biomass are separated, processed, and upgraded into a diverse slate of chemical products, akin to crude oil processing in a refinery [1–5]. In particular, furan derivatives such as 5-hydroxymethylfurfural are promising platform chemicals derived from sugars [6–8]. While aldoses such as glucose and xylose are abundant as major constituents of cellulose and hemicellulose, ketoses are more valuable for their higher yields to furans [9]. Therefore, ketose/aldose isomerization is a key reaction for enabling the conversion the furans platform for renewable chemicals.

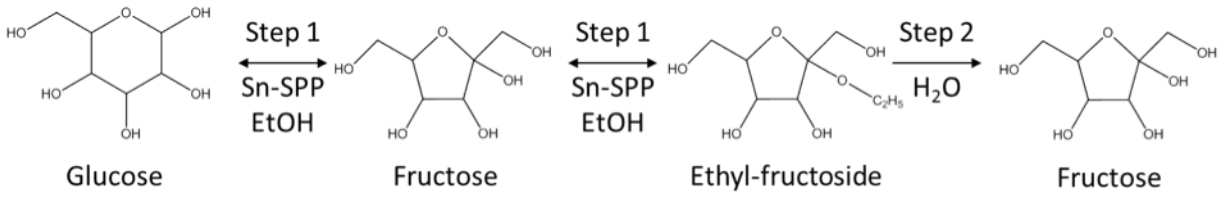

Figure 7.1: Reaction scheme for improving fructose yields from glucose using tandem reactions with fructose ketalization.

Lewis acidic zeolites such as Sn-Beta have been demonstrated to convert glucose [10] and xylose[11] into fructose and xylulose, respectively, via an intramolecular 1,2-H-shift reaction [12]. These catalysts have achieved 33% yield[10] to fructose in aqueous media, with a 9% yield to mannose, approaching the 50% equilibrium yield achieved with the glucose isomerase enzyme [13]. One strategy for boosting the fructose yield beyond the glucose/fructose equilibrium was proposed by Saravanamurugan and coworkers [14] (see Fig. 7.1). When glucose was reacted in methanolic solutions with H-USY zeolite, the fructose product formed an ether with methanol, producing methyl fructoside and shifting equilibrium towards the products. Subsequent addition of water restored the fructoside to fructose, producing a total fructose yield of over 55% [14]. In ethanol, however, H-USY catalyzed the acetalization of glucose as well, reducing yields to the fructose product, although side reactions can be reduced by optimizing the ratio of Lewis and Brønsted acids in the zeolite [15]. The same authors have also found H-USY to be useful for acetalization of furfural [16].

Ren and coworkers have also demonstrated glucose isomerization/fructose ketalization over the hierarchical zeolite Sn-SPP zeolite, achieving 65% fructose yield using a similar reaction procedure in ethanol [17]. The hierarchical mesoporous structure of the self-pillared pentasil (SPP) framework (see Fig. 7.2) also permitted isomerization of disaccharides. Pillared Sn-MWW, based on another zeolite framework, has also been shown to be active for mono- and di-saccharide isomerization through the same tandem reaction procedure [18]. A remarkable feature of both catalysts is the suppression of

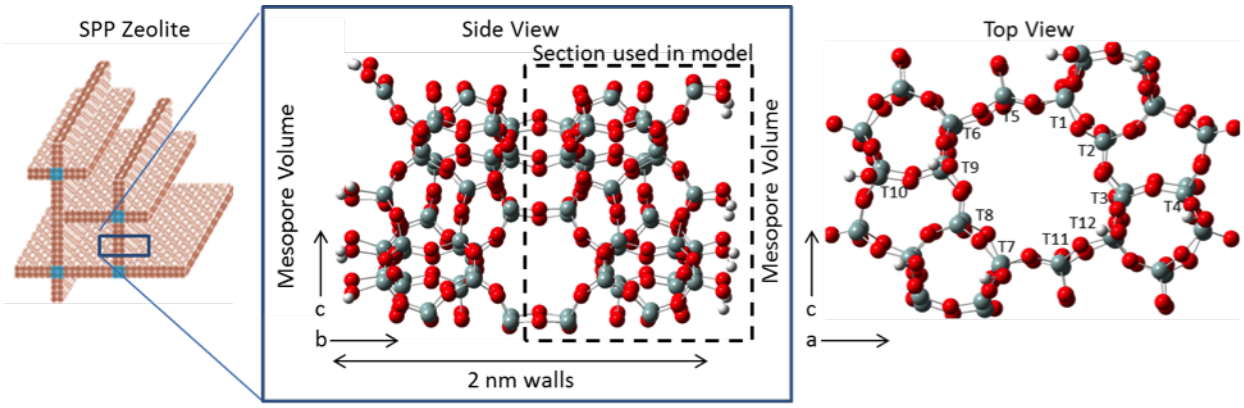

Figure 7.2: Structure of the self-pillared pentasil (SPP) zeolite. The cage walls are comprised of intergrown 2D layers of MFI framework zeolite, with a 2 nm thickness corresponding to the width of the b axis of the MFI unit cell. The catalyst model was constructed using one half of the MFI unit cell (dashed box), each side of which is terminated by eight silanol groups per unit cell.

the glucose acetal product. Interestingly, another mesoporous, Sn-containing zeolite, three dimensionally ordered mesoporous imprinted (3DOm-i) Sn-MFI was found to be active for glucose isomerization, but not fructose ketalization, in methanol [19].

The reaction of fructose to ethyl fructoside is formally a ketalization reaction. Acetals and ketals are textbook protecting groups and are effective for stabilizing aldehydes and ketones and protecting them from attack by nucleophiles and bases [20]. While Brønsted acid catalysis mechanisms have been proposed using organic chemistry principles [20], we have not found any proposed mechanisms for Lewis acid catalysis, nor any theoretical study examining either Brønsted or Lewis acid-catalyzed (ace)ketalization mechanisms. Moreover, the experimental data do not provide insight into how these pillared, Lewis-acidic zeolites catalyze the fructose ketalization but not the glucose acetalization, nor why other Lewis acid catalysts, such as Sn-BEA, catalyze the isomerization, but not the ketalization, in alcoholic media.

In this work, we apply electronic structure calculations to characterize the active site in Sn-SPP, and show the importance of the Sn-O-Si-OH moiety for the catalysis

of the ketalization, which is present in Sn-SPP but not in Sn-Beta.

7.3 Methods

Periodic density function theory calculations were performed using the GPAW software [21, 22] in the ASE framework [23]. Core electrons were represented with the PAW formalism [24, 25], while the valence electrons were represented with the Perdew-Burke-Ernzerhof (PBE) exchange-correlation functional [26]. Optimizations were performed using the quasi-Newton limited memory Broyden-Fletcher-Goldfarb-Shanno (LBFGS) optimizer [27]. Reaction pathways were computed using the nudged elastic band (NEB) method [28] with typically 8-12 images between local minima, with transition states identified using the dimer method [29–32]. Initial optimizations used a double-ζ plus polarization (DZP) linear combination of atomic orbitals (LCAO) basis set [33], with final optimizations performed using the finite difference approach with a grid spacing of 0.2 Å. Electronic energies were optimized to a precision to 10^{-6} eV and atomic coordinates were optimized to a force convergence threshold of 0.05 eV Å^{-1}. Frequencies and free energy corrections were calculated using finite differences, with a grid spacing of 0.18 Å and a tighter SCF convergence (10^{-8} eV). All calculations were performed at the Γ-point.

7.4 Active site of Sn-SPP

The self-pillared pentasil (SPP) zeolite is comprised of intergrown 2D layers of the MFI zeolite framework [34]. Atomic force microscopy (AFM) has shown the wall thickness to be 2 nm, and transmission electron microscopy (TEM) with FFT analysis showed the zeolite walls correspond to the b-axis of the MFI unit cell [34]. To model the SPP zeolite, we represent it as a single 2D layer of MFI zeolite, periodic in the a-c plane, as shown in Fig. 7.2. To accelerate the calculations and focus on the surface chemistry, the zeolite was cut in half along the b-axis, approximately halving the number of atoms in the calculation. The underside of the surface was terminated

with hydrogens, and these were constrained, along with the layer of atoms within 7 Å of the bottom of the periodic cell (52 atoms).

MFI has twelve distinct crystallographic locations (Fig. 7.2). In the Sn-SPP zeolite, there are more, because some of these sites are present inside the interior of the zeolite layer while others are at the surface. However, because hexoses are not admitted into the micropores of MFI [35] the relevant Sn site must be present at the surface. An inventory of these twelve surface sites on SPP is given in Table 1. Substituting Sn into each of these sites would generate a Sn site with different properties. Four sites are "terminal" sites, $HOSn(SiO)_3$ (T7, T9, T10, T12), while the remaining eight sites are "closed" sites, $Sn(SiO)_4$. The "terminal" sites are located where the MFI framework is terminated at the surface, and are distinct from the similar "open" sites of Sn-Beta, which are paired with a silanol produced through hydrolysis of a closed site or through incomplete condensation. The surface is densely populated with silanols; of the eight closed sites, two have three adjacent silanols (T8 and T11), four have one (T1, T3, T4, T6), and two have zero (T2 and T5) – although sites with zero adjacent SiOH have three or four 2nd nearest neighbor silanols (Table 1).

To identify the most thermodynamically stable site for Sn substitution, we optimized the geometries of Sn-SPP with Sn in each of these sites. The T8 site is most thermodynamically stable, closely followed by the "terminal" sites T10, T9, T7, and T12. Because ^{119}Sn-NMR of Sn-SPP found evidence of only tetrahedrally coordinated "closed" Sn sites [17], the T8 site was chosen as the site most consistent with the experimental and theoretical results. T8 has three adjacent silanols, and is located at the boundary of the MFI pore.

7.5 Reaction Mechanism Analysis

Ketalization occurs in two steps (Sch. 7.3a): addition of an alcohol to a ketone to form a hemiketal, and reaction of another alcohol with the hemiketal, eliminating water and forming the ketal. For the ketalization of fructose, the O5 hydroxyl of fructose and the ethanol hydroxyl react with the C2 keto group, generating two overall

Substitution	Relative E (kcal/mol)	Adjacent SiOH	Type of Site
T8	0	3	Closed
T10	0.39	1	Terminal
T9	0.55	1	Terminal
T7	1.64	0	Terminal
T12	2.38	0	Terminal
T11	4.12	3	Closed
T4	5.15	1	Closed
T3	7.70	1	Closed
T1	7.75	1	Closed
T5	8.48	0	Closed
T2	8.98	0	Closed
T6	12.18	1	Closed

Table 7.1: Relative stability of the Sn substitution at 12 surface locations on the SPP unit cell. Comments regarding the local environment of each Sn are provided, including the number of adjacent silanol groups (indicating Sn-O-Si-OH moieties), and whether or not the substitution occurs at a site where the MFI framework is terminated, generating a $HOSn(OSi)_3$, or a closed site, a $Sn(OSi)_4$. It should be noted that the sites with 0 NN still had 3-4 2nd NN silanols.

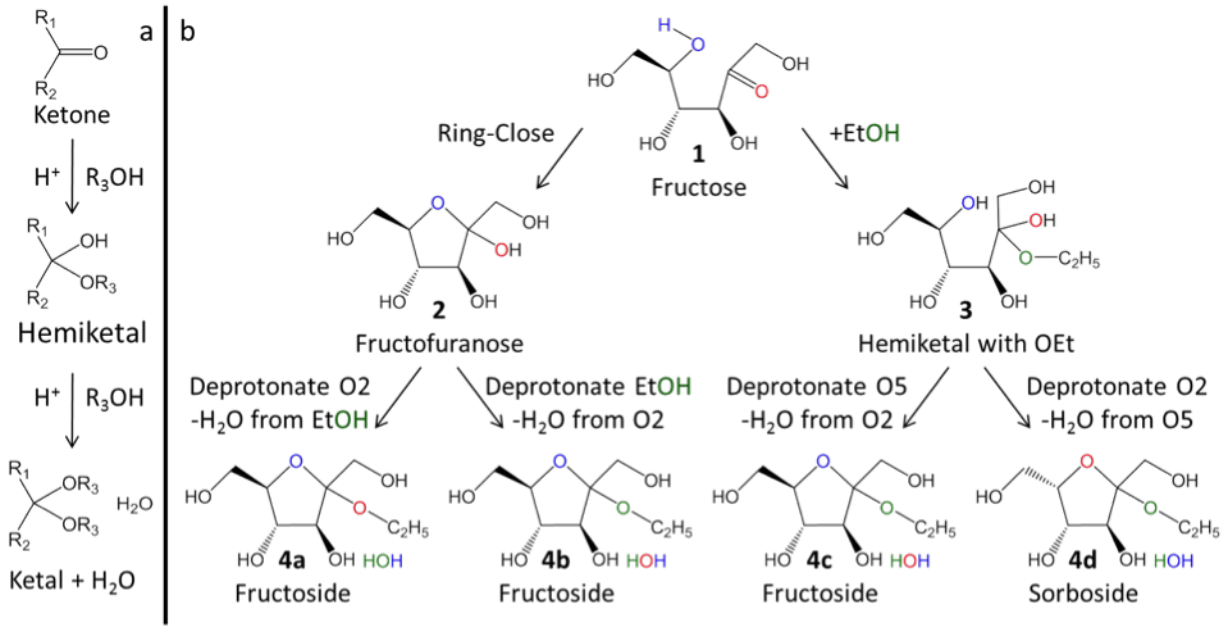

Figure 7.3: Scheme showing hemiketalization reactions of open fructose **1** to fructofuranose **2** and hemiketal **3**, followed by two pathways each to ketals **4a-d**, depending on which oxygen is eliminated in the water product.

paths for the formation of the ketal product (Scheme 2). Hemiketal formation with the O5 hydroxyl is synonymous with ring-closing, and produces fructofuranose **2**, whose anomeric hydroxyl reacts with the ethanol, eliminating water and forming the ketal. Alternatively, the C2 keto group can first react with the ethanol hydroxyl to form hemiketal **3**, followed by ring-closing and water elimination with the O5 hydroxyl to form the ketal.

In the final ketalization steps, two hydroxyls react to form the ketal and a water molecule. Distinct pathways are possible depending on which hydroxyl oxygen is eliminated as water and which is retained in the ketal, producing ketals **4a-4d** (Scheme 2). Tracer experiments with ^{18}O-labelling on ethanol and O2/O5 of fructose could potentially discriminate among products **4a**, **4b/4c**, and **4d**, but no such techniques have been reported in the literature, to our knowledge. Development of such techniques would be valuable for experimental validation of our proposed mechanism.

7.5.1 Hemiketal Formation Mechanisms

Lewis acid-catalyzed hemiketal formation has previously been studied in mechanistic studies of glucose isomerization that consider ring-opening and ring-closing reactions [12, 36–38]. These involve either O2 (the ketone) or O5 (the alcohol) coordinating to the Sn site. Hemiketalization Pathway A begins with deprotonation of the alcohol to a Sn-O-Si bridge, forming an SiOH and binding the alcohol O to Sn. The ketone C2 is then attacked by the alkoxy while the SiOH transfers its proton to the ketone O, forming the hemiketal and regenerating the active site. Pathway B starts with the ketone coordinating to the Sn. The alcohol hydroxyl deprotonates to a Sn-O-Si bridge while it attacks the ketone C2, forming a silanol and a deprotonated hemiketal. Protonation of the hemiketal from the silanol produces the hemiketal and regenerates the active site. Pathway C uses a silanol instead of the Sn site, and assists a proton transfer from the alcohol to the ketone in a concerted step with the C-O bond formation. In all cases, if the alcohol is the O5 hydroxyl, the product is fructofuranose **2**, while if the alcohol is ethanol, the product is hemiketal **3**. Reaction profiles are provided in Figures S1 and S2. Fructose ring-closing is facile, with pathway B giving a low barrier of 16.5 kcal/mol. Hemiketal formation with ethanol favors pathway A, and is less favorable than ring-closing, with a barrier of 29.5 kcal/mol.

7.5.2 Ketalization Mechanisms

Formation of the ketal from either hemiketal involves the C2 hydroxyl reacting with either the ethanol hydroxyl (for fructofuranose **2**) or the O5 hydroxyl (for hemiketal **3**). For each of these intermediates, Sn1 and Sn2 mechanisms are possible, either involving the surface SiOH or not (Sch. 7.4 and 7.5). This generates a total of 16 distinct potential pathways for consideration.

7.5.2.1 Sn2 Pathways

Sch. 7.4 shows the Sn2 pathways considered. In the Sn2 pathway without SiOH participation (Sch. 7.4a), one alcohol (R_2OH) deprotonates to the Sn-O-Si bridge, forming a SiOH, while the R_2O attacks another alcohol (R_1OH), whose C—OH bond breaks as the hydroxyl is transferred to the Sn. In a subsequent step, the SnOH and SiOH recombine to regenerate the active site and form the product water. This is similar to the Lewis acid catalyzed Sn2 etherification mechanism proposed by Christiansen, et al.[39] In the Sn2 pathway with SiOH participation (Sch. 7.4b), the Sn site is not invoked; instead, a surface silanol shuttles a proton from R_2OH to the R_1OH, forming a water leaving group as R_2O attacks R_1. Each of these pathways is possible for the formation of ketals **4a-d**, indicating a total of 8 potential mechanisms. However, Sn2 attacks on a tertiary carbon are extremely unfavorable due to steric hindrance, so paths to ketals **4b** and **4c** were excluded. In addition, Sn2 reactions eliminating the O5 hydroxyl as water would change the stereochemistry of C5, producing ethyl sorboside instead of ethyl fructoside. The Aminex HPX-87C column was used to separate the reaction products [17], and is capable of separating fructose and sorbose; because no sorbose was detected, pathways to ketal **4d** can be ruled out. With Sn2 pathways to **4b-d** ruled out, only pathways to ketal **4a** were considered.

Fig. 7.6 shows the reaction profiles for the Sn2 pathways. Both the Sn2 pathways computed have very large barriers; 46 kcal/mol without the SiOH participation, and 40.3 kcal/mol with the SiOH participation, indicating that this chemistry does not occur via an Sn2 mechanism.

7.5.2.2 Sn1 Pathways

Sch. 7.5 shows the Sn1 pathways considered. These begin with deprotonation of R_2OH and binding of the R_2O to the Sn site, whose Lewis acidity stabilizes the negative charge, distributing it among the Sn-O-Si bridge oxygens. The proton is transferred to the R_1OH alcohol, either directly (Sn1 without SiOH), or assisted by a surface silanol (Sn1 with SiOH), after which water is removed from R_1. This creates a metastable

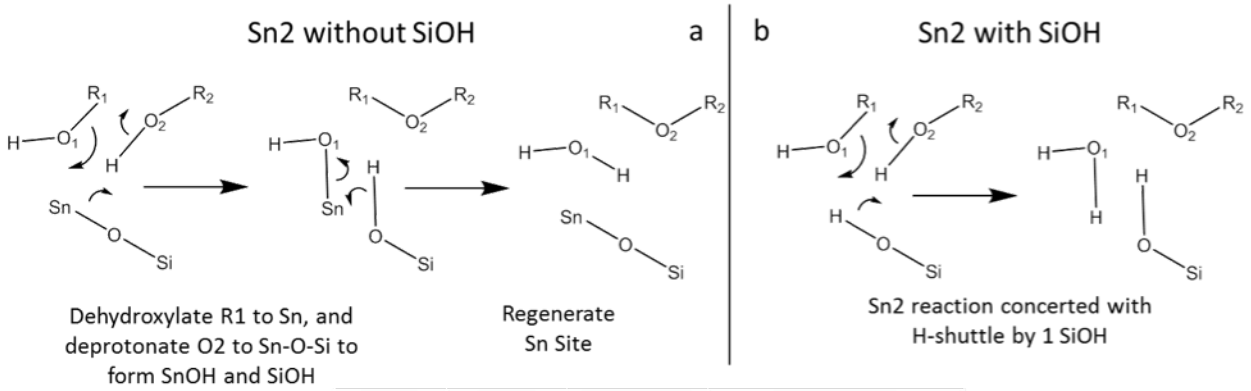

R1	R2	Product	Feasible?
Ethanol	C2	Ketal 4a	Yes
C2	Ethanol	Ketal 4b	No - Tertiary Sn2
C2	C5	Ketal 4c	No - Tertiary Sn2
C5	C2	Ketal 4d	No - Sorboside product

Figure 7.4: Summary of Sn2 ketalization pathways. a) Sn2 pathway catalyzed by the Lewis acid. b) Sn2 pathway catalyzed by a surface silanol. The inset table describes which product ketal is formed when R_1 and R_2 are from the ethanol, C2, or C5 fragments. Ketals **4b-d** are infeasible due to a tertiary Sn2 reaction or altering the stereochemistry at C5, producing ethyl sorboside, which was not detected in experiment.

intermediate with the R_2O^- coordinated to the Sn, as well as the R_1 carbocation, which is stabilized by a resonance structure with the oxonium (Sch. 7.5c). As such, these pathways bear a resemblance to the Sn1 mechanism for Brønsted-acid catalyzed ketalization [20], which generates an oxonium after protonation and dehydration of the hemiacetal. The innovation in this Lewis acid case is that the Brnsted proton comes from a substrate alcohol, which is stabilized by the Lewis acid. The final step is to bring R_2O^- to the R_1 carbocation, forming the final ketal product.

Therefore, ketals **4a** – **4d** may be produced through Sn1 pathways with or without silanol participation, indicating a total of 8 potential mechanisms. Formation of ketal **4a**, however, would move through a primary carbocation intermediate, which is likely unfavorable. We tested this for a silanol-assisted proton transfer, and found an intrinsic barrier of 50 kcal/mol. As with the Sn2 pathways, the pathway to ketal **4d** is likely to form ethyl sorboside, or at least a racemic mixture of fructoside and sorboside, which was not detected experimentally. A C5 carbocation would also not experience resonance stabilization from an oxonium, as the C2 carbocation does in the pathways to ketals **4b** and **4c**.

The energetics for the Sn1 pathways are given in Fig. 7.6. Of all these pathways, the HemiK Sn1 with SiOH is most favorable, with a maximum transition state energy at least 9 kcal/mol lower than the competing pathways. Of particular note is the importance of the adjacent silanol for stabilizing TS 1, Int and TS 2 – all these states are 8-9 kcal/mol more stable than the corresponding states in HemiK Sn1 without SiOH, the comparable mechanism without the favorable silanol interaction.

7.5.3 Glucose Acetalization Pathways

To compare glucose acetalization with fructose ketalization, we calculated the mechanism for a comparable pathway from glucose to ethyl-glucoside, with the same features as the most favorable fructose ketalization pathway. Open glucose reacts with ethanol to form a hemiacetal, followed by an Sn1 acetalization mechanism assisted by the surface SiOH. Although the hemiacetal formed is more stable than the hemiketal,

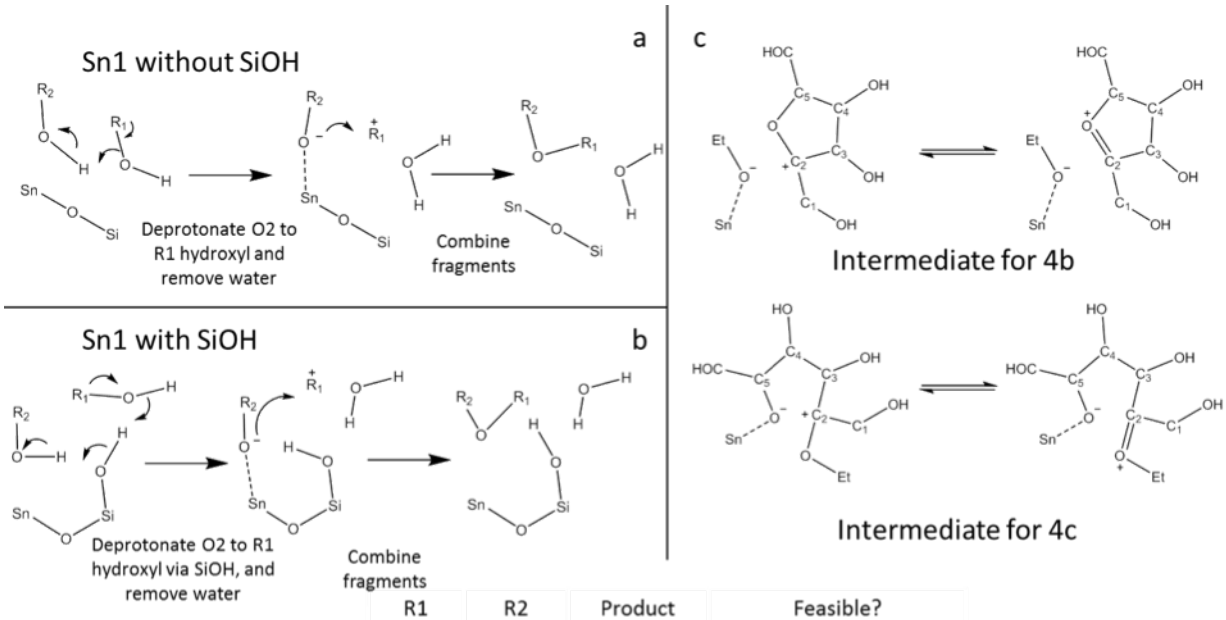

R1	R2	Product	Feasible?
Ethanol	C2	Ketal 4a	No - Primary C⁺
C2	Ethanol	Ketal 4b	Yes
C2	C5	Ketal 4c	Yes
C5	C2	Ketal 4d	No - Sorboside product

Figure 7.5: Summary of Sn1 ketalization pathways. All of these pathways invoke the Lewis acid site, which stabilizes the oxygen of the deprotonated hydroxyl on R_2, which transfers its proton to the R_1 hydroxyl either directly (a) or via a surface silanol (b), which stabilizes the deprotonated oxygen. The inset table describes which product ketal is formed when R_1 and R_2 are from the ethanol, C2, or C5 fragments. Ketal **4a** is excluded because it would require forming an unstable primary carbocation and ketal **4d** was excluded because stereochemistry changes at C5 would product ethyl-sorboside, which was not detected in experiment. c) The key carbocation intermediates in the Sn1 pathways for forming ketal **4b** and **4c** are shown, along with their preferred resonance structures as oxonium ions.

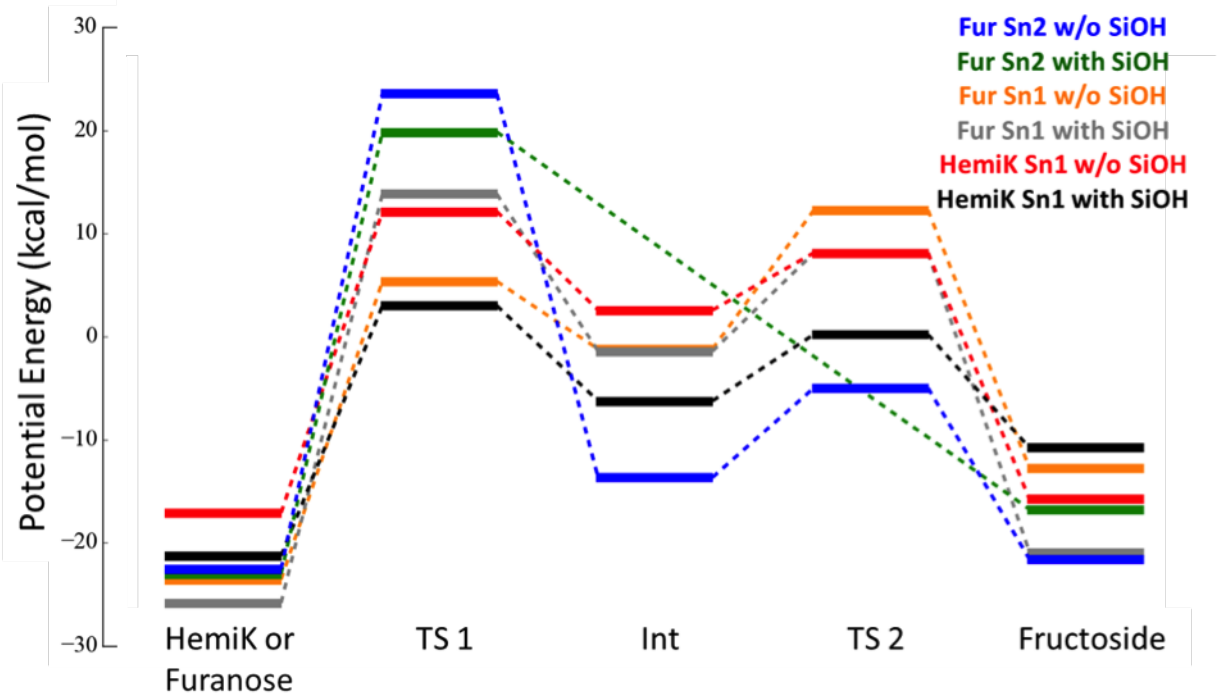

Figure 7.6: Reaction profiles to form ethyl fructoside from furanose or hemiketal and ethanol via Sn2 or Sn1 reactions, described in Sch. 7.4 and 7.5. Electronic binding energies (kcal/mol) are reported with respect to infinitely separated fructofuranose, ethanol, and catalyst. Fur Sn2 pathways proceed to ketal **4a**, Fur Sn1 pathways proceed to ketal **4b**, and HemiK Sn1 pathways proceed to ketal **4c**. In the Fur Sn2 w/o SiOH, TS 1 is the ketalization TS, and TS 2 is the TS for regeneration of the active site. In the Sn1 pathways, TS 1 is the dehydration TS and TS 2 is the ring-closing TS – in some cases, minor steps were required in between, and are reported in Appendix F.

the water removal and ring-closing transition states for acetalization are significantly higher energy than those for ketalization (Fig. 7.7). This is consistent with experiment, in which no ethyl glucoside is detected.

Although the Lewis acid in Sn-SPP cannot catalyze glucose acetalization, strong Brønsted acids such as sulfonic acid-functionalized SBA-15[40] and H_2SO_4 have been shown to catalyze glucose acetalization, but cause dehydration of fructose and formation of humins instead of fructose ketalization. Weaker Brønsted acids, such as those in H-USY, that catalyze both fructose ketalization and glucose acetalization [15], produce fructoside 16 times faster than glucoside, indicating a higher barrier for glucose compared to fructose on Brønsted acidic zeolites, as well.

Therefore, we conclude that the selectivity to fructoside is not a unique feature of the Sn-SPP zeolite; rather it is a consequence of an intrinsic difference in reactivity of glucose and fructose. In further support of this, gas-phase calculations (See Appendix F) for model hemiacetals and hemiketals show that the proton affinities of the anomeric hydroxyls of hemiketals are 9-12 kcal/mol greater than these of hemiacetals, and the oxonium intermediates of hemiketals are 13-14 kcal/mol more stable than those of hemiacetals, both indications of greater reactivity for ketalization in Sn1 mechanisms.

7.5.4 Glucose Isomerization

To complete the reaction network, we also computed a reaction pathway from open glucose to open fructose (Figure S3 in Appendix F). Following mechanisms for glucose isomerization on Lewis acids [12, 36, 41–43], we focused on one pathway, in which open glucose binds to the Sn in a bidentate configuration with O1 and O2. In a three-step reaction, O2 deprotonates to the Sn-O-Si bridge, followed by a 1,2-intramolecular H-shift, followed by reprotonation of the O1 hydroxyl. The H-shift is the highest barrier step for this reaction, with a TS energy comparable (2.8 kcal/mol) to the highest point for the ketalization reaction (3.0 kcal/mol), consistent with both products being observed in experiment.

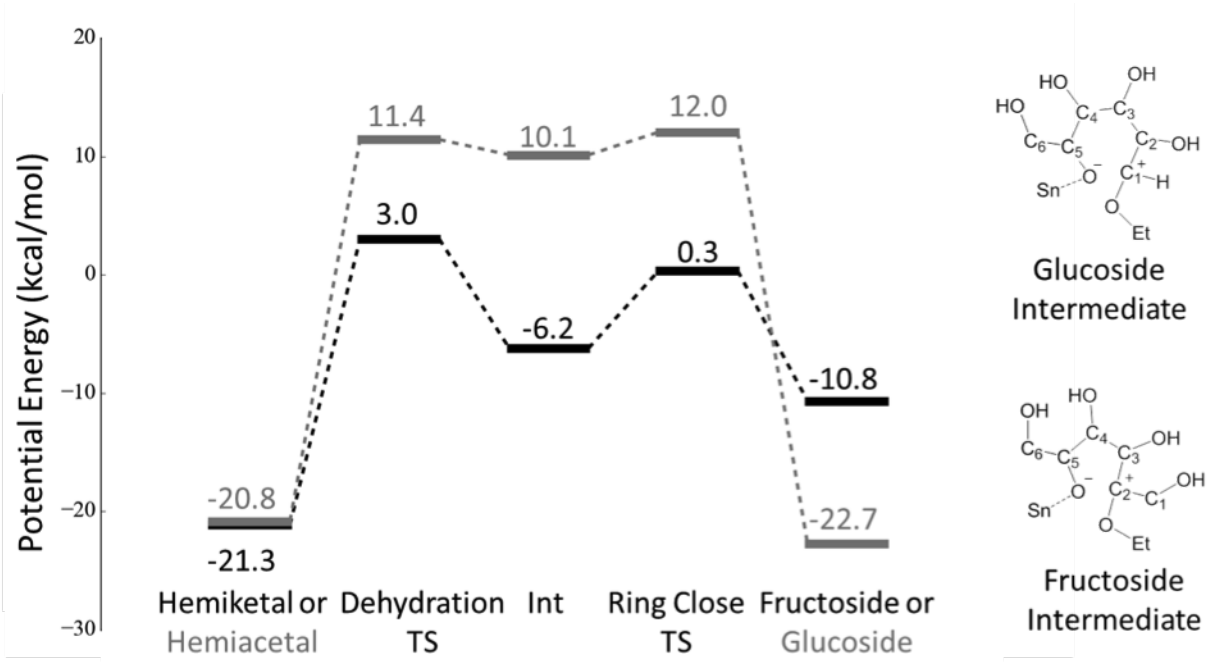

Figure 7.7: Reaction profiles comparing glucose acetalization with fructose ketalization, both following HemiK Sn1 with SiOH. Glucose acetalization is less favorable by over 9 kcal/mol compared to fructose ketalization.

7.5.5 Comparing Sn-SPP with Sn-Beta

The most favorable ketalization mechanism utilizes a silanol donating a proton to the anomeric hydroxyl, and also stabilizing the O5 hydroxyl of the hemiketal. In Sn-SPP, this silanol is connected to the Sn site as Sn-O-Si-OH, and so is positioned close enough to stabilize the key transition states and intermediates. However, the silanol in the most stable Sn-Beta open site geometries [44], is formed from the hydrolysis of a Sn-O-Si bridge, and is not connected to a Sn-O-Si bridge, but reaches across the gap created by the hydrolysis. Consequently, only the Sn1 pathway without SiOH is feasible; the Sn-Beta silanol cannot assist the ketalization as the Sn-O-Si-OH does in Sn-SPP (Fig. 7.8, inset).

The resulting free energy profiles for Sn-SPP and Sn-Beta are compared in Fig. 7.8. Using the energy span model [45, 46], the relative activation energies and turnover frequencies (TOF) for each catalyst can be estimated, by identifying the TOF-determining intermediate (TDI) and TOF-determining TS (TDTS) for each reaction. On Sn-Beta, the TDI is open fructose, with a binding free energy of -15.4 kcal/mol, and the TDTS is dehydration, with a free energy of 22.0 kcal/mol, giving an energy span δE = 37.4 kcal/mol. On Sn-SPP, the TDI is the hemiketal, with a binding free energy of -19.4, and the TDTS is the dehydration, with a binding free energy of 2.5 kcal/mol, giving an energy span δE = 21.9 kcal/mol.

7.6 Conclusions

The Sn-SPP zeolite is capable of catalyzing the selective ketalization of fructose in the presence of glucose specifically due to the activity of its Sn-O-Si-OH moiety. The silanol shuttles the proton from the O5 hydroxyl to the O2 hydroxyl to remove it as water, and also stabilizes the deprotonated O5 hydroxyl along with the Lewis acidic Sn. The Sn-Beta open site cannot catalyze ketalization because its silanol is too distant from the Sn site, and cannot stabilize the deprotonated O5 hydroxyl. Glucose acetalization is not catalyzed by Sn-SPP because the oxonium ion intermediate for glucose acetalization is much less stable than that of fructose. Strong Brønsted acids

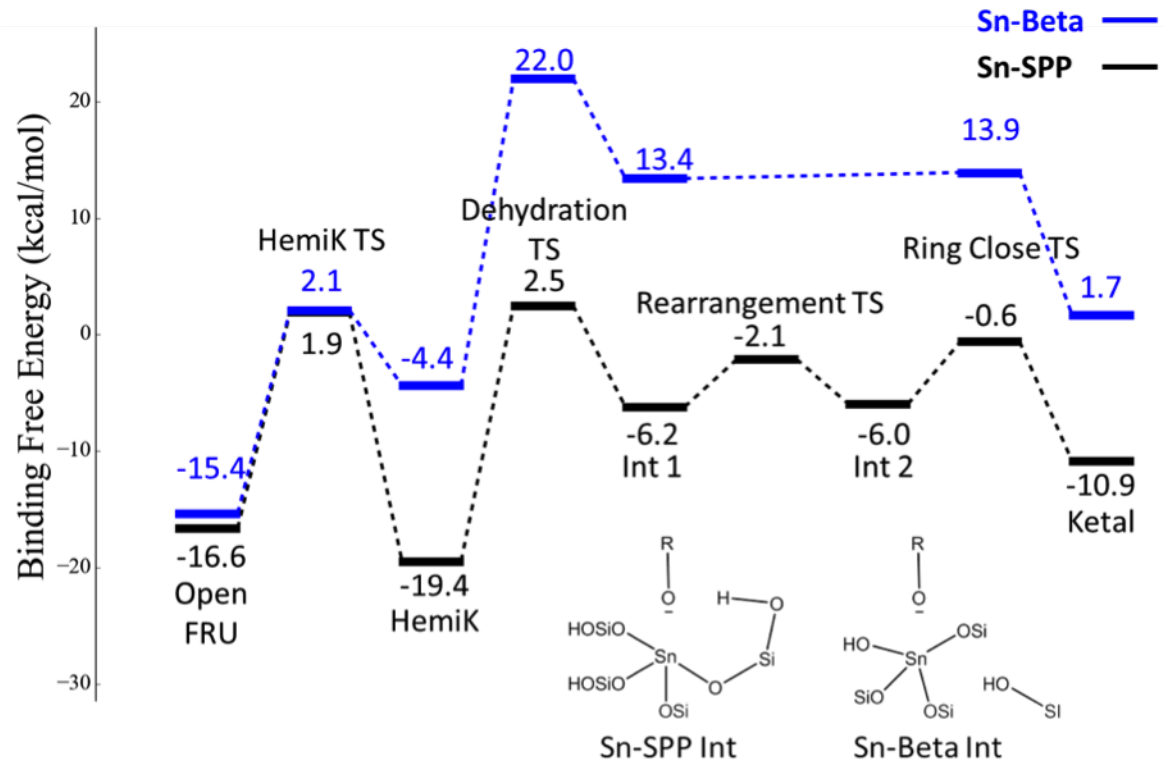

Figure 7.8: Free energy profiles for fructose ketalization on Sn-SPP and Sn-Beta, as well as schemes highlighting the relevant differences between their active sites.

are sufficient to active glucose acetalization, but are too harsh for fructose, which dehydrates. The surface silanols of Sn-SPP, positioned to work in concert with the Lewis acidic Sn site, form a gentler catalyst that isomerizes glucose and also selectively ketalizes fructose without dehydrating it.

7.7 Acknowledgements

Research was supported as part of the Catalysis Center for Energy Innovation, an Energy Frontier Research Center funded by the U.S. Department of Energy (DOE), Office of Science, Basic Energy Sciences (BES), under Award number DE-SC0001004. This research used resources of the National Energy Research Scientific Computing Center, a DOE Office of Science User Facility supported by the Office of Science of the U.S. Department of Energy under Contract No. DE-AC02-05CH11231. T.R.J. wishes to acknowledge funding from the National Science Foundation Graduate Research Fellowship Program under Grant No. 0750966, as well as the George W. Laird Merit Fellowship. Any opinions, findings, and conclusions or recommendations expressed in this material are those of the author(s) and do not necessarily reflect the views of the National Science Foundation. The authors would like to thank Limin Ren and Qiang Guo for helpful conversations and experimental insights, and Zhiqiang Zhang for helpful conversations and for providing the reaction profile plotting software.

REFERENCES

[1] B. Kamm, P. R. Gruber, and Kammm Michael. *Biorefineries Industrial Processes and Products*. Wiley-VCH, 2010. ISBN 3527329536.

[2] E. de Jong, A. Higson, P. Walsh, and M. Wellisch. Biobased Chemicals - Value Added Products from Biorefineries. *A report prepared for IEA Bioenergy-Task 42*, page 36, 2011.

[3] A. J. Ragauskas, C. K. Williams, B. H. Davison, G. Britovsek, J. Cairney, C. A. Eckert, W. J. Frederick Jr., J. P. Hallett, D. J. Leak, C. L. Liotta, J. R. Mielenz, R. Murphy, R. Templer, and T. Tschaplinski. The path forward for biofuels and biomaterials. *Science (New York, N.Y.)*, 311(5760):484–9, 2006. ISSN 1095-9203. doi: 10.1126/science.1114736.

[4] G. W. Huber. Breaking the Chemical and Engineering Barriers to Lignocellulosic Biofuels : Next Generation Hydrocarbon Biorefineries. *NSF*, pages 1–177, 2008.

[5] G. W. Huber and A. Corma. Synergies between bio- and oil refineries for the production of fuels from biomass. *Angewandte Chemie - International Edition*, 46 (38):7184–7201, 2007. ISSN 14337851. doi: 10.1002/anie.200604504.

[6] X. Tong, Y. Ma, and Y. Li. Biomass into chemicals: Conversion of sugars to furan derivatives by catalytic processes. *Appl. Catal., A*, 385(1-2):1–13, 2010. doi: 10.1016/j.apcata.2010.06.049.

[7] A. A. Rosatella, S. P. Simeonov, R. F. M. Frade, and C. A. M. Afonso. 5-Hydroxymethylfurfural (HMF) as a building block platform: Biological properties, synthesis and synthetic applications. *Green Chemistry*, 13(4):754, 2011. ISSN 1463-9262. doi: 10.1039/c0gc00401d.

[8] R. J. Van Putten, J. C. Van Der Waal, E. De Jong, C. B. Rasrendra, H. J. Heeres, and J. G. De Vries. Hydroxymethylfurfural, a versatile platform chemical made from renewable resources. *Chemical Reviews*, 113(3):1499–1597, 2013. ISSN 00092665. doi: 10.1021/cr300182k.

[9] R. J. Van Putten, J. N. Soetedjo, E. A. Pidko, J. C. van der Waal, E. J. Hensen, E. de Jong, and H. J. Heeres. Dehydration of different ketoses and aldoses to 5-hydroxymethylfurfural. *ChemSusChem*, 6(9):1681–1687, 2013. doi: 10.1002/cssc.201300345.

[10] M. Moliner, Y. Roman-Leshkov, M. E. E. Davis, Y. Román-Leshkov, and M. E. E. Davis. Tin-containing zeolites are highly active catalysts for the isomerization of glucose in water. *Proc Natl Acad Sci U S A*, 107(14):6164–6168, 2010. ISSN 1091-6490. doi: 10.1073/pnas.1002358107.

[11] V. Choudhary, A. B. Pinar, S. I. Sandler, D. G. Vlachos, and R. F. Lobo. Xylose isomerization to xylulose and its dehydration to furfural in aqueous media. *ACS Catalysis*, 1(12):1724–1728, 2011. ISSN 21555435. doi: 10.1021/cs200461t.

[12] R. Bermejo-Deval, R. S. S. Assary, E. Nikolla, M. Moliner, Y. Roman-Leshkov, S.-J. S.-J. Hwang, A. Palsdottir, D. Silverman, R. F. Lobo, L. A. Curtiss, and M. E. Davis. Metalloenzyme-like catalyzed isomerizations of sugars by Lewis acid zeolites. *Proceedings of the National Academy of Sciences*, 109(25):9727–9732, 2012. ISSN 0027-8424. doi: 10.1073/pnas.1206708109.

[13] Y. Takasaki. Studies on Sugar-isomerizing Enzyme. *Agricultural and Biological Chemistry*, 30(12):1247–1253, 1966. ISSN 0002-1369. doi: 10.1080/00021369.1966.10858758.

[14] S. Saravanamurugan, M. Paniagua, J. A. Melero, and A. Riisager. Efficient isomerization of glucose to fructose over zeolites in consecutive reactions in alcohol and

aqueous media. *Journal of the American Chemical Society*, 135(14):5246–5249, 2013. ISSN 00027863. doi: 10.1021/ja400097f.

[15] S. Saravanamurugan, A. Riisager, E. Taarning, and S. Meier. Combined Function of Brønsted and Lewis Acidity in the Zeolite-Catalyzed Isomerization of Glucose to Fructose in Alcohols. *ChemCatChem*, 8(19):3107–3111, 2016. ISSN 18673899. doi: 10.1002/cctc.201600783.

[16] J. M. Rubio-Caballero, S. Saravanamurugan, P. Maireles-Torres, and A. Riisager. Acetalization of furfural with zeolites under benign reaction conditions. *Catalysis Today*, 234:233–236, 2014. ISSN 09205861. doi: 10.1016/j.cattod.2014.03.004.

[17] L. Ren, Q. Guo, P. Kumar, M. Orazov, D. Xu, S. M. Alhassan, K. A. Mkhoyan, M. E. Davis, and M. Tsapatsis. Self-Pillared, Single-Unit-Cell Sn-MFI Zeolite Nanosheets and Their Use for Glucose and Lactose Isomerization. *Angewandte Chemie - International Edition*, 54(37):10848–10851, 2015. ISSN 15213773. doi: 10.1002/anie.201505334.

[18] L. Ren, Q. Guo, M. Orazov, D. Xu, D. Politi, P. Kumar, S. M. Alhassan, K. A. Mkhoyan, D. Sidiras, M. E. Davis, and M. Tsapatsis. Pillared Sn-MWW Prepared by a Solid-State-Exchange Method and its Use as a Lewis Acid Catalyst. *ChemCatChem*, 8(7):1274–1278, 2016. ISSN 18673899. doi: 10.1002/cctc.201600120.

[19] H. J. Cho, P. Dornath, and W. Fan. Synthesis of hierarchical Sn-MFi as lewis acid catalysts for isomerization of cellulosic sugars. *ACS Catalysis*, 4(6):2029–2037, 2014. ISSN 21555435. doi: 10.1021/cs500295u.

[20] J. Clayden, N. Greeves, S. Warren, and P. Wothers. *Organic Chemistry*. 2001. ISBN 0198503466. doi: 10.1086/278635.

[21] J. Mortensen, L. Hansen, and K. Jacobsen. Real-space grid implementation of the projector augmented wave method. *Physical Review B*, 71(3):035109, 2005. ISSN 1098-0121. doi: 10.1103/PhysRevB.71.035109.

[22] J. Enkovaara, C. Rostgaard, J. J. Mortensen, J. Chen, M. Dułak, L. Ferrighi, J. Gavnholt, C. Glinsvad, V. Haikola, H. a. Hansen, H. H. Kristoffersen, M. Kuisma, a. H. Larsen, L. Lehtovaara, M. Ljungberg, O. Lopez-Acevedo, P. G. Moses, J. Ojanen, T. Olsen, V. Petzold, N. a. Romero, J. Stausholm-Møller, M. Strange, G. a. Tritsaris, M. Vanin, M. Walter, B. Hammer, H. Häkkinen, G. K. H. Madsen, R. M. Nieminen, J. K. Nørskov, M. Puska, T. T. Rantala, J. Schiøtz, K. S. Thygesen, and K. W. Jacobsen. Electronic structure calculations with GPAW: a real-space implementation of the projector augmented-wave method. *Journal of physics. Condensed Matter*, 22(25):253202, 2010. ISSN 0953-8984. doi: 10.1088/0953-8984/22/25/253202.

[23] S. R. Bahn and K. W. Jacobsen. An object-oriented scripting interface to a legacy electronic structure code. *Computing in Science and Engineering*, 4(3):56–66, 2002. ISSN 15219615. doi: 10.1109/5992.998641.

[24] P. E. Blöchl. Projector augmented-wave method. *Physical Review B*, 50(24): 17953–17979, 1994. ISSN 01631829. doi: 10.1103/PhysRevB.50.17953.

[25] G. Kresse. From ultrasoft pseudopotentials to the projector augmented-wave method. *Physical Review B*, 59(3):1758–1775, 1999. ISSN 1098-0121. doi: 10.1103/PhysRevB.59.1758.

[26] J. P. Perdew, K. Burke, and M. Ernzerhof. Generalized Gradient Approximation Made Simple. *Physical Review Letters*, 77(18):3865–3868, 1996. ISSN 0031-9007. doi: 10.1103/PhysRevLett.77.3865.

[27] D. C. Liu and J. Nocedal. On the Limited Memory Method for Large Scale Optimization. *Math. Programming, B*, 45(3):503–528, 1989. ISSN 00255610. doi: 10.1007/BF01589116.

[28] G. Henkelman, B. P. Uberuaga, and H. Jónsson. Climbing image nudged elastic band method for finding saddle points and minimum energy paths. *Journal*

of Chemical Physics, 113(22):9901–9904, 2000. ISSN 00219606. doi: 10.1063/1.1329672.

[29] G. Henkelman and H. Jónsson. A dimer method for finding saddle points on high dimensional potential surfaces using only first derivatives. *Journal of Chemical Physics*, 111(15):7010–7022, 1999. ISSN 00219606. doi: 10.1063/1.480097.

[30] R. A. Olsen, G. J. Kroes, G. Henkelman, A. Arnaldsson, and H. Jónsson. Comparison of methods for finding saddle points without knowledge of the final states. *Journal of Chemical Physics*, 121(20):9776–9792, 2004. ISSN 00219606. doi: 10.1063/1.1809574.

[31] A. Heyden, A. T. Bell, and F. J. Keil. Efficient methods for finding transition states in chemical reactions: Comparison of improved dimer method and partitioned rational function optimization method. *Journal of Chemical Physics*, 123(22), 2005. ISSN 00219606. doi: 10.1063/1.2104507.

[32] J. Kästner and P. Sherwood. Superlinearly converging dimer method for transition state search. *Journal of Chemical Physics*, 128(1), 2008. ISSN 00219606. doi: 10.1063/1.2815812.

[33] A. H. Larsen, M. Vanin, J. J. Mortensen, K. S. Thygesen, and K. W. Jacobsen. Localized atomic basis set in the projector augmented wave method. *Physical Review B - Condensed Matter and Materials Physics*, 80(19):1–10, 2009. ISSN 10980121. doi: 10.1103/PhysRevB.80.195112.

[34] X. Zhang, D. Liu, D. Xu, S. Asahina, K. A. Cychosz, K. V. Agrawal, Y. Al Wahedi, A. Bhan, S. Al Hashimi, O. Terasaki, M. Thommes, and M. Tsapatsis. Synthesis of Self-Pillared Zeolite Nanosheets by Repetitive Branching. *Science*, 336(6089): 1684–1687, 2012. ISSN 0036-8075. doi: 10.1126/science.1221111.

[35] M. Orazov and M. E. Davis. Tandem catalysis for the production of alkyl lactates from ketohexoses at moderate temperatures. *Proceedings of the National Academy of Sciences*, 112(38):201516466, 2015. ISSN 0027-8424. doi: 10.1073/pnas.1516466112.

[36] G. Yang, E. A. Pidko, and E. J. M. Hensen. The mechanism of glucose isomerization to fructose over Sn-BEA zeolite: A periodic density functional theory study. *ChemSusChem*, 6(9):1688–1696, 2013. ISSN 18645631. doi: 10.1002/cssc.201300342.

[37] Y. P. P. Li, M. Head-Gordon, and A. T. T. Bell. Analysis of the reaction mechanism and catalytic activity of metal-substituted beta zeolite for the isomerization of glucose to fructose. *ACS Catalysis*, 4(5):1537–1545, 2014. ISSN 21555435. doi: 10.1021/cs401054f.

[38] S. K. Brand, T. R. Josephson, J. A. Labinger, S. Caratzoulas, D. G. Vlachos, and M. E. Davis. Methyl-Ligated Tin Silsesquioxane Catalyzed Reactions of Glucose. *Journal of Catalysis*, 341:62–71, 2016.

[39] M. A. Christiansen, G. Mpourmpakis, and D. G. Vlachos. Density functional theory-computed mechanisms of ethylene and diethyl ether formation from ethanol on γ-Al2O3(100). *ACS Catalysis*, 3(9):1965–1975, 2013. ISSN 21555435. doi: 10.1021/cs4002833.

[40] S. Saravanamurugan and A. Riisager. Solid acid catalysed formation of ethyl levulinate and ethyl glucopyranoside from mono- and disaccharides. *Catalysis Communications*, 17:71–75, 2012. ISSN 15667367. doi: 10.1016/j.catcom.2011.10.001.

[41] S. K. Brand, J. A. Labinger, and M. E. Davis. Tin Silsesquioxanes as Models for the "Open" Site in Tin-Containing Zeolite Beta. *ChemCatChem*, 8(1):121–124, 2016. ISSN 18673899. doi: 10.1002/cctc.201501067.

[42] N. Rai, S. Caratzoulas, and D. G. Vlachos. Role of silanol group in Sn-beta zeolite for glucose isomerization and epimerization reactions. *ACS Catalysis*, 3 (10):2294–2298, 2013. ISSN 21555435. doi: 10.1021/cs400476n.

[43] J. R. Christianson, S. Caratzoulas, and D. G. Vlachos. Computational Insight into the Effect of Sn-Beta Na Exchange and Solvent on Glucose Isomerization and Epimerization. *ACS Catalysis*, 5(9):5256–5263, 2015. ISSN 2155-5435. doi: 10.1021/acscatal.5b01258.

[44] T. R. Josephson, G. R. Jenness, D. G. Vlachos, and S. Caratzoulas. Distribution of open sites in Sn-Beta zeolite. *Microporous and Mesoporous Materials*, 245:45–50, 2017. ISSN 13871811. doi: 10.1016/j.micromeso.2017.02.065.

[45] S. Kozuch and S. Shaik. How to conceptualize catalytic cycles? the energetic Span model. *Accounts of Chemical Research*, 44(2):101–110, 2011. ISSN 00014842. doi: 10.1021/ar1000956.

[46] S. Kozuch. Steady State Kinetics of Any Catalytic Network: Graph Theory, the Energy Span Model, the Analogy between Catalysis and Electrical Circuits, and the Meaning of Mechanism. *ACS Catalysis*, 5(9):5242–5255, 2015. ISSN 2155-5435. doi: 10.1021/acscatal.5b00694.

Chapter 8

CONCLUSIONS AND OUTLOOK

8.1 Conclusions and Outlook

Concerns around the sustainability of our energy infrastructure have driven investment in biomass-derived fuels and chemicals. With an abundant supply of biomass from agricultural and forest residues, as well as energy crops, this growing industry could significantly displace petroleum as the primary feedstock for our fuel and chemical industry. The furans platform offers a diverse slate of chemical products derived from renewable sugars, but commercialization requires improvements in process efficiency borne from novel materials and understanding of process fundamentals. In this thesis, we have leveraged first-principles modeling to develop deeper insights into several key reactions for the production of fuels and chemicals from biomass through the furans platform,

1. The role of solvation in HMF stability
2. Structure-activity and structure-selectivity relationships for glucose isomerization in molecular analogues of Sn-Beta
3. The structure of open sites in Sn-Beta
4. The reaction mechanism for fructose ketalization on Sn-SPP.

8.1.1 Solvation effects in HMF stability

In Chapter 2 IR spectroscopy and DFT are integrated to characterize the solvent-solute interactions in mixtures of HMF, DMSO, and water and their effect on the liquid structure of HMF in solution. The HMF carbonyl, hydroxyl, and C=C bands are analyzed and compared with calculated spectra to explore the formation of

hydrogen bonds with water and DMSO. Analysis of binary mixtures reveal that DMSO binds more strongly than water to both the hydroxyl and carbonyl groups of HMF, giving evidence of preferential solvation of HMF by DMSO in DMSO/water mixtures. Analysis of the LUMO energies and orbitals of HMF solvated by DMSO and water show that water makes HMF more susceptible to nucleophilic attack, while DMSO makes HMF less susceptible. Evidence for preferential DMSO solvation and the influence of DMSO on LUMO energy of HMF provide an explanation for HMF's improved stability in aqueous solutions with even a small amount of DMSO co-solvent.

In Chapter 3 the fundamental physics behind the solvent-induced frequency shift (SIFS) of the HMF carbonyl stretch is investigated in further depth, and generalized to a broad range of solvents. Experimental IR spectra show that the carbonyl stretch is correlated with the Gutmann acceptor number of the solvent, an empirical measure of solvent Lewis acidity. HMF vibrational spectra were calculated using ab initio models with implicit, explicit, and implicit+explicit solvation, with the explicit solvation model giving the best agreement with experiment. Accounting for H-bonding interactions is essential for predicting the SIFS of the HMF carbonyl stretch, and the characteristics of these H-bonds were investigated using natural bond orbital (NBO) analysis and Bader?s atoms-in-molecules theory. NBO analysis shows that strong H-bonding interactions accompany a redshift in the carbonyl stretching frequency, which is associated with a weakening of the C=O and conjugated C=C bonds in HMF due to an increase in π-antibonding. SIFS were also correlated to the local electron density at the H-bond critical points, highlighting the role of local H-bond strength. By quantifying the withdrawal of electron density as a function of the frequency shift, we provide the first theoretical support for the Gutmann acceptor number as a measure of Lewis acidity.

8.1.2 Structure-activity relationships for glucose isomerization in Sn-Beta

Chapters 4 and 5 explore glucose isomerization on Sn-silsesquioxane catalysts – model catalysts designed to test the reactivity of various structural motifs in the active

sites of Sn-Beta. Chapter 4 examines a methyl-Sn-silsesquioxane as a model of the Sn-Beta "closed" site, while Chapter 5 examines two acetylacetonate-ligated (acac) Sn-silsesquioxanes with and without an adjacent silanol, as models of the open and Na-exchanged open sites of Sn-Beta.

The methyl-Sn-silsesquioxane is found to be active for glucose isomerization to fructose via 1,2-H-shift, and for glucose epimerization to mannose via 1,2-C-shift. Such activity is surprising, because previous studies indicated that Sn-Beta catalyzed glucose isomerization on open sites. The reaction mechanism is explored using DFT, which identifies the function of the Sn-O-Si moiety in methyl-Sn-silsisquioxane. In the most favorable reaction pathways, glucose binds to the Sn site in a bidentate configuration, and the Sn-O-Si bridge accepts a proton from the sugar to activate the hydride shift, and the Sn stabilizes an electron transfer through the conjugated π system formed at the H- or C-shift transition states. If the Sn-O-Si bridge is also active in Sn-Beta, the same reaction could occur on closed sites; albeit at a much lower rate than the open sites, as indicated by comparison of initial turn-over frequencies between Sn-silsesquioxanes and heterogeneous materials.

The acac-Sn-silsesquioxanes with and without the SiOH exhibit a selectivity shift in qualitative agreement with the Sn-Beta and Na-exchanged Sn-Beta – presence of the SiOH correlated with an increase in fructose selectivity over mannose. However, isotopic labeling reveals an inconsistency in the comparison. Sn-Beta produces mannose from two sequential H-shifts of glucose and Na-Sn-Beta produces mannose from the C-shift of glucose, but both acac-Sn-silsesquioxanes formed mannose from the C-shift of glucose. Reaction mechanisms computed on both acac-Sn-silsesquioxanes reveal that the Sn-O-Si is responsible for both fructose and mannose formation; the SiOH is not involved in the reaction mechanism. Instead, the acac ligands stabilize the C-shift reaction in both acac-Sn-silsesquioxanes, explaining the discrepancy between the model catalysts and the heterogeneous catalysts.

8.1.3 Distribution of open sites in Sn-Beta

An exhaustive survey of the possible open-site geometries in Sn-Beta reveals that the T1 and T9 sites of Sn-Beta are the most stable locations for Sn, although several sites are within 2 kcal/mol of the minimum. More importantly, the open site is characterized by a SiOH positioned opposite the SnOH; this geometry is favored at all T site substitutions. In this orientation, the SiOH proton is particularly acidic due to a Sn—O(H)Si interaction which arises when strong Brønsted bases like NH_3 and pyridine coordinate to the open site and abstract the proton (although binding to the Sn site is of comparable strength compared to binding to the SiOH). Identifying the origin of Brønsted acidity in the Sn-Beta zeolite could shed light on the traditionally Brønsted-acid catalyzed etherification which has been observed on Sn-Beta.

8.1.4 Fructose ketalization on Sn-SPP

The discovery of the remarkable activity of Sn-SPP for glucose isomerization and fructose ketalization left several unanswered questions, which are addressed through density functional theory calculations. The active site of Sn-SPP is characterized, which exhibits a "closed" site on the border of an MFI pore, with three adjacent SiOH groups, as Sn-O-Si-OH. Fructose ketalization is catalyzed via an Sn1 mechanism through a hemiketal formed from open fructose and ethanol. The O5 hydroxyl of the hemiketal coordinates to the Sn site, and transfers its proton to the O2 hydroxyl, which dehydrates, forming an oxonium intermediate, which ring-closes to form the ketal. The Sn-O-Si-OH of Sn-SPP is critical for assisting the proton transfer and stabilizing the oxonium intermediate; a comparable pathway without this interaction is 8 kcal/mol higher. Sn-Beta, whose SiOH is not immediately adjacent to the Sn, cannot stabilize this intermediate and also gives a higher barrier. Finally, glucose acetalization is not catalyzed on Sn-SPP because its oxonium intermediate is less stable than that of fructose, even with the Sn-O-Si-OH stabilization, providing insight into the high selectivity of Sn-SPP towards fructose ketalization.

8.2 Outlook and Future Work

The importance of biomass as a chemical feedstock will continue to grow as the environmental liabilities of non-renewable resources become more apparent, and the need for renewable technologies more urgent. Continued research in improving the efficiency, economics, and flexibility in biomass processing is needed to meet these future needs. New directions for research that follow from the work in this dissertation are discussed.

8.2.1 Effects of solvation in HMF stability

In Chapter 2, we demonstrate the preferential solvation of HMF by DMSO in DMSO/water solutions. Recently, these methods have been extended to other polar aprotic solvents[1]. In addition, the LUMO of solvated HMF was taken as an indication of its reactivity in solution. However, this is just a preliminary descriptor of its reactivity. A more rigorous treatment of the effects of solvation on the side reactions of HMF would first require an understanding of the reaction mechanism of HMF rehydration to levulinic acid [1] and polymerization to humins (which requires an understanding of the molecular structure and morphology of humins, first). Examining the roles of solvation on the key transition states and intermediates in these reaction networks would give a more robust picture of the effect of solvation on reactivity. Participation of the solvent could also fundamentally alter the reaction mechanism, as well [2, 3].

8.2.2 Integrating DFT with spectroscopy for liquid-phase characterization

To improve techniques for characterizing the structure of the liquid phase, better fundamental understanding of solvent-induced frequency shifts (SIFS) would be beneficial. The same methods used to characterize the fundamental origin of SIFS of carbonyls in Chapter 3 would be amenable to characterizing several other SIFS observed in the literature, including those on alcohols, carboxylic acids, esters, nitriles,

[1] George Tsilomelekis, unpublished results

amides, amines, etc.This would enable similar studies on molecules without a characteristic carbonyl stretching frequency to use as a probe of solvation. Acetonitrile and pyridine would be especially interesting cases – their frequency shifts are used to characterize Brønsted and Lewis acidic zeolites in the gas phase, and understanding their interactions in solution could lead to new applications in zeolite characterization in the condensed phase.

The present work characterizes SIFS of infrared spectra. However, DFT is also able to predict Raman, NMR, and VCD spectra as well, whose techniques may be more suitable for characterizing certain systems where IR peaks are unaffected by solvation or convoluted with solvent vibrations. Evaluating the influence of solvation on these characterization methods, and identifying the essential features of the solvation model needed to predict experimental shifts, could advance the utility of these methods, as well. Pairing these techniques with molecular dynamics also enables further investigation into effects of preferential solvation.

8.2.3 Water-stable Sn-silsesquioxanes

The Sn-silsesquioxanes studied are able to elucidate the roles of the Sn-O-Si moiety, and also the SiOH moiety (although the acac ligands conflated the study of the SiOH by stabilizing the C-shift). However, no Sn-silsesquioxane with a stable SnOH moiety has been synthesized in literature, even though this is considered to be a key attribute to the Sn-Beta open site. In addition, no current Sn-silsesquioxanes are stable in aqueous solution – a medium under which Sn-Beta is remarkably active.

One Ti-containing silsesquioxane has been reported to be stable in aqueous solution, $[(c\text{-}C_7H_{13})_7Si_6O_{11}]_3[TiOH]_4$ [4, 5]. This contains several TiOH groups in a tetrahedral cluster, coordinated together as Ti-O(H)-Ti groups. Given the similarities between Lewis acids Ti and Sn, perhaps a comparable compound could be synthesized with Sn and tested for stability and reactivity under aqueous conditions. Such a catalyst could bring insight into the role of the SnOH moiety. In addition, comparing

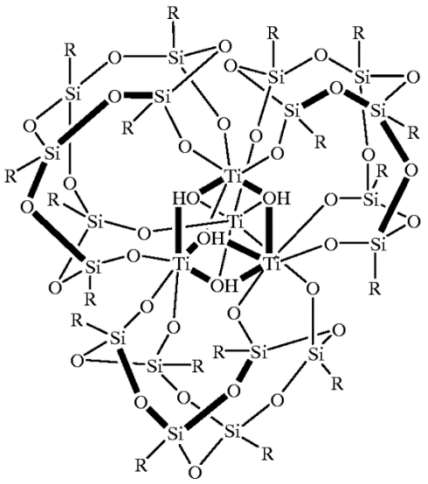

Figure 8.1: Water-stable Ti-silsesquioxane reported in [4, 5]. Synthesis using $SnCl_4$ might yield a water-stable Sn-silsesquioxane.

reactivity in aqueous conditions to that in the DMSO/benzene conditions used for the previous Sn-silsesquioxanes could reveal any effects of solvation on the former studies.

8.2.4 Active site characterization in Lewis acidic zeolites

The algorithm described in Chapter 6 for the characterization of the Sn-Beta active site can be extended to other Lewis acids and to other zeolite frameworks, so long as the unit cell is of reasonable size for high-throughput periodic DFT calculations. It could also be generalized to include doubly- and triply-hydrolyzed sites if those are relevant for other Lewis acids. Precisely characterizing and controlling active sites in zeolites is a "grand challenge" in modern zeolite science. Imagine screening a library of zeolite designs through first-principles, assessing their "synthesizability" (to identify the best, yet feasible material), and selecting a target structure for synthesis, characterization, and testing. Realizing this vision would require accurate models and new characterization and synthesis techniques. These new models must account for the effects of solvent, structure-directing agents (SDAs), and synthesis conditions, all of which affect the properties of the zeolite. For example, Sastre and coworkers found

that a model with explicit SDAs identified more accurate Al substitutions compared to the gas phase model [6]. Future analytical techniques that precisely characterize the location and environment around heteroatoms could be used to test model predictions and discriminate among computational methodologies, and future synthetic techniques capable of carefully position active site atoms would be able to leverage these predictive tools from computational chemistry [7, 8].

8.2.5 Leveraging fructose ketalization for improved HMF yields from glucose

The *in-situ* protection of fructose via ketalization may have potential for improving yields of furanics from glucose in a one-pot synthesis [9]. Because HMF undergoes side reactions with water, performing the reaction in an alcoholic media can reduce side reactions [10]. Moreover, a catalyst active for ketalization could simultaneously form acetals of HMF, which may protect the carbonyl of HMF, as well as improve its partition coefficient into an extracting solvent. The conversion of furanosides into furanics has not been explored, and could offer advantages compared to the dehydration of fructose. Fructose dehydration proceeds via the facile removal of the anomeric hydroxyl (creating an oxonium intermediate which may be susceptible to side reactions) followed by slower subsequent steps [11]; the analogous route for fructoside would begin with removal of the less-reactive alkoxyl group. Slowing down this step might cause substantial changes in the reaction network, and the effect of this on the reaction rates and selectivity would be worth exploring.

As the renewable chemicals industry grows, there will continue to be a need for deeper understanding of the fundamental aspects of these new processes. Continued application and development of electronic structure tools will facilitate catalyst and process design, and with it, a more viable and efficient green economy.

REFERENCES

[1] L. Yang, G. Tsilomelekis, S. Caratzoulas, and D. G. Vlachos. Mechanism of Brønsted Acid-Catalyzed Glucose Dehydration. *ChemSusChem*, 8(8):1334–1341, 2015. ISSN 1864564X. doi: 10.1002/cssc.201403264.

[2] J. Zhang, A. Das, R. S. Assary, L. A. Curtiss, and E. Weitz. A combined experimental and computational study of the mechanism of fructose dehydration to 5-hydroxymethylfurfural in dimethylsulfoxide using Amberlyst 70, PO43-/niobic acid, or sulfuric acid catalysts. *Applied Catalysis B: Environmental*, 181:874–887, 2016. ISSN 09263373. doi: 10.1016/j.apcatb.2014.10.056.

[3] L.-K. Ren, L.-F. Zhu, T. Qi, J.-Q. Tang, H.-Q. Yang, C.-W. Hu, L.-K. Ren, L.-F. Zhu, J.-Q. Tang, H.-Q. Yang, and C.-W. Hu. Performance of Dimethylsulfoxide and Brønsted Acid Catalysts in Fructose Conversion to 5-Hydroxymethylfurfural. *ACS Catalysis*, 7:2199–2212, 2017. ISSN 2155-5435. doi: 10.1021/acscatal.6b01802.

[4] H. C. L. Abbenhuis. Advances in Homogeneous and Heterogeneous Catalysis with Metal-Containing Silsesquioxanes. *Chemistry - A European Journal*, 6(1): 25–32, 2000. ISSN 0947-6539. doi: 10.1002/(SICI)1521-3765(20000103)6:1⟨25::AID-CHEM25⟩3.0.CO;2-Y.

[5] R. A. Van Santen, H. C. L. Abbenhuis, and M. L. W. Vorstenbosch. Method for producing silsasequioxane metal complexes, novel silasesquioxane metal complexes and use thereof. *United States Patent*, 6127557:1–7, 2000.

[6] G. Sastre, V. Fornes, and A. Corma. On the preferential location of Al and proton siting in zeolites: A computational and infrared study. *Journal of Physical Chemistry B*, 106(3):701–708, 2002. ISSN 10895647. doi: 10.1021/jp013189p.

[7] G. Sastre, A. Cantin, M. J. Diaz-Cabanas, and A. Corma. Searching organic structure directing agents for the synthesis of specific zeolitic structures: An experimentally tested computational study. *Chemistry of Materials*, 17(3):545–552, 2005. ISSN 08974756. doi: 10.1021/cm049912g.

[8] R. Simancas, D. Dari, N. Velamazán, N. M. T., A. Cantín, J. L. Jordá, G. Sastre, A. Corma, and F. Rey. Modular Organic Structure-Directing Agents for the Synthesis of Zeolites. *Science*, 330(November):1219–1223, 2010. doi: 10.1126/science.1196240.

[9] E. Nikolla, Y. Roman-Leshkov, M. Moliner, and M. E. Davis. "One-pot" synthesis of 5-(hydroxymethyl)furfural from carbohydrates using tin-beta zeolite. *ACS Catalysis*, 1(4):408–410, 2011. ISSN 21555435. doi: 10.1021/cs2000544.

[10] L. Lai and Y. Zhang. The production of 5-hydroxymethylfurfural from fructose in isopropyl alcohol: A green and efficient system. *ChemSusChem*, 4(12):1745–1748, 2011. ISSN 18645631. doi: 10.1002/cssc.201100489.

[11] S. Caratzoulas and D. G. Vlachos. Converting fructose to 5-hydroxymethylfurfural: a quantum mechanics/molecular mechanics study of the mechanism and energetics. *Carbohydr Res*, 346(5):664–672, 2011. doi: 10.1016/j.carres.2011.01.029.

Appendix A

SUPPORTING INFORMATION FOR CHAPTER 2

CHEMISTRY & SUSTAINABILITY
CHEMSUSCHEM
ENERGY & MATERIALS

Supporting Information

Origin of 5-Hydroxymethylfurfural Stability in Water/ Dimethyl Sulfoxide Mixtures

George Tsilomelekis, Tyler R. Josephson, Vladimiros Nikolakis,* and Stavros Caratzoulas*[a]

cssc_201300786_sm_miscellaneous_information.pdf

Table S1: Atomic coordinates of the optimized cis-HMF conformer

Tag	Atom	X	Y	Z
1	O2	3.0823	-1.1535	-0.0805
2	C6	2.6448	-0.0139	-0.0697
3	H6	3.3213	0.8651	-0.1143
4	C5	1.2408	0.3522	-0.0001
5	O3	0.2854	-0.6314	0.0569
6	C4	0.6279	1.5848	0.0153
7	H5	1.1302	2.5418	-0.0223
8	C3	-0.7730	1.3460	0.0912
9	H4	-1.5710	2.0723	0.1339
10	C2	-0.9232	-0.0191	0.1159
11	C1	-2.1236	-0.9138	0.2083
12	H3	-2.3001	-1.2049	1.2498
13	H2	-1.9285	-1.8352	-0.3578
14	O1	-3.3130	-0.2622	-0.2131
15	H1	-3.2523	-0.0792	-1.1605

Table S2: Atomic coordinates of the optimized trans-HMF conformer

Tag	Atom	X	Y	Z
1	O2	3.5643	-0.0397	-0.1131
2	C6	2.5079	-0.6533	-0.0672
3	H6	2.4798	-1.7614	-0.0805
4	C5	1.2045	-0.0149	0.0090
5	O3	0.1037	-0.8474	0.0464
6	C4	0.7864	1.2935	0.0551
7	H5	1.4366	2.1562	0.0378
8	C3	-0.6338	1.2666	0.1297
9	H4	-1.3110	2.1057	0.1913
10	C2	-0.9970	-0.0587	0.1232
11	C1	-2.3236	-0.7548	0.1973
12	H3	-2.5649	-1.0081	1.2358
13	H2	-2.2658	-1.6989	-0.3629
14	O1	-3.3900	0.0708	-0.2479
15	H1	-3.2654	0.2664	-1.1866

Table S3: Calculated IR frequencies and molecular absorptivities of all trans and cis HMF normal modes

	cis		trans	
Mode #	**Frequence [cm^{-1}]**	**Intensity [km/mol]**	**Frequency [cm^{-1}]**	**Intensity [km/mol]**
39	3682	31.1861	3681	30.2899
38	3166	0.2521	3167	0.8726
37	3146	0.9005	3156	0.0563
36	2974	8.8165	2971	10.0386
35	2921	27.1651	2916	34.2363
34	2827	105.9566	2846	83.153
33	1697	418.2064	1692	357.4497
32	1561	2.3293	1567	45.6251
31	1499	87.4515	1496	158.064
30	1444	6.8981	1446	5.1127
29	1394	7.1735	1388	58.35
28	1353	55.8063	1364	41.6402
27	1335	47.4474	1342	35.2489
26	1308	10.4006	1309	7.1137
25	1256	52.8174	1207	10.8975
24	1200	3.7668	1186	78.8628
23	1172	46.0487	1180	23.3758
22	1145	8.079	1143	9.0401
21	1049	91.852	1047	75.7287
20	1008	51.235	1003	45.0185
19	966	2.9515	974	0.3927
18	961	10.5364	969	2.3151
17	944	6.9406	940	41.5881
16	936	28.663	938	1.3676
15	858	0.3814	871	0.7458
14	788	52.8642	797	47.3742
13	748	61.7289	738	61.636
12	688	14.52	684	26.6705
11	625	3.2324	618	3.6219
10	593	1.7353	593	1.5206
9	488	3.3699	537	1.9686
8	424	13.8358	361	29.9825
7	340	84.2415	329	133.5716
6	298	85.7081	261	22.5015
5	232	7.9291	240	20.1345
4	173	11.6301	211	5.8465
3	136	1.0906	144	5.2902
2	130	3.7751	110	0.8176

1	45	7.0535	44	7.2152

Table S4: Displacement vectors of all normal vibrations of the trans conformer. The atom numbering and coordinates are shown in Table S1

Mode	Displacement Vectors				
	Tag	**X**	**Y**	**Z**	
1	1	0.02	0.03	0.15	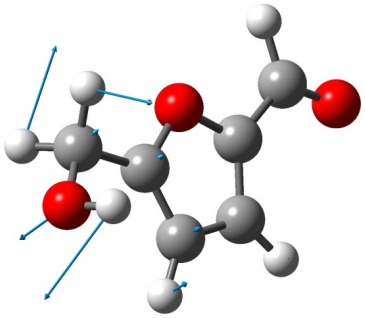
	2	0.03	0.01	0.08	
	3	0.04	0.01	0.1	
	4	0.01	-0.01	-0.03	
	5	0.02	-0.02	-0.06	
	6	-0.01	-0.01	-0.09	
	7	-0.03	0	-0.08	
	8	-0.02	-0.03	-0.16	
	9	-0.03	-0.04	-0.19	
	10	0.01	-0.04	-0.13	
	11	0.02	-0.06	-0.14	
	12	0.2	-0.39	-0.18	
	13	-0.09	0.12	-0.46	ν=43.71 cm^{-1}
	14	-0.05	0.1	0.3	
	15	-0.26	0.32	0.32	
	Tag	**X**	**Y**	**Z**	
2	1	0.03	-0.1	0.3	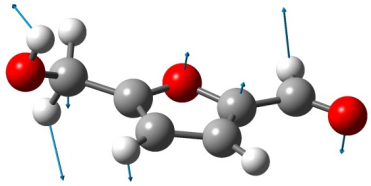
	2	-0.03	-0.02	-0.1	
	3	-0.11	-0.02	-0.38	
	4	0	0.04	-0.19	
	5	-0.02	0.07	-0.24	
	6	0.03	0.05	-0.05	
	7	0.04	0.04	0.03	
	8	0.03	0.07	0.03	
	9	0.05	0.08	0.15	
	10	0	0.08	-0.06	
	11	0.03	0.04	0.18	ν=110.24 cm^{-1}
	12	0.12	0.29	0.26	
	13	0.06	-0.1	0.42	
	14	-0.06	-0.16	0.05	
	15	-0.13	-0.36	0	
	Tag	**X**	**Y**	**Z**	
3	1	-0.06	0.29	0.14	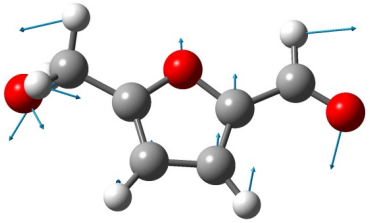
	2	0.07	0.04	-0.08	
	3	0.31	0.04	-0.23	
	4	-0.02	-0.16	-0.12	
	5	-0.02	-0.17	-0.05	
	6	0	-0.16	-0.09	
	7	0.02	-0.18	-0.12	ν=143.92 cm^{-1}
	8	0.02	-0.14	0.02	

	9	0.02	-0.14	0.07	
	10	0	-0.13	0.05	
	11	-0.09	0.07	0.15	
	12	-0.19	0.32	0.19	
	13	-0.26	-0.04	0.32	
	14	0.1	0.23	-0.05	
	15	0.23	0.09	-0.06	
4	**Tag**	**X**	**Y**	**Z**	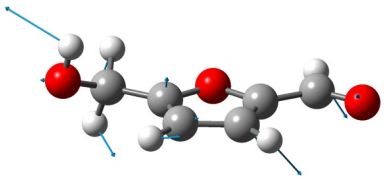 ν=211.01 cm^{-1}
	1	-0.04	0.13	-0.1	
	2	0.05	-0.03	0.12	
	3	0.21	-0.03	0.31	
	4	0.02	-0.11	0.11	
	5	-0.05	-0.03	-0.09	
	6	0.12	-0.08	0.14	
	7	0.21	-0.15	0.28	
	8	0.11	0.04	-0.06	
	9	0.18	0.09	-0.06	
	10	0	0.07	-0.18	
	11	-0.02	0.09	0.02	
	12	0.13	0.26	0.1	
	13	-0.05	-0.01	0.19	
	14	-0.14	-0.06	0.03	
	15	-0.41	-0.39	-0.07	
5	**Tag**	**X**	**Y**	**Z**	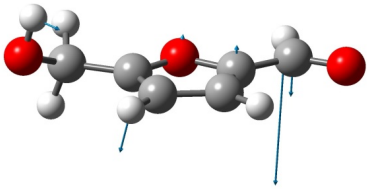 ν=240.37 cm^{-1}
	1	0.01	-0.03	-0.07	
	2	0	0.01	0.23	
	3	0	0	0.87	
	4	-0.01	0.03	-0.16	
	5	0.01	0	-0.14	
	6	-0.04	0.02	-0.05	
	7	-0.06	0.04	0.01	
	8	-0.03	-0.02	0.11	
	9	-0.04	-0.04	0.27	
	10	0	-0.03	0.02	
	11	0	-0.01	0.03	
	12	-0.03	0.02	0.03	
	13	-0.02	-0.03	0.05	
	14	0.04	0.02	-0.01	
	15	0.14	0.11	0.03	

	Tag	X	Y	Z	
6	1	-0.08	0.09	0.04	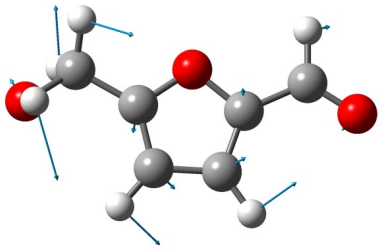
	2	0	-0.05	0	
	3	0.13	-0.05	0.09	
	4	-0.02	-0.1	-0.12	
	5	-0.08	0.02	0.06	
	6	0.12	-0.06	-0.13	
	7	0.22	-0.13	-0.26	
	8	0.13	0.09	0.1	
	9	0.24	0.17	0.15	
	10	-0.01	0.12	0.17	
	11	0.02	0	-0.09	
	12	-0.05	-0.31	-0.19	ν=261.26 cm^{-1}
	13	0.26	0.15	-0.33	
	14	-0.09	-0.12	-0.02	
	15	0.15	0.41	0.13	
7	1	-0.05	0.01	-0.01	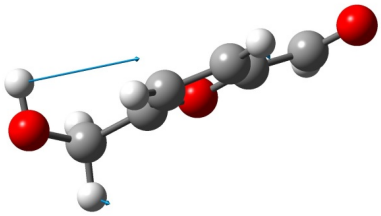
	2	-0.03	-0.01	0.01	
	3	-0.03	-0.01	-0.04	
	4	-0.02	-0.01	0.05	
	5	-0.01	0	-0.04	
	6	0	0	0.04	
	7	0.02	-0.01	0.1	
	8	0	0.01	-0.07	
	9	0.01	0.02	-0.06	
	10	0	0.01	-0.07	
	11	0.04	-0.01	0.05	ν=329.01 cm^{-1}
	12	0.07	0.1	0.09	
	13	0.03	-0.06	0.14	
	14	0.03	-0.05	0	
	15	0.59	0.71	0.23	
8	1	0.28	-0.04	-0.01	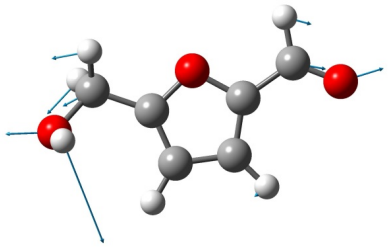
	2	0.2	0.07	-0.02	
	3	0.16	0.07	-0.03	
	4	0.09	0.03	0	
	5	0.04	-0.02	0.03	
	6	-0.02	0	-0.01	
	7	-0.09	0.05	-0.03	
	8	-0.02	-0.06	0.02	
	9	-0.02	-0.05	0.05	
	10	-0.04	-0.05	0.02	ν=361.20 cm^{-1}
	11	-0.2	0.07	0.02	
	12	-0.23	0.18	0.03	
	13	-0.24	0.01	0.1	

	14	-0.31	-0.04	-0.05	
	15	0.16	0.68	0.16	
9	**Tag**	**X**	**Y**	**Z**	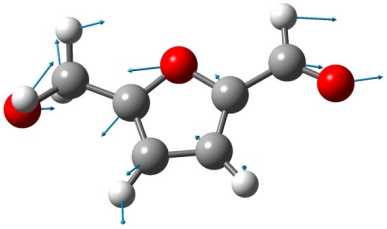 *v*=536.92 cm^{-1}
	1	0.28	-0.01	-0.02	
	2	0.21	0.05	0	
	3	0.31	0.04	0.01	
	4	-0.08	-0.14	0	
	5	-0.3	0.04	-0.06	
	6	-0.11	-0.14	0.07	
	7	-0.01	-0.2	0.18	
	8	-0.14	0.16	-0.11	
	9	0.01	0.28	-0.19	
	10	-0.19	0.16	0.09	
	11	0.03	-0.09	0.05	
	12	-0.02	-0.32	-0.02	
	13	0.22	0.02	-0.13	
	14	0.19	0	0.02	
	15	0.18	-0.22	-0.02	
10	**Tag**	**X**	**Y**	**Z**	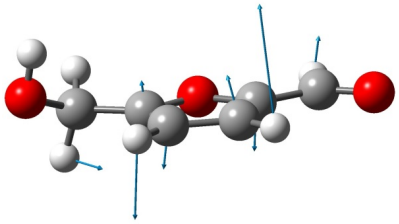 *v*=592.73 cm^{-1}
	1	0.04	0	-0.01	
	2	0.02	0.01	0.02	
	3	0.03	0.01	-0.22	
	4	-0.01	-0.03	0.27	
	5	-0.05	-0.01	-0.05	
	6	-0.06	-0.02	-0.24	
	7	-0.07	-0.03	-0.66	
	8	-0.03	0.02	0.23	
	9	-0.02	0.01	0.43	
	10	-0.02	0.02	-0.17	
	11	0.06	0.03	-0.03	
	12	0.19	0.17	0.03	
	13	0.01	-0.04	0.09	
	14	0.03	-0.01	0.01	
	15	0	0.03	0.02	
11	**Tag**	**X**	**Y**	**Z**	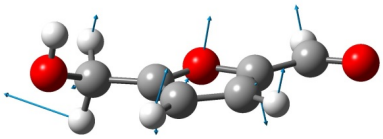 *v*=618.43 cm^{-1}
	1	-0.05	0.01	-0.02	
	2	-0.02	-0.03	0.06	
	3	-0.04	-0.02	-0.23	
	4	0.06	0.04	0.31	
	5	0.05	0.05	-0.32	
	6	0.08	0.05	-0.08	
	7	0.04	0.07	-0.24	
	8	0.06	-0.02	-0.13	
	9	0.09	0.01	-0.29	
	10	0	-0.03	0.33	
	11	-0.12	-0.09	0.08	

	12	-0.41	-0.4	-0.06	
	13	0.03	0.08	-0.19	
	14	-0.03	0.03	-0.02	
	15	0.03	-0.13	-0.04	
12	**Tag**	**X**	**Y**	**Z**	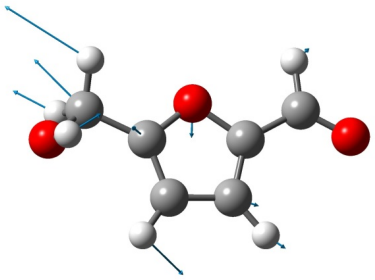 *v*=684.46 cm^{-1}
	1	-0.03	0.03	0.01	
	2	0.05	-0.1	-0.01	
	3	0.11	-0.09	0.03	
	4	0.07	0.03	-0.03	
	5	0	0.18	0.08	
	6	0.14	0.06	-0.03	
	7	0.1	0.09	-0.03	
	8	0.09	0.02	0.06	
	9	0.29	0.17	0.2	
	10	-0.15	-0.01	-0.19	
	11	-0.25	-0.32	0.05	
	12	-0.22	-0.17	0.09	
	13	-0.45	-0.35	0.08	
	14	0.07	0.05	0.01	
	15	0.21	-0.12	-0.01	
13	**Tag**	**X**	**Y**	**Z**	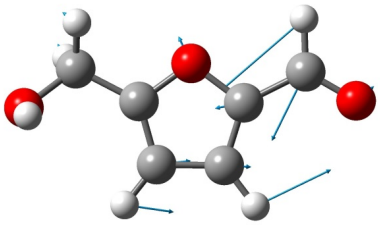 *v*=738.21 cm^{-1}
	1	0.1	-0.08	-0.01	
	2	-0.19	0.38	0.01	
	3	-0.46	0.39	0.03	
	4	-0.16	0.03	0.01	
	5	-0.07	-0.15	0.01	
	6	0.15	0.01	-0.01	
	7	0.42	-0.2	-0.02	
	8	0.19	-0.02	0	
	9	0.27	0.04	0.03	
	10	-0.01	-0.03	-0.03	
	11	-0.06	-0.07	0.01	
	12	-0.05	-0.08	0.01	
	13	-0.08	-0.06	-0.01	
	14	0.03	0	0	
	15	0.06	-0.04	0	
14	**Tag**	**X**	**Y**	**Z**	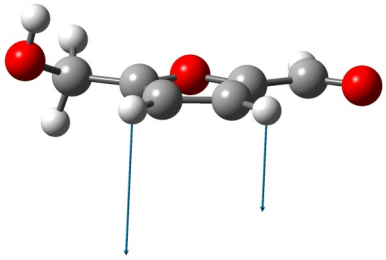 *v*=796.61 cm^{-1}
	1	0	0	0	
	2	0	0	0	
	3	0	0	-0.06	
	4	0	0	0.03	
	5	0	0	0.02	
	6	-0.01	0	-0.08	
	7	0.02	-0.01	0.56	
	8	-0.01	0	-0.1	
	9	0.03	-0.03	0.81	

	10	0	0	0.01	
	11	0	0.01	0.01	
	12	-0.03	-0.06	-0.01	
	13	0.04	0.04	-0.04	
	14	0	0	0	
	15	0	-0.04	-0.01	
15	**Tag**	**X**	**Y**	**Z**	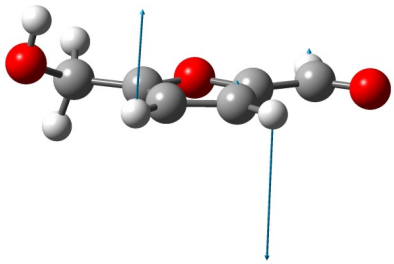 ν=871.45 cm^{-1}
	1	0	0	-0.01	
	2	0	0	0.02	
	3	-0.01	0	-0.11	
	4	0	0	0.02	
	5	0	0	0	
	6	-0.01	0	-0.13	
	7	0.03	-0.01	0.79	
	8	0.01	0	0.1	
	9	-0.01	0.03	-0.57	
	10	0	0	0	
	11	0	0	-0.01	
	12	0.02	0.06	0.01	
	13	-0.02	-0.03	0.04	
	14	0	0	0	
	15	-0.01	0.03	0.01	
16	**Tag**	**X**	**Y**	**Z**	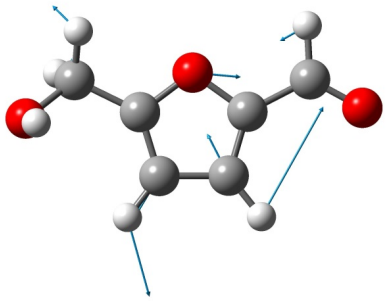 ν=937.87 cm^{-1}
	1	-0.02	-0.02	0	
	2	-0.06	0.08	0	
	3	-0.15	0.08	0.01	
	4	-0.01	-0.09	0	
	5	0.26	0.03	-0.01	
	6	-0.11	-0.23	0	
	7	0.35	-0.59	-0.03	
	8	-0.14	0.22	0.01	
	9	0.11	0.43	0.03	
	10	0.07	0.07	0	
	11	-0.01	-0.12	0.02	
	12	-0.07	0.02	0.03	
	13	-0.13	-0.15	0.07	
	14	-0.06	0.05	-0.02	
	15	0	0.02	-0.02	

	Tag	X	Y	Z	
17	1	0.01	0	0	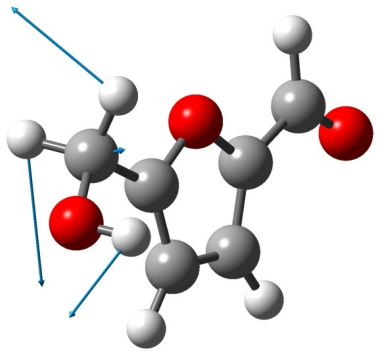
	2	-0.01	0.03	0.02	
	3	-0.03	0.03	-0.07	
	4	0	-0.01	0	
	5	-0.03	0.09	-0.01	
	6	0	-0.05	0.01	
	7	-0.03	-0.03	-0.03	
	8	0.02	-0.05	-0.04	
	9	0.13	0.02	0.1	
	10	-0.01	-0.03	0.11	
	11	0.02	-0.03	-0.16	
	12	0.04	0.61	0.01	
	13	-0.14	-0.37	0.4	ν=940.28 cm^{-1}
	14	0.04	-0.02	0.03	
	15	-0.39	0.26	0.04	
18	Tag	X	Y	Z	
	1	0	-0.02	0.02	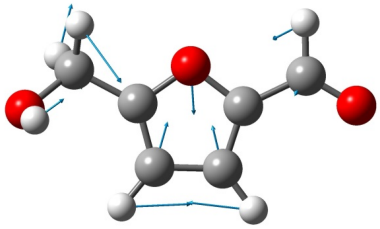
	2	-0.07	0.11	-0.07	
	3	-0.15	0.1	0.31	
	4	0.03	-0.04	0.02	
	5	0.02	0.27	0.01	
	6	-0.06	-0.24	-0.01	
	7	-0.36	-0.04	0.04	
	8	0.07	-0.25	0	
	9	0.38	-0.02	-0.06	
	10	-0.07	-0.03	-0.05	
	11	0.05	0.11	0.08	ν=968.96 cm^{-1}
	12	0.07	-0.29	-0.02	
	13	0.21	0.31	-0.25	
	14	-0.02	-0.01	-0.02	
	15	0.16	-0.12	-0.02	
19	Tag	X	Y	Z	
	1	0	0	-0.06	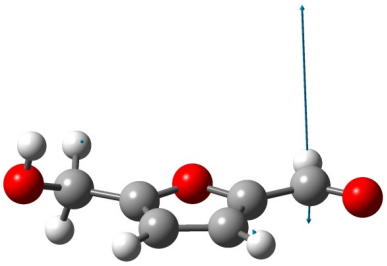
	2	0	0.01	0.22	
	3	-0.07	0.02	-0.94	
	4	0	0	-0.09	
	5	0.01	0.03	0.01	
	6	-0.01	-0.03	0.02	
	7	-0.05	0	-0.09	
	8	0.01	-0.03	0	
	9	0.05	0	0.04	
	10	-0.01	0	-0.02	ν=973.71 cm^{-1}
	11	0	0.02	0.02	
	12	0.02	-0.09	0	
	13	0.03	0.07	-0.06	

	14	-0.01	0	0	
	15	0.06	-0.04	-0.01	
20	**Tag**	**X**	**Y**	**Z**	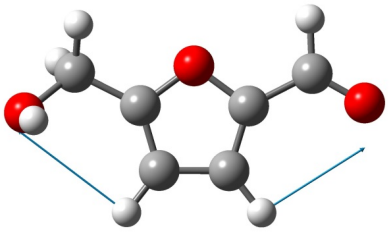 *v*=1002.93 cm^{-1}
	1	0.01	0	0	
	2	0.01	0	0	
	3	0.05	0	-0.01	
	4	-0.04	-0.01	0	
	5	-0.01	0.09	0	
	6	0.09	0.01	-0.01	
	7	0.56	-0.34	-0.02	
	8	-0.07	-0.05	0.01	
	9	-0.58	-0.45	0	
	10	0.01	-0.01	0	
	11	0.02	0	0.01	
	12	0.02	-0.01	0	
	13	0.02	0.01	-0.01	
	14	-0.01	0.01	-0.01	
	15	0.01	0	0	
21	**Tag**	**X**	**Y**	**Z**	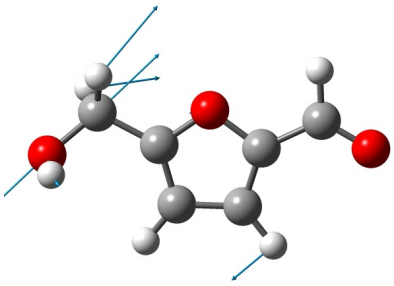 *v*=1046.98 cm^{-1}
	1	0.01	0	0	
	2	0	0	0	
	3	0.04	0	0	
	4	-0.02	-0.01	0	
	5	-0.12	0.02	0.01	
	6	-0.01	0.03	0	
	7	-0.24	0.21	0.02	
	8	0.06	-0.02	-0.01	
	9	0.05	-0.05	0.02	
	10	0.06	-0.02	0.02	
	11	0.35	-0.32	0.09	
	12	0.4	-0.02	0.16	
	13	0.33	-0.36	0.21	
	14	-0.27	0.24	-0.1	
	15	0.05	0.03	-0.13	
22	**Tag**	**X**	**Y**	**Z**	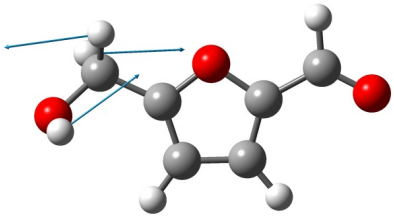 *v*=1143.39 cm^{-1}
	1	0	0	0	
	2	-0.01	0	0	
	3	-0.08	0.01	0.01	
	4	0.06	0.02	0	
	5	-0.06	0.02	0	
	6	-0.02	-0.02	0	
	7	0.03	-0.05	0	
	8	0	0.03	-0.01	
	9	-0.01	0.02	0.02	
	10	0.08	-0.03	0.05	
	11	-0.03	0.02	-0.05	

	12	0.56	0.02	0.09	
	13	-0.56	0.03	-0.11	
	14	-0.02	-0.01	0.01	
	15	0.47	-0.31	0	
23	**Tag**	**X**	**Y**	**Z**	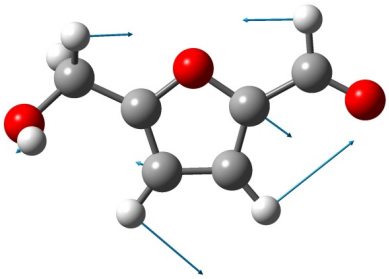
	1	-0.03	0.02	0	
	2	0.01	-0.02	0	
	3	-0.35	-0.01	0.02	
	4	0.22	0.18	-0.01	
	5	-0.07	-0.07	0	
	6	0.05	-0.04	0	
	7	0.49	-0.36	-0.03	
	8	-0.14	-0.06	0.01	
	9	0.37	0.35	-0.01	
	10	-0.11	-0.05	0	
	11	0.05	0.02	0.01	
	12	0.07	0	0.01	ν=1180.12 cm^{-1}
	13	0.31	0.01	0.04	
	14	0	0.02	-0.01	
	15	-0.09	0.06	-0.01	
24	**Tag**	**X**	**Y**	**Z**	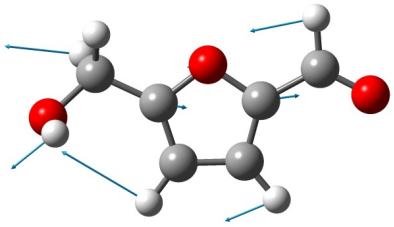
	1	-0.02	0.01	0	
	2	-0.04	0.05	0	
	3	-0.38	0.06	0.02	
	4	0.22	-0.02	-0.01	
	5	-0.12	0.01	0.01	
	6	-0.01	-0.1	0	
	7	-0.3	0.11	0.01	
	8	0.03	0.09	0.01	
	9	-0.48	-0.32	0	
	10	0.16	0.03	-0.04	
	11	-0.05	-0.04	0.04	ν=1185.95 cm^{-1}
	12	-0.44	-0.08	-0.05	
	13	0.05	-0.01	0	
	14	0.02	-0.01	-0.01	
	15	-0.26	0.19	0	
25	**Tag**	**X**	**Y**	**Z**	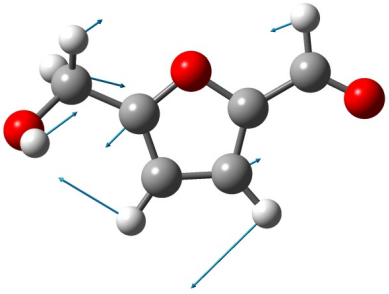
	1	-0.02	-0.01	0	
	2	-0.03	0.05	0	
	3	-0.19	0.06	0.02	
	4	0.08	-0.04	0	
	5	0.09	-0.07	-0.01	
	6	0.16	-0.07	-0.01	
	7	-0.43	0.37	0.03	
	8	-0.07	-0.02	0	
	9	-0.37	-0.26	0.02	

	10	-0.19	0.17	0.04	*v*=1206.77 cm^{-1}
	11	-0.02	-0.02	-0.06	
	12	0.38	0.13	0.07	
	13	0.17	-0.09	0.09	
	14	-0.01	0.02	0.01	
	15	0.24	-0.15	0.01	
26	**Tag**	**X**	**Y**	**Z**	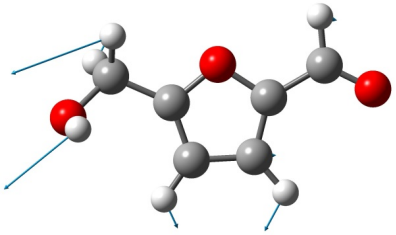 *v*=1308.89 cm^{-1}
	1	0	-0.01	0	
	2	-0.02	0.03	0	
	3	0.1	0.03	-0.01	
	4	0	-0.04	0	
	5	0	0.01	0	
	6	0.13	0	-0.01	
	7	-0.14	0.22	0.01	
	8	-0.11	0.01	0.01	
	9	0.07	0.18	0	
	10	-0.01	-0.03	0	
	11	0.08	0.01	0.08	
	12	0.1	-0.15	0.05	
	13	-0.64	0.16	-0.21	
	14	0.02	-0.03	-0.05	
	15	-0.47	0.32	-0.04	
27	**Tag**	**X**	**Y**	**Z**	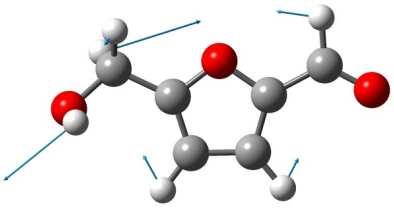 *v*=1341.57 cm^{-1}
	1	0.01	0.02	0	
	2	0.03	-0.05	0	
	3	-0.27	-0.05	0.01	
	4	-0.01	0.04	0	
	5	0.03	-0.02	0	
	6	-0.12	0	0.01	
	7	0.1	-0.18	-0.01	
	8	0.12	-0.01	-0.01	
	9	-0.11	-0.22	0	
	10	-0.05	0.07	0.02	
	11	-0.05	-0.03	0.06	
	12	0.61	-0.14	0.19	
	13	-0.07	0.07	-0.1	
	14	0.04	0	-0.05	
	15	-0.45	0.33	-0.04	
28	**Tag**	**X**	**Y**	**Z**	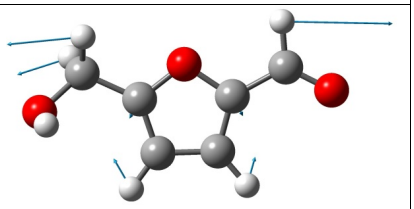 *v*=1363.67 cm^{-1}
	1	-0.04	-0.06	0	
	2	-0.05	0.07	0	
	3	0.74	0.07	-0.04	
	4	0.05	0	0	
	5	-0.02	0.01	0	
	6	0.01	-0.01	0	
	7	-0.01	0.02	0	

	8	-0.03	0.01	0	
	9	0.02	0.06	0	
	10	0.06	-0.03	0	
	11	-0.11	-0.01	0.01	
	12	0.42	-0.07	0.12	
	13	0.44	0	0.04	
	14	0.01	0.01	-0.02	
	15	-0.13	0.1	-0.01	
29	**Tag**	**X**	**Y**	**Z**	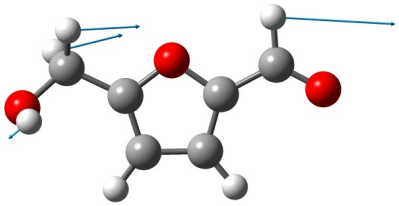 *v*=1388.44 cm^{-1}
	1	-0.05	-0.05	0	
	2	-0.01	0.04	0	
	3	0.69	0.05	-0.03	
	4	0.06	0.13	0	
	5	0	-0.05	0	
	6	-0.07	-0.06	0	
	7	0.06	-0.18	-0.01	
	8	0.08	-0.04	-0.01	
	9	-0.1	-0.2	0	
	10	-0.07	0.12	0	
	11	0.09	-0.02	0	
	12	-0.34	0.08	-0.07	
	13	-0.48	0.01	-0.08	
	14	0	-0.01	0.01	
	15	0.06	-0.04	0.01	
30	**Tag**	**X**	**Y**	**Z**	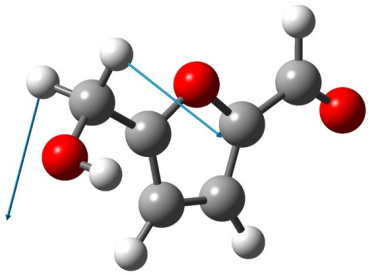 *v*=1445.83 cm^{-1}
	1	0	0	0	
	2	0	0	0	
	3	-0.02	0	0	
	4	-0.01	0	0	
	5	0	0	0	
	6	0.01	0	0	
	7	0	0.01	0	
	8	-0.01	-0.01	0	
	9	0.03	0.02	0	
	10	0.02	0.01	0	
	11	-0.02	-0.07	0.03	
	12	-0.05	0.68	0.18	
	13	0.13	0.33	-0.6	
	14	0	-0.01	0.01	
	15	0.01	-0.02	0	

	Tag	X	Y	Z
31	1	0	0.02	0
	2	0.12	-0.1	-0.01
	3	-0.12	-0.11	0.01
	4	-0.29	0.33	0.02
	5	-0.04	-0.04	0
	6	0.15	-0.21	-0.01
	7	-0.28	0.07	0.01
	8	-0.16	-0.24	0.01
	9	0.33	0.11	-0.02
	10	0.36	0.33	-0.02
	11	-0.13	-0.07	0
	12	0.01	-0.23	-0.01
	13	-0.04	-0.2	0.21
	14	0.01	0.01	0
	15	-0.05	0.04	0

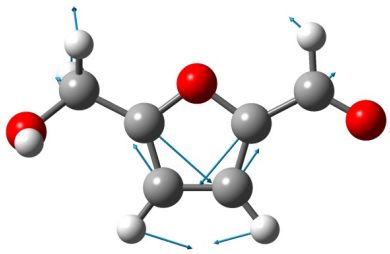

v=1495.98 cm^{-1}

	Tag	X	Y	Z
32	1	-0.01	0	0
	2	0.08	-0.06	-0.01
	3	0.07	-0.07	0
	4	-0.18	0.32	0.02
	5	0.01	0.01	0
	6	0.13	-0.29	-0.01
	7	-0.47	0.1	0.03
	8	0.11	0.3	0
	9	-0.45	-0.1	0.02
	10	-0.12	-0.33	0
	11	0.04	0.05	0
	12	0.07	0.09	0.02
	13	0.19	0.1	-0.08
	14	0	0	0
	15	-0.01	-0.01	0

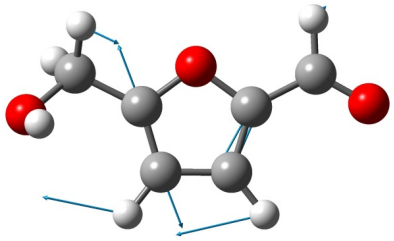

v=1567.18 cm^{-1}

	Tag	X	Y	Z
33	1	-0.39	-0.22	0.02
	2	0.62	0.3	-0.03
	3	-0.49	0.26	0.03
	4	-0.04	-0.08	0
	5	-0.02	0.02	0
	6	-0.02	0.05	0
	7	0.05	0.02	0
	8	0.01	0	0
	9	0.03	0.02	0
	10	0.01	-0.03	0
	11	-0.01	0	0
	12	0.04	0	0.01
	13	0.03	0	0

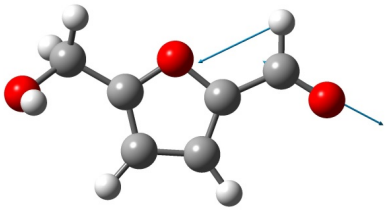

v=1692.03 cm^{-1}

	14	0	0	0	
	15	-0.02	0	0	
34	**Tag**	**X**	**Y**	**Z**	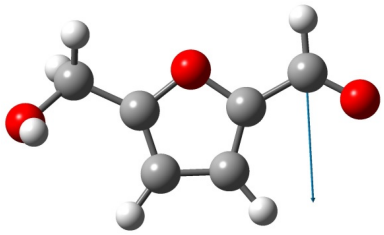
	1	0	0	0	
	2	0	-0.08	0	
	3	0	1	0.01	
	4	0	0	0	
	5	0	0	0	
	6	0	0	0	
	7	0	0	0	
	8	0	0	0	
	9	0	0	0	
	10	0	0	0	
	11	0	0	0	*v*=2846.03 cm^{-1}
	12	0	0	0	
	13	0	-0.01	-0.01	
	14	0	0	0	
	15	0	0	0	
35	**Tag**	**X**	**Y**	**Z**	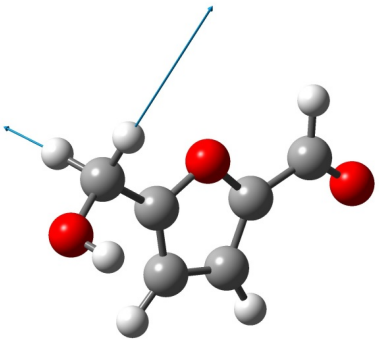
	1	0	0	0	
	2	0	0	0	
	3	0	-0.01	0	
	4	0	0	0	
	5	0	0	0	
	6	0	0	0	
	7	0	0	0	
	8	0	0	0	
	9	0	0	0	
	10	0	0	0	
	11	0	0.07	0.01	
	12	-0.07	-0.06	0.33	
	13	0.04	-0.79	-0.49	*v*=2915.73 cm^{-1}
	14	0	0	0	
	15	0	0	0	
36	**Tag**	**X**	**Y**	**Z**	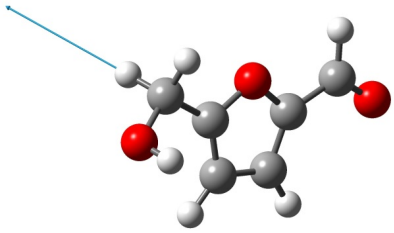
	1	0	0	0	
	2	0	0	0	
	3	0	0	0	
	4	0	0	0	
	5	0	0	0	
	6	0	0	0	
	7	0	0	0	
	8	0	0	0	
	9	0	0	0	*v*=2971.35 cm^{-1}
	10	0	0	0	
	11	0.02	-0.01	-0.09	

	12	-0.21	-0.21	0.89	
	13	-0.01	0.28	0.16	
	14	0	0	0	
	15	0.01	0	-0.01	
37	**Tag**	**X**	**Y**	**Z**	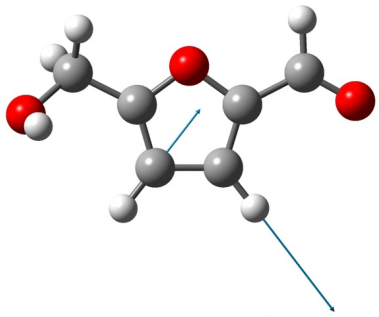
	1	0	0	0	
	2	0	0	0	
	3	0	0	0	
	4	0	0	0	
	5	0	0	0	
	6	-0.04	-0.05	0	
	7	0.43	0.58	-0.01	
	8	-0.04	0.05	0	
	9	0.43	-0.54	-0.04	
	10	0	0	0	
	11	0	0	0	
	12	0	0	0	*v*=3156.01 cm^{-1}
	13	0	0	0	
	14	0	0	0	
	15	0	0	0	
38	**Tag**	**X**	**Y**	**Z**	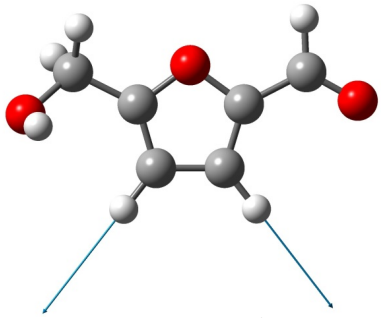
	1	0	0	0	
	2	0	0	0	
	3	0	0	0	
	4	0	0	0	
	5	0	0	0	
	6	-0.04	-0.05	0	
	7	0.41	0.55	-0.01	
	8	0.04	-0.05	0	
	9	-0.45	0.56	0.04	
	10	0	0	0	
	11	0	0	0	
	12	0	0	0	*v*=3167.23 cm^{-1}
	13	0	0	0	
	14	0	0	0	
	15	0	0	0	
39	**Tag**	**X**	**Y**	**Z**	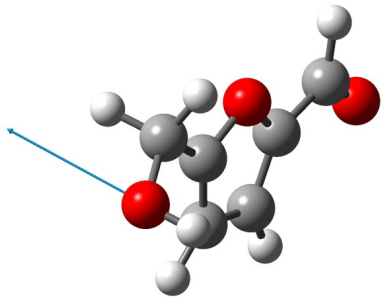
	1	0	0	0	
	2	0	0	0	
	3	0	0	0	
	4	0	0	0	
	5	0	0	0	
	6	0	0	0	
	7	0	0	0	
	8	0	0	0	
	9	0	0	0	

	10	0	0	0	ν=3680.63 cm^{-1}
	11	0	0	0	
	12	0	0	0.01	
	13	0	0	0	
	14	0.01	0.01	-0.06	
	15	-0.12	-0.21	0.97	

Table S5: Displacement vectors of all normal vibrations of the cis conformer. The atom numbering and coordinates are shown in Table S1

Mode	Displacement Vectors				
	Atom #	**X**	**Y**	**Z**	
1	1	0.04	0.03	0.11	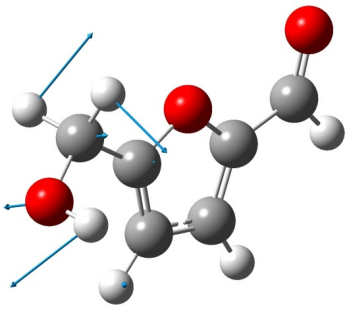
	2	0.02	0.02	0.07	
	3	0	0.03	0.11	
	4	0.01	-0.01	-0.02	
	5	0.02	-0.02	-0.08	
	6	-0.01	-0.02	-0.03	
	7	-0.02	-0.01	0.01	
	8	-0.01	-0.04	-0.1	
	9	-0.02	-0.05	-0.1	
	10	0.01	-0.04	-0.12	
	11	0.02	-0.06	-0.18	
	12	0.23	-0.39	-0.23	ν=45.17 cm^{-1}
	13	-0.11	0.12	-0.51	
	14	-0.05	0.09	0.27	
	15	-0.28	0.31	0.29	
	Tag	**X**	**Y**	**Z**	
2	1	-0.22	-0.15	0.24	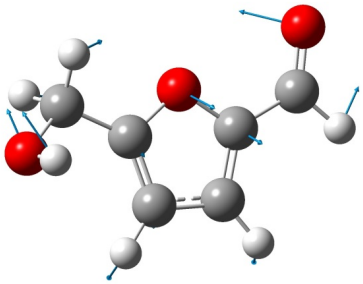
	2	-0.01	-0.07	-0.02	
	3	0.14	-0.19	-0.05	
	4	0.02	0.1	-0.21	
	5	0.01	0.12	-0.32	
	6	0.05	0.12	0.06	
	7	0.06	0.12	0.22	
	8	0.05	0.13	0.16	
	9	0.07	0.14	0.39	
	10	0.02	0.12	-0.07	
	11	0.12	0	0.04	
	12	0.23	0.06	0.07	ν=128.99 cm^{-1}
	13	0.24	-0.02	0.11	
	14	-0.02	-0.25	0.06	
	15	-0.1	-0.29	0.05	
	Tag	**X**	**Y**	**Z**	
3	1	0.22	0.13	0.24	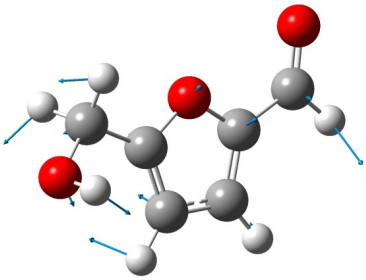
	2	0	0.05	-0.15	
	3	-0.15	0.16	-0.41	
	4	-0.04	-0.1	-0.23	
	5	-0.04	-0.1	-0.18	
	6	-0.03	-0.1	-0.02	
	7	-0.02	-0.1	0.01	
	8	-0.01	-0.08	0.21	
	9	0	-0.08	0.42	
	10	-0.03	-0.08	0.09	ν=136.46 cm^{-1}

	11	-0.11	0.03	0.08	
	12	-0.24	0.14	0.09	
	13	-0.18	-0.03	0.16	
	14	0	0.16	-0.07	
	15	0.16	0.19	-0.05	
4	**Tag**	**X**	**Y**	**Z**	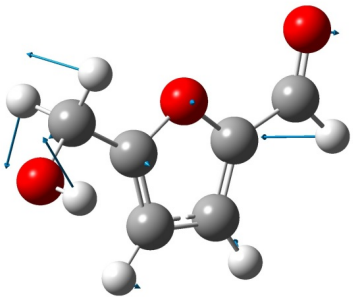 *v*=173.27 cm^{-1}
	1	0.14	0.05	-0.07	
	2	0.03	0	0.16	
	3	-0.04	0.07	0.5	
	4	0	-0.06	0.03	
	5	-0.05	-0.03	-0.14	
	6	0.05	-0.04	0.06	
	7	0.1	-0.06	0.19	
	8	0.03	0.02	-0.08	
	9	0.07	0.06	-0.07	
	10	-0.03	0.03	-0.15	
	11	-0.06	0.08	0.12	
	12	0.01	0.38	0.21	
	13	-0.11	-0.08	0.37	
	14	-0.09	-0.04	0.03	
	15	-0.21	-0.38	-0.04	
5	**Tag**	**X**	**Y**	**Z**	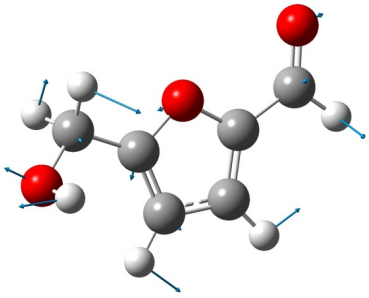 *v*=231.91 cm^{-1}
	1	0.19	0.01	0.04	
	2	0.02	-0.05	-0.14	
	3	-0.1	0.03	-0.48	
	4	0	-0.08	0.05	
	5	-0.11	0.03	0.12	
	6	0.13	-0.02	0.01	
	7	0.23	-0.08	-0.06	
	8	0.09	0.14	0.04	
	9	0.19	0.25	0	
	10	-0.07	0.15	0.05	
	11	-0.03	0.04	-0.13	
	12	0.03	-0.22	-0.19	
	13	0.15	0.18	-0.31	
	14	-0.19	-0.18	0	
	15	-0.31	-0.07	0.01	

	Tag	X	Y	Z
6	1	0.03	0	-0.05
	2	0	-0.01	0.12
	3	-0.01	0.01	0.46
	4	-0.02	-0.02	-0.09
	5	-0.04	0.01	-0.02
	6	0.01	-0.01	-0.1
	7	0.03	-0.02	-0.15
	8	0.01	0.03	0.03
	9	0.04	0.07	0.08
	10	-0.02	0.03	0.09
	11	0.01	-0.01	0.01
	12	-0.04	-0.1	-0.02
	13	0.1	0.05	-0.05
	14	-0.01	-0.07	-0.01
	15	0.38	0.71	0.16

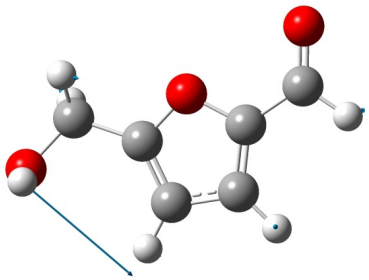

v=298.16 cm^{-1}

	Tag	X	Y	Z
7	1	0	0	0.03
	2	-0.01	0	-0.08
	3	-0.02	0	-0.35
	4	0	0	0.1
	5	0	0	-0.02
	6	0	0	0.1
	7	0.01	0	0.18
	8	-0.01	-0.01	-0.08
	9	0	0	-0.09
	10	-0.01	-0.01	-0.11
	11	0	0.01	0.05
	12	0.03	0.18	0.1
	13	-0.03	-0.08	0.18
	14	-0.01	-0.05	0
	15	0.39	0.72	0.17

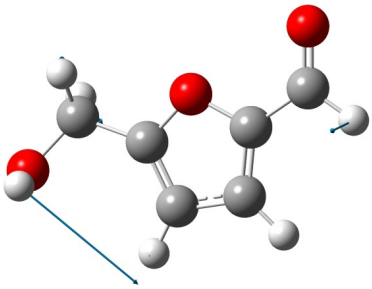

v=339.76 cm^{-1}

	Tag	X	Y	Z
8	1	-0.04	-0.05	-0.01
	2	0.2	0.04	0.01
	3	0.36	-0.08	0.05
	4	0.17	0.15	-0.03
	5	0.22	0.03	0.04
	6	0.01	0.08	-0.04
	7	-0.17	0.17	-0.09
	8	0.04	-0.12	0.06
	9	-0.03	-0.19	0.1
	10	0.08	-0.12	0.02
	11	-0.22	0.04	-0.01
	12	-0.29	0.18	0.01
	13	-0.33	-0.04	0.09

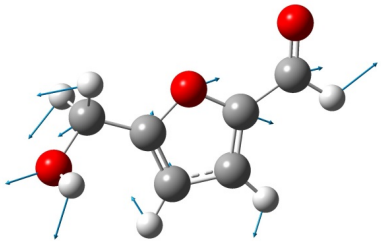

v=423.79 cm^{-1}

	14	-0.34	-0.05	-0.05	
	15	-0.21	0.3	0.02	
9	**Tag**	**X**	**Y**	**Z**	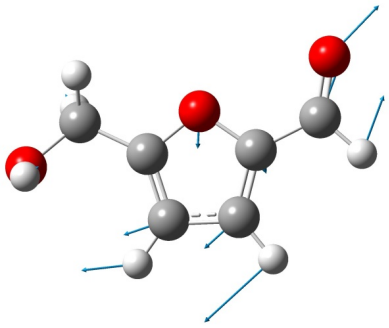
	1	0.33	-0.22	-0.01	
	2	0.16	-0.25	-0.01	
	3	0.19	-0.29	-0.03	
	4	0.03	0.14	0	
	5	-0.05	0.2	-0.02	
	6	-0.23	0.13	0.03	
	7	-0.46	0.26	0.09	
	8	-0.26	0.03	-0.03	
	9	-0.31	-0.03	-0.04	
	10	-0.1	0.02	0.01	
	11	-0.02	-0.08	0.03	
	12	-0.04	-0.09	0.02	
	13	-0.03	-0.07	0.01	ν=487.63 cm^{-1}
	14	0.06	0.04	0	
	15	0.09	-0.04	-0.01	
10	**Tag**	**X**	**Y**	**Z**	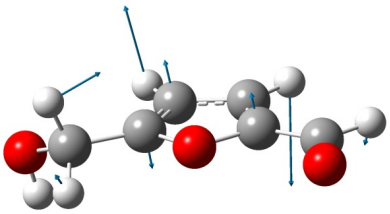
	1	0.02	-0.01	-0.01	
	2	-0.02	-0.02	0.03	
	3	-0.05	-0.01	-0.13	
	4	-0.01	0	0.21	
	5	0	-0.01	0.01	
	6	-0.06	-0.01	-0.22	
	7	-0.08	-0.01	-0.6	
	8	-0.02	0	0.25	
	9	-0.04	-0.04	0.48	
	10	0.01	0	-0.22	
	11	0.06	0.06	-0.05	ν=593.09 cm^{-1}
	12	0.2	0.3	0.04	
	13	-0.03	-0.07	0.14	
	14	0.01	-0.01	0.01	
	15	-0.04	0.07	0.02	
11	**Tag**	**X**	**Y**	**Z**	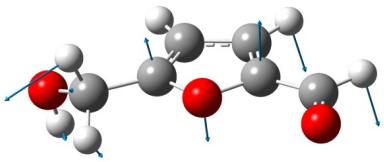
	1	-0.02	0.01	0	
	2	0.03	0.03	0.02	
	3	0.04	0.01	-0.37	
	4	0.05	0.01	0.39	
	5	-0.02	0.02	-0.32	
	6	0.05	0.01	-0.13	
	7	0.05	0	-0.35	
	8	0.04	0.01	-0.07	ν=625.10 cm^{-1}
	9	0.09	0.07	-0.18	
	10	-0.03	0	0.27	
	11	-0.08	-0.1	0.08	

	12	-0.27	-0.41	-0.05	
	13	0.04	0.08	-0.17	
	14	0	0.02	-0.01	
	15	0.07	-0.12	-0.04	
12	**Tag**	**X**	**Y**	**Z**	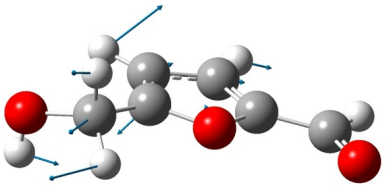 *v*=688.12 cm^{-1}
	1	-0.02	0.02	0	
	2	0.02	0.03	0	
	3	0.04	0.02	0.05	
	4	0.02	0.03	-0.03	
	5	-0.05	0.13	0.07	
	6	0.16	0.05	-0.03	
	7	0.2	0.03	-0.04	
	8	0.13	0.04	0.06	
	9	0.32	0.25	0.18	
	10	-0.15	-0.04	-0.18	
	11	-0.19	-0.35	0.05	
	12	-0.18	-0.21	0.09	
	13	-0.37	-0.41	0.08	
	14	0.07	0.06	0.01	
	15	0.21	-0.08	-0.01	
13	**Tag**	**X**	**Y**	**Z**	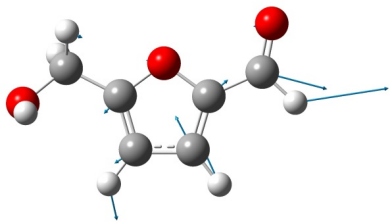 *v*=748.13 cm^{-1}
	1	-0.13	0	0.01	
	2	0.42	0.19	-0.02	
	3	0.65	0.01	-0.03	
	4	0.15	-0.09	-0.01	
	5	-0.12	-0.04	0.02	
	6	-0.08	-0.25	0	
	7	-0.07	-0.26	0.02	
	8	-0.16	0.07	0.01	
	9	0.01	0.26	0.08	
	10	-0.13	0.1	-0.03	
	11	0.01	0.02	0.01	
	12	0.07	-0.03	0	
	13	0.1	0.06	-0.03	
	14	0.04	0	0.01	
	15	0.06	-0.04	0	
14	**Tag**	**X**	**Y**	**Z**	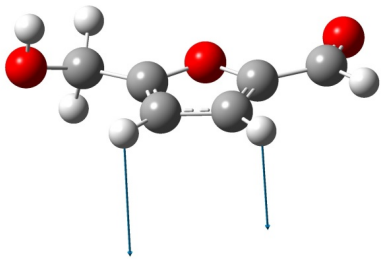 *v*=787.96 cm^{-1}
	1	0	0	0	
	2	0	0	0.01	
	3	-0.01	0	-0.07	
	4	0	0	0.03	
	5	0	0	0.02	
	6	0	0	-0.09	
	7	0.03	0.01	0.61	
	8	0	0	-0.09	
	9	0.03	-0.01	0.77	

	10	0.01	0	0.01	
	11	0	0.01	0.01	
	12	-0.02	-0.06	-0.01	
	13	0.03	0.04	-0.04	
	14	0	0	0	
	15	0	-0.03	-0.01	
15	**Tag**	**X**	**Y**	**Z**	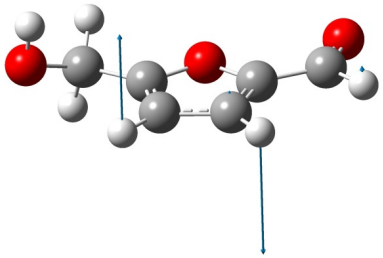 ν=857.83 cm^{-1}
	1	0	0	-0.01	
	2	0	0	0.02	
	3	-0.01	0	-0.12	
	4	0	0	0.01	
	5	0	0.01	0	
	6	-0.01	-0.01	-0.13	
	7	0.02	0.01	0.75	
	8	0.01	0	0.11	
	9	-0.02	0.02	-0.62	
	10	0	0	0	
	11	0	-0.01	-0.01	
	12	0.01	0.07	0.01	
	13	-0.02	-0.04	0.04	
	14	0	0	0	
	15	-0.02	0.03	0.01	
16	**Tag**	**X**	**Y**	**Z**	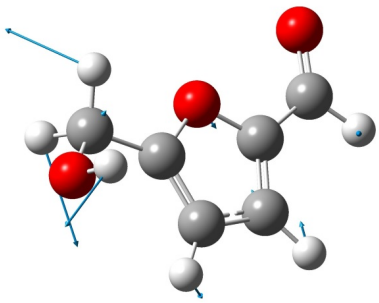 ν=936.42 cm^{-1}
	1	-0.01	0.01	-0.01	
	2	-0.04	-0.01	0.03	
	3	-0.1	0.03	-0.1	
	4	0.02	-0.04	-0.01	
	5	0.03	0.15	-0.02	
	6	-0.01	-0.13	0.01	
	7	0.01	-0.16	-0.03	
	8	-0.02	-0.02	-0.04	
	9	0.12	0.13	0.1	
	10	0.01	-0.01	0.11	
	11	0.03	-0.05	-0.14	
	12	-0.07	0.56	0.02	
	13	-0.07	-0.38	0.39	
	14	0.02	0	0.02	
	15	-0.41	0.19	0.03	

	Tag	X	Y	Z	
17	1	0.01	0.01	0	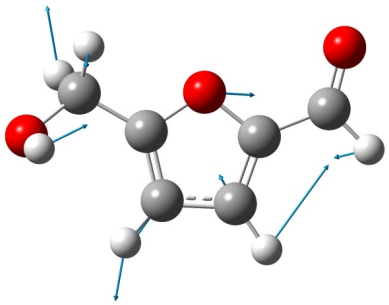
	2	-0.1	-0.04	-0.02	
	3	-0.18	0.03	0.1	
	4	-0.01	-0.09	0.01	
	5	0.27	0.05	-0.01	
	6	-0.07	-0.17	0	
	7	0.39	-0.41	0.02	
	8	-0.17	0.19	0.03	
	9	-0.1	0.3	-0.05	
	10	0.07	0.08	-0.07	
	11	0.01	-0.09	0.12	
	12	-0.02	-0.38	0.02	ν=944.13 cm^{-1}
	13	-0.06	0.09	-0.19	
	14	-0.1	0.05	-0.04	
	15	0.27	-0.1	-0.05	
	Tag	**X**	**Y**	**Z**	
18	1	-0.01	0.02	0.02	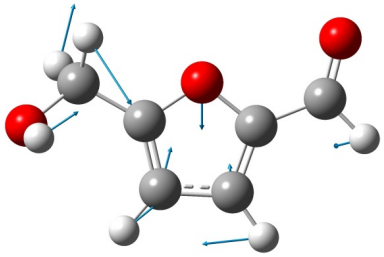
	2	-0.05	-0.01	-0.1	
	3	-0.1	0.06	0.42	
	4	0.05	-0.03	0.03	
	5	-0.03	0.26	0.01	
	6	0	-0.16	-0.01	
	7	-0.33	0	0.07	
	8	0.09	-0.22	0.02	
	9	0.19	-0.13	-0.06	
	10	-0.05	-0.04	-0.06	
	11	0.03	0.12	0.09	
	12	0.12	-0.33	-0.03	ν=960.49 cm^{-1}
	13	0.15	0.37	-0.28	
	14	-0.02	-0.01	-0.02	
	15	0.23	-0.12	-0.03	
	Tag	**X**	**Y**	**Z**	
19	1	0	0	0.05	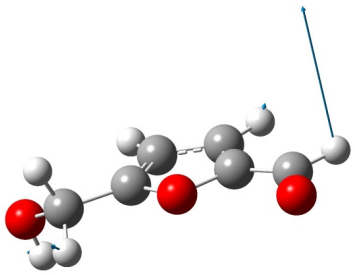
	2	0	0	-0.22	
	3	0.07	0	0.92	
	4	0	0.01	0.08	
	5	0	-0.05	0	
	6	0	0.03	-0.03	
	7	0.06	0.01	0.11	
	8	-0.01	0.04	0	
	9	-0.03	0.03	-0.01	
	10	0.01	0.01	0.03	
	11	0	-0.03	-0.04	ν=966.04 cm^{-1}
	12	-0.05	0.14	0	
	13	-0.03	-0.12	0.11	

	14	0.01	0	0.01	
	15	-0.12	0.06	0.01	
20	**Tag**	**X**	**Y**	**Z**	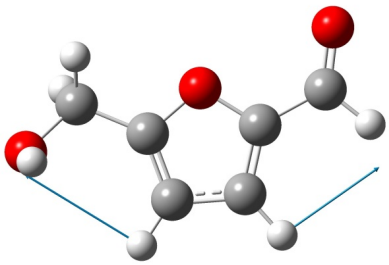 *v*=1008.24 cm^{-1}
	1	0	0	0	
	2	0.03	0.01	0	
	3	0.05	-0.01	0	
	4	-0.02	-0.01	0	
	5	-0.03	0.06	0	
	6	0.1	0.03	-0.01	
	7	0.6	-0.23	-0.02	
	8	-0.07	-0.04	0.01	
	9	-0.52	-0.53	0.01	
	10	0	0	0	
	11	0.01	0	0	
	12	0.01	0.01	0	
	13	0.01	0	0.01	
	14	-0.01	0	0	
	15	0	0.01	0	
21	**Tag**	**X**	**Y**	**Z**	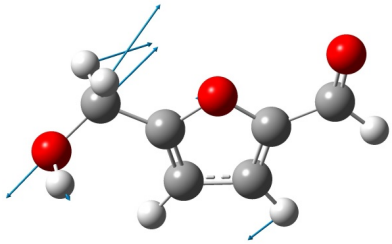 *v*=1048.71 cm^{-1}
	1	-0.01	0	0	
	2	0.03	0.01	0	
	3	0.04	0.01	0	
	4	0.01	-0.01	0	
	5	-0.13	-0.01	0.01	
	6	0	0.03	0	
	7	-0.24	0.16	0.02	
	8	0.06	-0.01	-0.01	
	9	0	-0.08	0.02	
	10	0.05	0	0.02	
	11	0.39	-0.26	0.08	
	12	0.4	0.05	0.15	
	13	0.4	-0.31	0.22	
	14	-0.31	0.2	-0.09	
	15	0.04	0.04	-0.12	
22	**Tag**	**X**	**Y**	**Z**	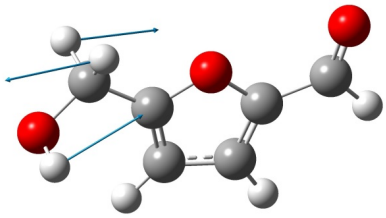 *v*=1144.81 cm^{-1}
	1	0	0	0	
	2	-0.01	0	0	
	3	-0.02	0.01	0.01	
	4	0.03	0.01	0	
	5	-0.05	0.01	0	
	6	-0.02	-0.01	0	
	7	0.01	-0.03	0	
	8	0	0.03	-0.01	
	9	-0.02	0.01	0.02	
	10	0.09	-0.02	0.05	
	11	-0.03	0.01	-0.05	

	12	0.54	0.12	0.08	
	13	-0.58	-0.07	-0.09	
	14	-0.02	-0.01	0.01	
	15	0.51	-0.24	-0.01	
23	**Tag**	**X**	**Y**	**Z**	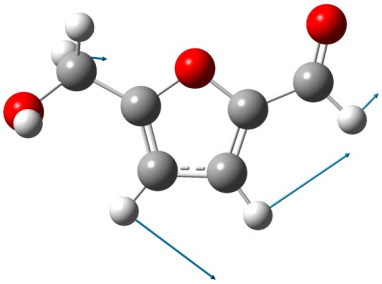
	1	0.02	-0.01	0	
	2	0.01	0	0	
	3	0.17	-0.13	0	
	4	-0.08	0.11	0	
	5	0.02	-0.02	0	
	6	-0.01	0.02	0	
	7	0.57	-0.28	-0.02	
	8	-0.04	-0.09	0	
	9	0.46	0.46	-0.02	
	10	-0.1	-0.08	0.02	
	11	0.05	0.04	-0.01	
	12	0.23	0.06	0.02	*v*=1172.15 cm^{-1}
	13	0.08	0.04	0	
	14	-0.02	0.01	0	
	15	0.08	-0.05	-0.01	
24	**Tag**	**X**	**Y**	**Z**	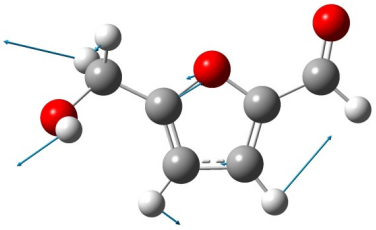
	1	0.01	-0.01	0	
	2	-0.01	0.01	0	
	3	0.05	-0.04	-0.01	
	4	0.05	0.09	0	
	5	-0.17	0.03	0.01	
	6	-0.15	-0.03	0.01	
	7	0.42	-0.34	-0.02	
	8	0.06	0.06	0	
	9	0.15	0.16	-0.02	
	10	0.27	-0.11	-0.05	
	11	0	0	0.07	*v*=1199.50 cm^{-1}
	12	-0.5	-0.23	-0.08	
	13	-0.11	0.06	-0.08	
	14	0.01	-0.02	-0.02	
	15	-0.36	0.16	0	
25	**Tag**	**X**	**Y**	**Z**	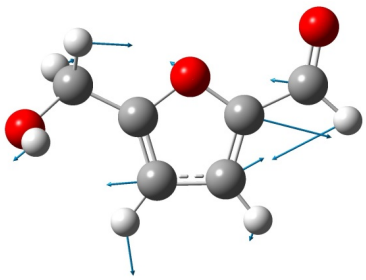
	1	0	0.04	0	
	2	-0.21	-0.07	0.01	
	3	-0.47	0.14	0.02	
	4	0.47	0.22	-0.03	
	5	-0.1	-0.11	0.01	
	6	0.24	-0.08	-0.01	
	7	-0.07	0.11	0	
	8	-0.29	-0.03	0.02	
	9	-0.01	0.31	-0.01	

	10	-0.04	-0.03	-0.01	*v*=1256.08 cm^{-1}
	11	-0.02	0	0.02	
	12	0.13	-0.02	0.04	
	13	0.31	0.08	0.02	
	14	0.01	0.01	-0.01	
	15	-0.15	0.08	-0.01	
26	**Tag**	**X**	**Y**	**Z**	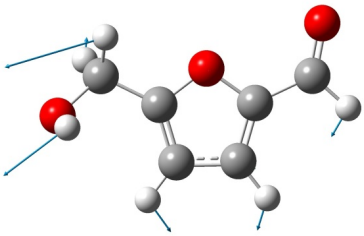 *v*=1308.18 cm^{-1}
	1	-0.01	-0.01	0	
	2	0.05	0.01	0	
	3	-0.14	0.16	0	
	4	-0.05	-0.09	0	
	5	0	0.02	0	
	6	0.1	0.07	-0.01	
	7	-0.1	0.19	0	
	8	-0.1	-0.01	0	
	9	0.11	0.23	0	
	10	0	-0.05	0	
	11	0.1	0.03	0.07	
	12	0.04	-0.14	0.02	
	13	-0.69	0.04	-0.18	
	14	0.02	-0.02	-0.05	
	15	-0.46	0.22	-0.02	
27	**Tag**	**X**	**Y**	**Z**	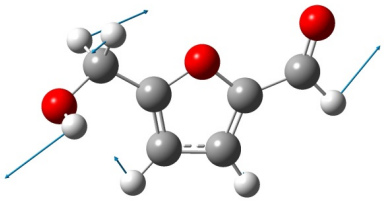 *v*=1334.70 cm^{-1}
	1	0.01	0.03	0	
	2	-0.06	-0.02	0	
	3	0.34	-0.34	-0.01	
	4	0.01	0.07	0	
	5	0.02	-0.02	0	
	6	-0.04	-0.06	0	
	7	-0.02	-0.09	0	
	8	0.07	0	0	
	9	-0.11	-0.2	0.01	
	10	-0.04	0.07	0.01	
	11	-0.03	-0.04	0.06	
	12	0.52	-0.06	0.16	
	13	-0.19	0.05	-0.12	
	14	0.03	0	-0.05	
	15	-0.5	0.26	-0.03	
28	**Tag**	**X**	**Y**	**Z**	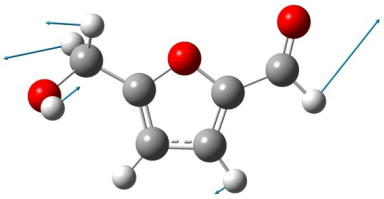 *v*=1353.29 cm^{-1}
	1	0.01	0.06	0	
	2	-0.06	-0.03	0	
	3	0.52	-0.5	-0.02	
	4	-0.02	0.02	0	
	5	-0.01	-0.01	0	
	6	0.07	-0.04	0	
	7	-0.15	0.07	0.01	

	8	-0.03	-0.01	0	
	9	-0.02	0.01	0	
	10	0	0.03	-0.01	
	11	0.08	0.02	-0.02	
	12	-0.5	0.01	-0.12	
	13	-0.32	-0.07	-0.01	
	14	-0.02	-0.01	0.02	
	15	0.21	-0.12	0.01	
29	**Tag**	**X**	**Y**	**Z**	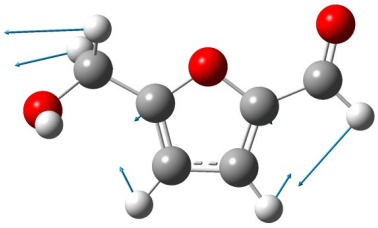 *v*=1394.22 cm^{-1}
	1	0	-0.05	0	
	2	0.01	0	0	
	3	-0.42	0.36	0.02	
	4	0.06	0.12	0	
	5	0.02	-0.05	0	
	6	-0.09	-0.04	0	
	7	0.16	-0.19	0	
	8	0.1	-0.02	-0.01	
	9	-0.08	-0.24	0.01	
	10	-0.14	0.09	0.01	
	11	0.12	0.01	0	
	12	-0.4	0.02	-0.08	
	13	-0.55	-0.07	-0.07	
	14	0	-0.01	0.01	
	15	0.07	-0.03	0.01	
30	**Tag**	**X**	**Y**	**Z**	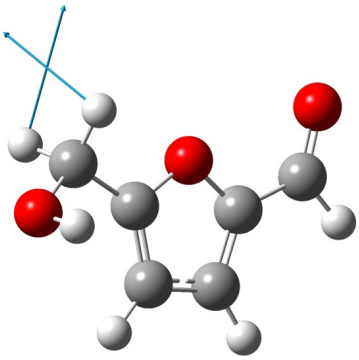 *v*=1443.62 cm^{-1}
	1	0	0	0	
	2	0	0	0	
	3	0.01	-0.01	0	
	4	0.01	0	0	
	5	0	0	0	
	6	0	0	0	
	7	0	0	0	
	8	0.01	0.02	0	
	9	-0.03	-0.02	0	
	10	-0.02	-0.01	0	
	11	0	0.08	-0.03	
	12	0.15	-0.66	-0.19	
	13	-0.06	-0.35	0.6	
	14	0	0.01	-0.01	
	15	-0.02	0.02	0	

	Tag	X	Y	Z	
31	1	0.03	-0.09	0	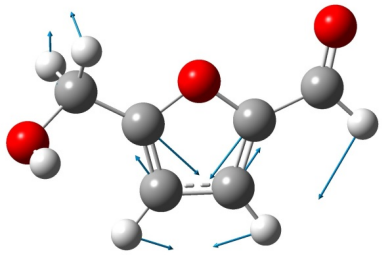
	2	0.09	0.04	-0.01	
	3	-0.3	0.36	0.01	
	4	-0.29	0.27	0.01	
	5	-0.03	-0.05	0	
	6	0.18	-0.19	-0.01	
	7	-0.3	0.03	0.01	
	8	-0.11	-0.22	0.01	
	9	0.24	0.13	-0.02	
	10	0.26	0.34	-0.02	
	11	-0.1	-0.07	0	
	12	0.02	-0.2	-0.02	
	13	-0.01	-0.18	0.18	
	14	0.01	0.01	0	
	15	-0.04	0.03	0	
					v=1499.13 cm^{-1}
32	1	0.03	-0.08	0	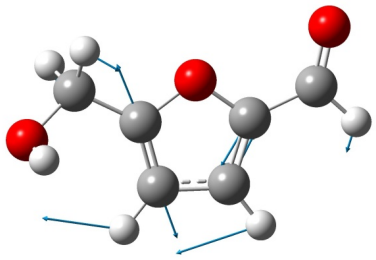
	2	0.03	0.06	0	
	3	-0.08	0.16	0	
	4	-0.2	0.24	0.01	
	5	0.01	0.01	0	
	6	0.18	-0.25	-0.01	
	7	-0.49	0.06	0.02	
	8	0.06	0.31	-0.01	
	9	-0.44	-0.16	0.02	
	10	-0.08	-0.35	0.01	
	11	0.03	0.05	0	
	12	0.04	0.11	0.02	
	13	0.16	0.13	-0.09	
	14	0	0	0	
	15	0	-0.02	0	
					v=1560.98 cm^{-1}
33	1	-0.17	0.41	0	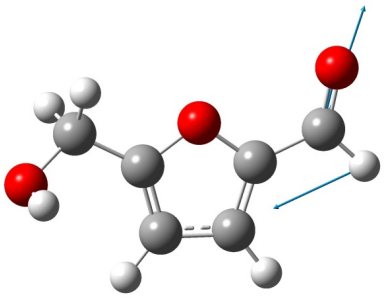
	2	0.32	-0.62	-0.01	
	3	-0.52	0.13	0.03	
	4	-0.08	0.09	0	
	5	0.01	-0.01	0	
	6	-0.02	-0.03	0	
	7	-0.03	-0.04	0	
	8	0.03	0.04	0	
	9	-0.03	-0.02	0	
	10	0.01	-0.03	0	
	11	-0.01	0	0	
	12	0.04	0.01	0.01	
	13	0.03	0.01	0	
					v=1697.27 cm^{-1}

	14	0	0	0	
	15	-0.02	0	0	
34	**Tag**	**X**	**Y**	**Z**	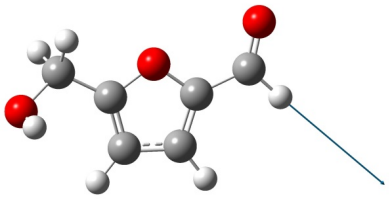 *v*=2827.07 cm^{-1}
	1	0	0	0	
	2	-0.05	-0.06	0	
	3	0.63	0.77	-0.04	
	4	0	0	0	
	5	0	0	0	
	6	0	0	0	
	7	-0.01	-0.01	0	
	8	0	0	0	
	9	0	0	0	
	10	0	0	0	
	11	0	0	0	
	12	0	0	0	
	13	0	0	0	
	14	0	0	0	
	15	0	0	0	
35	**Tag**	**X**	**Y**	**Z**	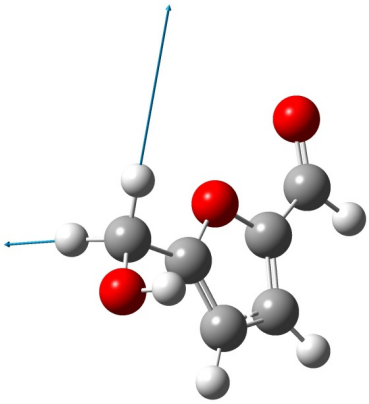 *v*=2920.94 cm^{-1}
	1	0	0	0	
	2	0	0	0	
	3	0	0	0	
	4	0	0	0	
	5	0	0	0	
	6	0	0	0	
	7	0	0	0	
	8	0	0	0	
	9	0	0	0	
	10	0	0	0	
	11	-0.01	0.07	0.01	
	12	-0.06	-0.08	0.36	
	13	0.15	-0.77	-0.49	
	14	0	0	0	
	15	0	0	0	
36	**Tag**	**X**	**Y**	**Z**	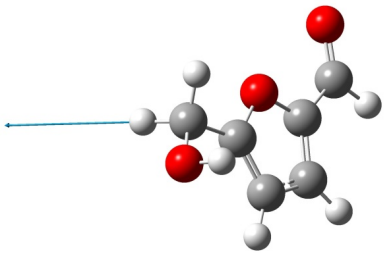 *v*=2974.12 cm^{-1}
	1	0	0	0	
	2	0	0	0	
	3	0	0	0	
	4	0	0	0	
	5	0	0	0	
	6	0	0	0	
	7	0	0	0	
	8	0	0	0	
	9	0	0	0	
	10	0	0	0	
	11	0.02	-0.01	-0.09	

	12	-0.16	-0.24	0.88	
	13	-0.05	0.3	0.18	
	14	0	0	0	
	15	0.01	0	-0.01	
37	**Tag**	**X**	**Y**	**Z**	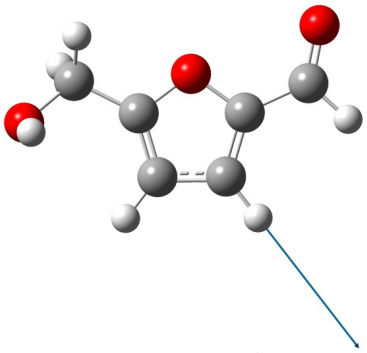 *v*=3145.69 cm^{-1}
	1	0	0	0	
	2	0	0	0	
	3	0	0	0	
	4	0	0	0	
	5	0	0	0	
	6	-0.04	-0.08	0	
	7	0.44	0.84	-0.03	
	8	-0.02	0.02	0	
	9	0.22	-0.21	-0.01	
	10	0	0	0	
	11	0	0	0	
	12	0	0	0	
	13	0	0	0	
	14	0	0	0	
	15	0	0	0	
38	**Tag**	**X**	**Y**	**Z**	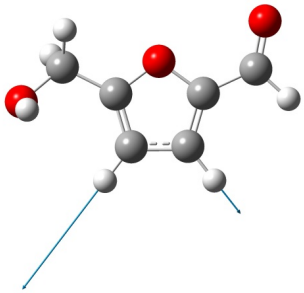 *v*=3165.89 cm^{-1}
	1	0	0	0	
	2	0	0	0	
	3	0	0	0	
	4	0	0	0	
	5	0	0	0	
	6	-0.02	-0.02	0	
	7	0.14	0.26	-0.01	
	8	0.06	-0.06	0	
	9	-0.7	0.64	0.04	
	10	0	0	0	
	11	0	0	0	
	12	0	0	0	
	13	0	0	0	
	14	0	0	0	
	15	0	0	0	

	Tag	X	Y	Z	
39	1	0	0	0	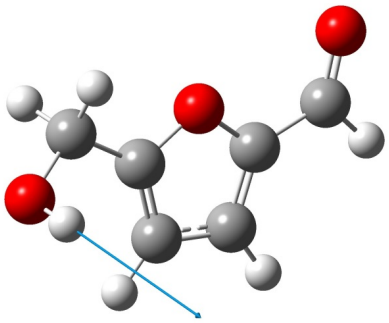
	2	0	0	0	
	3	0	0	0	
	4	0	0	0	
	5	0	0	0	
	6	0	0	0	
	7	0	0	0	
	8	0	0	0	
	9	0	0	0	
	10	0	0	0	
	11	0	0	0	
	12	0	0	-0.01	
	13	0	0	0	v=3682,03 cm^{-1}
	14	0	-0.01	0.06	
	15	0.05	0.19	-0.98	

Table S6: Compositions (Molar fractions, x) of the HMF/DMSO/D_2O mixtures

x_{HMF}	x_{DMSO}	x_{D2O}
0.231	0.769	0.000
0.220	0.710	0.080
0.213	0.709	0.079
0.194	0.645	0.161
0.174	0.579	0.248
0.174	0.579	0.248
0.153	0.508	0.339
0.130	0.435	0.435
0.130	0.435	0.435
0.107	0.357	0.536
0.100	0.796	0.084
0.083	0.275	0.642
0.082	0.643	0.275
0.066	0.831	0.091
0.060	0.469	0.469
0.057	0.189	0.755
0.054	0.662	0.284
0.049	0.849	0.093
0.039	0.859	0.095
0.039	0.672	0.289
0.039	0.480	0.480
0.032	0.678	0.290
0.030	0.485	0.485
0.029	0.097	0.874
0.023	0.488	0.488

x_{HMF}	x_{D2O}
0.219	0.781
0.198	0.802
0.132	0.868
0.072	0.928
0.057	0.943

x_{HMF}	x_{DMSO}
0.210	0.790
0.134	0.866
0.064	0.936
0.032	0.968

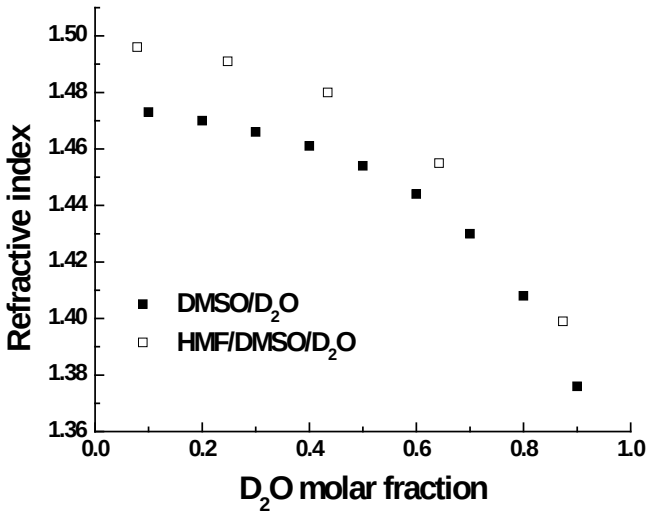

Figure S 1: Refractive indices as a function of D_2O molar fraction for DMSO/D_2O and HMF/DMSO/ D_2O solutions

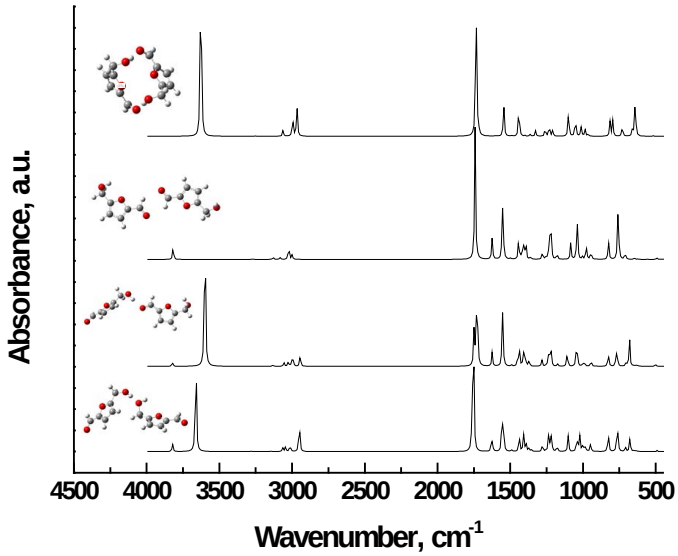

Figure S 2: Calculated IR spectra of HMF dimers shown in Scheme 2

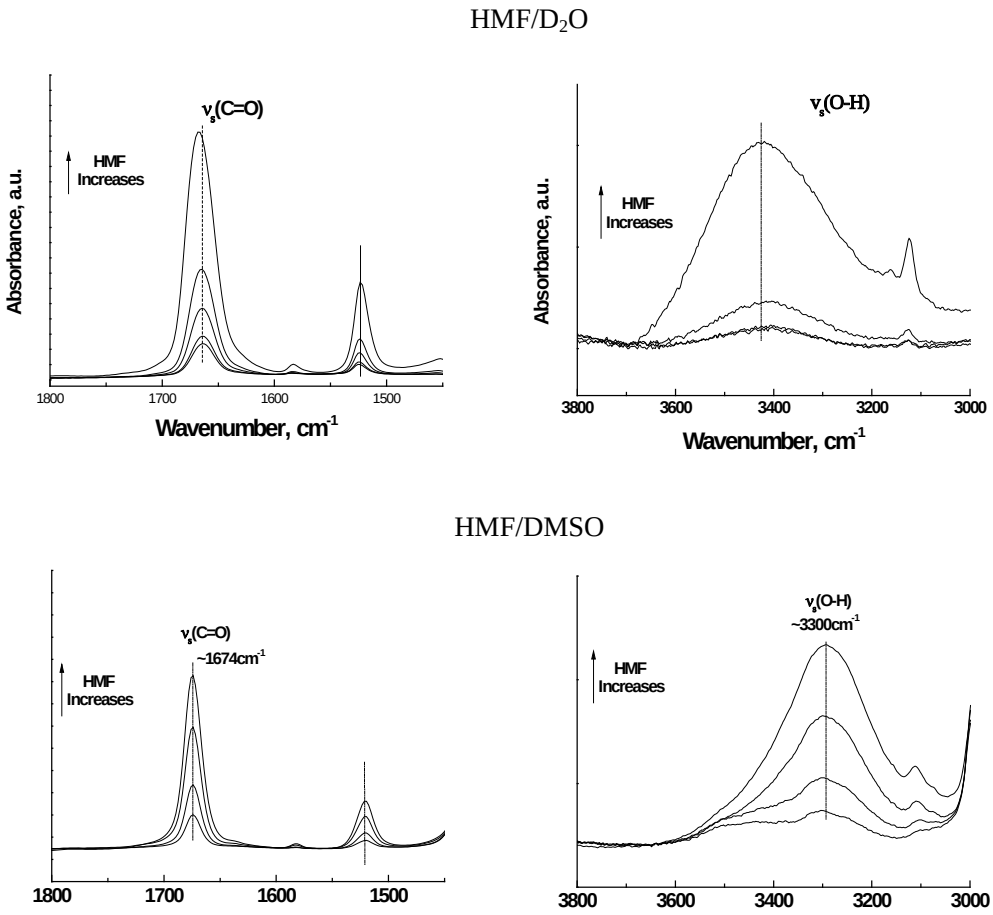

Figure S 3: ATR/FTIR spectra of HMF/D_2O and HMF/DMSO binary mixtures with varying HMF concentration; T=25°C, resolution=4cm^{-1}, Number of scans=32

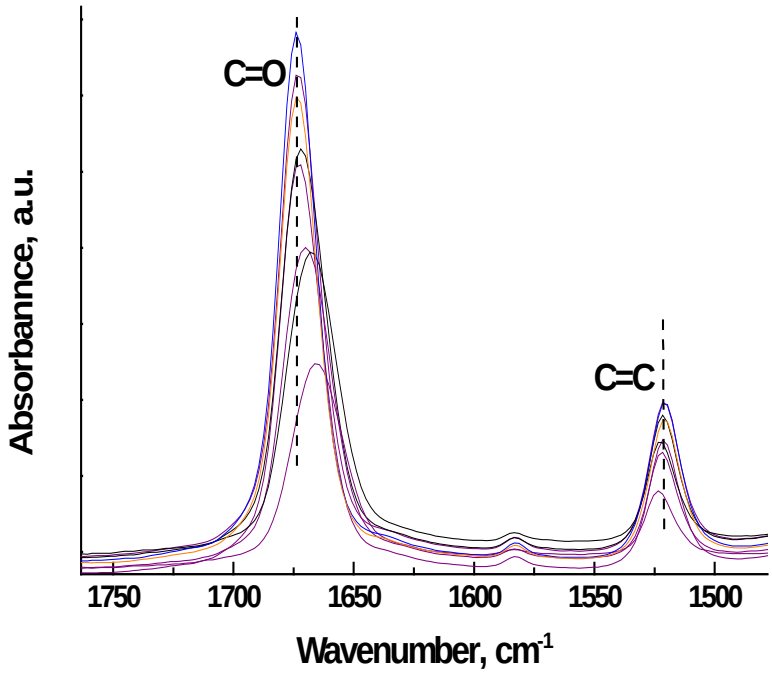

Figure S 4:Effect of D_2O on the C=C and C=O stretching vibrations of HMF at HMF/DMSO/D2O and constant HMF/DMSO=0.3 molar ratio; T=25°C, resolution=4cm^{-1}, Number of scans=32

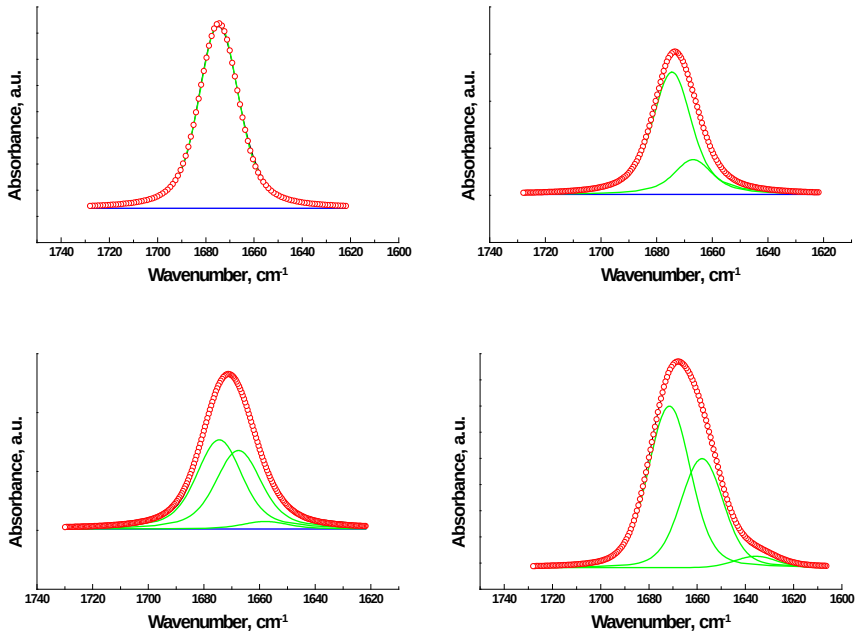

Figure S 5: Deconvolution of carbonyl region of ternary HMF/DMSO/D_2O solutions

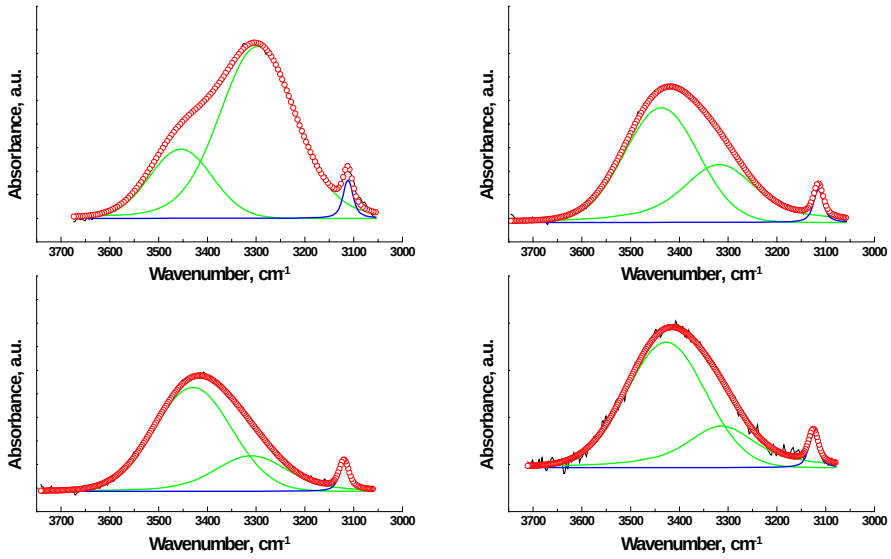

Figure S 6: Deconvolution of hydroxyl group region of ternary HMF/DMSO/D_2O solutions

Table S7: – Other local minimum found while searching HMF-DMSO configuration space

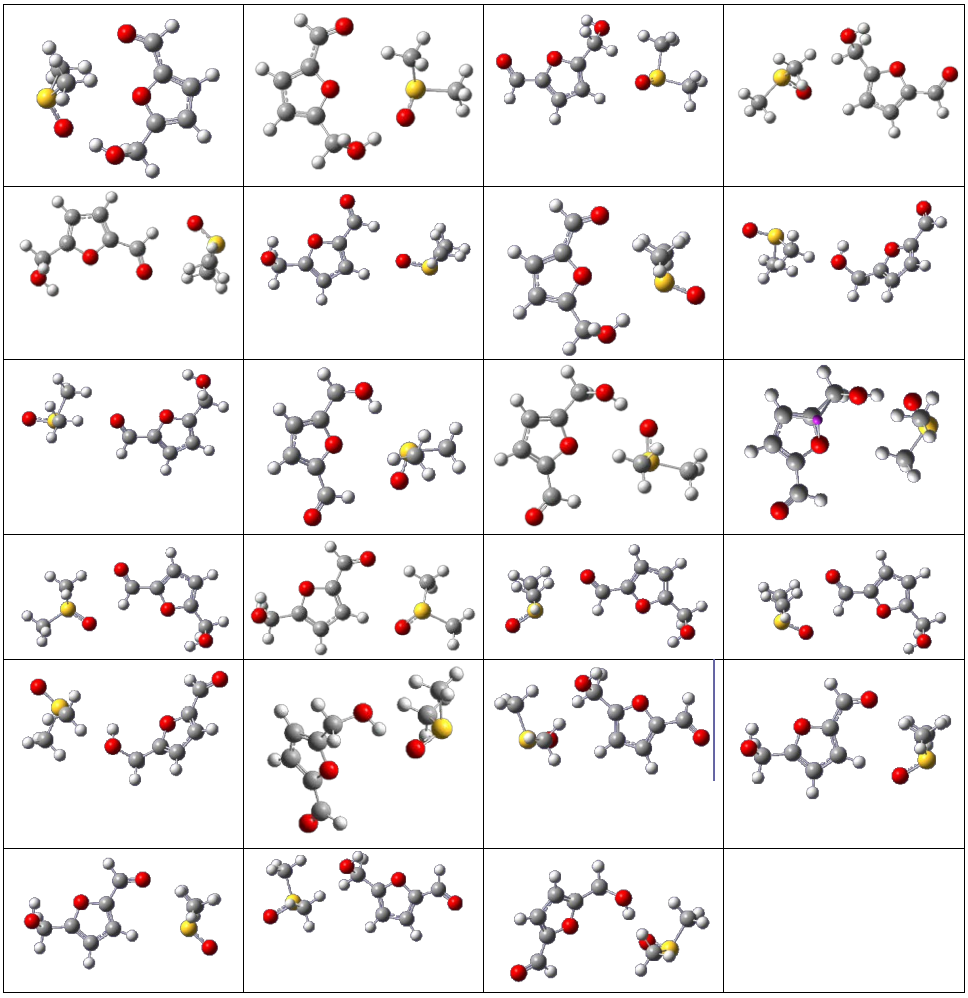

Table S8: – Other local minimum found while searching HMF-H_2O configuration space

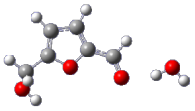	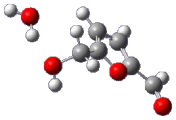	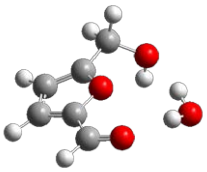	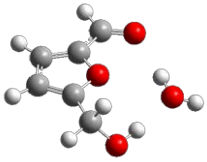
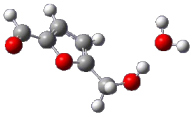	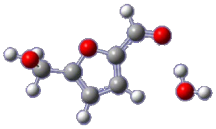	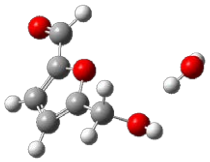	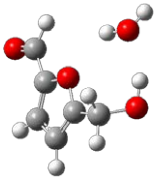
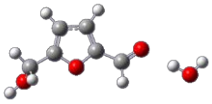	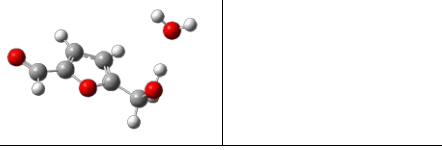		

Appendix B

SUPPORTING INFORMATION FOR CHAPTER 3

Figure S1, containing images of the HMF/solvent complexes optimized in CPCM solvent, Table S1, containing the experimental ν(C=O) and several solvent properties with regression statistics, Table S2, containing geometry information calculated for gas-phase complexes, Table S3, containing the same for complexes in implicit solvent, Tables S4-S6, containing data from NBO analysis of isolated HMF in implicit solvent, Tables S7-S9 containing data from NBO analysis of HMF/solvent complexes in vacuum, and Table S10, containing data from Bader analysis of HMF/solvent complexes in vacuum. This material is available free of charge via the Internet at http://pubs.acs.org.

Solvent-Induced Frequency Shifts of 5-Hydroxymethylfurfural Deduced via Infrared Spectroscopy and *ab initio* Calculations

Tyler Josephson, George Tsilomelekis, Vladimiros Nikolakis, Dionisios G. Vlachos, Stavros Caratzoulas[1]

Catalysis Center for Energy Innovation, Department of Chemical and Biomolecular Engineering

University of Delaware, 150 Academy Street, Newark, DE 19716

Supporting Information

[1] Author to whom correspondence should be addressed; Email: cstavros@udel.edu

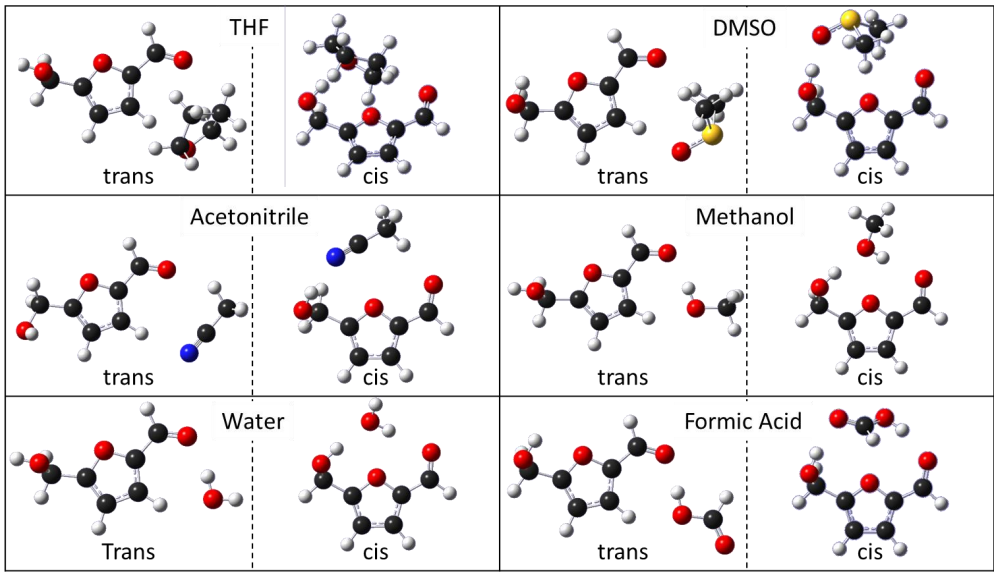

Figure S1 - Lowest energy structures optimized with MP2/aug-cc-pVDZ in CPCM solvent. Compared with gas phase configurations, several structures had significant changes in geometry, such as the bridge structure for the aprotic solvents having zero H-bonding between HMF carbonyl and solvent.

Table S1 - Pure-component solvent properties and vibrational frequencies of HMF ν(C=O). To compare these properties as descriptors of ν(C=O), the R^2 value from the linear regression is given, with plots included in the SI.

Properties of Pure Solvents									HMF Carbonyl Frequency	
Solvent	Solvent Type	Acceptor Number	Donor Number	Dielectric Constant (ε_r)	Polarity (Y)	Refractive index	Polarizability (P)	Dipole Moment (debye)	ν(C=O) 1	ν(C=O) 2**
toluene	nonpolar	8.2*	0.1	2.4	0.318	1.497	0.3829	0.36	1685	
ethylacetate	Polar aprotic	9.3	17.1	6	0.625	1.372	0.3061	1.88	1684.0	
THF	Polar aprotic	8	20	7.6	0.688	1.407	0.3288	1.75	1683.6	
acetone	Polar aprotic	12.5	17	20.7	0.868	1.359	0.2975	2.69	1681	
acetonitrile	Polar aprotic	18.9	14.1	37.5	0.924	1.344	0.2873	3.924	1679.8	
DMSO	Polar aprotic	19.3	29.8	46.7	0.938	1.479	0.3725	3.96	1674	
2-propanol	Alcohol	33.8	21.1	19.9	0.863	1.377	0.3094	1.66	1674.7	1686.2
1-propanol	Alcohol	37.3	19.8	20.3	0.865	1.386	0.3153	3.09	1673.8	1688.6
ethanol	Alcohol	37.9	19.2	24.6	0.887	1.361	0.2988	1.66	1673.2	1685.5
methanol	Alcohol	41.5	19	32.7	0.914	1.328	0.2763	1.7	1672	1685
D2O	Acid	54.8	18	80.1	0.963	1.333	0.2798	1.87	1663	
acetic acid	Acid	52.9	12.7	6.2	0.634	1.372	0.3061	1.74	1661.0	1684.3
formic acid	Acid	83.6	19	58.5	0.950	1.37	0.3048	1.41	1650	
	ν(C=O) 1 R^2	0.9436	0.0072	0.3152	0.1035	0.0244	0.0252	0.1336	1	

*AN is not available for toluene – this is the value for benzene

**In alcohol solvents and acetic acid, ν(C=O) splits into two vibrations.

Table S2 - Geometries of the H-bonds between HMF carbonyl and explicit solvent ligand in gas phase, calculated by mp2/aug-cc-pVDZ. When two solvent H atoms participate in H-bonds with the HMF carbonyl O, both are reported. Changes are reported with gas phase solvent molecules as the reference states.

Explicit Solvent		C=O ⋯ H distance[Å]	C=O ⋯ H distance 2 [Å]	Solvent H-X length [Å]	Δ Solvent H-X length [Å]	Solvent H-X length 2 [Å]	Δ Solvent H-X length 2 [Å]
THF	cis	2.9591		1.0991	-0.0034		
	trans	2.6231	2.7243	1.1010	-0.0015	1.0989	-0.0005
ACN	cis	2.1962		1.1006	0.0014		
	trans	2.3165		1.0984	-0.0009		
DMSO	cis	2.7252	2.9405	1.0975	-0.0031	1.0976	-0.0031
	trans	2.3658	2.3612	1.0998	-0.0009	1.0998	-0.0008
MeOH	cis	2.2106		0.9728	0.0071		
	trans	1.9004		0.9750	0.0093		
H2O	cis	2.2128		0.9734	0.0074		
	trans	1.9152		0.9755	0.0096		
FA	cis	1.8275		0.9851	0.0150		
	trans	1.7560		0.9870	0.0170		

Table S3 - Properties of the H-bond between HMF carbonyl and explicit solvent ligand in implicit solvent. When two solvent H atoms participate in H-bonds with the HMF carbonyl O, both are reported. Changes are reported with gas phase solvent molecules as the reference states.

Solvent		O1 ⋯ H distance[Å]	O1 ⋯ H Distance 2 [Å]	Solvent H-X length [Å]	Δ Solvent H-X length [Å]	Solvent H-X length 2 [Å]	Δ Solvent H-X length 2 [Å]
THF	cis	3.0481		1.0993	-0.0081		
	trans	2.6212		1.1018	-0.0056		
ACN	cis	2.5517		1.0992	0.0006		
	trans	2.3502		1.0985	0.0000		
DMSO	cis	2.7882	2.9632	1.0978	0.0051	1.0979	0.0052
	trans	2.4184		1.0996	0.0069		
MeOH	cis	2.3308		0.9731	0.0059		
	trans	1.8678		0.9767	0.0095		
H2O	cis	2.1982		0.9741	0.0067		
	trans	1.8844		0.9771	0.0097		
FA	cis	1.7232		0.9941	0.0218		
	trans	1.6909		0.9953	0.0230		

Table S4 – NBO results for HMF in CPCM solvent. HMF dipole moment, NBO partial charges on the carbonyl, and changes in occupancy of π bonding orbitals for carbonyl and ring double bonds, and lone pairs on carbonyl oxygen. Changes are reported with gas phase cis or trans HMF as the reference state.

	CPCM Solvent	qC1	ΔqC1	qO1	ΔqO1	π(C1=O1)	Δπ(C1=O1)	π(C2=C3)	Δπ(C2=C3)	π(C4=C5)	Δπ(C4=C5)	LP1 O1 (sp)	ΔLP1 O1 (sp)	LP2 O1 (p)	ΔLP2 O1 (p)
Trans HMF	Vacuum	0.3382		-0.5470		1.9778		1.7794		1.7894		1.9844		1.8867	
	THF	0.3435	0.0052	-0.6050	-0.0580	1.9801	0.0023	1.7687	-0.0107	1.7694	-0.0200	1.9848	0.0004	1.8967	0.0100
	ACN	0.3437	0.0055	-0.6145	-0.0675	1.9805	0.0027	1.7662	-0.0132	1.7650	-0.0244	1.9849	0.0005	1.8983	0.0116
	DMSO	0.3437	0.0055	-0.6151	-0.0681	1.9805	0.0026	1.7663	-0.0131	1.7652	-0.0241	1.9849	0.0005	1.8982	0.0115
	MeOH	0.3437	0.0055	-0.6142	-0.0673	1.9804	0.0026	1.7664	-0.0130	1.7653	-0.0240	1.9849	0.0005	1.8982	0.0115
	H2O	0.3437	0.0055	-0.6159	-0.0689	1.9805	0.0027	1.7660	-0.0135	1.7646	-0.0248	1.9849	0.0005	1.8985	0.0117
	FA	0.3437	0.0055	-0.6153	-0.0683	1.9805	0.0027	1.7661	-0.0133	1.7649	-0.0245	1.9849	0.0005	1.8984	0.0116
Cis HMF	Vacuum	0.3347		-0.5386		1.9770		1.7787		1.7920		1.9841		1.8849	
	THF	0.3395	0.0047	-0.6056	-0.0670	1.9793	0.0023	1.7629	-0.0159	1.7758	-0.0162	1.9846	0.0005	1.8976	0.0127
	ACN	0.3397	0.0050	-0.6167	-0.0781	1.9797	0.0028	1.7592	-0.0196	1.7723	-0.0198	1.9847	0.0006	1.8997	0.0148
	DMSO	0.3397	0.0050	-0.6174	-0.0788	1.9797	0.0027	1.7594	-0.0193	1.7725	-0.0196	1.9847	0.0006	1.8996	0.0147
	MeOH	0.3397	0.0050	-0.6164	-0.0778	1.9797	0.0027	1.7595	-0.0193	1.7726	-0.0195	1.9847	0.0006	1.8995	0.0146
	H2O	0.3397	0.0050	-0.6183	-0.0797	1.9798	0.0028	1.7589	-0.0199	1.7720	-0.0201	1.9847	0.0007	1.8998	0.0150
	FA	0.3397	0.0050	-0.6176	-0.0790	1.9797	0.0028	1.7591	-0.0196	1.7722	-0.0198	1.9847	0.0006	1.8997	0.0148

Table S5 - Changes in occupancy of π* anti-bonding orbitals for carbonyl and ring double bonds. Changes are reported with gas phase trans or cis HMF as the reference state.

	CPCM Solvent	π*(C=O)	dπ*(C=O)	π*(C2=C3)	dπ*(C2=C3)	π*(C4=C5)	dπ*(C4=C5)
Trans HMF	Vacuum	0.1561		0.3114		0.2836	
	THF	0.1853	0.0292	0.3228	0.0114	0.2781	-0.0055
	ACN	0.1913	0.0352	0.3254	0.0141	0.2774	-0.0062
	DMSO	0.1909	0.0348	0.3253	0.0139	0.2774	-0.0062
	MeOH	0.1908	0.0347	0.3252	0.0139	0.2774	-0.0062
	H2O	0.1918	0.0357	0.3257	0.0143	0.2773	-0.0063
	FA	0.1914	0.0353	0.3255	0.0141	0.2773	-0.0062
Cis HMF	Vacuum	0.1613		0.3186		0.2784	
	THF	0.1928	0.0316	0.3222	0.0036	0.2712	-0.0072
	ACN	0.1993	0.0381	0.3232	0.0046	0.2699	-0.0085
	DMSO	0.1989	0.0377	0.3231	0.0045	0.2700	-0.0084
	MeOH	0.1988	0.0375	0.3231	0.0045	0.2700	-0.0084
	H2O	0.1999	0.0386	0.3233	0.0046	0.2698	-0.0086
	FA	0.1994	0.0382	0.3232	0.0046	0.2699	-0.0085

Table S6 - Percentage of non-Lewis electrons depicted in Lewis structures in Error! Reference source not found.**. Changes are reported with gas phase cis or trans HMF as the reference state.**

	CPCM Solvent	% Non-Lewis in A	Δ Non-Lewis A	% Non-Lewis in B	Δ Non-Lewis B	% Non-Lewis in C	Δ Non-Lewis C	% Non-Lewis in D	Δ Non-Lewis D
Trans HMF	Vacuum	1.847%		2.898%		3.523%		3.808%	
	THF	1.873%	0.025%	2.882%	-0.016%	3.444%	-0.079%	3.694%	-0.114%
	ACN	1.880%	0.033%	2.883%	-0.015%	3.431%	-0.092%	3.673%	-0.135%
	DMSO	1.880%	0.033%	2.883%	-0.015%	3.432%	-0.091%	3.674%	-0.134%
	MeOH	1.880%	0.032%	2.883%	-0.015%	3.432%	-0.091%	3.675%	-0.133%
	H2O	1.881%	0.034%	2.883%	-0.015%	3.430%	-0.093%	3.671%	-0.137%
	FA	1.881%	0.033%	2.883%	-0.015%	3.431%	-0.092%	3.673%	-0.135%
Cis HMF	Vacuum	1.864%		2.853%		3.478%		3.759%	
	THF	1.876%	0.012%	2.818%	-0.034%	3.368%	-0.110%	3.635%	-0.124%
	ACN	1.881%	0.017%	2.816%	-0.037%	3.349%	-0.129%	3.613%	-0.146%
	DMSO	1.881%	0.017%	2.816%	-0.037%	3.350%	-0.128%	3.615%	-0.144%
	MeOH	1.881%	0.016%	2.816%	-0.037%	3.351%	-0.127%	3.615%	-0.144%
	H2O	1.882%	0.017%	2.815%	-0.037%	3.348%	-0.130%	3.612%	-0.148%
	FA	1.881%	0.017%	2.816%	-0.037%	3.349%	-0.129%	3.613%	-0.146%

Table S7 – HMF/explicit solvent complex in vacuum. NBO partial charges on the carbonyl, and changes in occupancy of π bonding orbitals for carbonyl and ring double bonds, and lone pairs on carbonyl oxygen. Changes are reported with gas phase cis or trans HMF as the reference state.

Explicit Solvent		qC1	ΔqC1	qO1	ΔqO1	π(C1=O1)	Δπ(C1=O1)	π(C2=C3)	Δπ(C2=C3)	π(C4=C5)	Δπ(C4=C5)	LP1 O1 (sp)	ΔLP1 O1 (sp)	LP2 O1 (p)	ΔLP2 O1 (p)
Vacuum	cis	0.342		-0.54486		1.977		1.773		1.786		1.984		1.887	
	trans	0.335		-0.53859		1.977		1.779		1.792		1.984		1.885	
THF	cis	0.336	0.001	-0.556	-0.0172	1.978	0.001	1.771	-0.008	1.777	-0.015	1.983	-0.001	1.886	0.001
	trans	0.344	0.002	-0.564	-0.0190	1.978	0.001	1.762	-0.012	1.783	-0.003	1.983	-0.001	1.889	0.001
ACN	cis	0.343	0.009	-0.578	-0.0389	1.979	0.002	1.763	-0.016	1.768	-0.024	1.979	-0.005	1.889	0.004
	trans	0.347	0.005	-0.583	-0.0378	1.979	0.002	1.765	-0.008	1.780	-0.007	1.980	-0.004	1.891	0.004
DMSO	cis	0.336	0.001	-0.574	-0.0351	1.978	0.001	1.767	-0.012	1.768	-0.024	1.983	-0.001	1.888	0.003
	trans	0.347	0.005	-0.586	-0.0413	1.979	0.001	1.753	-0.020	1.777	-0.009	1.980	-0.005	1.890	0.003
MeOH	cis	0.339	0.004	-0.575	-0.0364	1.978	0.001	1.768	-0.011	1.770	-0.022	1.982	-0.003	1.887	0.002
	trans	0.353	0.012	-0.585	-0.0398	1.980	0.002	1.752	-0.021	1.772	-0.014	1.974	-0.011	1.883	-0.004
H2O	cis	0.341	0.006	-0.578	-0.0394	1.978	0.001	1.767	-0.012	1.769	-0.023	1.981	-0.003	1.887	0.002
	trans	0.354	0.012	-0.587	-0.0422	1.980	0.002	1.752	-0.021	1.772	-0.014	1.975	-0.010	1.884	-0.003
FA	cis	0.351	0.016	-0.603	-0.0644	1.980	0.003	1.751	-0.028	1.754	-0.038	1.968	-0.016	1.883	-0.002
	trans	0.358	0.017	-0.598	-0.0535	1.981	0.003	1.749	-0.025	1.759	-0.027	1.966	-0.019	1.876	-0.012

Table S8 – Gas phase complexes: changes in occupancy of π* anti-bonding orbitals for carbonyl and ring double bonds. Changes are reported with gas phase cis or trans HMF as the reference state.

Explicit Solvent		π*(C=O)	Δπ*(C=O)	π*(C2=C3)	Δπ*(C2=C3)	π*(C4=C5)	Δπ*(C4=C5)
Vacuum	cis	0.149		0.311		0.281	
	trans	0.161		0.319		0.278	
THF	cis	0.174	0.013	0.326	0.008	0.270	-0.008
	trans	0.163	0.014	0.307	-0.004	0.281	0.000
ACN	cis	0.186	0.025	0.332	0.013	0.270	-0.008
	trans	0.178	0.029	0.312	0.001	0.283	0.002
DMSO	cis	0.187	0.025	0.331	0.013	0.267	-0.011
	trans	0.183	0.034	0.303	-0.008	0.277	-0.004
MeOH	cis	0.184	0.023	0.331	0.012	0.270	-0.008
	trans	0.182	0.033	0.313	0.002	0.280	0.000
H2O	cis	0.185	0.024	0.332	0.013	0.271	-0.007
	trans	0.182	0.033	0.313	0.002	0.280	0.000
FA	cis	0.209	0.048	0.336	0.018	0.265	-0.014
	trans	0.201	0.052	0.320	0.010	0.275	-0.006

Table S9 - Energies (kcal/mol) of delocalization from 2nd order perturbation theory delocalization for complexes in gas phase. For configurations in which two solvent σ*(H-X) are interacting with the carbonyl O lone pairs, both are reported. Changes are reported with gas phase trans HMF as the reference state.

Explicit Solvent		π(C1=O1) → π*(C2=C3)	π(C2=C3) → π*(C1=O1)	π(C2=C3) → π*(C4=C5)	π(C4=C5) → π*(C2=C3)	π(C4=C5) → π*(C4=C5)	LP1(O1) → σ*(H-X) of solvent	LP1(O1) → σ*(H-X) 2 of solvent	LP2(O1) → σ*(H-X) of solvent	LP2(O1) → σ*(H-X) 2 of solvent
Vacuum	cis	5.93	23.21	14.1	18.9	0.98				
	trans	5.47	21.79	14.66	18.97	0.86				
THF	cis	5.8	24.53	13.83	19.88	0.67	0.46		0.9	
	trans	5.21	23.16	15.15	18.81		0.15	0.35	0.18	0.08
ACN	cis	5.58	26.03	13.85	20.43	0.71	2.75		1.74	
	trans	5.11	24.71	14.39	19.6	1.05	2.44		0.32	
DMSO	cis	5.71	25.83	13.54	20.66	0.8	0.07	0.44	0.18	0.81
	trans	4.98	25.72	14.65	19.53	0.67	1.12	1.01	0.6	0.6
MeOH	cis	5.85	25.15	13.64	20.42	0.88	1.16		3.17	
	trans	4.95	25.33	14.96	19.61	0.55	5.28		8.94	
H2O	cis	5.82	25.33	13.64	20.48	0.89	1.26		3.48	
	trans	4.95	25.39	14.96	19.64	0.55	4.7		8.13	
FA	cis	5.28	28.72	13.62	21.6	0.91	7.66		11.88	
	trans	4.79	27.36	14.39	20.8	0.77	8.56		18.44	

Table S10 – Characterization of the bond critical points between the HMF carbonyl O and the solvent H in the gas phase complexes.

		Bond Critical Point 1				Bond Critical Point 2*			
Solvent		ρ (au)	Kinetic E (au)	$\nabla^2\rho$ (au)	Potential E (au)	ρ (au)	Kinetic E (au)	$\nabla^2\rho$ (au)	Potential E (au)
THF	cis	0.0031	0.0040	0.0056	-0.0023	0.0027	0.0035	0.0050	-0.0021
	trans	0.0017	0.0023	0.0033	-0.0012	0.0020	0.0026	0.0038	-0.0014
ACN	cis	0.0095	0.0112	0.0141	-0.0083				
	trans	0.0078	0.0095	0.0123	-0.0067				
DMSO	cis	0.0072	0.0054	0.0062	-0.0045	0.0040	0.0030	0.0038	-0.0022
	trans	0.0088	0.0067	0.0075	-0.0059	0.0085	0.0064	0.0072	-0.0057
MeOH	cis	0.0086	0.0100	0.0127	-0.0073	0.0082	0.0110	0.0143	-0.0076
	trans	0.0278	0.0202	0.0200	-0.0205				
H2O	cis	0.0104	0.0119	0.0147	-0.0091	0.0079	0.0107	0.0141	-0.0074
	trans	0.0278	0.0203	0.0202	-0.0205				
FA	cis	0.0310	0.0305	0.0322	-0.0288				
	trans	0.0403	0.0296	0.0298	-0.0294				

*In the cases of trans-THF, cis-DMSO, and trans-DMSO, the 2nd bond critical point listed here corresponds to a second solvent hydrogen interacting with HMF carbonyl O.
In the cases of cis-THF, cis-MeOH, and cis-H2O, the 2nd bond critical point listed here corresponds to a single solvent H interacting with both the carbonyl O and the furan O of HMF

Appendix C

SUPPORTING INFORMATION FOR CHAPTER 4

SUPPORTING INFORMATION

Methyl-Ligated Tin Silsesquioxane Catalyzed Reactions of Glucose

Stephen K. Brand,[1] Tyler R. Josephson,[2] Jay A. Labinger,[1] Stavros Caratzoulas,[2] Dionisios G. Vlachos[2] and Mark E. Davis[1,*]

[1]Division of Chemistry and Chemical Engineering, California Institute of Technology, Pasadena, CA 91125

[2]Catalysis Center for Energy Innovation, Department of Chemical and Biomolecular Engineering, University of Delaware, Newark, DE 19715

*Corresponding author. E-mail: mdavis@cheme.caltech.edu

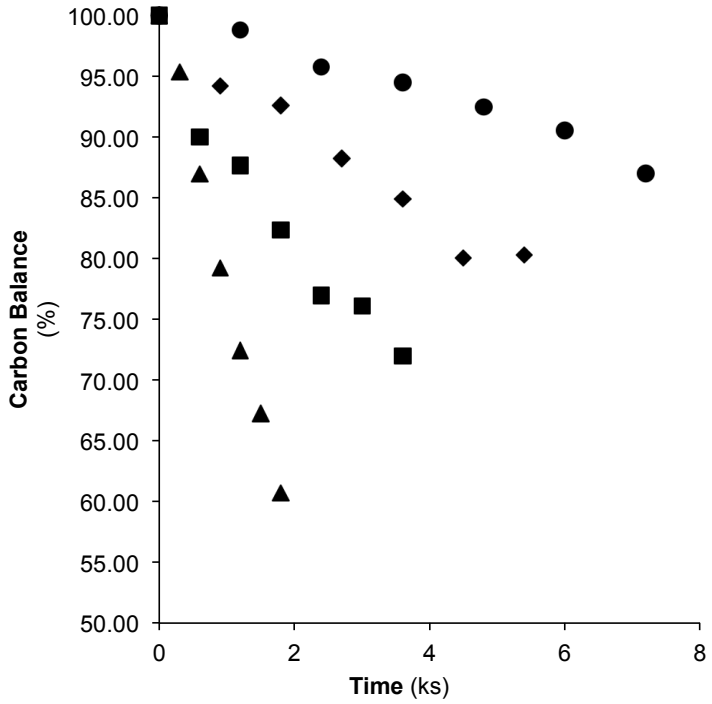

Figure S.1. Carbon balance for reaction testing carried out using 2% (w/w) glucose in an equivolumetric DMSO:benzene solution with **1a** (1:75 Sn/glucose molar ratio) at 363 K (●), 373 K (◆), 383 K (■), 393 K (▲).

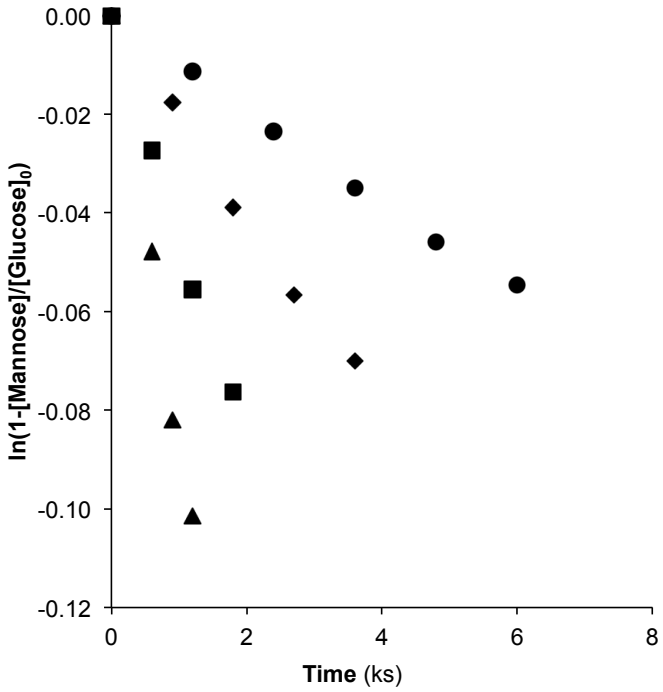

Figure S.2. First order epimerization reaction of glucose to mannose. Reaction testing was carried out using 2% (w/w) glucose in an equivolumetric DMSO:benzene solution with **1a** (1:75 Sn/glucose molar ratio) at 363 K (●), 373 K (◆), 383 K (■), 393 K (▲).

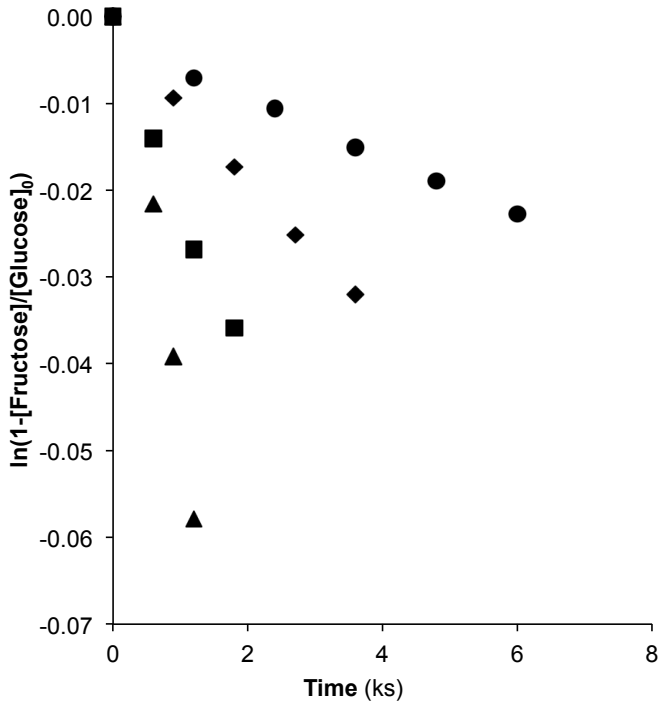

Figure S.3. First order isomerization reaction of glucose to fructose. Reaction testing was carried out using 2% (w/w) glucose in an equivolumetric DMSO:benzene solution with **1a** (1:75 Sn/glucose molar ratio) at 363 K (●), 373 K (◆), 383 K (■), 393 K (▲).

Table S.1. Kinetic rate constants for the epimerization and isomerization of glucose. Reaction testing was carried out using 2% (w/w) glucose in an equivolumetric DMSO:benzene solution with **1a** (1:75 Sn/glucose molar ratio).

	Product Hexose	
	Mannose	Fructose
Temperature (K)	k (s^{-1}, 10^3)	k (s^{-1}, 10^3)
363	9.398	3.985
373	20.189	9.165
383	43.713	20.876
393	85.902	45.073

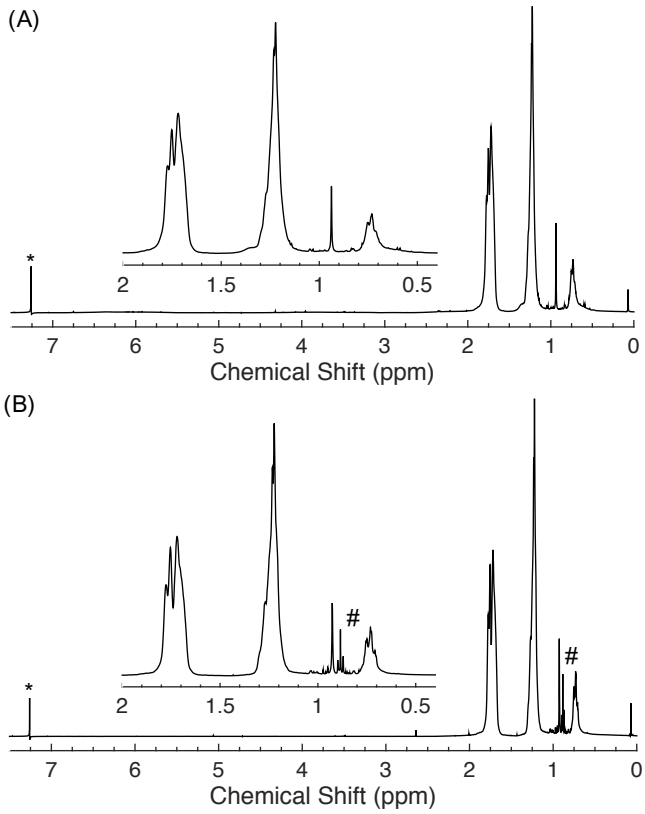

Figure S.4. ^{1}H NMR spectral comparison of as-synthesized **1a** catalyst (A) with **1a** separated (B) from a 2% (w/w) glucose in an equivolumetric DMSO:Benzene solution at 393 K after 1 hour using a 1:75 Sn/glucose molar ratio. The * denotes the chloroform solvent peak, while the # designates a residual hexane peak.

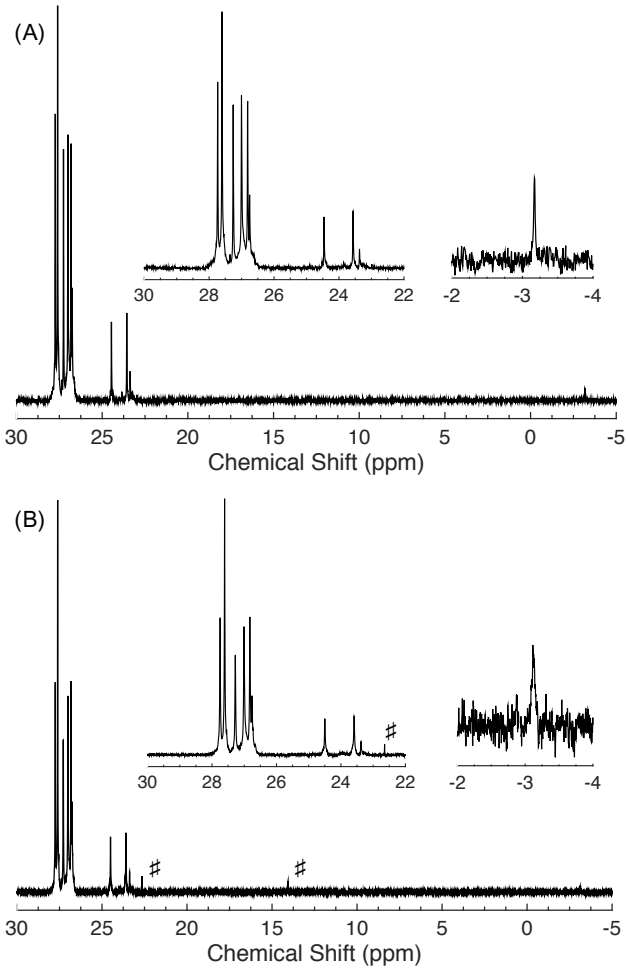

Figure S.5. ^{13}C NMR spectral comparison of as-synthesized **1a** catalyst (A) with **1a** separated (B) from a 2% (w/w) glucose in an equivolumetric DMSO:Benzene solution at 393 K after 1 hour using a 1:75 Sn/glucose molar ratio. The # denote residual hexane peaks.

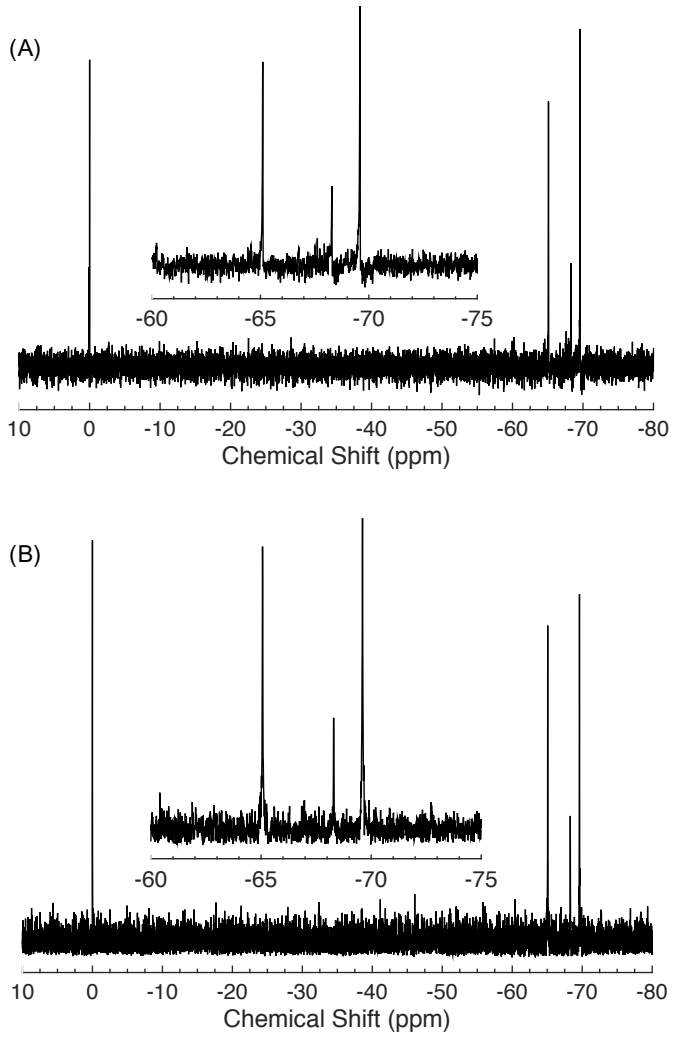

Figure S.6. ^{29}Si NMR spectral comparison of as-synthesized **1a** catalyst (A) with **1a** separated (B) from a 2% (w/w) glucose in an equivolumetric DMSO:Benzene solution at 393 K after 1 hour using a 1:75 Sn/glucose molar ratio.

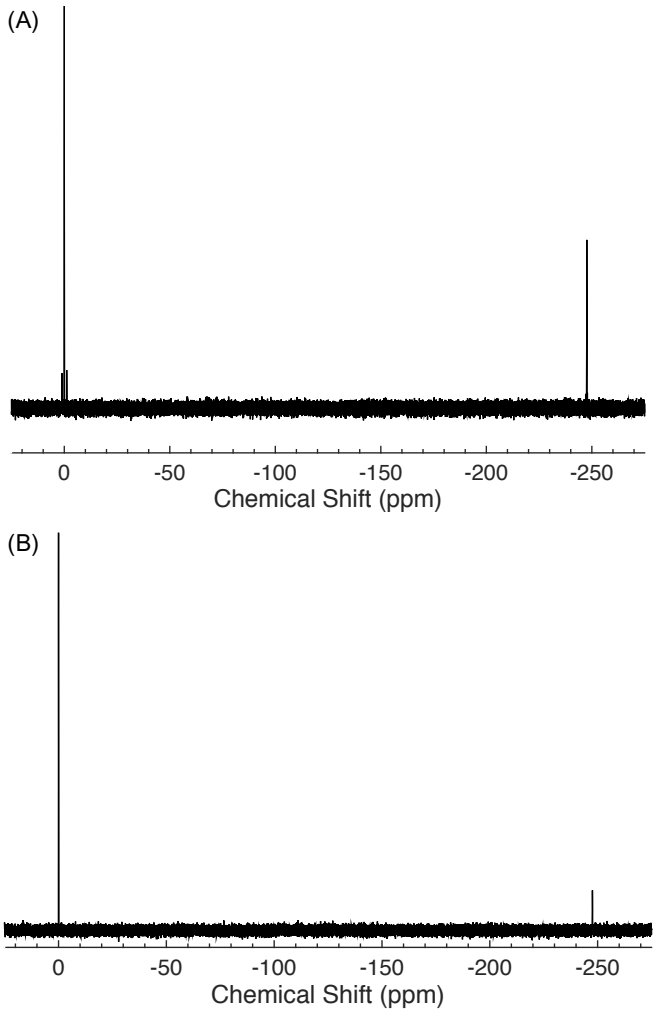

Figure S.7. ^{119}Sn NMR spectral comparison of as-synthesized **1a** catalyst (A) with **1a** separated (B) from a 2% (w/w) glucose in an equivolumetric DMSO:Benzene solution at 393 K after 1 hour using a 1:75 Sn/glucose molar ratio.

Appendix D

SUPPORTING INFORMATION FOR CHAPTER 5

The Supporting Information is available free of charge on the ACS Publications website at DOI: 10.1021/acscatal.6b03128.

Lewis structures of catalysts 1a and 1b from NBO analysis, free energy profiles for the reaction pathways on 1a and 1b, free energies for all of these optimized intermediates and transition states on 1a and 1b, description of the analysis of key reaction steps using Bader?s atoms in molecules theory, and an analysis of bond critical points

Supporting Information

1,2-H versus 1,2-C-shift on Sn-Silsesquioxanes

Tyler R. Josephson[1], Stephen K. Brand[2], Stavros Caratzoulas[3*], Dionisios G. Vlachos[1,3]

[1]*Department of Chemical and Biomolecular Engineering, University of Delaware, Newark, DE 19716*

[2]*Division of Chemistry and Chemical Engineering, California Institute of Technology, Pasadena, CA 91125*

[3]*Catalysis Center for Energy Innovation, University of Delaware, Newark, DE 19716*

[*]*Corresponding author: cstavros@udel.edu*

Lewis structures from NBO analysis of catalysts 1a and 1b

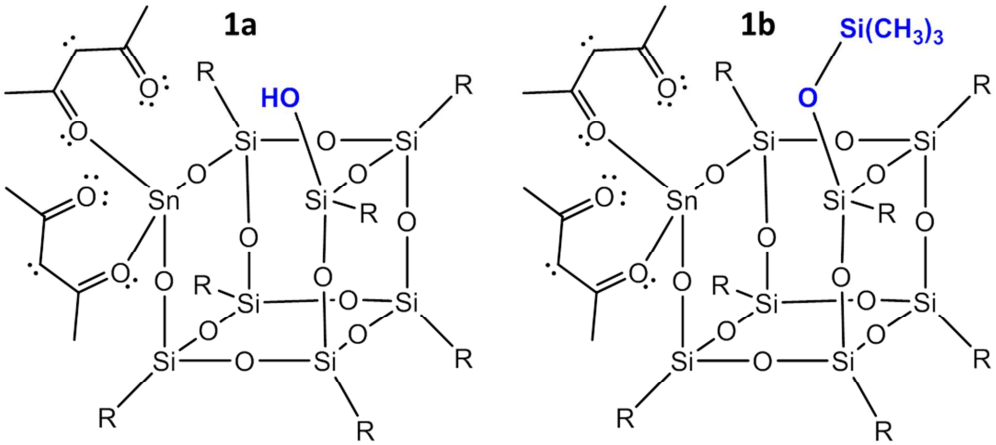

Figure S1. The most stable resonance structures of 1a and 1b are characterized by four covalent Sn-O bonds. Each acac ligand has one bond to Sn, two C=O, a lone pair on C3, and only one lone pair on the O bonded to Sn.

Table S1. Free energies at 353 K for H-shift and C-shift reactions on Sn-O-Si bridges on **1a** and **1b**. Electronic energies were calculated using basis set B (see computational methods), and zero-point corrections and entropic contributions were calculated using basis set A. Free energies are reported with respect to isolated glyceraldehyde and catalyst.

Sn-O-Si Bridge Mechanisms		B-1	B-2 TS	B-3	B-4 TS	B-5	B-6 TS	B-7
1a	H-shift	12.48	24.47	5.57	28.30	11.18	21.55	17.99
	C-shift	12.48	24.47	5.57	32.83	9.73	26.86	22.96
1b	H-shift	2.89	25.61	2.81	27.52	-1.41	8.59	6.16
	C-shift	2.89	25.61	2.81	38.13	1.42	16.26	0.32

		O1-1	O1-2 TS	O1-3	O1-4 TS	O1-5
1a	H-shift	19.40	46.27	7.90	21.82	3.13
	C-shift	20.45	41.19	16.93	26.86	22.96
1b	H-shift	8.45	34.79	0.27	8.59	6.16
	C-shift	13.42	28.27	13.50	20.93	9.47

		O2-1	O2-2 TS	O2-3	O2-4 TS	O2-5
1a	H-shift	13.64	19.06	5.25	37.15	-0.55
	C-shift	13.64	19.06	7.90	42.70	20.75
1b	H-shift	9.61	13.86	0.59	35.27	9.38
	C-shift	9.61	13.86	0.76	37.58	1.82

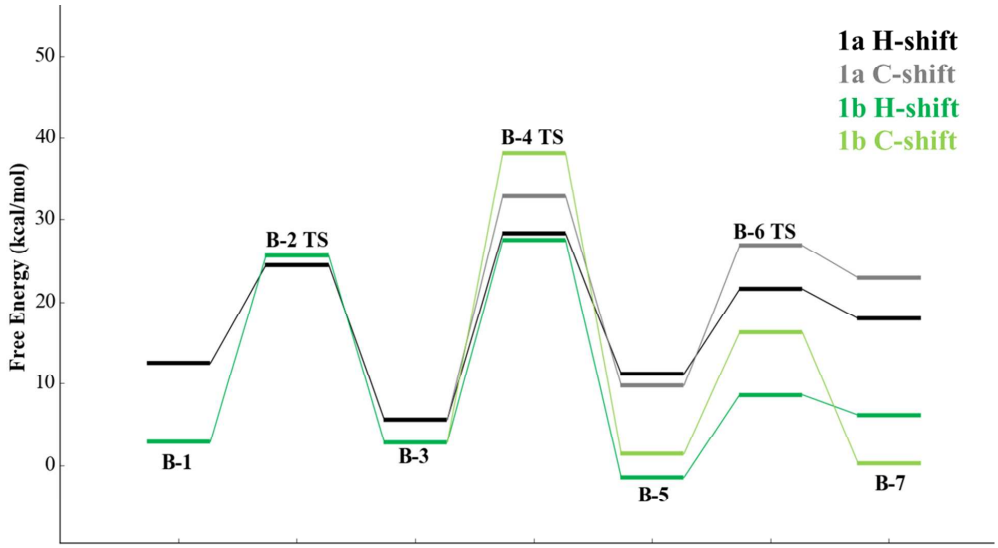

Figure S2 – Free energy profiles of H/C-shift on 1a and 1b through the bidentate pathway.

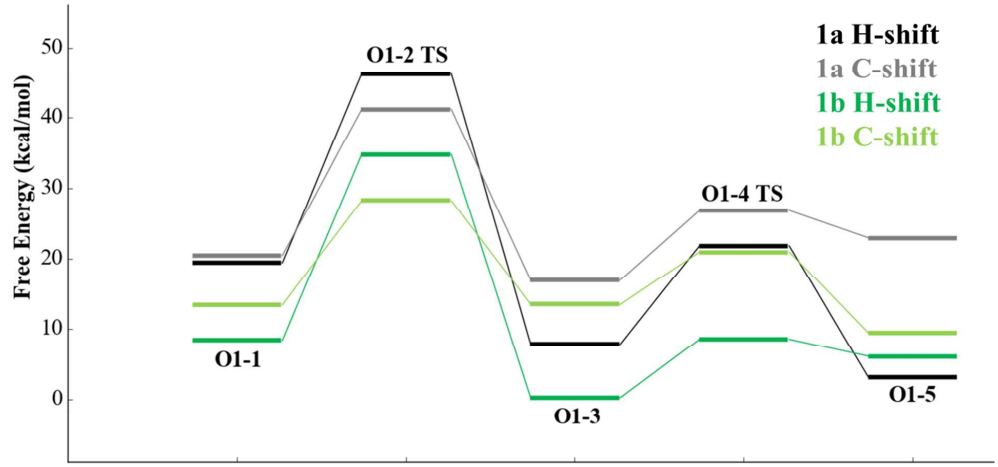

Figure S3 – Free energy profiles of H/C-shift on 1a and 1b through the O1 binding pathway.

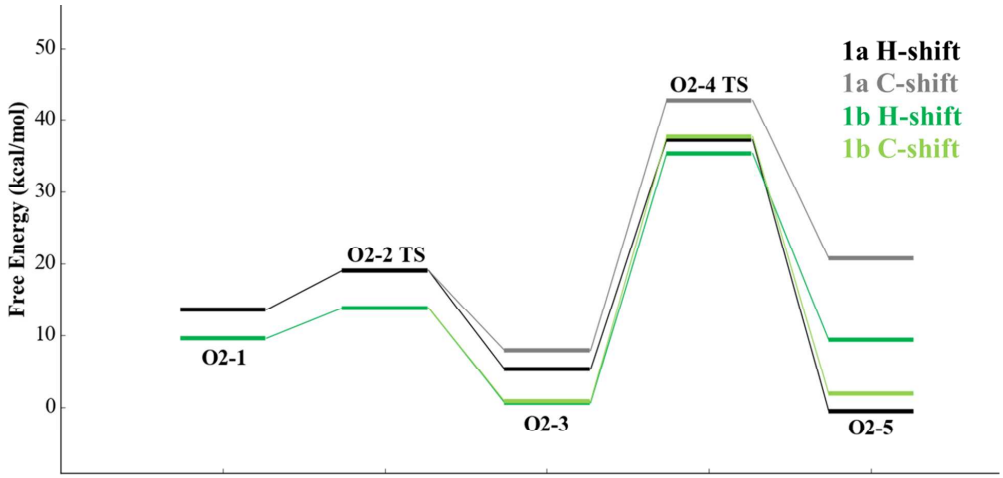

Figure S4 – Free energy profiles of H/C-shift on 1a and 1b through the O2 binding pathway.

Table S2. Free energies at 353 K for H-shift and C-shift reactions using the SiOH moiety in **1a**. Electronic energies were calculated using basis set B (see computational methods), and zero-point corrections and entropic contributions were calculated using basis set A. “sb” indicates a pathway in which the silanol transfers protons to a Sn-O-Si bridge, “la” indicates an acac ligand interacting with O3 of the sugar, “lb” indicates an acac ligand assisting the H-shift through an interaction with the transferring H, and “sl” indicates a proton transfer between the silanol and a ligand O. Free energies are reported with respect to isolated glyceraldehyde and catalyst.

Mechanisms Unique to 1a		O1sb-1	O1sb-2 TS	O1sb-3	O1sb-4 TS	O1sb-5
1a	H-shift	23.00	47.20	11.85	21.55	17.99
	C-shift	14.36	47.59	18.34	18.24	10.43

		O2sb-1	O2sb-2 TS	O2sb-3	O2sb-4 TS	O2sb-5
1a	H-shift	10.43	18.24	20.40	43.20	18.61
	C-shift	10.43	18.24	18.34	47.59	14.36

		O1sb-la-1	O1sb-la-2 TS	O1sb-la-3
1a	H-shift	16.74	38.77	13.20

		O1sb-lb-1	O1sb-lb-2 TS	O1sb-lb-3
1a	H-shift	16.32	32.72	16.72

		O2sl-1	O2sl-2 TS	O2sl-3	O2sl-4 TS	O2sl-5
1a	H-shift	13.80		12.74	35.09	13.97
	C-shift	13.80		13.80	28.15	18.98

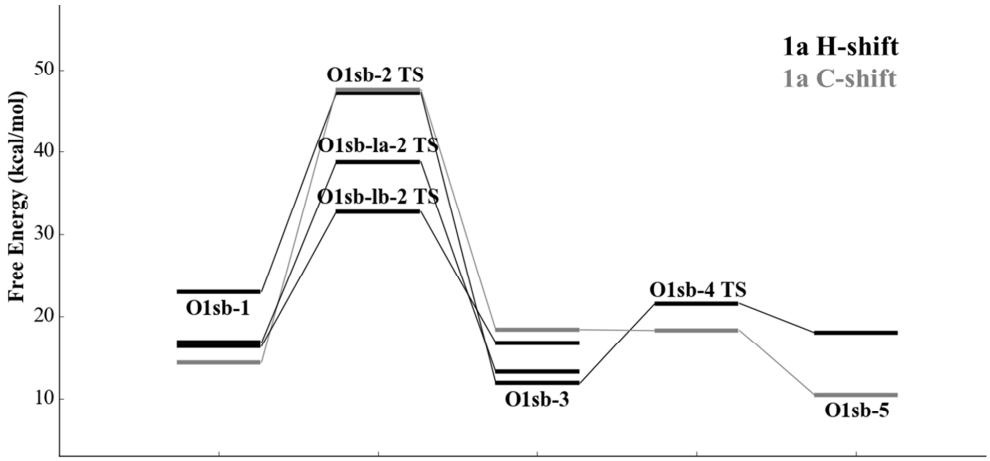

Figure S5 – Free energy profiles of H/C-shift on 1a through the O1sb, O1sb-la, and O1sb-lb pathways.

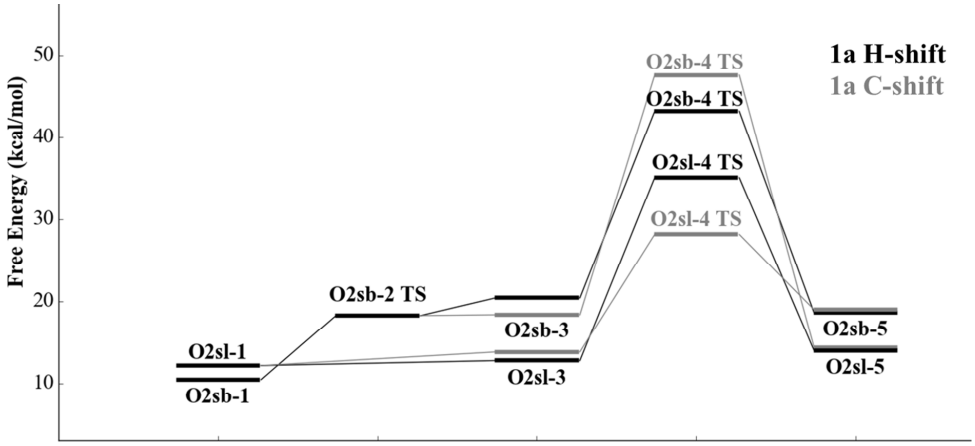

Figure S6 – Free energy profiles of H/C-shift on 1a through the O2sb and O2sl pathways.

Bader Analysis of H/C-shift Transition States on 1a

During the bidentate H-shift reaction, the C2-H bond is stretched from 1.10 to 1.36 Å at the TS. The electron density ρ at the BCP decreases from 0.168 to 0.121, indicating a weakening of the bond, and the Laplacian $\nabla^2(\rho)$ changes sign, from -0.139 to 0.102, indicating a switch from a region of local charge concentration to charge depletion. The ellipticity of the C2-H BCP increases from 3.12e-4 to 3.74, further indicating a dramatic weakening of the bond. At the H-shift TS, the transferring H does not yet have a bond with C1, even though the C1-H distance is only 1.38 Å; no C1-H BCP is observed, nor is there a (3,+1) ring critical point (RCP) present in the C1-C2-H triangle.

Likewise, in the bidentate C-shift reaction, the C2-C3 bond is stretched from the reactant to the C-shift TS, which is accompanied by a decrease in ρ (from 0.173 to 0.078), an increase in $\nabla^2(\rho)$ (from 0.072 to 0.161), and an increase in ellipticity (from 3.90e-3 to 1.06), indicating severe weakening in the C-C bond. The BCP is between C1 and C3 at the TS, but there is no BCP between C2 and C3, nor a RCP in the C1-C2-C3 triangle. The C3-O3 distance contracts slightly, from 1.41 to 1.36 Å, and this is accompanied by an increase in ρ at the BCP from 0.237 to 0.258, a sign change in $\nabla^2(\rho)$ from 0.092 to -0.026, and an increase in ellipticity from 4.89e-3 to 1.70e-2, all signatures of increased π character in the C3-O3 bond. While the C3-O3 bond is strengthened, the O3-H bond is weakened slightly, with a small decrease in ρ from 0.241 to 0.238, a small increase in $\nabla^2(\rho)$ from -0.528 to -0.484, and a slight increase in ellipticity from 4.88e-3 to 6.20e-3.

The bidentate C-shift reaction has a TS energy of 32.8 kcal/mol, the O2sl pathway has a TS energy of 28.2 kcal/mol, and the O1sb pathway has a TS energy of 47.6 kcal/mol. The stability of each TS is correlated to the ρ, $\nabla^2(\rho)$, and ε of the C3-O3 bond, reinforcing the importance of stabilizing the C3 moiety at the C-shift transition state.

Table S3. Bader Analysis of Select Bond Critical Points (BCPs) for gas-phase glyceraldehyde (GLY) and various intermediate and transition states.

Gas-phase GLY	**ρ**	**$\nabla^2(\rho)$**	**ε (ellipticity)**
C2-C3	1.74E-01	6.79E-02	2.33E-03
C2-H	1.68E-01	-1.39E-01	2.08E-03
C3-O3	2.38E-01	8.77E-02	9.09E-03
O3-H	2.42E-01	-5.41E-01	5.56E-03
HO3-O1	2.57E-02	7.34E-02	6.57E-01

OH_H_B-4 DP GLY	**ρ**	**$\nabla^2(\rho)$**	**ε (ellipticity)**
C2-C3	1.73E-01	7.02E-02	3.90E-03
C2-H	1.68E-01	-1.39E-01	3.19E-04

C3-O3	2.37E-01	9.24E-02	4.89E-03
O3-H	2.41E-01	-5.28E-01	4.88E-03
HO3-OHSi	3.46E-02	9.04E-02	1.68E-01

OH_H_B-5 Bidentate H-Shift TS	**ρ**	**$\nabla^2(\rho)$**	**ε (ellipticity)**
C2-C3	1.80E-01	4.84E-02	1.28E-02
C2-H	1.21E-01	1.02E-01	3.47E+00
C3-O3	2.41E-01	7.41E-02	8.45E-03
O3-H	2.38E-01	-4.94E-01	5.52E-03
HO3-OHSi	3.56E-02	9.27E-02	6.78E-03

OH_C_B-5 Bidentate C-shift TS	**ρ**	**∇2(ρ)**	**ε (ellipticity)**
C1-C3	7.83E-02	1.61E-01	1.06E+00
C2-H	1.71E-01	-1.62E-01	7.63E-03
C3-O3	2.58E-01	-2.59E-02	1.70E-02
O3-H	2.38E-01	-4.84E-01	6.20E-03
HO3-OHSi	3.40E-02	8.88E-02	3.61E-02

OH_C_O2sl-4 Ligand-Assist C-Shift TS	**ρ**	**∇2(ρ)**	**ε (ellipticity)**
C2-C3	8.00E-02	1.63E-01	7.94E-01
C2-H	1.71E-01	-1.56E-01	1.06E-02
C3-O3	2.68E-01	-7.71E-02	1.42E-02
O3-H	2.35E-01	-4.54E-01	5.54E-03
HO3-ligand O1	2.97E-02	8.22E-02	6.97E-02
HO3-ligand O2	2.80E-02	7.62E-02	6.81E-02

OH_C_O1sb-2 O1 C-shift TS	**ρ**	**∇2(ρ)**	**ε (ellipticity)**
C1-C2	2.15E-01	-7.01E-02	7.47E-03
C1-C3	8.98E-02	1.67E-01	3.44E-01
C2-H	1.71E-01	-1.58E-01	8.51E-03
C3-O3	2.56E-01	-1.48E-02	1.59E-02
O3-H	2.37E-01	-4.77E-01	5.11E-03
HO3-OLigand	3.58E-02	9.45E-02	9.13E-03

Appendix E

SUPPORTING INFORMATION FOR CHAPTER 6

SUPPORTING INFORMATION

Distribution of Open Sites in Sn-Beta Zeolite

Tyler R. Josephson[a], Glen R. Jenness[a], Dionisios G. Vlachos[a], Stavros Caratzoulas[a]*

[a]Catalysis Center for Energy Innovation, 221 Academy Street

University of Delaware, Newark, DE 19716, USA

*Corresponding author: cstavros@udel.edu

To organize the open sites, we propose a grouping method by characterizing the geometry surrounding each "gap" in **Error! Reference source not found.**, which has been summarized in Table S1. Inspection of the structure reveals that the "channels" are inside the *t-bea-1* tile, framing the 12-ring channels; the "medium cage" is the pocket inside the *t-mtw* tile, framing the 6-ring channel, and the "small cage" is the pocket inside the *t-bet* tile, framing the 5-ring channels. Every T site except for T1 and T2 is adjacent two 12-ring channels, one along the a-axis and one along b; T1 and T2 are adjacent to only one 12-ring channel in either a or b. T1, T3, T8, and T2, T4, T9 together carve out the medium cage, and all T sites except for T9 are adjacent to one or two small cages.

Table S1 – Local geometry information for all T sites in the BEA framework, and an assignment of each "Gap" around the Sn site to each location.

	Gap A	Gap B	Gap C	Gap D
T1	Channel	Medium Cage	Small Cage	Small Cage
T2	Channel	Medium Cage	Small Cage	Small Cage
T3	Channel	Channel	Medium Cage	Small Cage
T4	Channel	Channel	Medium Cage	Small Cage
T5	Channel	Channel	Small Cage	Small Cage
T6	Channel	Channel	Small Cage	Small Cage
T7	Channel	Channel	Small Cage	Small Cage
T8	Channel	Channel	Medium Cage	Small Cage
T9	Channel	Channel	Medium Cage	Medium Cage

Table S2 – Relative PBE and PBE-d3 energies (kcal/mol) of open sites. Gaps A, B, C, and D are described in Table S1, and bridge oxygens are labelled according to which T sites each one bridges. PBE reference is the energy of geometry T9-O29B; PBE-d3 reference is energy of geometry T1-O17B.

		PBE				PBE-d3			
		A	B	C	D	A	B	C	D
T1	O12	**1.15**	11.42	42.86	15.47	4.46	9.83	41.83	13.15
T1	O13	14.33	12.89	32.46	9.10	15.65	11.33	31.45	6.76
T1	O17	12.83	1.71	16.68	5.97	13.38	**0.00**	15.69	3.62
T1	O18	13.91	5.29	14.02	6.14	14.01	4.14	13.04	3.49
T2	O12	**2.67**	15.96	22.23	14.85	6.11	12.95	19.71	12.97
T2	O24	11.28	10.39	43.51	16.17	11.78	9.15	41.78	14.62
T2	O28	12.67	8.38	45.71	5.90	13.93	6.80	44.35	**3.34**
T2	O29	14.88	6.57	34.99	5.61	15.77	4.28	33.69	3.78
T3	O13	3.67	9.34	9.89	9.89	**5.92**	9.73	7.77	7.77
T3	O34	14.15	**0.51**	31.17	17.15	14.66	2.93	29.48	14.71
T3	O35	11.08	13.00	15.76	12.52	10.38	13.17	13.55	11.00
T3	O38	18.44	8.39	10.10	18.08	19.81	8.53	9.83	15.99
T4	O24	**2.57**	20.93	12.80	8.13	**4.27**	21.48	11.26	5.75
T4	O34	14.98	2.66	22.02	17.23	15.36	5.82	20.09	14.99
T4	O46	11.73	18.36	15.53	12.24	12.26	19.18	13.65	11.07
T4	O49	9.30	13.53	21.46	15.33	9.40	14.42	20.72	13.23
T5	O35	13.98	14.69	11.11	19.48	14.07	15.24	10.36	17.84
T5	O55	4.78	**1.94**	12.20	20.94	6.24	**5.79**	11.00	19.51
T5	O56	17.63	4.59	15.11	24.11	17.84	7.24	12.28	22.00
T5	O57	15.70	13.40	14.68	27.18	17.33	14.29	12.58	25.27
T6	O46	10.90	16.89	14.94	13.17	11.92	17.31	12.93	12.00
T6	O56	12.82	**2.16**	24.83	13.61	13.69	5.49	22.74	11.26
T6	O66	3.07	10.28	17.05	10.77	**4.86**	11.39	15.18	8.79
T6	O68	15.24	19.44	15.62	10.67	16.87	20.47	14.44	8.01
T7	O17	16.67	4.31	14.75	15.13	15.87	7.33	13.62	14.00
T7	O17	**3.57**	5.64	16.97	17.71	**6.90**	9.08	14.80	15.97
T7	O57	15.05	22.17	23.72	13.54	15.76	23.76	21.90	12.34
T7	O57	18.17	7.34	12.96	20.85	19.42	10.69	11.76	19.45
T8	O18	11.26	7.54	16.21	12.46	10.89	7.11	14.50	11.17
T8	O28	20.64	5.67	21.48	13.50	19.48	7.93	20.85	12.20
T8	O38	**3.22**	23.99	20.30	27.26	**5.42**	24.21	19.36	26.59
T8	O68	18.93	18.87	13.19	22.97	19.10	18.82	12.28	21.55
T9	O29	0.58	9.84	22.81	13.52	1.47	8.89	21.36	11.72
T9	O29	11.53	**0.00**	18.78	20.19	10.09	**1.37**	17.59	18.75
T9	O49	6.91	12.91	13.44	16.35	6.69	12.70	12.54	14.34
T9	O49	13.83	8.54	22.48	13.87	13.74	8.03	20.94	13.01

Table S3 – PBE energies for exchange between closed site and open site in the presence of water and without. Reference for gas-phase conversion is energy of most stable site, T9_O29B. Reference for water-assisted conversion is infinitely separated T9_O29B and a water molecule.

Gas-phase	Energy	Water-assisted	Energy
Water adsorbed on T9	-5.26		
Deprotonation TS	10.56		
T9_O49A (adjacent)	6.89		
SiOH rotation TS	9.42		
T9_O49A_b (adjacent)	8.11	Water adsorbed on T9_O49B	-3.14
Proton transfer TS	19.48	Proton transfer TS	-2.02
T9_O29A (opposite)	0.57	Water adsorbed on T9_O29B	-8.03

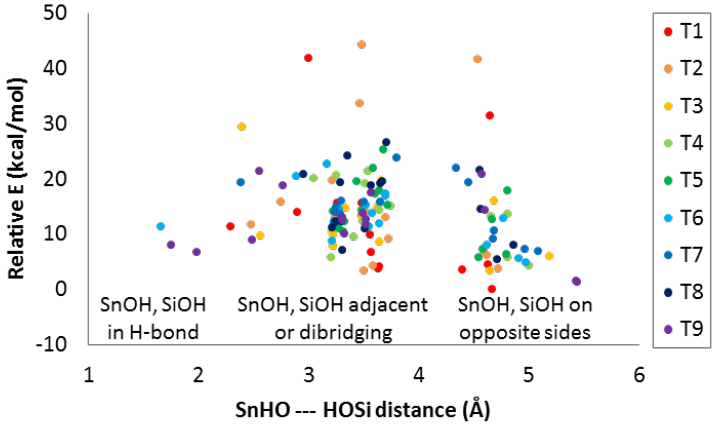

Figure S1 - – Relative PBE-d3 energy (kcal/mol) of open sites with respect to the distance between the oxygen of SnOH and the hydrogen of SiOH. The largest O-H distances (> 4 Å) correspond to geometries in which the SnOH and SiOH are on opposite sides, the shortest distances (< 2 Å) are approximate H-bonds between SiOH and SnOH, and the intermediate distances include the other structures, including the dibridging geometries.

Appendix F

SUPPORTING INFORMATION FOR CHAPTER 7

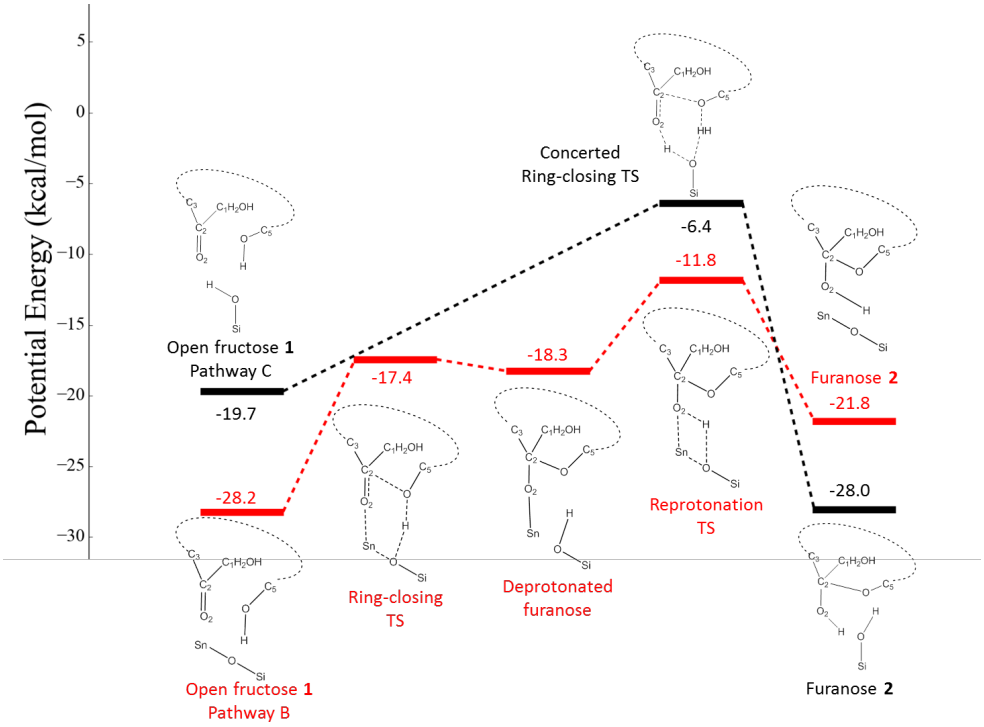

Figure S1 - Hemiketalization pathways calculated for open fructose ring-closing to fructofuranose 2. Electronic binding energies (kcal/mol) are reported with respect to infinitely separated fructofuranose, ethanol, and catalyst.

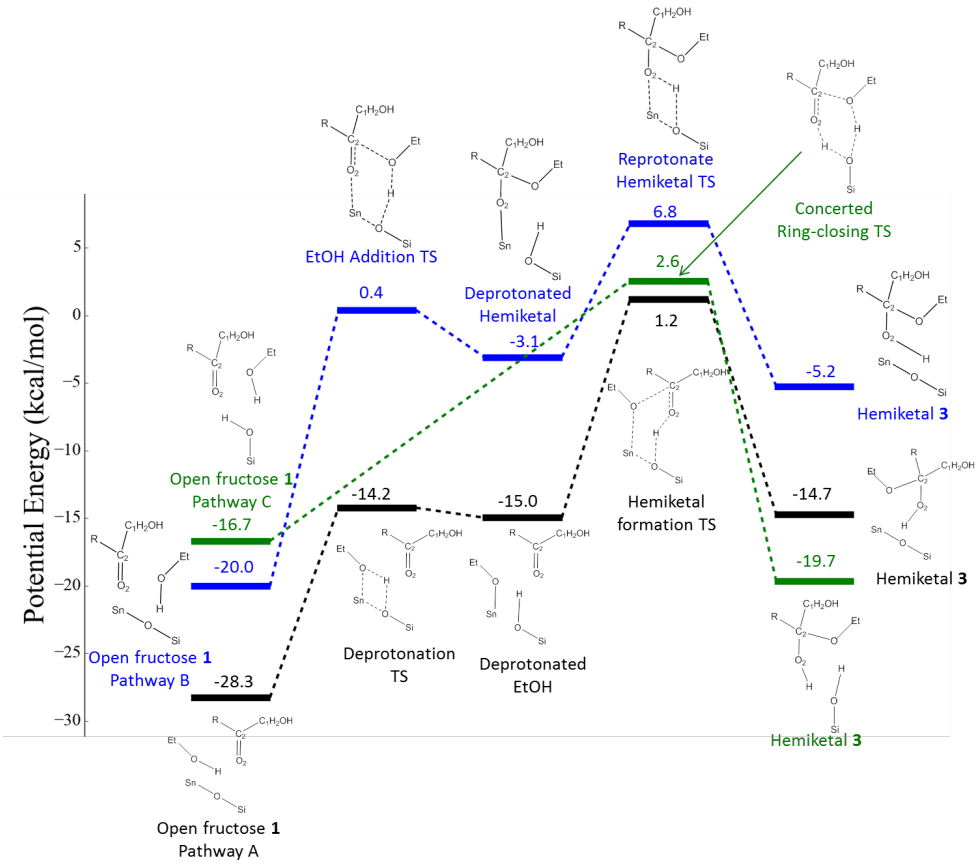

Figure S2 - Hemiketalization pathways calculated for open fructose reaction to hemiketal 2. Electronic binding energies (kcal/mol) are reported with respect to infinitely separated fructofuranose, ethanol, and catalyst.

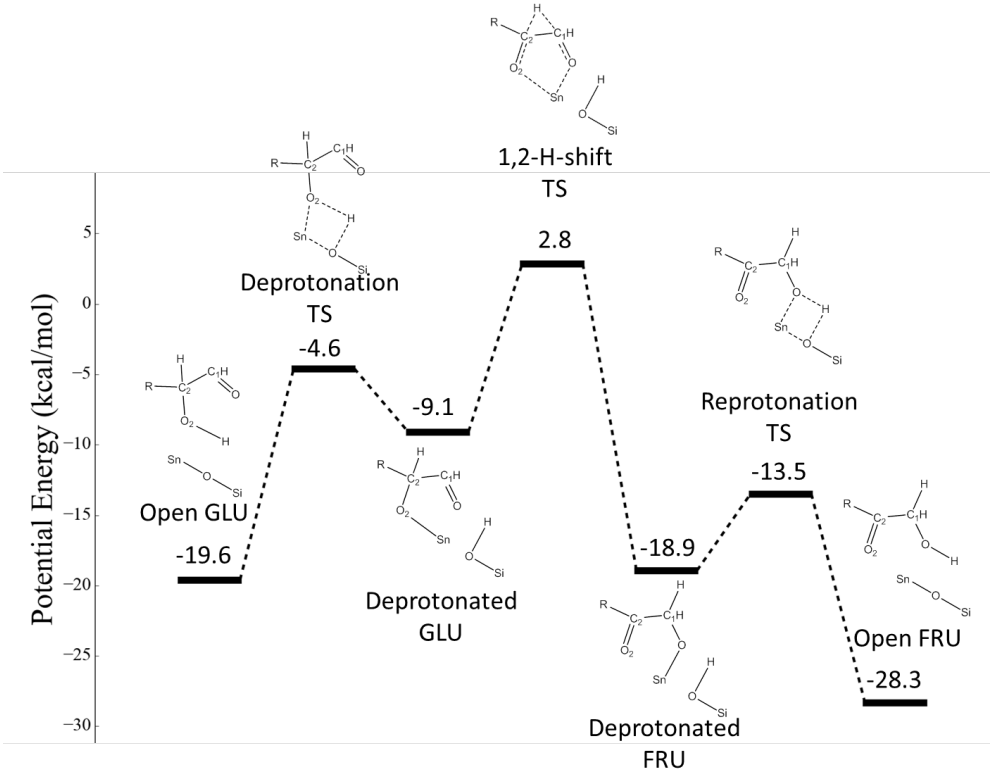

Figure S3 - Reaction profile for glucose isomerization reaction on Sn-SPP. Reaction follows bidentate reaction mechanism with a chelate-like intermediate. Electronic binding energies (kcal/mol) are reported with respect to infinitely separated fructofuranose, ethanol, and catalyst.

Gas-phase oxonium stability was investigated using Gaussian 09, at the M062X/aug-cc-pvdz theory level. While a 5-ring hemiketal is only 0.7 kcal/mol more stable than its 6-ring counterpart, the hemiketal hydroxyl has significantly greater proton affinity than the hemiacetal hydroxyl, and the dehydrated oxonium for the hemiketal is 13.3 kcal/mol more stable. The same trends are also observed for the linear hemiketal and hemiacetal tested.

So, hemiketals are more reactive for Sn1 mechanisms, both due to increased proton affinity and increased oxonium stability.

	Intermediate	Protonated OH	Water removed
5-ring hemiketal	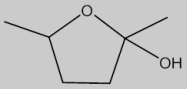 1a Rel. ΔG = 0	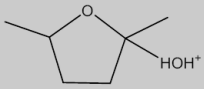 1b PA: 213.4	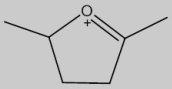 1c Rel. ΔG = 0
6-ring hemiacetal	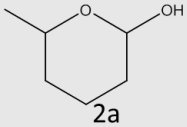 2a Rel. ΔG = 0.7	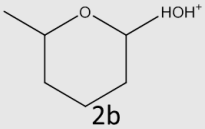 2b PA: 201.0	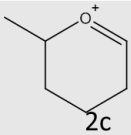 2c Rel. ΔG = 13.3
Linear hemiketal	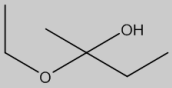 3a Rel. ΔG = 0	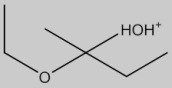 3b PA: 212.0	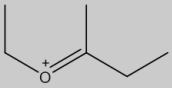 3c Rel. ΔG = 0
Linear hemiacetal	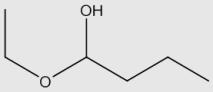 4a Rel. ΔG = 4.2	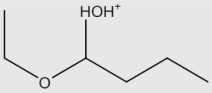 4b PA: 203.1	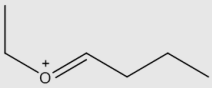 4c Rel. ΔG = 14.2

Figure S4 – Gas-phase calculations for model hemiketals and hemiacetals. Free energies are reported in kcal/mol. Relative free energies for 1a-c and 2a-c are reported with respect to 1a and 1c, and for 3a-c and 4a-c with respect to 3a and 3c.

Appendix G

PERMISSION LETTERS

JOHN WILEY AND SONS LICENSE
TERMS AND CONDITIONS

Mar 31, 2017

This Agreement between Tyler R Josephson ("You") and John Wiley and Sons ("John Wiley and Sons") consists of your license details and the terms and conditions provided by John Wiley and Sons and Copyright Clearance Center.

License Number	4079360921983
License date	
Licensed Content Publisher	John Wiley and Sons
Licensed Content Publication	ChemSusChem
Licensed Content Title	Origin of 5-Hydroxymethylfurfural Stability in Water/Dimethyl Sulfoxide Mixtures
Licensed Content Author	George Tsilomelekis,Tyler R. Josephson,Vladimiros Nikolakis,Stavros Caratzoulas
Licensed Content Date	Jan 10, 2014
Licensed Content Pages	10
Type of use	Dissertation/Thesis
Requestor type	Author of this Wiley article
Format	Print and electronic
Portion	Full article
Will you be translating?	No
Title of your thesis / dissertation	Leveraging First-Principles Modeling for Deeper Insights into Biomass Processing
Expected completion date	Apr 2017
Expected size (number of pages)	350
Requestor Location	Tyler R Josephson 221 Academy Street ISE Laboratory NEWARK, DE 19716 United States Attn: Tyler R Josephson
Publisher Tax ID	EU826007151
Billing Type	Invoice
Billing Address	Tyler R Josephson 221 Academy Street ISE Laboratory NEWARK, DE 19716 United States Attn: Tyler R Josephson
Total	0.00 USD
Terms and Conditions	

TERMS AND CONDITIONS

("Marks") of WILEY or its licensors is granted hereunder, and you agree that you shall not assert any such right, license or interest with respect thereto

- NEITHER WILEY NOR ITS LICENSORS MAKES ANY WARRANTY OR REPRESENTATION OF ANY KIND TO YOU OR ANY THIRD PARTY, EXPRESS, IMPLIED OR STATUTORY, WITH RESPECT TO THE MATERIALS OR THE ACCURACY OF ANY INFORMATION CONTAINED IN THE MATERIALS, INCLUDING, WITHOUT LIMITATION, ANY IMPLIED WARRANTY OF MERCHANTABILITY, ACCURACY, SATISFACTORY QUALITY, FITNESS FOR A PARTICULAR PURPOSE, USABILITY, INTEGRATION OR NON-INFRINGEMENT AND ALL SUCH WARRANTIES ARE HEREBY EXCLUDED BY WILEY AND ITS LICENSORS AND WAIVED BY YOU.

- WILEY shall have the right to terminate this Agreement immediately upon breach of this Agreement by you.

- You shall indemnify, defend and hold harmless WILEY, its Licensors and their respective directors, officers, agents and employees, from and against any actual or threatened claims, demands, causes of action or proceedings arising from any breach of this Agreement by you.

- IN NO EVENT SHALL WILEY OR ITS LICENSORS BE LIABLE TO YOU OR ANY OTHER PARTY OR ANY OTHER PERSON OR ENTITY FOR ANY SPECIAL, CONSEQUENTIAL, INCIDENTAL, INDIRECT, EXEMPLARY OR PUNITIVE DAMAGES, HOWEVER CAUSED, ARISING OUT OF OR IN CONNECTION WITH THE DOWNLOADING, PROVISIONING, VIEWING OR USE OF THE MATERIALS REGARDLESS OF THE FORM OF ACTION, WHETHER FOR BREACH OF CONTRACT, BREACH OF WARRANTY, TORT, NEGLIGENCE, INFRINGEMENT OR OTHERWISE (INCLUDING, WITHOUT LIMITATION, DAMAGES BASED ON LOSS OF PROFITS, DATA, FILES, USE, BUSINESS OPPORTUNITY OR CLAIMS OF THIRD PARTIES), AND WHETHER OR NOT THE PARTY HAS BEEN ADVISED OF THE POSSIBILITY OF SUCH DAMAGES. THIS LIMITATION SHALL APPLY NOTWITHSTANDING ANY FAILURE OF ESSENTIAL PURPOSE OF ANY LIMITED REMEDY PROVIDED HEREIN.

- Should any provision of this Agreement be held by a court of competent jurisdiction to be illegal, invalid, or unenforceable, that provision shall be deemed amended to achieve as nearly as possible the same economic effect as the original provision, and the legality, validity and enforceability of the remaining provisions of this Agreement shall not be affected or impaired thereby.

- The failure of either party to enforce any term or condition of this Agreement shall not constitute a waiver of either party's right to enforce each and every term and condition of this Agreement. No breach under this agreement shall be deemed waived or excused by either party unless such waiver or consent is in writing signed by the party granting such waiver or consent. The waiver by or consent of a party to a breach of any provision of this Agreement shall not operate or be construed as a waiver of or consent to any other or subsequent breach by such other party.

- This Agreement may not be assigned (including by operation of law or otherwise) by you without WILEY's prior written consent.

- Any fee required for this permission shall be non-refundable after thirty (30) days from receipt by the CCC.

- These terms and conditions together with CCC's Billing and Payment terms and conditions (which are incorporated herein) form the entire agreement between you and WILEY concerning this licensing transaction and (in the absence of fraud) supersedes all prior agreements and representations of the parties, oral or written. This Agreement may not be amended except in writing signed by both parties. This Agreement shall be binding upon and inure to the benefit of the parties' successors, legal representatives, and authorized assigns.

- In the event of any conflict between your obligations established by these terms and conditions and those established by CCC's Billing and Payment terms and conditions, these terms and conditions shall prevail.

- WILEY expressly reserves all rights not specifically granted in the combination of (i) the license details provided by you and accepted in the course of this licensing transaction, (ii) these terms and conditions and (iii) CCC's Billing and Payment terms and conditions.

- This Agreement will be void if the Type of Use, Format, Circulation, or Requestor Type was misrepresented during the licensing process.

- This Agreement shall be governed by and construed in accordance with the laws of the State of New York, USA, without regards to such state's conflict of law rules. Any legal action, suit or proceeding arising out of or relating to these Terms and Conditions or the breach thereof shall be instituted in a court of competent jurisdiction in New York County in the State of New York in the United States of America and each party hereby consents and submits to the personal jurisdiction of such court, waives any objection to venue in such court and consents to service of process by registered or certified mail, return receipt requested, at the last known address of such party.

WILEY OPEN ACCESS TERMS AND CONDITIONS
Wiley Publishes Open Access Articles in fully Open Access Journals and in Subscription journals offering Online Open. Although most of the fully Open Access journals publish open access articles under the terms of the Creative Commons Attribution (CC BY) License only, the subscription journals and a few of the Open Access Journals offer a choice of Creative Commons Licenses. The license type is clearly identified on the article.
The Creative Commons Attribution License
The Creative Commons Attribution License (CC-BY) allows users to copy, distribute and transmit an article, adapt the article and make commercial use of the article. The CC-BY license permits commercial and non-
Creative Commons Attribution Non-Commercial License
The Creative Commons Attribution Non-Commercial (CC-BY-NC)License permits use, distribution and reproduction in any medium, provided the original work is properly cited and is not used for commercial purposes.(see below)

Creative Commons Attribution-Non-Commercial-NoDerivs License
The Creative Commons Attribution Non-Commercial-NoDerivs License (CC-BY-NC-ND) permits use, distribution and reproduction in any medium, provided the original work is properly cited, is not used for commercial purposes and no modifications or adaptations are made. (see below)
Use by commercial "for-profit" organizations

ACS Publications
Most Trusted. Most Cited. Most Read.

Title: Solvent-Induced Frequency Shifts of 5-Hydroxymethylfurfural Deduced via Infrared Spectroscopy and ab Initio Calculations

Author: Tyler R. Josephson, George Tsilomelekis, Christina Bagia, et al

Publication: The Journal of Physical Chemistry A

Publisher: American Chemical Society

Date: Dec 1, 2014

PERMISSION/LICENSE IS GRANTED FOR YOUR ORDER AT NO CHARGE

This type of permission/license, instead of the standard Terms & Conditions, is sent to you because no fee is being charged for your order. Please note the following:

- Permission is granted for your request in both print and electronic formats, and translations.
- If figures and/or tables were requested, they may be adapted or used in part.
- Please print this page for your records and send a copy of it to your publisher/graduate school.
- Appropriate credit for the requested material should be given as follows: "Reprinted (adapted) with permission from (COMPLETE REFERENCE CITATION). Copyright (YEAR) American Chemical Society." Insert appropriate information in place of the capitalized words.
- One-time permission is granted only for the use specified in your request. No additional uses are granted (such as derivative works or other editions). For any other uses, please submit a new request.

BACK CLOSE WINDOW

ELSEVIER LICENSE
TERMS AND CONDITIONS

Mar 31, 2017

This Agreement between Tyler R Josephson ("You") and Elsevier ("Elsevier") consists of your license details and the terms and conditions provided by Elsevier and Copyright Clearance Center.

License Number	4079371371760
License date	Mar 31, 2017
Licensed Content Publisher	Elsevier
Licensed Content Publication	Journal of Catalysis
Licensed Content Title	Methyl-ligated tin silsesquioxane catalyzed reactions of glucose
Licensed Content Author	Stephen K. Brand,Tyler R. Josephson,Jay A. Labinger,Stavros Caratzoulas,Dionisios G. Vlachos,Mark E. Davis
Licensed Content Date	September 2016
Licensed Content Volume	341
Licensed Content Issue	n/a
Licensed Content Pages	10
Start Page	62
End Page	71
Type of Use	reuse in a thesis/dissertation
Intended publisher of new work	other
Portion	full article
Format	both print and electronic
Are you the author of this Elsevier article?	Yes
Will you be translating?	No
Order reference number	
Title of your thesis/dissertation	Leveraging First-Principles Modeling for Deeper Insights into Biomass Processing
Expected completion date	Apr 2017
Estimated size (number of pages)	350
Elsevier VAT number	GB 494 6272 12
Requestor Location	Tyler R Josephson 221 Academy Street ISE Laboratory NEWARK, DE 19716

Print This Page

Copyright Clearance Center RightsLink®

Home Account Info Help

ACS Publications
Most Trusted. Most Cited. Most Read.

Title: 1,2-H- versus 1,2-C-Shift on Sn-Silsesquioxanes

Author: Tyler R. Josephson, Stephen K. Brand, Stavros Caratzoulas, et al

Publication: ACS Catalysis

Publisher: American Chemical Society

Date: Jan 1, 2017

Logged in as:
Tyler Josephson
LOGOUT

PERMISSION/LICENSE IS GRANTED FOR YOUR ORDER AT NO CHARGE

This type of permission/license, instead of the standard Terms & Conditions, is sent to you because no fee is being charged for your order. Please note the following:

- Permission is granted for your request in both print and electronic formats, and translations.
- If figures and/or tables were requested, they may be adapted or used in part.
- Please print this page for your records and send a copy of it to your publisher/graduate school.
- Appropriate credit for the requested material should be given as follows: "Reprinted (adapted) with permission from (COMPLETE REFERENCE CITATION). Copyright (YEAR) American Chemical Society." Insert appropriate information in place of the capitalized words.
- One-time permission is granted only for the use specified in your request. No additional uses are granted (such as derivative works or other editions). For any other uses, please submit a new request.

BACK CLOSE WINDOW

ELSEVIER LICENSE
TERMS AND CONDITIONS

Mar 31, 2017

This Agreement between Tyler R Josephson ("You") and Elsevier ("Elsevier") consists of your license details and the terms and conditions provided by Elsevier and Copyright Clearance Center.

License Number	4079380077739
License date	Mar 31, 2017
Licensed Content Publisher	Elsevier
Licensed Content Publication	Microporous and Mesoporous Materials
Licensed Content Title	Distribution of open sites in Sn-Beta zeolite
Licensed Content Author	Tyler R. Josephson,Glen R. Jenness,Dionisios G. Vlachos,Stavros Caratzoulas
Licensed Content Date	June 2017
Licensed Content Volume	245
Licensed Content Issue	n/a
Licensed Content Pages	6
Start Page	45
End Page	50
Type of Use	reuse in a thesis/dissertation
Intended publisher of new work	other
Portion	full article
Format	both print and electronic
Are you the author of this Elsevier article?	Yes
Will you be translating?	No
Order reference number	
Title of your thesis/dissertation	Leveraging First-Principles Modeling for Deeper Insights into Biomass Processing
Expected completion date	Apr 2017
Estimated size (number of pages)	350
Elsevier VAT number	GB 494 6272 12
Requestor Location	Tyler R Josephson 221 Academy Street ISE Laboratory NEWARK, DE 19716 United States Attn: Tyler R Josephson
Publisher Tax ID	98-0397604
Total	0.00 USD

Terms and Conditions

INTRODUCTION

1. The publisher for this copyrighted material is Elsevier. By clicking "accept" in connection with completing this licensing transaction, you agree that the following terms and conditions apply to this transaction (along with the Billing and Payment terms and conditions established by Copyright Clearance Center, Inc. ("CCC"), at the time that you opened your Rightslink account and that are available at any time at http://myaccount.copyright.com).

GENERAL TERMS

2. Elsevier hereby grants you permission to reproduce the aforementioned material subject to the terms and conditions indicated.
3. Acknowledgement: If any part of the material to be used (for example, figures) has appeared in our publication with credit or acknowledgement to another source, permission must also be sought from that source. If such permission is not obtained then that material may not be included in your publication/copies. Suitable acknowledgement to the source must be made, either as a footnote or in a reference list at the end of your publication, as follows:
"Reprinted from Publication title, Vol /edition number, Author(s), Title of article / title of chapter, Pages No., Copyright (Year), with permission from Elsevier [OR APPLICABLE SOCIETY COPYRIGHT OWNER]." Also Lancet special credit - "Reprinted from The Lancet, Vol. number, Author(s), Title of article, Pages No., Copyright (Year), with permission from Elsevier."
4. Reproduction of this material is confined to the purpose and/or media for which permission is hereby given.
5. Altering/Modifying Material: Not Permitted. However figures and illustrations may be altered/adapted minimally to serve your work. Any other abbreviations, additions, deletions and/or any other alterations shall be made only with prior written authorization of Elsevier Ltd. (Please contact Elsevier at permissions@elsevier.com). No modifications can be made to any Lancet figures/tables and they must be reproduced in full.
6. If the permission fee for the requested use of our material is waived in this instance, please be advised that your future requests for Elsevier materials may attract a fee.
7. Reservation of Rights: Publisher reserves all rights not specifically granted in the combination of (i) the license details provided by you and accepted in the course of this licensing transaction, (ii) these terms and conditions and (iii) CCC's Billing and Payment terms and conditions.
8. License Contingent Upon Payment: While you may exercise the rights licensed immediately upon issuance of the license at the end of the licensing process for the transaction, provided that you have disclosed complete and accurate details of your proposed use, no license is finally effective unless and until full payment is received from you (either by publisher or by CCC) as provided in CCC's Billing and Payment terms and conditions. If full payment is not received on a timely basis, then any license preliminarily granted shall be deemed automatically revoked and shall be void as if never granted. Further, in the event that you breach any of these terms and conditions or any of CCC's Billing and Payment terms and conditions, the license is automatically revoked and shall be void as if never granted. Use of materials as described in a revoked license, as well as any use of the materials beyond the scope of an unrevoked license, may constitute copyright infringement and publisher reserves the right to take any and all action to protect its copyright in the materials.
9. Warranties: Publisher makes no representations or warranties with respect to the licensed material.
10. Indemnity: You hereby indemnify and agree to hold harmless publisher and CCC, and their respective officers, directors, employees and agents, from and against any and all claims arising out of your use of the licensed material other than as specifically authorized pursuant to this license.

11. No Transfer of License: This license is personal to you and may not be sublicensed, assigned, or transferred by you to any other person without publisher's written permission.
12. No Amendment Except in Writing: This license may not be amended except in a writing signed by both parties (or, in the case of publisher, by CCC on publisher's behalf).
13. Objection to Contrary Terms: Publisher hereby objects to any terms contained in any purchase order, acknowledgment, check endorsement or other writing prepared by you, which terms are inconsistent with these terms and conditions or CCC's Billing and Payment terms and conditions. These terms and conditions, together with CCC's Billing and Payment terms and conditions (which are incorporated herein), comprise the entire agreement between you and publisher (and CCC) concerning this licensing transaction. In the event of any conflict between your obligations established by these terms and conditions and those established by CCC's Billing and Payment terms and conditions, these terms and conditions shall control.
14. Revocation: Elsevier or Copyright Clearance Center may deny the permissions described in this License at their sole discretion, for any reason or no reason, with a full refund payable to you. Notice of such denial will be made using the contact information provided by you. Failure to receive such notice will not alter or invalidate the denial. In no event will Elsevier or Copyright Clearance Center be responsible or liable for any costs, expenses or damage incurred by you as a result of a denial of your permission request, other than a refund of the amount(s) paid by you to Elsevier and/or Copyright Clearance Center for denied permissions.

LIMITED LICENSE

The following terms and conditions apply only to specific license types:
15. **Translation**: This permission is granted for non-exclusive world **English** rights only unless your license was granted for translation rights. If you licensed translation rights you may only translate this content into the languages you requested. A professional translator must perform all translations and reproduce the content word for word preserving the integrity of the article.
16. **Posting licensed content on any Website**: The following terms and conditions apply as follows: Licensing material from an Elsevier journal: All content posted to the web site must maintain the copyright information line on the bottom of each image; A hyper-text must be included to the Homepage of the journal from which you are licensing at http://www.sciencedirect.com/science/journal/xxxxx or the Elsevier homepage for books at http://www.elsevier.com; Central Storage: This license does not include permission for a scanned version of the material to be stored in a central repository such as that provided by Heron/XanEdu.
Licensing material from an Elsevier book: A hyper-text link must be included to the Elsevier homepage at http://www.elsevier.com . All content posted to the web site must maintain the copyright information line on the bottom of each image.

Posting licensed content on Electronic reserve: In addition to the above the following clauses are applicable: The web site must be password-protected and made available only to bona fide students registered on a relevant course. This permission is granted for 1 year only. You may obtain a new license for future website posting.
17. **For journal authors:** the following clauses are applicable in addition to the above:
Preprints:
A preprint is an author's own write-up of research results and analysis, it has not been peer-reviewed, nor has it had any other value added to it by a publisher (such as formatting, copyright, technical enhancement etc.).
Authors can share their preprints anywhere at any time. Preprints should not be added to or enhanced in any way in order to appear more like, or to substitute for, the final versions of articles however authors can update their preprints on arXiv or RePEc with their Accepted Author Manuscript (see below).

If accepted for publication, we encourage authors to link from the preprint to their formal publication via its DOI. Millions of researchers have access to the formal publications on ScienceDirect, and so links will help users to find, access, cite and use the best available version. Please note that Cell Press, The Lancet and some society-owned have different preprint policies. Information on these policies is available on the journal homepage.
Accepted Author Manuscripts: An accepted author manuscript is the manuscript of an article that has been accepted for publication and which typically includes author-incorporated changes suggested during submission, peer review and editor-author communications.
Authors can share their accepted author manuscript:

- immediately
  - via their non-commercial person homepage or blog
  - by updating a preprint in arXiv or RePEc with the accepted manuscript
  - via their research institute or institutional repository for internal institutional uses or as part of an invitation-only research collaboration work-group
  - directly by providing copies to their students or to research collaborators for their personal use
  - for private scholarly sharing as part of an invitation-only work group on commercial sites with which Elsevier has an agreement
- After the embargo period
  - via non-commercial hosting platforms such as their institutional repository
  - via commercial sites with which Elsevier has an agreement

In all cases accepted manuscripts should:

- link to the formal publication via its DOI
- bear a CC-BY-NC-ND license - this is easy to do
- if aggregated with other manuscripts, for example in a repository or other site, be shared in alignment with our hosting policy not be added to or enhanced in any way to appear more like, or to substitute for, the published journal article.

Published journal article (JPA): A published journal article (PJA) is the definitive final record of published research that appears or will appear in the journal and embodies all value-adding publishing activities including peer review co-ordination, copy-editing, formatting, (if relevant) pagination and online enrichment.
Policies for sharing publishing journal articles differ for subscription and gold open access articles:
Subscription Articles: If you are an author, please share a link to your article rather than the full-text. Millions of researchers have access to the formal publications on ScienceDirect, and so links will help your users to find, access, cite, and use the best available version.
Theses and dissertations which contain embedded PJAs as part of the formal submission can be posted publicly by the awarding institution with DOI links back to the formal publications on ScienceDirect.
If you are affiliated with a library that subscribes to ScienceDirect you have additional private sharing rights for others' research accessed under that agreement. This includes use for classroom teaching and internal training at the institution (including use in course packs and courseware programs), and inclusion of the article for grant funding purposes.
Gold Open Access Articles: May be shared according to the author-selected end-user license and should contain a CrossMark logo, the end user license, and a DOI link to the formal publication on ScienceDirect.
Please refer to Elsevier's posting policy for further information.
18. **For book authors** the following clauses are applicable in addition to the above:
Authors are permitted to place a brief summary of their work online only. You are not

allowed to download and post the published electronic version of your chapter, nor may you scan the printed edition to create an electronic version. **Posting to a repository:** Authors are permitted to post a summary of their chapter only in their institution's repository.
19. **Thesis/Dissertation**: If your license is for use in a thesis/dissertation your thesis may be submitted to your institution in either print or electronic form. Should your thesis be published commercially, please reapply for permission. These requirements include permission for the Library and Archives of Canada to supply single copies, on demand, of the complete thesis and include permission for Proquest/UMI to supply single copies, on demand, of the complete thesis. Should your thesis be published commercially, please reapply for permission. Theses and dissertations which contain embedded PJAs as part of the formal submission can be posted publicly by the awarding institution with DOI links back to the formal publications on ScienceDirect.

Elsevier Open Access Terms and Conditions
You can publish open access with Elsevier in hundreds of open access journals or in nearly 2000 established subscription journals that support open access publishing. Permitted third party re-use of these open access articles is defined by the author's choice of Creative Commons user license. See our open access license policy for more information.
Terms & Conditions applicable to all Open Access articles published with Elsevier:
Any reuse of the article must not represent the author as endorsing the adaptation of the article nor should the article be modified in such a way as to damage the author's honour or reputation. If any changes have been made, such changes must be clearly indicated.
The author(s) must be appropriately credited and we ask that you include the end user license and a DOI link to the formal publication on ScienceDirect.
If any part of the material to be used (for example, figures) has appeared in our publication with credit or acknowledgement to another source it is the responsibility of the user to ensure their reuse complies with the terms and conditions determined by the rights holder.
Additional Terms & Conditions applicable to each Creative Commons user license:
CC BY: The CC-BY license allows users to copy, to create extracts, abstracts and new works from the Article, to alter and revise the Article and to make commercial use of the Article (including reuse and/or resale of the Article by commercial entities), provided the user gives appropriate credit (with a link to the formal publication through the relevant DOI), provides a link to the license, indicates if changes were made and the licensor is not represented as endorsing the use made of the work. The full details of the license are available at http://creativecommons.org/licenses/by/4.0.
CC BY NC SA: The CC BY-NC-SA license allows users to copy, to create extracts, abstracts and new works from the Article, to alter and revise the Article, provided this is not done for commercial purposes, and that the user gives appropriate credit (with a link to the formal publication through the relevant DOI), provides a link to the license, indicates if changes were made and the licensor is not represented as endorsing the use made of the work. Further, any new works must be made available on the same conditions. The full details of the license are available at http://creativecommons.org/licenses/by-nc-sa/4.0.
CC BY NC ND: The CC BY-NC-ND license allows users to copy and distribute the Article, provided this is not done for commercial purposes and further does not permit distribution of the Article if it is changed or edited in any way, and provided the user gives appropriate credit (with a link to the formal publication through the relevant DOI), provides a link to the license, and that the licensor is not represented as endorsing the use made of the work. The full details of the license are available at http://creativecommons.org/licenses/by-nc-nd/4.0.
Any commercial reuse of Open Access articles published with a CC BY NC SA or CC BY NC ND license requires permission from Elsevier and will be subject to a fee.
Commercial reuse includes:

- Associating advertising with the full text of the Article
- Charging fees for document delivery or access

- Article aggregation
- Systematic distribution via e-mail lists or share buttons

Posting or linking by commercial companies for use by customers of those companies.

20. **Other Conditions**:

v1.9

Questions? customercare@copyright.com or +1-855-239-3415 (toll free in the US) or +1-978-646-2777.